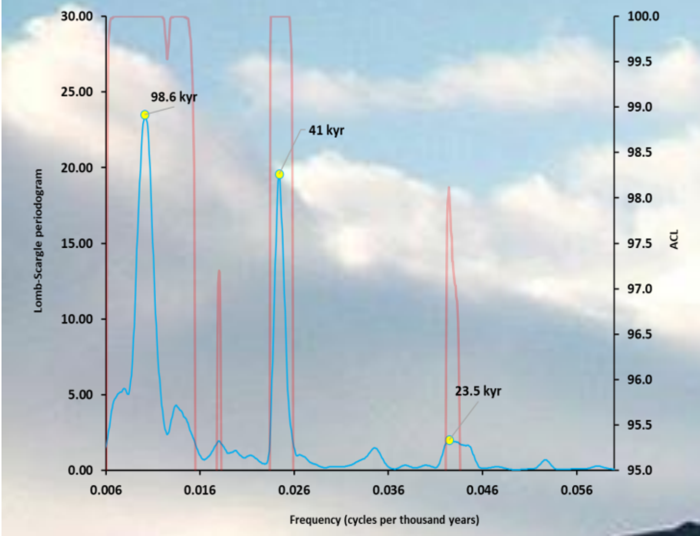

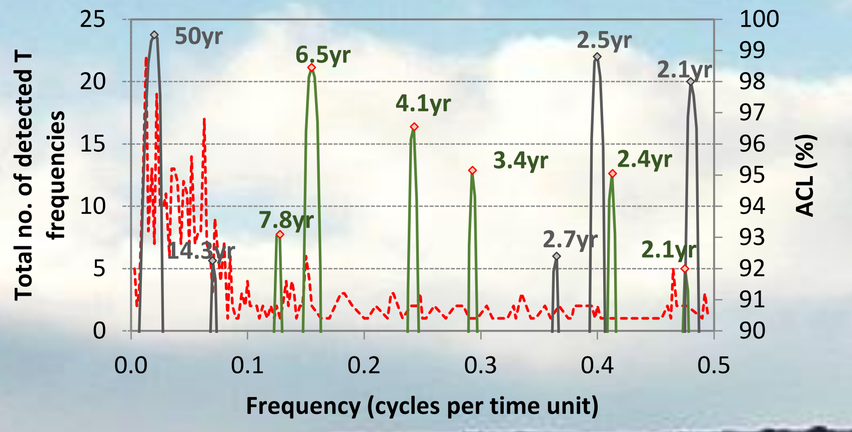

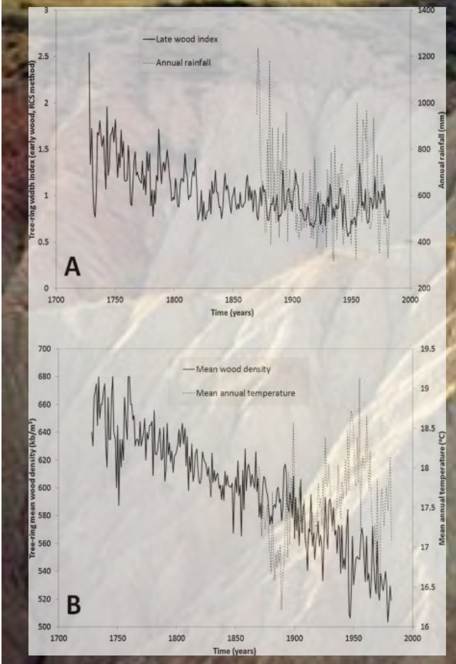

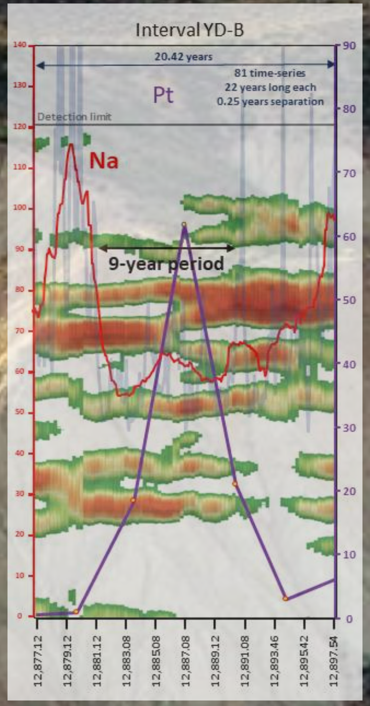

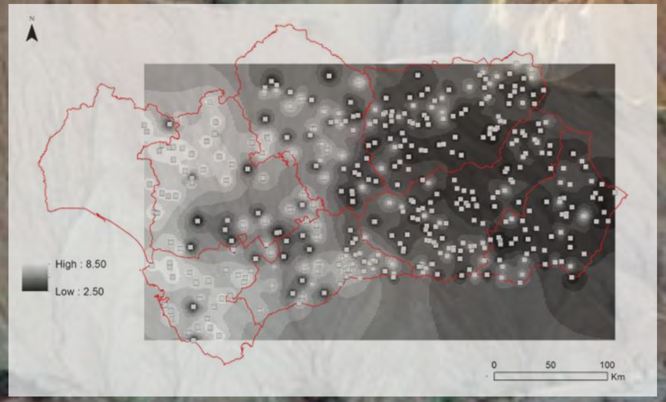

Global evolution of paleoclimate during the Quaternary Period: cyclostratigraphic integration of terrestrial and marine proxies

José Sánchez Morales

PhD Thesis

2023

Global evolution of paleoclimate during the Quaternary Period: cyclostratigraphic integration of terrestrial and marine proxies

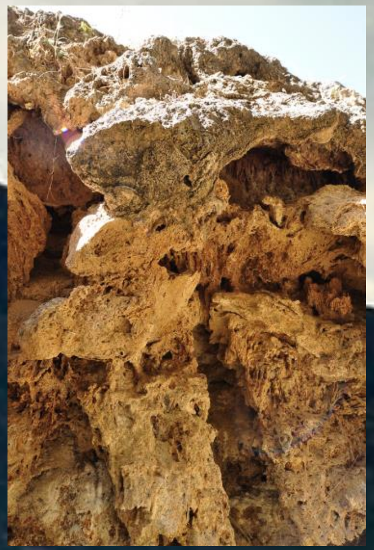

José Sánchez Morales
PhD Thesis, 2023

Programa Doctorado
Ciencias de la Tierra

UNIVERSIDAD
DE GRANADA

Editor: Universidad de Granada. Tesis Doctorales
Autor: Jose Sánchez Morales
ISBN: 978-84-1117-892-1
URI: https://hdl.handle.net/10481/82539

Universidad de Granada

Escuela Internacional de Posgrado

Global evolution of paleoclimate during the Quaternary Period: cyclostratigraphic integration of terrestrial and marine proxies

Tesis Doctoral presentada por:
José Sánchez Morales
Doctorando de la Universidad de Granada,
Programa de Doctorado en Ciencias de la Tierra (B08.56.1)

Tesis Doctoral co-dirigida por:
Francisco Javier Rodríguez Tovar
Catedrático de Paleontología de la Universidad de Granada

Eulogio Pardo Igúzquiza
Doctor en Ciencias Geológicas

Granada, 2023

UNIVERSIDAD
DE GRANADA
Departamento de Estratigrafía
y Paleontología

Programa Doctorado
Ciencias de la Tierra

ugr Universidad de Granada

Programa Doctorado
Ciencias de la Tierra

D. Francisco Javier Rodríguez Tovar, Catedrático de la Universidad de Granada y co-director de la presente Tesis Doctoral.

D. Eulogio Pardo Igúzquiza, Doctor, investigador del IGME, y co-director de la presente Tesis Doctoral.

HACEN CONSTAR:

Que la presente tesis titulada **Global evolution of paleoclimate during the Quaternary Period: cyclostratigraphic integration of terrestrial and marine proxies**, cumple las condiciones necesarias para que su autor, **José Sánchez Morales**, opte al título de Doctor en Ciencias Geológicas por la Universidad de Granada.

Granada, enero de 2023

VºBº del Co-Director	VºBº del Co-Director	Doctorando
Fdo. Francisco Javier Rodríguez Tovar	Fdo. Eulogio Pardo Igúzquiza	Fdo. José Sánchez Morales

Agradecimientos

Quisiera agradecer por su paciencia y comprensión a toda mi familia. Sin su apoyo moral y emocional esta tesis doctoral hubiera sido imposible de realizar.

A mis directores Francisco Javier Rodríguez Tovar y Eulogio Pardo Igúzquiza, por instruirme en el clima Cuaternario y en las técnicas metodológicas apropiadas para su estudio. Gracias a ellos he podido manejar una ingente cantidad de datos, sin perder el foco necesario y el rigor científico.

A Francisco Javier Rodríguez Tovar por guiarme en el arduo a la vez que satisfactorio camino de la investigación científica, sabiendo lidiar con los problemas de una forma pragmática y efectiva.

Al planeta Tierra por su complejidad, sus secretos y sus enigmas.

A todos los hombres y mujeres de todos los tiempos que habiendo contribuido al conocimiento científico general, se han dedicado especialmente al estudio geológico del clima en épocas pasadas.

Table of Contents

APPENDIXES

ABSTRACT

The Quaternary period comprises a recognisable climate succession of glacial and interglacial periods for the last 2.58 Ma. The Quaternary climate has governed all past and present aspects of human evolution, and it will do so in the future. Thus, to advance in understanding Quaternary paleoclimate history is considered as of special interest to improve knowledge of past, present and future climates. The Quaternary climate is primarily affected by Milankovitch orbital forcing which constitutes the main driver of the observed climate variability, but also by sub-Milankovitch solar variability at shorter time scales. The general aim of this Thesis is to improve the understanding of some of the past climate changes occurred during the Quaternary, based on a detailed cyclostratigraphic analysis of selected proxies.

This PhD Thesis has used the framework of the cyclostratigraphic analysis, which assumes that the climate signal is preserved in the geological record, and more specifically the spectral analysis methodology, for identifying the involved climate cycles. This research has aimed for shedding light on some diverse but hot topics in Quaternary paleoclimate research from a global perspective. The present work analyses the availability of open proxy data in deep, including a detailed assessment of their geographic and temporal properties, considering both marine and terrestrial environments. By doing that, it has been proven that it is possible to re-use third-party scientific data for new research. Thus, different scientific objectives have been targeted, including the development of new methodologies for the study of paleoclimate. A novel computer method for visualising results from spectral analysis applied to Milankovitch cycles is presented. At a local and short-temporal scale a new method for reconstructing climate variables using tree-ring data has been successfully applied to the Sierra de las Nieves (southern Spain). The spectral analysis applied to precipitation and temperature data for the past decades has revealed new evidence linking the Andalusia hydroclimate variability with the Mediterranean Oscillation. At a global scale, new categorisation of the climatic cycles occurring during the Holocene period, by using oxygen time series and derived from speleothems, is presented here, which speaks of Eurasia having a different evolution and climate forcing at millennial time scales. Respect to abrupt climate changes, new insights into the onset of the last cold glacial before the Holocene, known as the Younger Dryas period, are exposed by linking sodium and wind variables, and Platinum spikes to a lesser extent. All these advancements contribute to the understanding of the most recent Earth's past climate and lay the foundations for future research using climate proxy data for a global perspective.

RESUMEN

El periodo Cuaternario contiene una reconocible sucesión climática de periodos glaciares e interglaciares acaecida durante los últimos 2.58 Ma. El clima cuaternario ha gobernado todos los aspectos pasados y presentes de la evolución humana, y continuará siendo así en el futuro. Por consiguiente, avanzar en la comprensión del paleoclima del Cuaternario se considera de especial interés para mejorar el conocimiento de climas pasados, presentes y futuros. El clima cuaternario está dominado principalmente por los ciclos orbitales de Milankovitch, que controlan la observada variabilidad climática, y por los ciclos solares a escalas temporales menores, sub- Milankovitch. El propósito general de la presente tesis es mejorar el conocimiento de algunos de los cambios climáticos acontecidos durante el Cuaternario, sobre la base de un análisis cicloestratigráfico detallado de indicadores paleoclimáticos seleccionados.

La presente tesis doctoral ha seguido la estructura metodológica del análisis cicloestratigráfico, que asume que la señal climática se ha preservado en el registro geológico, y en concreto se ha utilizado la metodología del análisis espectral, para identificar los ciclos climáticos implicados. Se trata de abordar algunos temas de especial interés en la investigación paleoclimática del Cuaternario desde una perspectiva global. El presente trabajo analiza en detalle la disponibilidad de datos de libre acceso de indicadores paleoclimáticos, incluyendo un preciso análisis de sus propiedades geográficas y temporales, considerando ambientes terrestres y marinos. Se ha podido constatar la posibilidad de reutilizar datos procedentes de investigaciones previas para llevar a cabo nuevas investigaciones de interés. Se plantearon diferentes objetivos científicos, incluyendo el desarrollo de nuevas metodologías para el estudio del paleoclima. Se presenta un novedoso método de software para visualizar resultados de análisis espectral aplicado a ciclos de Milankovitch. A escala local se ha utilizado un nuevo método para la reconstrucción de variables climáticas de siglos pasados, usando anillos de árboles en la Sierra de las Nieves (sur de España). El análisis espectral aplicado a datos de precipitación y temperatura de las últimas décadas ha revelado nuevas evidencias de la conexión entre la variabilidad hidroclimática en Andalucía con la denominada Oscilación Mediterránea. A escala global, se presenta la caracterización de ciclos climáticos que ocurrieron durante el Holoceno, mediante el uso de series temporales de oxígeno procedentes de espeleotemas, que indican que Eurasia tuvo distinta evolución y control climático a escalas temporales milenarias. Respecto de cambios climáticos bruscos, se presentan nuevas evidencias sobre el comienzo del último periodo frío glacial previo al Holoceno, conocido como Younger Dryas, integrando datos de sodio, variables de viento y picos de concentración de platino. La investigación

desarrollada en esta tesis contribuye al conocimiento del periodo climático más reciente, sentando las bases para futuros trabajos integrando datos procedentes de indicadores paleoclimáticos desde una perspectiva global.

1 Chapter I. Introduction

This chapter introduces the Quaternary climate (1.1), focusing on the "Quaternary subdivisions and their climate basis" (1.1.1), "Orbital forcing and Pleistocene glaciations" (1.1.2) and "The Upper Pleistocene and Holocene climates" (1.1.3). Then, "Cyclostratigraphic analysis" (1.2) is presented as the best methodology framework for the study of the Quaternary climate variability, including "Definition" (1.2.1), "Milankovitch band cycles and astrochronology" (1.2.2), "Sub-Milankovitch cycles" (1.2.3) and "Spectral analysis" (1.2.4). Finally, the "Motivation and Research hypotheses" (1.3) covers the justification and the scientific framework of the present work.

1.1 Quaternary climate

1.1.1 Quaternary subdivisions and their climate basis

The Quaternary period comprises the last 2.58 Myr according to the chronostratigraphic scale (Gradstein and Ogg, 2020) from the most recent official Geological Time Scale (GTS2020). The present research uses the widely used subdivision of the Quaternary, into Holocene (Present – 11.7 Ka b2k; before AD 2000) and Pleistocene (0.0117 – 2.58 Ma b2k), and it does not adopt the proposed Anthropocene (Crutzen and Stoermer, 2000), which is under strong debate today (Gibbard and Head, 2020). Minor subdivisions, or stages, are also defined in the GTS2020 for the two main Series of the Quaternary System: Meghalayan (Present – 4.2 Ka b2k), Northgrippian (4.2 – 8.2 Ka b2k) and Greenlandian (8.2 – 11.7 Ka b2k) for the Holocene, and Upper Pleistocene – unnamed stage – (0.0117 – 0.129 Ma b2k), Chibanian (0.129 – 0.774 Ma b2k), Calabrian (0.774 – 1.8 Ma b2k) and Gelasian (1.8 – 2.58 Ma b2k) for the Pleistocene.

The Quaternary climate has been often referred as the Quaternary glaciation as this geological period is punctuated by an initial and recognisable global cooling between 2.8 and 2.4 Ma. However, it was not until 2009 when the International Union of Geological Sciences (IUGS) ratified the proposal of lowering the boundary of the Quaternary System/Period from 1.8 to 2.58 Ma. Before 2009, the Global Stratotype Section and Point (GSSP) for the Calabrian Stage defined by the Vrica stratotype (Calabria, Italy), was considered the base of the Pleistocene, hence of the Quaternary (base was dated at 1.80 Ma by astronomical calibration). Prior to the ratification, the Gelasian Stage defined by the GSSP at Monte San Nicola in southern Sicily, was considered part of the Neogene System (base was dated at 2.588 Ma by astronomical tuning). The rationale behind this important adoption was that the Gelasian Stage better represented the initiation of the major cooling events (Gibbard et al., 2005). Thus, the base of the Gelasian stage (which notably coincides with the Marine Isotope Stage (MIS) number 103), underlines the importance of the climate origin for defining the start of the Quaternary. Additionally, this boundary also approximates the Gauss–Matuyama palaeomagnetic reversal (Rio et al., 1998), convenient when the stratigraphic correlation must be carried out globally outside the stratotype section and/or to non-marine sediments.

Although the beginning of the Quaternary officially approximates MIS 103, the start of the cooling trend is in fact formed by a succession of different cooling phases starting earlier than MIS 103 with the MIS denoted as G10 (inside the Pliocene) up to the younger MIS 96 (Gibbard et al., 2010). This is precisely another main characteristic of the whole Quaternary climate, in the sense that it is affected by climatic cycles of diverse magnitude and temporal scale, resulting in the existence of glacial-interglacial sequences over the entire length of this period. These cycles within the Quaternary are recognisable in the sedimentary record, particularly in the marine record, which has the advantage of deriving the global ice volume by means of benthic foraminiferal $\delta^{18}O$ record. One main characteristic of these climatic fluctuations is the asymmetric transition between glacial and interglacial states. This characteristic has not gone unnoticed: any glacial cycle during the late Pleistocene takes much longer to develop glacial conditions (~10 times) than to develop an interglacial by means of an abrupt termination (Broecker and Van Donk, 1970).

The significance of these climate cycles in the Quaternary has allowed a climate-based approach for further studying and subdividing this period. The most adopted methodology today is the analysis of oxygen isotope time series ($\delta^{18}O$), which are extracted from analyses on microfossils in deep sea cores, followed by the classification method of using odd numbers for interglacials (starting with the warm MIS 1 for the Holocene) and even numbers for glacial periods. Thus, at least 103 MIS events have been defined so far reflecting major temperature fluctuations during the Quaternary (Lisiecki and Raymo, 2005). The Quaternary $\delta^{18}O$ time series also allows the definition of isotope substages (e.g., see Shackleton (1969) for the identification of the substages MIS 5a, 5b, 5c, 5d, and 5e). There has been less formality and structures at establishing these substages over time, although there has been a recent attempt for rigorously label them (Railsback et al., 2015). For instance, the substages 5a, 5c and 5e would represent warmer periods whereas 5b and 5d would represent colder periods, all five substages within the warm MIS 5.

As today, the Upper Pleistocene Subseries (0.0117-0.129 Ma) currently does not have a defined official stage (or unnamed), although the consensus is that its base should coincide with the onset of the interglacial MIS 5e (Gibbard and Head, 2020), which approximates the terrestrial interglacial in northwest Europe known as the Eemian stage. The last 129 Ka not only includes the onset of the last interglacial, but the glacial period towards MIS 5, 4, 3 and 2, being the number 2 corresponding to the so-called Last Glacial. The excellent resolution of the EPICA Dome C ice core in Antarctica, as well as the presence of a methane spike which aligns well with rising temperatures from North Atlantic proxies, including the increase of temperate tree pollen in Europe, made this core to be proposed as becoming the future GSSP for the Upper Pleistocene (Head, 2019), although to date no decision has been made yet.

The stratigraphic successions for the Quaternary have been defined mostly by using both marine microfossils and magnetostratigraphic criteria (GTS2020), but still every series holds significant climate information describing the main aspects of the Quaternary paleoclimate evolution. Thus, starting with the Pleistocene series, the Gelasian (1.8-2.58 Ma) is characterized by the evidence of northern hemisphere glacial cycles paced by obliquity (Lourens et al., 2005). The Calabrian (0.774-1.8 Ma), the former lower boundary of the Quaternary, reflects the arrival of northern fauna (cold species) to the Mediterranean as well as the continuation (or stabilization) of the glacial cycles from the Calabrian stage (Cita et al., 2012). It follows the important "Middle Pleistocene Transition" (MPT), which timing is still debatable and varying depending on different criteria and/or authors. But, if taken between 0.7 and 1.25 Ma (Elderfield et al., 2012), the MPT was initiated and terminated within the Calabrian stage. However, a longer duration for the MPT has been proposed: 0.4 and 1.4 Ma (Head and Gibbard, 2015), therefore affecting the Chibanian stage (0.129-0.774 Ma). In any case, the Chibanian clearly exposes the occurrence of the quasi-100 Kyr glacial cycles after the MPT (Head and Gibbard, 2015; Suganuma et al., 2021). All these three stages of the Pleistocene Series have their corresponding GSSPs defined in marine sediments.

Alternatively, it is worth noting that there is an immense amount of past and present paleoclimate research based on terrestrial records, such as glacial deposits, loess and/or lake records that have contributed to the climate knowledge of the Quaternary, well outside the marine scope, but even when their correlation to ocean sediments is feasible at a global scale, this is usually best limited to the last glacial-interglacial cycle (Gibbard and Head, 2020). On the other hand, the uncontestably highly precision of speleothems and ice cores make them good candidates for future Quaternary stratigraphic divisions, based on global climate fluctuations over terrestrial environments. For instance, the Greenland Ice Core Chronology 2005 (GICC05), which was based on visual annual layer counting from three ice cores (NGRIP, GRIP and DYE-3), including variations in $\delta^{18}O$, δD and impurity data (Svensson et al., 2008), represents the best available time scale for the last 60 Ka (Wolff et al., 2010), but its uncertainty largely increases prior 60 Ka (Wolff et al., 2010; Groen and Storey, 2022). The INTIMATE (INTegration of Ice-core, MArine and TErrestrial records) project provided with an extended Greenland ice chronology reaching back as far as ~120 Ka (Rasmussen et al., 2014). The future project of an 1.5-Myr ice core in Antarctica (Wolff et al., 2022) would certainly improve the existing limitation of Antarctic ice records at ~800 Ka, and speleothems from East Asia at ~640 Ka (Cheng et al., 2016b). The prospect of extending the current ice based chronologies is especially important, as it can potentially allow for better synchronization of both Greenland ice-cores and speleothems (U-Th) time scales.

1.1.2 Orbital forcing and Pleistocene glaciations

The current Earth climate's paleoclimate paradigm to justify the observed alternation of glacials and interglacials during the Quaternary (and other geological periods) invokes changes in Earth's orbit (Milankovitch, 1941; Hays et al., 1976; Imbrie and Imbrie, 1980; Maslin, 2016), hence the term "orbital forcing". Therefore, the orbital variations are the main cause for the received insolation variations over time, being ultimately responsible for the occurrence of past, or future, ice ages. Milankovitch postulated that negative variations in summer insolation at 65 °N were the main cause for the building up of ice ages, because of the crucial facts that the glaciers would be mostly affected by summer insolation and the continental mass was mainly located in the northern hemisphere (Milankovitch, 1941).

Broadly speaking, the influence of the Sun, Moon and other planets to a lesser extent, exerts the combination of three distinct orbital parameters known as eccentricity (principal periods at 95, 99, 124, 131 and 405 Kyr), obliquity (principal period at 41 Kyr) and precession (principal periods at 24, 22, 19 and 17 Kyr) (periods from Hinnov and Hilgen, 2012). The eccentricity relates to the movement of the Earth around the Sun and it changes from nearly circular to elliptical, the obliquity relates to the movement of the Earth's axial tilt with respect to the orbital plane and it varies between 22.1 and 24.5 degrees, and the precession is the combined result of two movements: (1) change in the orientation of the Earth's rotational axis which describes a cone in space and (2) precession of the Earth's orbit around the Sun (Maslin, 2016). The eccentricity component is the weakest of all three at producing insolation variations, although it does modulate the amplitude of the precession cycle (Lisiecki, 2010).

Different orbital astronomical solutions have been developed over time (e.g., Berger, 1978a, 1978b; Laskar et al., 2004, 2011a) and this has helped the settlement of the so-called "astronomical tuning" methods (Hays et al., 1976; Imbrie et al., 1984; Martinson et al., 1987; Muller and MacDonald, 2002), which aim for producing time scales from empirical paleoclimate time series by tuning to the corresponding estimated insolation time series and their orbital components. One of the first and widely used orbitally tuned timescales was the SPECMAP of the Quaternary (Imbrie et al., 1984; Thompson and Goldstein, 2006). Nonetheless, all the orbital solutions have the important constrain of their validity range, although the Quaternary period is well within any validity interval and outside this limitation; e.g., 2.58 Ma against a validity limit of 60 Ma (Laskar et al., 2011b).

However, the paleoclimate debate about the causes of the climate response to orbital forcing is far from being fully resolved. Especially problematic in the Milankovitch theory are the observed ~100 Kyr glacial cycles in the geological record for the past ~700-800 Kyr. These 100 Kyr cycles represent a change to the previous succession of glacial cycles separated by ~40 Kyr that are observable at earlier Pleistocene records, without any expected change in the solar forcing configuration. Precisely, the MPT accounts for the change from one cyclicity state to the other. The MPT is not solely characterised by a profound change in cyclicity, but for an increasingly non-linear response to orbital forcing, including strong asymmetry in global ice volume cycles and a stepped decrease in the relative durations of interglacials (Head and Gibbard, 2015). Some authors have even recommended the adoption of the term Early-Middle Pleistocene transition, or EMPT, instead of Middle Pleistocene transition, or MPT (Head and Gibbard, 2015).

One of the initial assumptions for operating with the orbital forcing framework was based on a linear climate response to precession and obliquity (Hays et al., 1976), but it was relaxed in favour of non-linear responses for the 100 Kyr cycles. It was suggested that the building up and dynamics of the ice sheets could hold the most plausible answer to this problem, mainly because the eccentricity cycle was out of phase with the observed glacial cycles (1) and the radiation change contribution of the eccentricity was known to be too small (2). But also, even assuming that the eccentricity cycle was pacing the observed 100 Kyr variability in the late Pleistocene, the lack of the 413 Kyr long component of eccentricity in the δ^{18}O record was problematic (Imbrie and Imbrie, 1980; Imbrie et al, 1993). Consequently, it was a matter of time that the 100 Kyr cyclicity for the last 1.2 Myr was explained as the response from internal feedback mechanisms involving the atmosphere, land and oceans that were modulating the driving orbital force (Imbrie et al., 1993). Later on, it was the interaction between obliquity and the eccentricity-modulation of precession the factors that were considered to be responsible for the observed 100 Kyr ice ages cyclicity (Raymo, 1997). Some authors have objected that the dubious role of eccentricity in the late Pleistocene, cannot diminish the importance of the eccentricity forcing for the early Pleistocene record prior to the MPT (Clemens and Tiedemann, 1997).

As opposed to the former studies supporting the direct or indirect role of eccentricity in the framework of orbital forcing, different studies support that it is the obliquity cycle the driver of the 100 Kyr climatic cycles in the late Pleistocene. One of these proposals is that the obliquity insolation maxima are very effective at causing basal warming in ice sheets but only when these are thick enough. Therefore, the climate state skips one or two obliquity cycles until the deglaciation process can be effective, thus producing glaciation durations of 80-120 Kyr on average as a result (Huybers and Wunsch, 2005), implying that the transition from ~40 to ~100 Kyr does not involve any change in the physics of glacial cycles (Huybers, 2007). Another proposal using Pleistocene derived temperature records supported a key role of obliquity throughout the entire Pleistocene by introducing the existence of non-linear responses to obliquity forcing (Liu et al., 2008). More recently, it has been proposed that the change in the frequency of obliquity cycles after the MPT, but also for the existence of larger ice sheets, would be the consequence of an increase in the deglaciation threshold and in the number of skipped insolation peaks (Tzedakis et al., 2017).

1.1.3 The Upper Pleistocene and Holocene climates

The last glacial period or the period since the last interglacial MIS 5, is characterised by a millennial scale (sub-Milankovitch) climate variability as seen through the numerous datasets extracted from ice cores (Wolff et al., 2010). When looking at the last ~123 Ka the temperature record is characterised by the presence of the so-called Dansgaard–Oeschger (D–O) climatic events (Bond et al., 1993; Dansgaard et al., 1993; Broecker et al., 2010), which are defined as atmosphere and ocean fluctuations that alternated between full glacial conditions, or stadials, and relatively mild conditions, or interstadials. A total of twenty-five D–O events were recognised in the paleoclimate record, mainly in the northern hemisphere but not limited to. Furthermore, the so-called Greenland Stadials (GS) and Greenland Interstadials (GI) from the Greenland ice chronologies (Rasmussen et al., 2006, 2014) truly reflect the timing and duration of D–O events. Their southern expressions are "delayed" temperature variations in the Antarctic ice record, that have been explained by means of the Atlantic Meridional Overturning Circulation (AMOC) and the bipolar seesaw mechanism connecting the Atlantic Ocean with the Southern Ocean (EPICA Community Members, 2006). In the South, the Antarctic temperature record is more considered to be of opposite sign and "asynchronous" to the northern hemisphere record (Gottschalk et al., 2015; Menviel et al., 2020). In any case, the carbon cycle response to D–O events cannot be solely attributed to changes in the AMOC (Gottschalk et al., 2015). Other authors have suggested that the ice shelf and sea ice interactions, together with ocean circulation, would explain the D–O events (Boers et al., 2018). The nature and processes behind the

AMOC is still highly debated (Menviel et al., 2020). Other important phenomena involving ice-sea dynamics within the context of the last glacial period are the Heinrich events (Heinrich, 1988). These events were episodic ice-rafted debris discharges from the northern hemisphere ice sheet that have been found in marine sediments, and typically occurred during some -not all- cold stadials of the D–O events. Although both phenomena are intrinsically related, their origin is still unknown (Mann et al., 2021).

The Holocene Series, comprising 11,700 years of Earth's history (Present – 11.7 Ka b2k), has been recently divided into Lower, Middle and Upper Holocene respectively (Walker et al., 2018; Walker et al., 2019), including the three new corresponding stages: the Greenlandian, the Northgrippian and the Meghalayan. The criteria for subdividing the Holocene is based on event stratigraphy and/or climate events that have been recognised globally in many paleoclimate archives and/or proxies: the ~8.2 Ka BP and ~4.2 Ka BP climate events (Walker et al., 2019; Gibbard and Head, 2020).

The Greenlandian is the lowest stage of the Holocene Series which ended the Greenland stadial 1 (GS-1), or Younger Dryas period. It starts (11.7 Ka b2k) by an abrupt rise of temperature (~10 °C), accompanied by heavier isotope values, reduced dust concentrations and sea salt values, and increased annual ice-layer thickness (Walker et al., 2019). The Northgrippian represents the Middle Holocene, corresponding to a sharp global cooling event (~8.2 Ka BP) that is marked by a decrease in temperature (~5 °C), including lighter oxygen and deuterium values, decreased annual ice-layer thickness, minimum atmospheric methane and increased atmospheric CO_2, and increased dust (Walker et al., 2019). The Meghalayan marks the beginning of the Upper Holocene at 4.2 Ka BP, representing an abrupt reduction in precipitation and/or enhanced aridification that affected mainly mid- and low latitudes.

Despite the consensus at differentiating the Holocene climate at millennial-scale into three main phases: early deglaciation phase, Holocene Thermal Optimum and Neoglacial period (Wanner et al., 2011), and more recently at establishing the stratigraphic boundaries for the Holocene Stages (Walker et al., 2019), the causes of the global climate swifts at 4.2 and 8.2 Ka remain unclear. For example, the quasi periodic nine ice-rafting pulses, or “Bond” cycles, identified in the North-Atlantic sediments as strong cold episode evidence (Bond et al., 1997), were proposed to be driven by solar forcing (Bond et al., 2001). In this context, the 4.2 Ka transition corresponds chronologically to the 4th “Bond” cycle in the Holocene (numbered 0 to 8). However, recent work has suggested that the North Atlantic does not hold evidence for a widespread cold climatic anomaly around 4.2 Ka, but for an overall decline in temperature starting at 5 Ka and intercalated by multi-decadal century-scale fluctuations (Bradley and Bakke, 2019). The involved phenomena in the development of the 4.2 event in northern latitudes has been attributed primarily to the strengthening and expansion of the Siberian high-pressure cell blocking the westerlies, bringing aridity to Europe and W Asia (Perşoiu et al., 2019). The proposed causes for explaining cold events during the Holocene includes not only processes such as meltwater flux into the North Atlantic, low solar activity, explosive volcanic eruptions, and fluctuations of the thermohaline, but internal dynamics and/or feedbacks (Wanner et al., 2011). The 8.2 Ka event has been often invoked as the result of capping the oceanic thermohaline circulation by freshwater forcing generated by a massive outflow from the glacial lakes Agassiz and Ojibway through the Hudson Strait (Barber et al., 1999). The slowdown of the Atlantic Meridional Overturning Circulation (AMOC) is still referred as the most probable cause for the 8.2 event (Morrill et al., 2013) and represents a good scenario for freshwater forcing simulations (Matero et al., 2017).

1.2 Cyclostratigraphic analysis

1.2.1 Definition

The term "Cyclostratigraphy" has been defined as *"the study of stratigraphic records of environmental cycles"* (Fischer et al., 1990; Weedon, 2003). In paleoclimate research, we consider these repeated variations in the strata, or cycles, from the point of view of their origin or genesis, which means that they were influenced by climate processes that are periodic or quasi-periodic, and capable of transmitting their cyclical behaviour to the sedimentary record (Gilbert, 1895). These cycles can be potentially caused by basically two main types of processes, first are those oscillating systems internal to the Earth's atmosphere-ocean-cryosphere system and secondly are those external forcing mechanisms, such as solar variability, Earth-orbital changes and/or volcanic eruptions, to cite the most important.

In cyclostratigraphy, these processes can range from the hour to the age of the Earth (Mitchell, 1976). The sedimentary record is distorted and incomplete by definition, so it was emphasized that in order for the stratigraphic variations to become cycles, the idealized environmental models to produce the cycles should be predictable. In this context of irregularity, the stochastic models are more suitable predictors (Schwarzacher, 1975). Assuming the term "cycle" requires the property of time attached to it, which means that it is produced at regular or quasi-regular intervals, it is a requirement the identification of the nature mechanism that causes the cycle (Schwarzacher, 2000).

The origin of the concept of "Allocycles" suggesting that the stratigraphic patterns are caused by forces outside the depositional system can be traced back to the 19th century.

For instance, first attempts to link the global climate with the orbital dynamics were made long ago, such as the idea of Pleistocene glacial epochs to be caused by cosmical causes (Croll, 1875), or the interpretation of the sedimentary record as variations caused by the orbital precessional cycle (Gilbert, 1895). Thanks to the advancement of the research of the Pleistocene during the 20th century, which expanded the view of the climate linked to orbital parameters, the study of astronomical cycles applied to earlier geological periods outside the Quaternary was attempted (Fischer, 1986). Inevitably, cyclostratigraphic research is primarily found in either stratigraphy and/or sedimentary studies (Rodríguez-Tovar, 2014). Today, the cyclostratigraphy is an essential part of the paleoclimate research and a very active field of research (Laskar, 2020). Actually, the presence of cyclic sediments in the geological strata is almost a requirement for defining GSSPs by the International Commission on Stratigraphy (Gradstein and Ogg, 2020).

1.2.2 Milankovitch band cycles and astrochronology

The cyclostratigraphy has largely benefited from advancement in astronomical models capable of predicting the Earth's movement across the Space but also from improvements in data analysis techniques (Hinnov, 2000), which has led to the development of the discipline called astrochronology and the creation of the astronomical time scale or ATS (Hinnov and Hilgen, 2012). The evolution of the cyclostratigraphy is highly linked to the process of validating the Milankovitch theory (occurrence of ice ages driven by astronomical cycles), which took place over the 20th century and in just a few decades. Thus, the Milankovitch cycles are central to the cyclostratigraphy.

It is worth noting that the harmonic analysis of the orbital parameters eccentricity (dimensionless), obliquity (degrees) and precession (dimensionless) reveals the quasi-periodic nature of these parameters (Hinnov and Hilgen, 2012). Thus, it is possible to detect principal components at 95, 99, 124, 131 and 405 Kyr for the eccentricity, 41 Kyr for the obliquity (with minor components at 29, 39 and 54 Kyr), and 17, 19, 22 and 24 Kyr for the precession. However, the inverse exercise of obtaining the main frequencies for the Milankovitch cycles, by analysing the incoming insolation for a particular region and for a specific day of the year, does not produce the same values. This is explained because the interannual radiation depends on the astronomical position of the Earth (day of the year), Sun's elevation (time of the day) and the latitude of the analysed region. This is particularly important to consider when analysing time series at astronomical scales, because for instance when analysing interannual time series at the time of the equinoxes (i.e., 21st March) obliquity signal is negligible. Another example is the precession cycle increasing its detectability in the hemisphere at its insolation maxima but decreasing at the opposite hemisphere (Berger at al., 1993).

Perhaps, the most useful feature of the astronomical modelling applied to paleoclimate research, hence the existence of the ATS, refers to the fact that is possible to correlate signal frequencies recorded in the sediments with the frequencies predicted by the theoretical models. The critical part is the choice of the target insolation curve generated by the astronomical models (Hinnov and Hilgen, 2012). The proposed time scales -astronomically tuned- of SPECMAC stack (Imbrie et al., 1984) and Ruddiman et al. (1986) for the late Pleistocene ice ages, was expanded into the Middle-Early Pleistocene and Pliocene (Shackleton et al., 1990). The addition of longer oxygen isotope records over time (i.e., Devils Hole), allowed more refinements in the orbital solutions (i.e., Laskar et al., 2004). The SPECMAC was improved by the publish of LR04 benthic $d^{18}O$ stack (Lisiecki and Raymo, 2005), and more recently we are able to go into much earlier periods due to the availability of more detailed astronomical solutions (Laskar, 2020), which has definitely conflicted the previously estimated radio-isotopic ages, generally ~3 to 12% younger than astronomical ages (Hinnov and Hilgen, 2012).

1.2.3 Sub-Milankovitch cycles

Long recognised and/or detected cycles representative of climate variability arise as a product of the internal variability of the Earth's climate system. These cycles are ultimately governed by Milankovitch cycles, but they are not driven directly by orbital forcing, hence the term Sub-Milankovitch band cycles. Additionally, to the internal variability, it is important to include those known cycles directly attributed to the solar activity, or Solar band, from millennial time scales to one year. Below one year, or Calendar band, refers to those cycles related to gravitational changes in the Earth-Moon system (tides) and those related to Earth's planet behaviour, such as the rotation induced circadian rhythms (daily) and the translation induced annual period, which ultimately translates into solar energy variations.

Generally, the climate response to these forcing mechanisms is non-linear as it involves feedbacks internal to the climate system. The first direct consequence is that this non-linearity likely distorts any obtained periods (and their amplitudes) of the significant frequencies in the analysed time series. Not all cycles exhibiting millennial scale periodicity below 19-21 Kyr can be considered outside astronomical forcing in the sub-Milankovitch category. In other words, some of the identified millennial scale cycles in the climate record are truly attributed to orbital forcing, because they are known sub-products or harmonics of orbital cycles, such as for instance the identification of the 11 Kyr and 5.5 Kyr cycles as harmonics of the precession cycle in equatorial regions (Berger et al., 2006).

On the other hand, the likelihood of a climate event predominantly manifested at specific astronomical configurations is not necessarily considered a sign of a linear response to orbital forcing either. Thus, the ice rafting noted as Heinrich events found in the North Atlantic domain, have been documented during times of winter minimum/summer maximum insolation and during summer minimum/winter maximum insolation, which coincided with a half precession cycle (Heinrich, 1988). However, the stadial-to-interstadial onset phases at which these events occurred had no systematic differences with other similar onset periods where no Heinrich events have been documented (Capron et al., 2021). Therefore, we need to be cautious at categorising a millennial scale cycle as derived from climate internal variability when it can be linked to orbital forcing under certain circumstances, or vice versa.

In the cyclostratigraphic analysis of the paleoclimate since the last glacial, one of the most important climate variability features at millennial time scales is the quasi 1,470-yr pacing of the Dansgaard-Oeschger (DO) events. This is perhaps one of the best canon examples of climate internal variability without a known driving mechanism. It has been traditionally interpreted as the expression of the North Atlantic Deep Water formation variability, but it has also been decoupled from it (Schulz, 2002). More recent tools such as the INTIMATE stratigraphic template, and the higher resolution of their defined Greenland Stadials (GS) and Greenland Interstadials (GI), potentially allows for further refinement of the classical DO periodicity, including the identification of new candidate DO events (Rasmussen et al., 2014). The debate on the causes and/or origin of the DO events is still unresolved (Capron et al., 2021 and references therein). The Heinrich events (layers of ice rafted debris (IRD) in the North Atlantic) happened during some of the DO events, but they are not usually considered a periodic climate feature but an irregular expression of the ice-sheet dynamics, although their exact causality is unknown (Pedro et al., 2022).

During the Holocene, similar ~1,470-year (±500) cycles known as Bond cycles (Bond et al. 1993, 1997, 2001) were associated with cold periods and surface circulation changes, in which migration of icy waters from the north to the south produced ice-rafting deposits. The Bond cycles were considered as mini DO events within the relatively stable Holocene (Bond et al., 1997). Later on, the Bond cycles were tentatively linked to solar variability, although amplified by hydrographic changes affecting the North Atlantic Deep Water production (Bond et al., 2001). The importance of the 1,500-yr cycles has also been spotted at Holocene storm dynamics in coastal sedimentary sequences (Sorrel et al., 2012).

A quasi 2,400-yr cycle was found in the analysis of radiocarbon concentration data and involved in the modulation of the solar Vries cycle ~200 yr (Sonnet, 1984). This millennial scale cycle has been detected in tree rings (Usoskin et al., 2016), and also linked to long-term solar activity (Charvátová, 2000). It has also been interpreted as a climatic effect on the rate of radiocarbon transfer between the atmosphere and the ocean for the last 8 Ka (Vasiliev and Dergachev, 2002).

Additionally, to the Solar band cycles at millennial time scales, there are important cycles directly measurable from the observations of solar variability, such as the quasi periodic ~11-yr Schwabe cycle of Wolf sunspot number series or the more stable magnetic 22-yr Hale cycle (Berger et al., 1990). Other cycles have been inferred from higher frequency solar cycles, such as the ~88-yr Gleissberg cycle and the ~200-yr Vries cycle. The Gleissberg cycle, first identified in 1862, strengthens and weakens the 11-year cycle and it is linked to the cyclic activity of sunspot formation (Peristykh et al., 2003). The ~200-year solar cycle (de Vries cycle) is a dominant cycle during the Holocene (Raspopov et al., 2008).

Another important group of climate cycles are those periodic or quasi-periodic climate phenomena internal to the climate system that operate in a decadal and centennial variability, also included in the Solar band. The strongest mode of natural climate variability today is the so-called El Niño/Southern Oscillation (ENSO) capable of altering the global atmospheric circulation. ENSO is a climatic oscillation of the tropical Pacific, atmosphere-ocean coupled, that oscillates between positive and warm (El Niño) and negative and cold (La Niña) phases with a periodicity of 2 to 8 years (Torrence and Compo, 1998; Rahmstorf, 2002; Wang and Fiedler, 2006). The presence of the ENSO in the past climate has been intensively studied, but the results on the timing and intensity of the ENSO through past climate lacks agreement. It has been proposed that one way to mitigate the problem would be to study the inverse phase relationships between the East Asian summer monsoon (EASM) and the Indian Ocean summer monsoon (ISM), because they are highly dependent on interannual time scales (Hong et al., 2005). The EASM evolution seems to be driven by strong internal feedback processes rather than by changing insolation (Chen et al., 2015). Similarly, the ISM variability is affected by other modes of climate variability (Reddy and Gandhi, 2022). The ENSO shows great complexity in both spatial and time domains (Timmermann et al., 2018).

The term teleconnections is largely used in paleoclimate research for referring to the interconnexion between modes of climate variability, and it is not uncommon the proposal of climate linkages between different climatic regions. Thus, there are multiple teleconnection examples, such as between the ENSO and the Pacific Decadal Oscillation or PDO (Verdon and Franks, 2006), the North Atlantic Oscillation (NAO) and the ENSO (Xu et al., 2018), the North America rainfall and the ENSO (Dee et al., 2020), or even age dependent between EASM intensity and AMOC before 7 Ka BP (Liu et al., 2020), just to cite a few. Another important climate oscillation in the northern hemisphere domain is the Arctic Oscillation (Deser, 2000).

The Calendar band contains those variations in energy received from the Sun at semidiurnal to annual scales (Rodríguez-Tovar, 2014). Plants and animals can potentially reflect these solar energy changes in their accretionary hard tissues. A canonical example are tree-ring growth patterns that can be explained by environmental changes affecting meteorological variables such as temperature and precipitation. The Dendroclimatology discipline precisely use these relationships to reconstruct past climates (Fritts, 1976). The methods for detrending the so-called "growth trend" from the tree-ring chronologies have improved over the years, allowing for a better extraction of the climate signal from trees, especially the low-frequency trends at centennial and/or millennial scales (Helama et al., 2004; Matskovsky and Helama, 2016).

An important surface temperature reconstruction at hemispheric and global scale using different proxies for the last 2,000 years (Mann et al., 2008), illustrated well both the potential and limitations of extracting the climate signal from trees. The referred study used a total of 1,209 proxy series, mainly from tree-ring data (85%), plus from additional marine sediments, lacustrine, ice cores, coral, and historical evidence (15%). It was known the challenge of capturing millennial-scale variations at using tree-ring records (i.e., Esper et al., 2004). In that logic, the authors used in their work tree-ring data based on well replicated chronologies and from conservative detrending treatments, both for maximizing the preservation of the low-frequency climate signal (and associated noise). However, the average length of the majority (926 datasets) of the time series was no longer than 300 years, which related to the modern group of the used tree ring data, therefore limiting the reconstruction of multi-centennial variability in that period. On the other hand, the average length of the less abundant (40 datasets) old tree ring data (<1200 AD) was ~500-700 years, increasing the reliability of the multi-centennial climate information for older periods. Despite the limitations at tracing the temperature trends at millennial time scales, the aforementioned multiproxy dataset was critical to further propose the relationship between the climate periods known as the Little Ice Age and the Medieval Warm period, and the El Niño/La Niña pattern and the North Atlantic Oscillation–Arctic Oscillation in a later climate reconstruction using the climate field reconstruction (CFR) methodology (Mann et al., 2009).

1.2.4 Spectral analysis

A essential step in the paleoclimate research of environmental cycles is the time series analysis by computer methods (Schwarzacher, 2000). The right mathematical framework in cyclostratigraphy is the usage of the theory of stochastic processes (Schwarzacher, 1975), including spectral analysis, which divides the power spectrum or spectral density function into its frequency components, and assimilates the detection of peaks in the frequency domain as the existence of periodical components.

Despite the fact that the Earth's climate has proven to be complex and chaotic, the most common methods in paleoclimate research are those based on linear techniques, and not those techniques (i.e., chaos theory) better prepared for nonlinear data analysis (Trauth, 2021). In this scenario, any time series can be represented as the linear sum of a periodic component (1), a trend component (2), and a random noise (3). The periodic component (1) is idealized by a linear combination of one/multiple sine/cosine wave/s with different amplitudes, frequencies, and phase angles. The trend component (2) must be removed in the time series for a correct interpretation of the power spectra results (Pardo-Igúzquiza et al., 2000), for example by adjusting a polynomial curve to the data and subtracting the curve from the data. Time series that are trend-free requires constant mean and the covariance function between two points to be a function of the distance between them only. The noise (3) can be modelled according to different autocorrelation behaviours (i.e., white noise, red noise, etc.), or stationarity (stationary vs. non-stationary) or distribution (i.e., normal distribution). Another important aspect to bear in mind when performing spectral analysis is the signal-to-noise ratio, which is desirable to be high. The noise model choice was important in the context of traditional autoregressive models because it potentially masked true signals, and missed significant spectra (Hinnov, 2000). Today, the addition of 10% of white noise to the sinusoid insolation forcing sinusoid can be used as representative of the internal climate variability (Berends et al., 2021).

Amongst all the different available spectral analysis techniques, the best approach is the usage of more than one spectral estimator -whenever possible- because this may outweigh the limitation of one particular method (Pardo-Igúzquiza et al., 1994). Historically, the most used spectral analysis techniques have been the Fourier-based methods. In Fourier-based methods, periodic functions are composed of a sum of sinusoids, but they are also valid to non-periodic functions that can be transformed by the Fourier Transform. Alternatively, the Discrete Fourier Transform (DFT) is a frequency domain representation of the time series and it is particularly useful as the real data is generally sampled from nature, and almost never continuous. The estimation of the DFT was improved by the Fast Fourier Transform algorithm (Cooley and Tukey, 1965) by reducing the necessary number of operations. Interestingly, the sampling ratio is critical to avoid aliasing which refers to the generation of a sinusoid of larger period than the signal when sampling frequency is higher than the signal itself. According to the Nyquist-Shannon sampling theorem, the sampling frequency must be at least twice the frequency of interest (Nyquist frequency).

The Fourier-based methods can be classified into direct and indirect methods (Pardo-Igúzquiza et al., 1994). The direct methods use the Fourier Transform on the experimental data by either attaching a simpler taper or window (Periodogram) or various tapers (Thompson adaptative). The indirect methods estimate the covariance of the experimental data followed by the Fourier transform (Blackman-Tukey). Other methods outside the domain of Fourier-based ones, they have its validity within the study of continuous variables by using an autoregressive model approach (Maximum entropy) or binary variables (Walsh spectrum). Also, the Fourier transform remains the principal statistical tool in cross-correlation analysis (Hinnov, 2000).

The Periodogram was invented by Arthur Schuster in 1898 and uses the squared absolute Fourier transform of the time series. For that reason, it has been subject to improvement over time. It estimates the power spectral density for the Nyquist range, the sampling frequency, and the length of the time series. Some statistical inconsistency has been found for this estimator (Pardo-Igúzquiza et al., 1994), which can be improved by multiplying the experimental time series by a weighting function before calculating the periodogram (data windowing). But also, it can increase its reliability by applying a type of smoothing process. The Walsh method is an alternative way to produce the spectrum (Welch, 1967), it consists of the average of the periodograms calculated from equal length subsections of the data after being detrended and tapered, with optimum results when using 50% of overlap of the subsections (Weedon, 2003).

On the other hand, the Thomson's multitaper method (Thomson, 1982) uses the average of multiple tapered periodograms which helps to increase the signal-to-noise ratio of the spectrum and to suppress spectral leakage without increasing the estimation variance (Trauth, 2021). In detail, the experimental data is multiplied by discrete prolate spheroidal sequences to improve the leakage which has it root in applying data windowing to a sinusoid. This method is highly recommended for evenly spaced or regular time series (Trauth, 2021).

The third main method in this category is the Blackman-Tukey method (Blackman and Tukey, 1958), and its novelty is that it uses the complex Fourier transform but using the covariance function. This method uses as inputs the number of steps of the covariance function or correlogram lags, the choice of a data windowing or taper (i.e., Parzen), and the DFT computation. Some bias problems have been recognised with this method despite its popularity (Hinnov, 2000).

Outside the Fourier-based methods, the Maximum Entropy method is an autoregressive type (and stochastic) spectral method (Jaynes, 1957; Burg, 1967). It has been considered a good estimator because of its high resolution and its satisfactory performance with short time series (Pardo-Igúzquiza and Rodríguez-Tovar, 2021). It assumes that the time series behaves as white noise (Trauth, 2021) and seeks the autocorrelation function that best fits the data. Some authors have suggested a number of 25% of the data series as the number of terms in the autocorrelation sequence (Pardo-Igúzquiza et al., 1994). Also, the Walsh method deals with the power spectrum estimation of binary variables (Weedon, 2003).

The Lomb-Scargle periodogram (Lomb, 1976; Scargle, 1982; Press et al., 1992) has its greatest achievement in being able to deal with uneven time series (Pardo-Igúzquiza and Rodríguez-Tovar, 2012; Trauth, 2021). This method has been chosen as the most reliable spectral estimator in this research, and it will be treated in much more detail in section 4.5.2, as well as in the sections corresponding to the methodologies for the case studies. This estimator can be combined effectively with the permutation test as a non-parametric method for testing the statistical significance of power spectrum estimation in cyclostratigraphic research (Pardo-Igúzquiza and Rodríguez-Tovar, F.J., 2000).

The time-frequency analysis deals with time series that are exhibit non-stationary behaviour, therefore they have amplitude and frequency variations over time. Wavelet analysis has become a popular method in paleoclimate research (i.e., Torrence & Compo 1998). This research has developed a novel method of visualization (see section 4.7) in the time-frequency analysis domain, offering an alternative for the current state-of-art of time-frequency representation methods.

1.3 Motivation and research hypotheses

As it has been highlighted, the Quaternary period comprises a recognisable climate succession of glacial and interglacial periods for the last 2.58 Ma. The Quaternary climate has governed all past and present aspects of human evolution, and it will do so in the future. If we are destined to answer the question: What is the right place of the present-day climate into the longer Quaternary paleoclimate history? . If *the present is the key to understand the past* (Charles Lyell 1797-1875), using the past climate to unlock the unknowns of the present climate seems inevitable. In the current social paradigm of global warming, climatologists need finding historical and/or paleoclimate evidence of other similar past climate states to challenge their predictions. By doing so, past climates can potentially contribute to the understanding of the current climate dynamics and helping with the validation of the current theories about climate. Particularly important for the scientific community is not solely identifying the driving forces behind the Quaternary climate shifts, but to evaluate the response of the Earth's climate to those forcing mechanisms. For example, the Paleoclimate Modelling Intercomparison Project (PMIP) selected some specific Quaternary climate states to be evaluated against current climate modelling experiments. The chosen periods were the last millennium (850–1849 CE), mid-Holocene (6 Ka), Last Glacial Maximum (21 Ka), Last Interglacial (127 Ka) and mid-Pliocene Warm Period (3.2 Ma), based not only on the climate characteristics but on the availability of data. They illustrate the importance of covering diverse past climate scenarios for understanding the current Earth's climate and its future evolution. To approach paleoclimate research in the Quaternary paleoclimate different proxies can be used, providing valuable information on the environmental and/or climate dominant conditions of the past climate.

The Quaternary climate has different facets depending on the spatial-temporal scale of the observations. As it has been exposed, the Quaternary climate is primarily affected by orbital forcing which constitutes the main driver of the observed climate variability. The alternance of the glacial and interglacial periods during the Quaternary has been explained by the Milankovitch theory and/or by means of astronomical forcing, hence the existence of variations in received insolation as the cause to explain the long-term climate fluctuations. On the other hand, the sub-Milankovitch cycles are recognised as proof of the incidence of the solar variability in the climate at shorter time scales. However, it is not clear how different climate forcings integrate into the observed paleoclimate variability, because of the existence of internal climate feedback mechanisms but also local and/or regional noise added during the recording of the climate signal. The cyclostratigraphy framework, and particularly the spectral analysis, allow identification of the frequencies of the involved climate forcings, assuming they are periodic. However, the spectral analysis methodology needs to be carefully assessed, as it can for example produce statistical artifacts or averaged cycles, deriving in wrong conclusions.

Thus, this PhD Thesis, focusing on different but interrelated aspects of the Quaternary climate from a global perspective, will try to approach and adopt several research hypotheses:

- There are numerous proxies both in marine and terrestrial ecosystems with potential for paleoclimate research on the Quaternary. Their usage may be limited by several aspects such as their spatial distribution, temporal coverage, and temporal resolution, among others. Which are the most suitable paleoclimate archives and proxies for paleoclimate research of the Quaternary? Which are the advantages and/or disadvantages of each proxy category?
- The increasing availability of open paleoclimate data allows advancing in paleoclimate research by a compilation and integration of different datasets at a global scale. Are the paleoclimate datasets easily searchable and retrievable from available open repositories?
- The cyclostratigraphic analysis in combination with other statistical methods has the potential to be used for the assessment of past climate variability at different spatial-temporal scales during the Quaternary. What are the available spectral analysis techniques that can be applied to the study of time series generated from paleoclimate proxies? What are the advantages and/or disadvantages of each method?
- The Quaternary climate is driven by long-term periodic or quasi-periodic forcings but it can be punctuated by catastrophic events and/or by regional/local constraints affecting their expression in the geological record. What is the impact of these abrupt events on the long-term background Quaternary climate? How these events can be traced using cyclostratigraphic analysis?

2 Chapter II. Objectives and Thesis layout

2.1 Objectives

The general aim of this Thesis is to improve the understanding of some of the past climate changes occurred during the Quaternary, based on a detailed cyclostratigraphic analysis of selected proxies. Within this framework the specific objectives of this research have been:

- To characterize the current availability of open paleoclimate data on the Quaternary at proxy level.
- To develop different methodologies for proxy data extraction, manipulation, and visualization.
- To evaluate the state-of-art of modern spectral analysis techniques and apply different software programs and tools to different theoretical scenarios, for assessing their suitability in the study of the past climate.
- To cover different climatic phenomena at variable temporal intervals during the Quaternary at varying resolution: i.e., last centuries, last several millennia and an abrupt climate event.
- To evaluate the most appropriate proxy according to the particular case study (i.e., climatic phenomena, ecosystem, sampling resolution, etc.).
- To characterize modern hydrometeorological variability at regional scale using precipitation and temperature data in a region characterised by climate contrasts and governed by important climate oscillations (i.e., Southern Spain).
- To assess existing tree-ring data methodologies for designing potential improvements to be applied to worldwide paleoclimate reconstructions in the terrestrial ecosystem from the last millennia.
- To assess Holocene climate variability at global scale by integrating datasets from localized terrestrial settings (speleothems datasets from caves).
- To evaluate the prospects of catastrophic events as triggering of climate shifts in the Quaternary by analysing a worldwide phenomena by using marine proxies (i.e., Younger Dryas).

2.2 Thesis layout

Chapter 1 presents the Quaternary climate aspects and their subdivisions. It explains the importance of the orbital forcing and the Pleistocene glaciations preceding the Holocene climate. It introduces the cyclostratigraphy analysis, the Milankovitch theory, and the emergence of the Astrochronology. It follows by compiling the different spectral analysis methodologies, and its usefulness in the context of paleoclimate research. Finally, the scope and research hypotheses are presented.

Chapter 2 introduces the general aim and specific objectives of this PhD Thesis.

Chapter 3 presents the results derived from the analysis carried out on the available main paleoclimate data repositories, including their temporal coverage and geographic distribution.

Chapter 4 describes the main methodology techniques used in this research, including the special case of development of a novel software code for generating visualizations from spectral analysis results using stablished terrain methods.

Chapter 5 corresponds to the first case study, containing the published version of the chapter entitled "Spatial distribution of climatic cycles in Andalusia (Southern Spain)" of the book: Theory and Applications of Time Series Analysis (Sánchez-Morales et al., 2019b).

Chapter 6 contains the second case study, corresponding to the published version of the article entitled "A new method for reconstructing past-climate trends using tree-ring data and kernel smoothing" for the journal Dendrochronologia (Sánchez-Morales et al., 2019a).

Chapter 7 consists of the third case study, presenting a global scale meta-analysis on $\delta^{18}O$ time series from speleothems covering the Holocene period, to find similarities and differences amongst the underlaying forcing mechanisms.

Chapter 8 contains the fourth case study, describing a novel approach for the study of the occurrence of the Younger Dryas, using cyclostratigraphic analysis on ice cores and wind data, in the context of the different theories available for explaining the last cold period before the current warm Holocene.

Chapter 9 summarises the results and the conclusions of this research, suggesting additional research and data compilations to advance in the conducted research.

3 Chapter III. Data Sources

A considerable amount of time has been dedicated researching on the paleoclimate datasets available for the Quaternary period, including the assessment of their geographic, temporal and metadata features, covering marine and terrestrial paleoclimate categories, according to the objectives of the research. Thus, a mature level of understanding on the potentiality of selected public repositories, paleoclimate archives and paleoclimate proxies was reached. This assessment was carried out at specific time intervals during the research period, generating snapshots of the data at given points in time.

Amongst all research institutions in the paleoclimate/climate scientific context, this thesis has examined the most widely recognized web portals and/or online repositories amongst the scientific community. All the selected sites are online repositories offering datasets freely used or openly accessible. The list of these catalogues and the time period in which these datasets were investigated has been:

- The National Oceanic and Atmospheric Administration (NOAA). (2016-2022)
- Agencia Estatal de Meteorología (AEMET). (2017-2019)
- Artic Data Center. (2019-2022)
- Copernicus Climate Change Service (C3S) and its associated Climate Data Store (CDS). (2019-2022)
- Speleothem Isotopes Synthesis and Analysis database (SISAL). (2020-2022)

The geographic scope of the above datasets differs from one another. Thus, the NOAA, CDS and SISAL data repositories have a global scope. On the other hand, AEMET is geographically circumscribed to Europe and the Artic Data Center covers datasets only related to the Artic. From the temporal point of view, only NOAA, Artic Data Center and SISAL have datasets that go back well beyond present-day climate, as AEMET and CDS cover mainly the 20th and 21st centuries (occasionally the 19th century). The SISAL database only hosts one type of paleoclimate archive: speleothems. From the user perspective, each of these paleoclimate data repositories has different web design and content structure, which aligns with their funding scope and/or scientific objectives. Therefore, a tailored assessment has been implemented for each repository, producing distinct levels of assessment on each case.

3.1 National Oceanic and Atmospheric Administration (NOAA)

The National Oceanic and Atmospheric Administration (NOAA; https://www.noaa.gov/), funded by the U.S. government, grants access to a vast data archive which is accessible from the internet and is free of charge. The NOAA is widely known for the regular practice of publishing modern climate data, either from ground instruments or from satellites, which serves the purpose of assessing current climate aspects. The main aspect of NOAA for the conducted research is that it holds a substantial paleoclimate archive in many fields or areas of paleoclimate research (https://www.ncei.noaa.gov/products/paleoclimatology). Because of the collaborative principle of this paleoclimate archive, researchers in Earth Sciences from all over the World have the opportunity of submitting their data and sharing it with the rest of the scientific community. This research has witnessed the increase in the number of studies over the years (223.26% of average increase in the number of studies for the period 2016-2022).

The process of assessing the paleoclimate archives available at NOAA started in July/August 2016 and took over one month to be completed. In 2022, a final update on the number of studies per category has been obtained. A summary of the conducted assessment per paleoclimate category is presented in Table 3.1. As per 2016, 12 major paleoclimate categories were considered for this assessment: Ice Cores, Corals & Sclerosponges, Tree Rings, Paleolimnology (Lakes), Pollen, Climate Reconstructions, Boreholes, Other Collections, Fire History, Speleothems, Plant Macrofossils and Paleoceanography, as well as 6 minor archives such as Insect, Historical, Paleo modelling, Lake-levels, Climate forcing and Loess & Eolian Dust. Although most of the studies, especially those from the major categories, are hosted and maintained by NOAA, there are 3 exceptions: Pollen, Other Collections and Plant Macrofossils. For these 3, most of the studies contained external references to the Neotoma Paleoecology database (https://apps.neotomadb.org/explorer/). For instance, the Pollen category had 8,565 available studies in 2016, but only 9 of them had a NOAA reference, while the remaining 8,556 studies (>99%) contained a Neotoma reference.

Every study has a unique URL or identifier (e.g., https://www.ncei.noaa.gov/access/paleo-search/study/9957). This gives access to the associated metadata information which follows a pre-defined structure. The structure of the online reference includes the following information: Originator, citation information, metadata files, data files, use constraints, distributor, resource description, data coverage, keywords, parameters, variables, summary/abstract, and study notes. All this information is contained within metadata files in XML format (Extensible Markup Language).

Every study has its associated metadata file (e.g., http://www1.ncdc.noaa.gov/pub/data/metadata/published/paleo/dif/xml/noaa-cave-9957.xml), allowing a global and more detailed assessment programmatically by using scraping techniques (4.1.1 NOAA datasets download process). This technique facilitates a detailed analysis for all the studies available in the 12 major categories.

Paleoclimate archives	**Number of studies (2016)**	**Number of Studies (2022)**	**Variation (2016-2022)**	**Geographic domain**	**Geographic hot spots**	**Top three variables (proxies)***	**Total number of files (available URLs to download)****
Ice Cores	**261**	**382**	**+46.36%**	Terrestrial /Marine	Greenland, Antarctica, glaciers in Andes, Rocky Mountains, Himalayas, and Kilimanjaro	1. ‘delta 18O PDB (per mille)’ (37 studies) 2. ‘methane concentration (parts per billion by volume)’ (20 studies) 3. ‘carbon dioxide concentration (parts per million by volume)’ (19 studies)	**808**
Corals & Sclerosponges	**183**	**297**	**+62.30%**	Marine shallow	Equatorial and tropical areas	1. ‘del18O’ (69 studies) 2. ‘del13C’ (40 studies) 3. ‘SrCa’ (30 studies)	**497**
Tree Rings	**4,515**	**6,853**	**+51.78%**	Terrestrial	Northern Hemisphere (North America and Europe)	1. ‘ring width’ (4,297 studies) 2. ‘latewood width’ (616 studies) 3. ‘earlywood width’ (614 studies)	**19,790**
Paleolimnology (Lakes)	**284**	**699**	**+146.13%**	Terrestrial	Americas, Europe, Africa, and China	1. ‘geochemistry’ (126 studies) 2. ‘physical properties’ (104 studies) 3. ‘oxygen isotopes’ (50 studies)	**852**
Pollen	**9**	**76**	**+744.44%**	Terrestrial	Not assessed	Not assessed	**13**
Climate Reconstructions	**394**	**2,315**	**+487.56%**	Terrestrial /Marine	Northern Hemisphere	1. ‘air temperature’ (88 studies) 2. ‘precipitation’ (53 studies) 3. ‘sea surface temperature’ (25 studies)	**805**
Boreholes	**953**	**1,027**	**+7.76%**	Terrestrial	North America, Europe, Asia, south of Africa and Australia	1. ‘physical properties’ (953 studies)	**1,865**
Other Collections	**61**	**90**	**+47.54%**	Terrestrial	Not assessed	Not assessed	**114**

Fire History		**613**	**832**	**+35.73%**	Terrestrial	North America and Chile	1. 'fire scar dates' (516 studies) 2. 'tree species' (451 studies) 3. 'Pinus ponderosa Douglas ex C. Lawson' (209 studies)	**2,433**
Speleothems		**149**	**266**	**+78.52%**	Terrestrial	Mid-latitudes	1. 'oxygen isotopes' (128 studies) 2. 'carbon isotopes' (68 studies) 3. 'lithology' (14 studies)	**325**
Plant Macrofossils		**297**	**309**	**+4.04%**	Terrestrial	North America	1. 'population abundance' (297 studies)	**888**
Paleoceanography		**710**	**1,094**	**+124.18%**	Marine	Global	1. 'population abundance' (819 studies) 2. 'oxygen isotopes' (466 studies) 3. 'carbon isotopes' (304 studies)	**3,214**
Minor datasets	**Insect**	**9**	**93**	**+933.33%**	Terrestrial	Alaska	Not assessed	-
	Historical	**20**	**61**	**+205.00%**	Terrestrial	Europe	Not assessed	-
	Paleo modelling	**23**	**73**	**+217.39%**	Terrestrial /Marine	Not assessed	Not assessed	-
	Lake-levels	**10**	**36**	**+260.00%**	Terrestrial	Europe, Central Asia, and Africa	Not assessed	-
	Climate forcing	**30**	**182**	**+506.67%**	Terrestrial /Marine	Not assessed	Not assessed	-
	Loess & Eolian Dust	**15**	**24**	**+60.00%**	Terrestrial	China	Not assessed	-

* Extracted from the NOAA web classification within the General Description for each study (lot of studies do not have this information included as many studies have a blank value in the metadata description field of the variables.

** There are more datasets than studies. Commonly the datasets are presented in different data formats, or there are additional datasets, configuration files for specific software, or the datasets are split into smaller files.

Table 3.1. Summary table of the Paleoclimate NOAA categories including their quantitative and qualitative assessment.

3.1.1 Ice Cores

The ice cores archive contained 261 studies in 2016 and 382 in 2022. The geographical distribution of the ice cores studies in 2016 is shown in Figure 3.1. The circles in the map correspond to individual studies with a unique geographic location, and the crosses to, more or less, the central position of groups of studies with several locations. For instance, the crosses located near the Equator represent studies from both Greenland and Antarctica. Although the NOAA does not publish the geographic location of each individual study for these groups in the metadata files, this information can be extracted from the original reports. Overall, the ice cores are exclusively located around the poles, Greenland, and mountain glaciers.

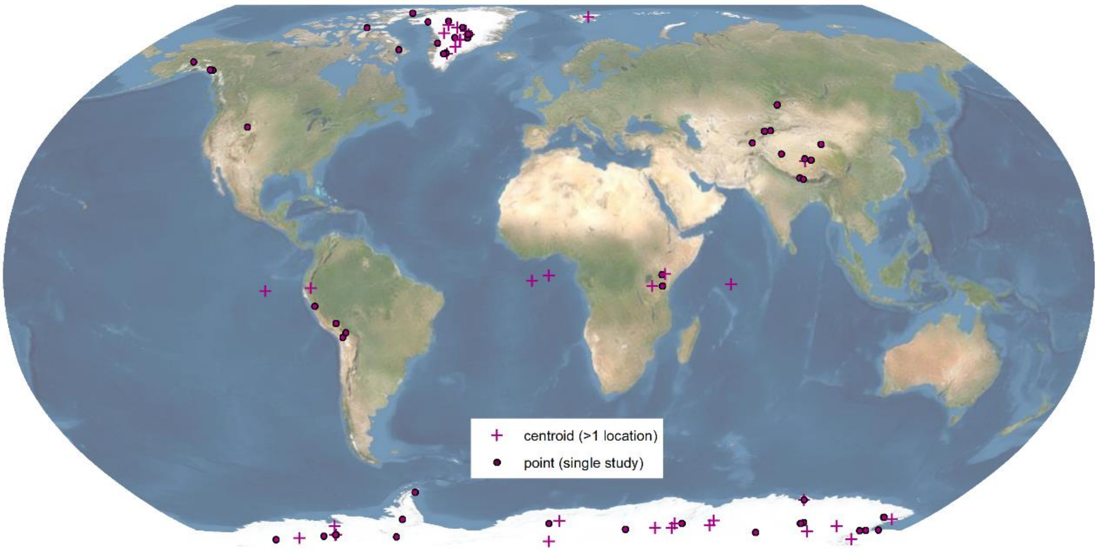

Figure 3.1. Geographic distribution of NOAA ice cores datasets containing 261 studies (August-2016).

According to the conducted temporal assessment of the datasets from ice cores (Figure 3.2A), the largest time span of the ice cores is ~808 kyr and is located in Antarctica. The time span of the ice cores in Greenland is ~386 kyr, less than half of the Antarctica ones. In Figure 3.2B the distribution of the reached ice ages of the cores from northern to southern latitudes is presented, showing that Antarctica has the oldest ice cores. The oldest dates reach approximately the top of the Calabrian (Pleistocene), which is estimated to be between 0.774 and 1.80 Ma (Cohen et al., 2013; updated).

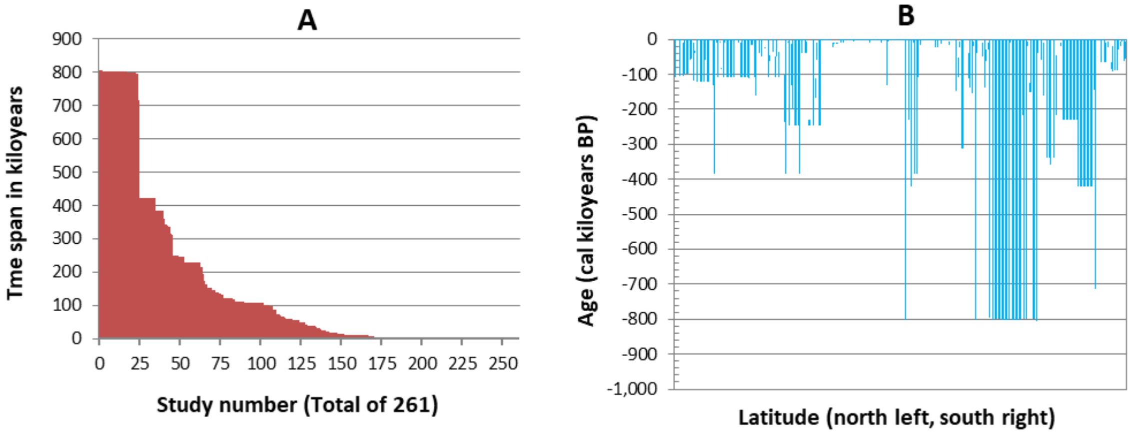

Figure 3.2. A) Time spans of all the studies in the ice cores category, sorted from largest to smallest. B) Earliest year per study in the ice cores category, sorted by latitude (e.g., Greenland left, Antarctica right).

3.1.2 Corals and sclerosponges

The corals and sclerosponges archive contained 183 studies in 2016 and 497 in 2022. The geographical distribution of the corals and sclerosponges studies in 2016 is shown in Figure 3.3. The datasets are almost exclusively located around the Tropics.

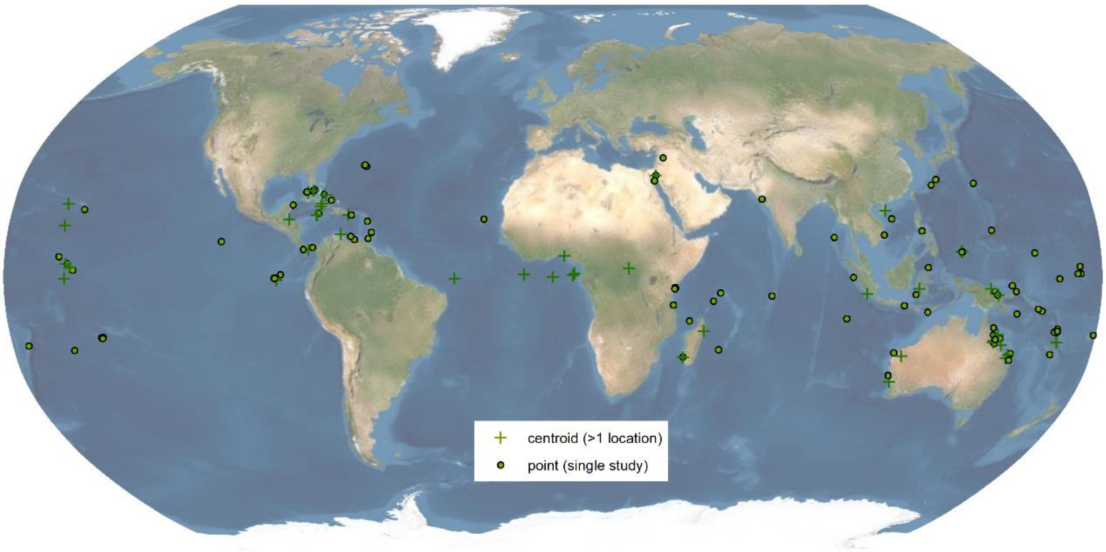

Figure 3.3. Geographic distribution of NOAA corals and sclerosponges datasets containing 183 studies (August-2016).

According to the conducted temporal assessment of the corals and sclerosponges, the largest time span is ~130 kyr for one multi-study (Figure 3.4A). According to their ages (Figure 3.4B), there are only 5 studies that go beyond the Holocene period (0-11.7 ka), being the majority of the studies within the Holocene. The earliest ages are for three studies in Barbados island spanning around 20,000 years ago, reaching the last glacial maximum (Fairbanks, 1990).

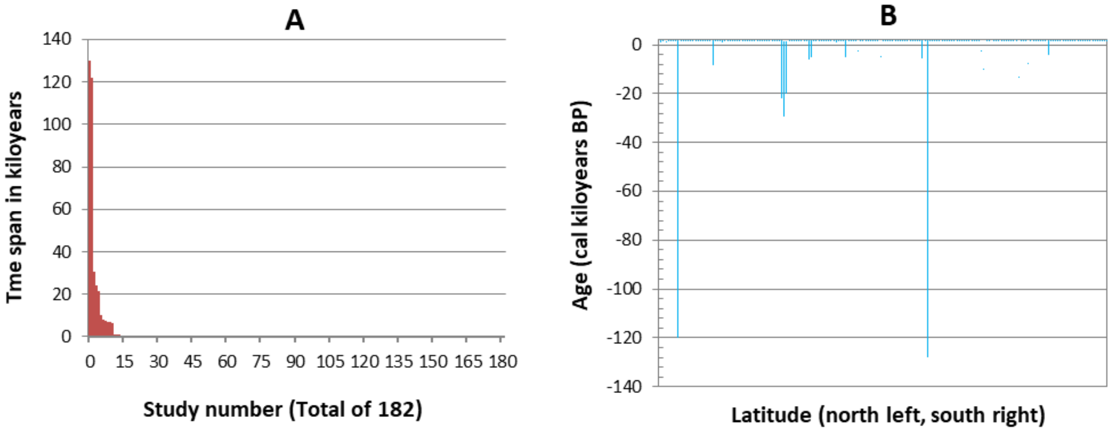

Figure 3.4. A) Time spans of all the studies in the corals and sclerosponges category, sorted from largest to smallest. B) Earliest year per study in the corals and sclerosponges category, sorted by latitude (e.g., Tropic of Cancer, 34.5° north, left, to Tropic of Capricorn, 28.5° south, right).

3.1.3 Tree rings

The tree rings archive contained 4,515 studies in 2016 and 6,853 in 2022. The geographical distribution of the tree rings studies in 2016 is shown in Figure 3.5. The high-density areas are mainly located in North America, Europe, Chile, and New Zealand. Furthermore, there is an enormous difference between the northern and the southern latitudes which are clearly underrepresented because of the much smaller continental surface within the temperate climate band. Another important aspect of the tree rings studies is the lack of studies in the tropics. This is explained because the tree species to produce rings need seasonal contrast and this factor happens almost exclusively in the temperate climate zone for both hemispheres.

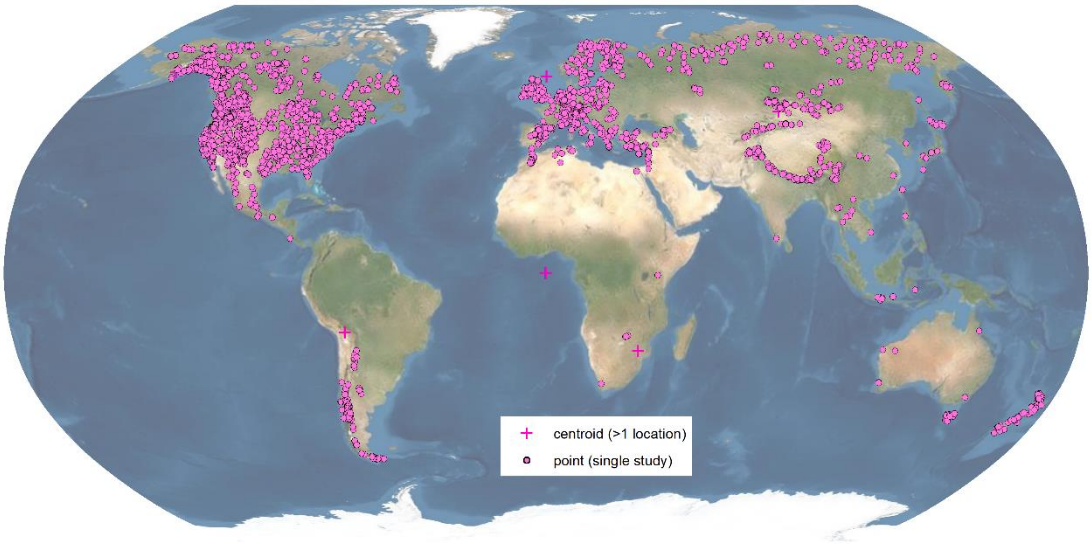

Figure 3.5. Geographic distribution of NOAA tree rings datasets containing 4,515 studies (August-2016).

According to the conducted temporal assessment of the tree rings datasets (Figure 3.6), the largest time span of the tree rings is ~8,000 years for one study in Methuselah Walk (California, USA) (Figure 3.6A). All the tree rings studies are within the Holocene, but most of them cover the last millennia or just some centuries from present day (Figure 3.6B), which evidences their temporal consistency. It is common practice in dendrochronology to build a dataset from different samples of the same tree, and from different trees nearby or from the same area, that after dated are called chronologies (Fritts, 1976). Therefore, the time span and the age of the dataset is in fact the overlap of several tree ring chronologies.

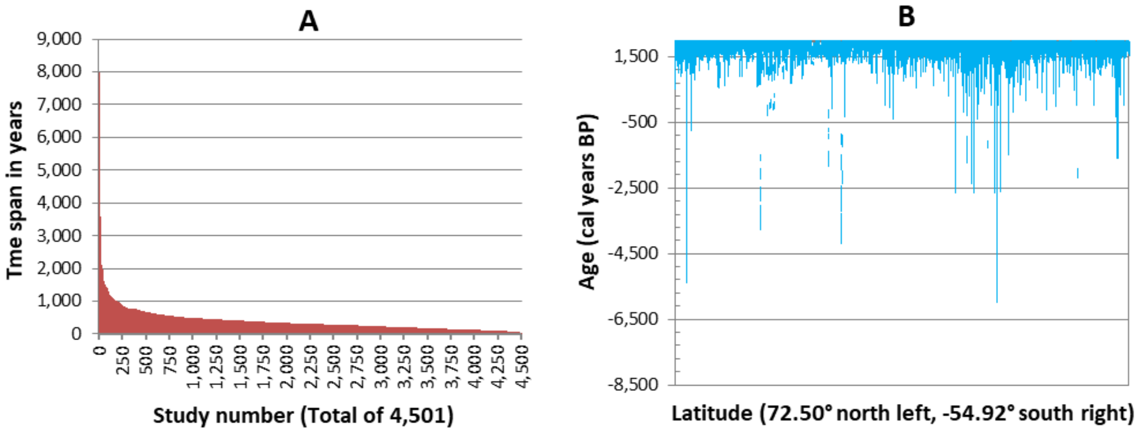

Figure 3.6. A) Time spans of all the studies in the tree rings category, sorted from largest to smallest. B) Earliest year per study in the tree rings category, sorted by latitude.

3.1.4 Paleolimnology (Lakes)

The lakes archive contained 284 studies in 2016 and 699 in 2022. The geographical distribution of the lakes studies in 2016 is shown in Figure 3.7. The areas with greater number of lake studies are generally well distributed across the globe, with Asia and Oceania with the least number of studies.

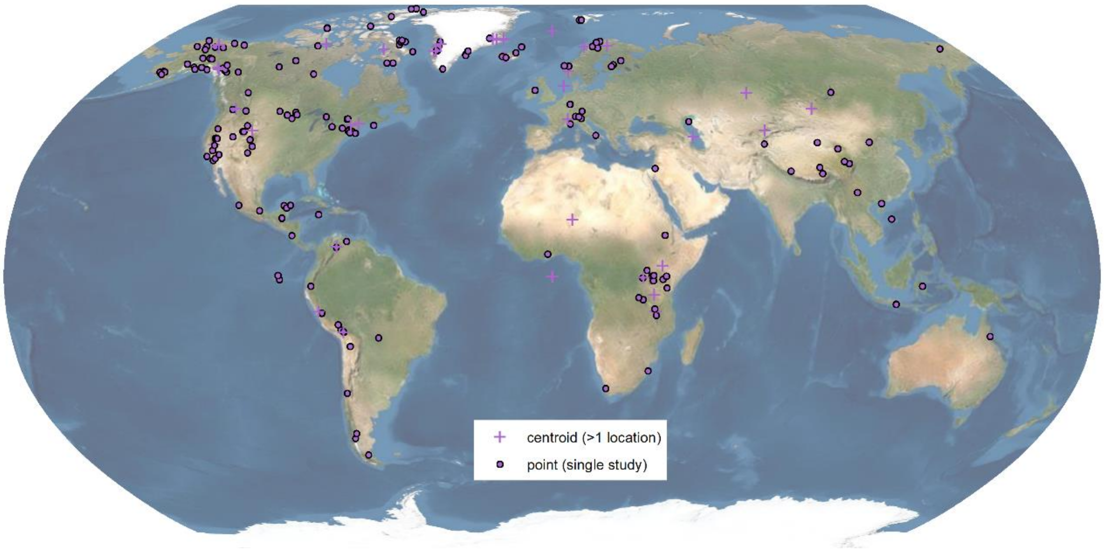

Figure 3.7. Geographic distribution of NOAA paleolimnology datasets containing 284 studies (August-2016).

According to the conducted temporal assessment of the lakes for those studies with searchable earliest and most recent years (Figure 3.8), the largest time span of the lakes is ~ 3.47 Myr for one study in NE Russia, which surpasses the Quaternary period. However, the majority of the studies have a time span below 100 kyr (Figure 3.8A), and ages under 100 ka (Figure 3.8B).

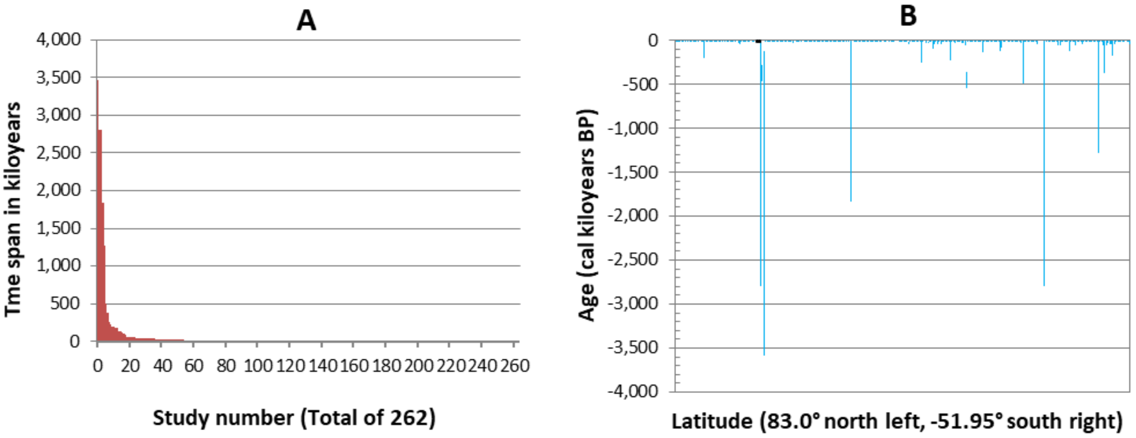

Figure 3.8. A) Time spans of all the studies in the paleolimnology (lakes) category, sorted from largest to smallest. B) Earliest year per study in the paleolimnology (lakes) category, sorted by latitude.

3.1.5 Pollen

The Pollen archive is poorly populated in NOAA, containing 9 studies in 2016 and 76 in 2022. The geographical distribution of the pollen studies in 2016 is shown in Figure 3.9.

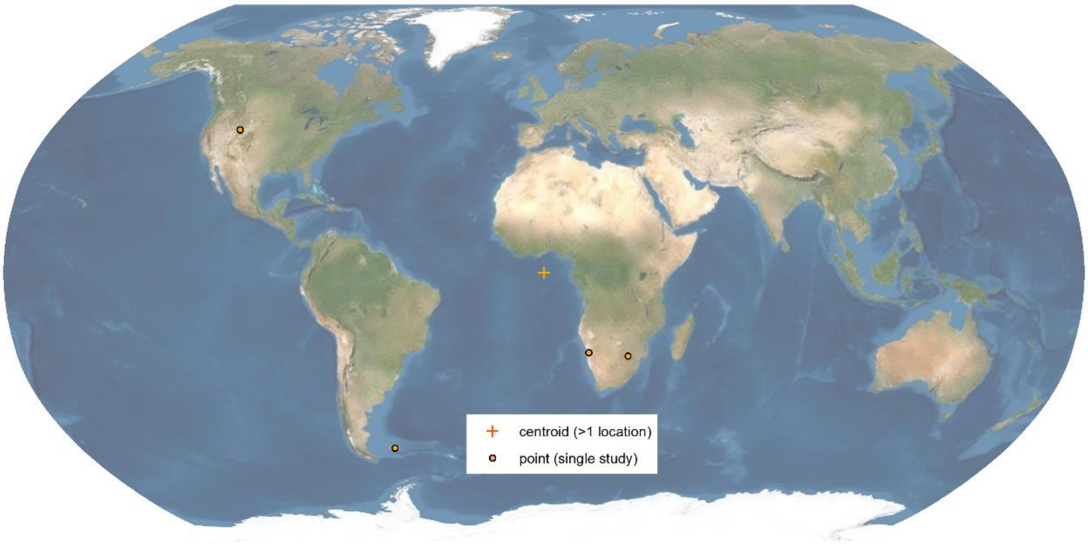

Figure 3.9. Geographic distribution of NOAA pollen datasets containing 9 studies (August-2016).

3.1.6 Climate reconstructions

The climate reconstructions archive contained 394 studies in 2016 and 805 in 2022. The geographical distribution of the climate reconstructions studies in 2016 is shown in Figure 3.10. The areas with greater number of studies are North America, Europe, and China.

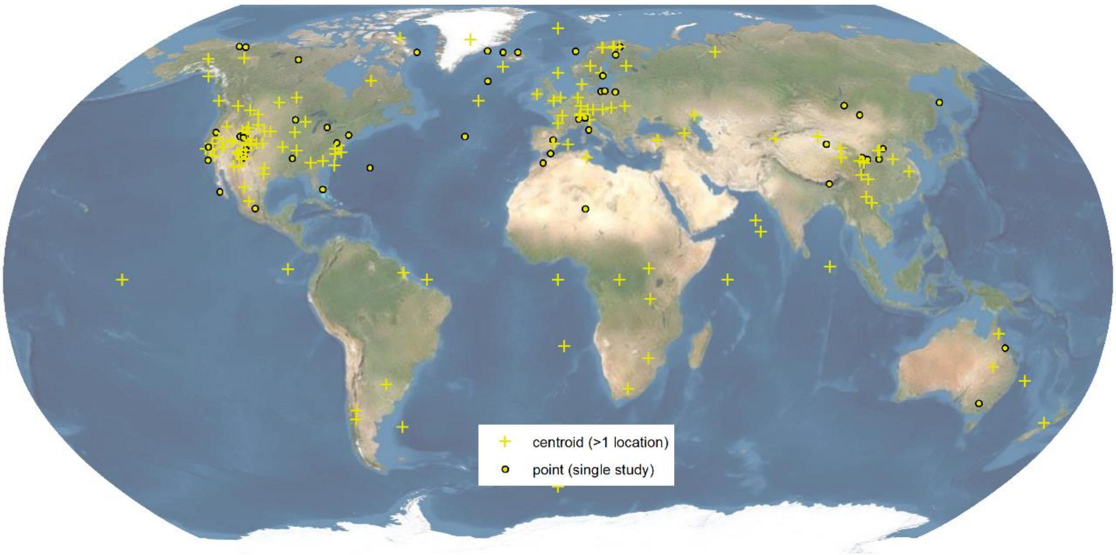

Figure 3.10. Geographic distribution of NOAA climate reconstructions datasets containing 394 studies (August-2016).

The conducted temporal assessment of the climate reconstructions (Figure 3.11) is based on 193 studies as 201 studies lack of completed ages in the metadata files. The largest time span of this category is ~ 5.3 Myr for one global study reconstructing sea levels, which surpasses the Quaternary period. However, the majority of the climate reconstructions have a time span below 50 kyr (Figure 3.11A), and ages under 50 ka (Figure 3.11B).

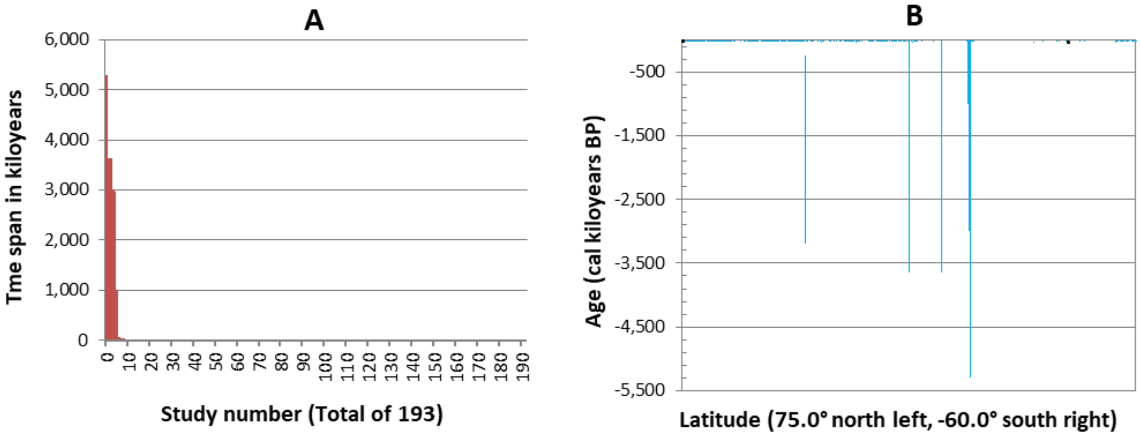

Figure 3.11. A) Time spans of all the studies in the climate reconstructions category, sorted from largest to smallest. B) Earliest year per study in the climate reconstructions category, sorted by latitude.

3.1.7 Boreholes

The boreholes archive contained 953 studies in 2016 and 1,027 in 2022. All these datasets belong to the "Global Database of Borehole Temperatures and Climate

Reconstructions" (Huang et al., 2000). The geographical distribution of the boreholes studies in 2016 is shown in Figure 3.12. All continents have available studies, although South America and North Africa are underrepresented.

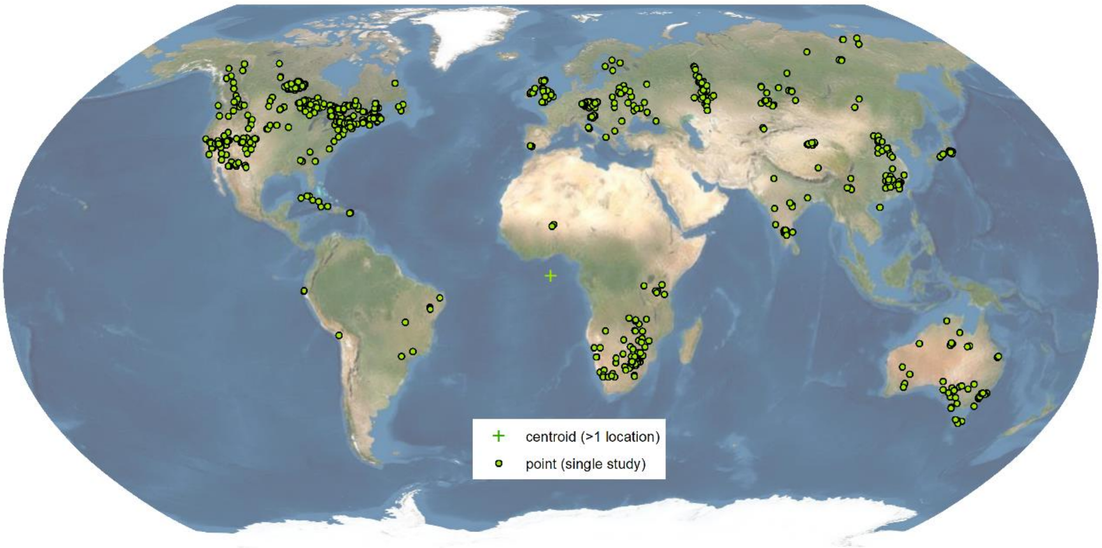

Figure 3.12. Geographic distribution of NOAA boreholes datasets containing 953 studies (August-2016).

According to the conducted temporal assessment of the boreholes (Figure 3.13), the time span is consistent between 504 years and 459 years, with no major differences across hemispheres.

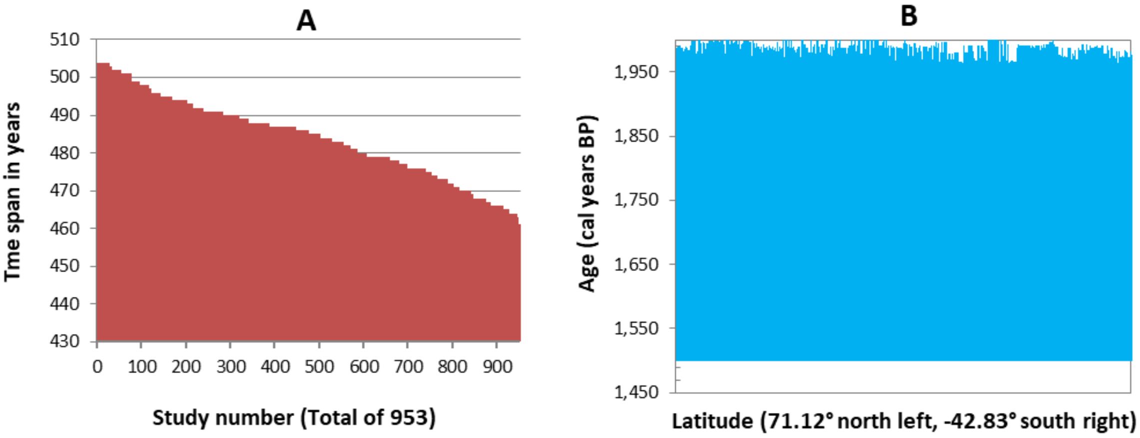

Figure 3.13. A) Time spans of all the studies in the boreholes category, sorted from largest to smallest. B) Earliest year per study in the boreholes category, sorted by latitude.

3.1.8 Other Collections

The "Other Collections" archive is under-represented in NOAA, containing 61 studies in 2016 and 90 in 2022. The geographical distribution of the "Other Collections" studies in 2016 is shown in Figure 3.14.

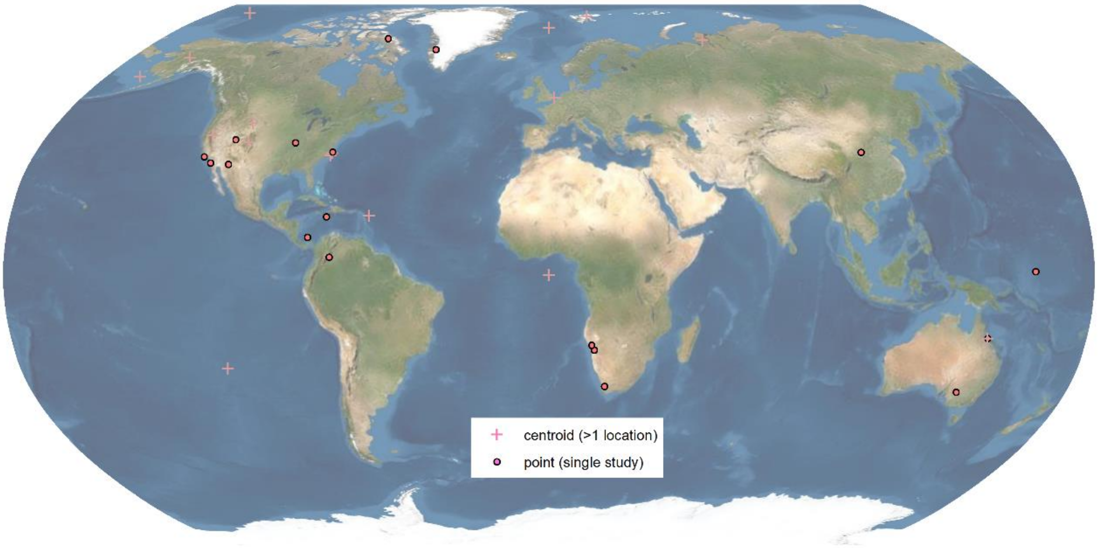

Figure 3.14. Geographic distribution of NOAA other collections datasets representing the other collections category containing 61 studies (August-2016).

3.1.9 Fire History

The “Fire History” archive contained 613 studies in 2016 and 832 in 2022. The geographical distribution of the “Fire history” studies in 2016 is shown in Figure 3.15. The vast majority of studies are located in North America, although there is also a cluster of studies located in Chile and Argentina.

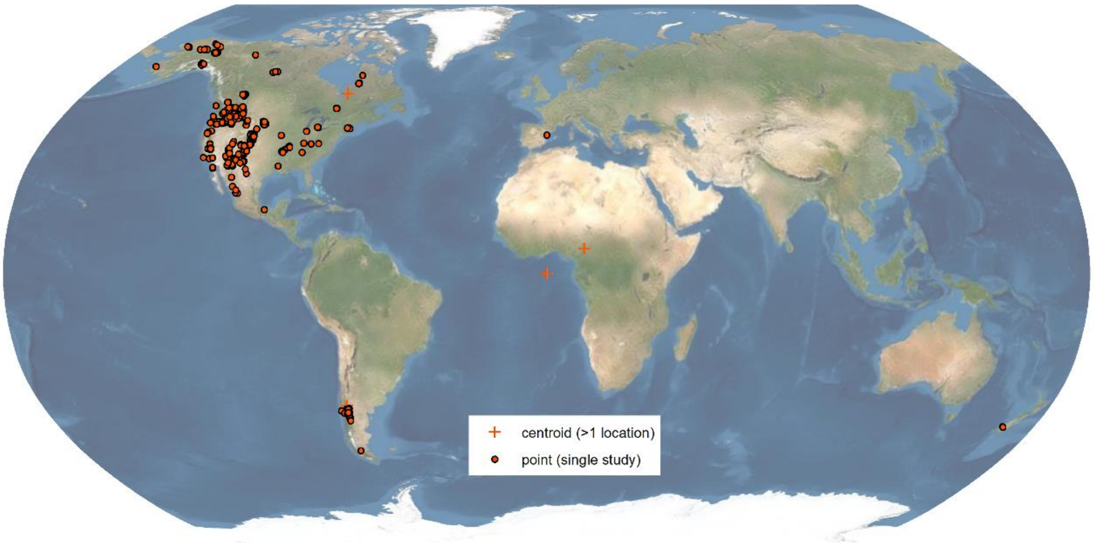

Figure 3.15. Geographic distribution of NOAA “Fire history” datasets containing 613 studies (August-2016).

According to the conducted temporal assessment of the "Fire history" datasets (Figure 3.16), the largest time span is ~ 35.5 kyr for one study in Alaska. Although there are a few studies extending beyond the Holocene period, the majority of them have a time span below 10 kyr (Figure 3.16A), and ages under 10 ka (Figure 3.16B).

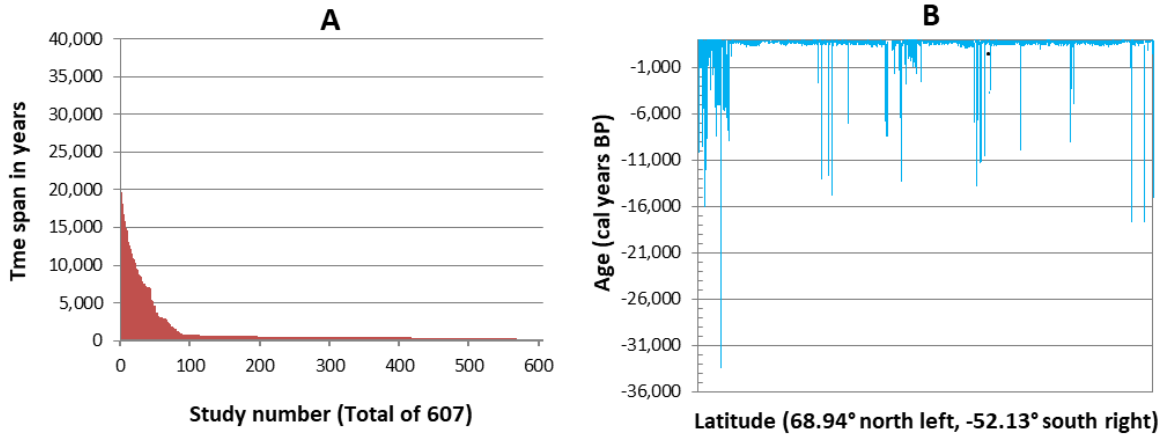

Figure 3.16. A) Time spans of all the studies in the "Fire history" category, sorted from largest to smallest. B) Earliest year per study in the "Fire history" category, sorted by latitude.

3.1.10 Speleothems

The Speleothems archive contained 149 studies in 2016 and 266 in 2022. The geographical distribution of the speleothems studies in 2016 is shown in Figure 3.17. The locations are driven by the presence of present and/or past karst formations. There is an extended distribution of datasets worldwide although the polar and subpolar regions do not have any studies.

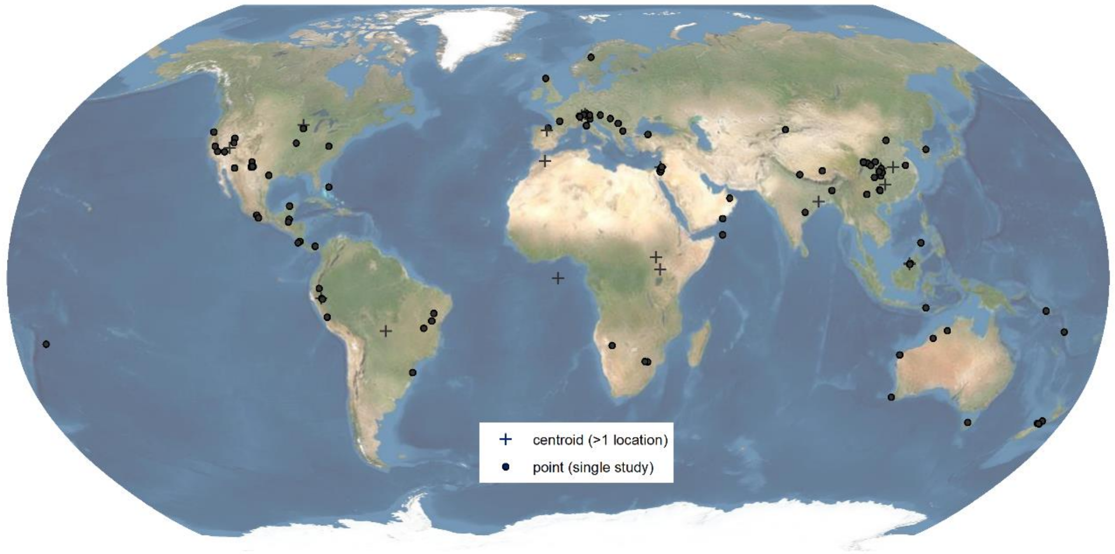

Figure 3.17. Geographic distribution of NOAA speleothems datasets containing 149 studies (August-2016).

According to the conducted temporal assessment of the speleothems (Figure 3.18), the largest time span of the speleothems is ~ 3 Ma attributed to the Ashalim Cave in Israel (the most recent age for that study is 115 ka BP). Although there are a few studies spanning a few hundreds of thousands of years, the majority of them have a time span of tens of thousands of years (Figure 3.18A), and ages generally under 100 ka (Figure 3.18B).

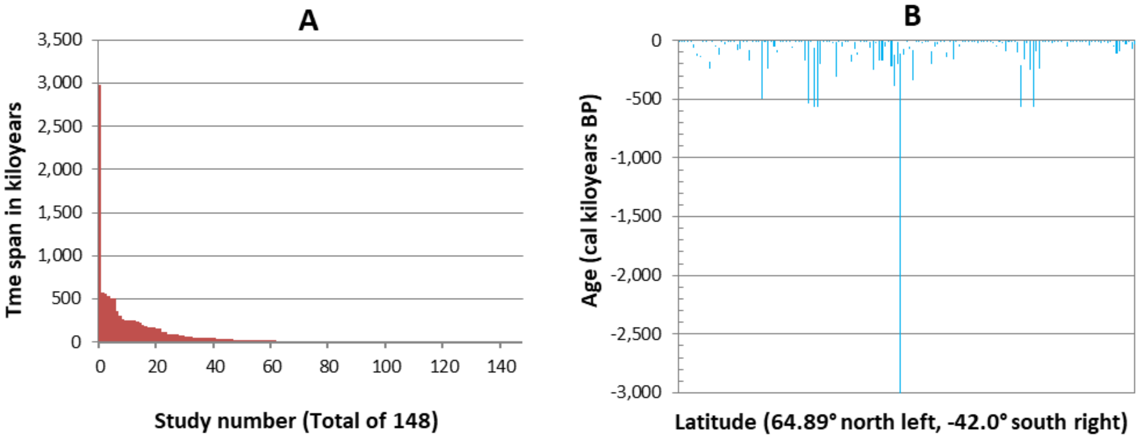

Figure 3.18. A) Time spans of all the studies in the speleothems category, sorted from largest to smallest. B) Earliest year per study in the speleothems category, sorted by latitude.

3.1.11 Plant Macrofossils

The Plant Macrofossils archive contained 297 studies in 2016 and 309 in 2022. The geographical distribution of the Plant Macrofossils studies in 2016 showed that they were exclusively concentrated in North America (Figure 3.19).

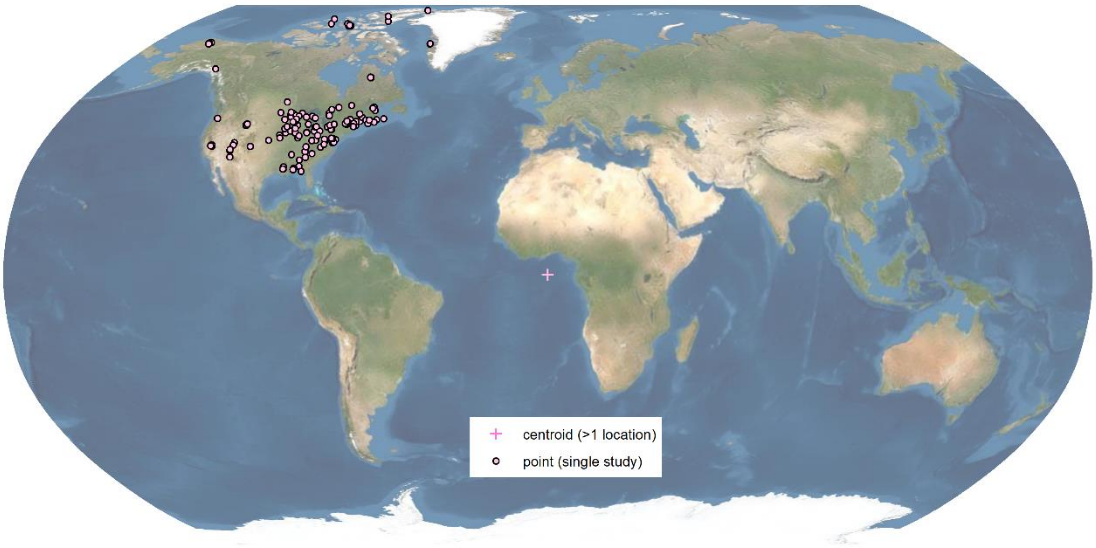

Figure 3.19. Geographic distribution of NOAA Plant Macrofossils datasets containing 297 studies (August-2016).

According to the conducted temporal assessment of the Plants Macrofossils (Figure 3.20), the largest time span is ~ 62 kyr in Lake Tulane. Although there are a few studies spanning tens of thousands of years, the majority of them have a time span ranging from a few thousands of years to a few decades (Figure 3.20A), and ages below 20 ka (Figure 3.20B).

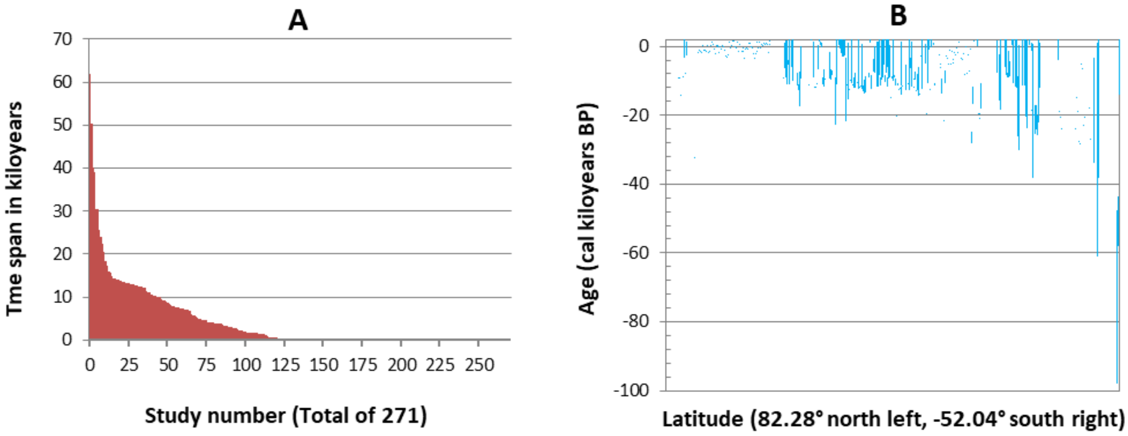

Figure 3.20. A) Time spans of all the studies in the Plant Macrofossils category, sorted from largest to smallest. B) Earliest year per study in the Plant Macrofossils category, sorted by latitude.

3.1.12 Paleoceanography

The Paleoceanography archive contained 710 studies in 2016 and 1,094 in 2022. The geographical distribution of the Paleoceanography studies in 2016 (Figure 3.21) showed that there is a good spread of the datasets across all oceans with approximately half of the studies (319) located within the exclusive economic zone (EEZ) areas, or below 200 nautical miles from the coast (using World EEZ v11 from marineregions.org).

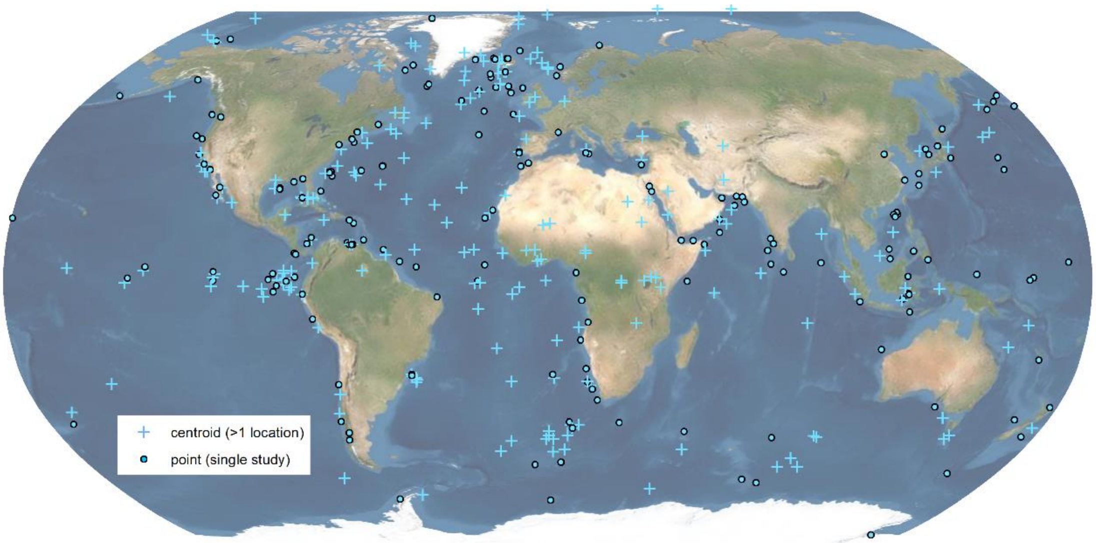

Figure 3.21. Geographic distribution of NOAA paleoceanography datasets containing 710 studies (August-2016).

According to the conducted temporal assessment of the Paleoceanography (Figure 3.22), 34 studies out of 710 have their earliest ages older than the Quaternary (2.58 Ma). Although there are a few studies spanning millions of years, the majority of them have a time span from a few hundreds of thousand years to a few millennia (Figure 3.22A), and ages under 5 Ma (Figure 3.22B).

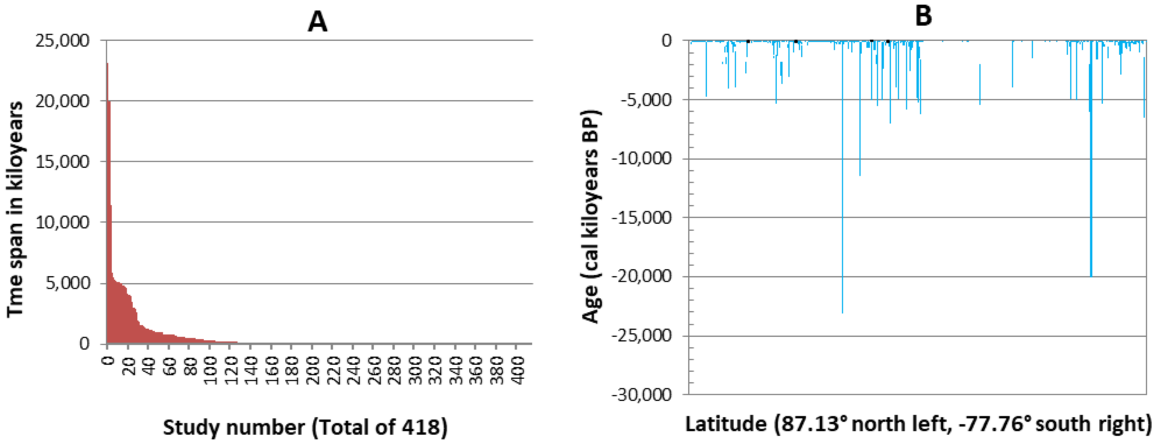

Figure 3.22. A) Time spans of all the studies in the Paleoceanography category, sorted from largest to smallest. B) Earliest year per study in the Paleoceanography category, sorted by latitude.

3.1.13 Minor Datasets

The Minor Datasets archive comprises the following six categories: Insect, Historical, Paleo Modelling, Lake-levels, Climate Forcing and Loess & Eolian Dust. This archive is under-represented in NOAA, containing 107 studies in 2016, although its importance has grown in recent years with 469 studies in 2022. The geographical distribution of the Minor Datasets studies in 2016 is shown in Figure 3.23.

3.1.14 Summary of temporal coverage

The temporal coverage of the paleoclimate categories over the Quaternary period is very heterogenous. The categories Paleoceanography (0-23 Myr), Speleothems (0-2.98 Myr), Climate Reconstructions (0-5.3 Myr) and Paleolimnology (Lakes) (0-3.46 Myr) are the only ones with studies both covering the whole of the Quaternary period and extending beyond it (Figure 3.24). The categories Corals and Sclerosponges (0-130 Kyr), Tree rings (0-7.8 Kyr), Boreholes (0-0.5 Kyr), Plant macrofossils (0-56 Kyr) and Fire History (0-35 Kyr) are limited to the Upper Pleistocene (<129 Ka). The Pollen, Minor Datasets and Other Collections have not been assessed regarding their temporal coverage because of their small number of available studies.

Thus, the study of the Quaternary period has important time constraints depending on the type of the selected paleoclimate archive, mainly related to the temporal resolution and the time span. For example, even though Tree Rings datasets have high resolution (~ 1 yr), their time age usually spans a few centuries at best, whereas marine cores from the Paleoceanography category can potentially span the whole of the Quaternary, although at much lower resolution.

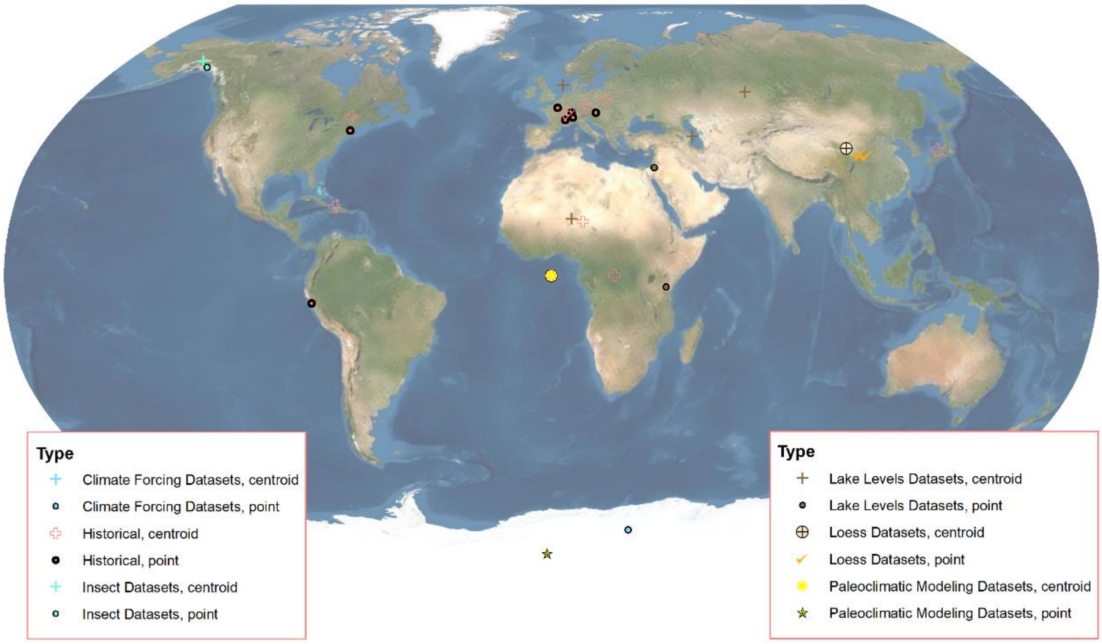

Figure 3.23. Geographic distribution of NOAA minor datasets containing 107 studies (August-2016).

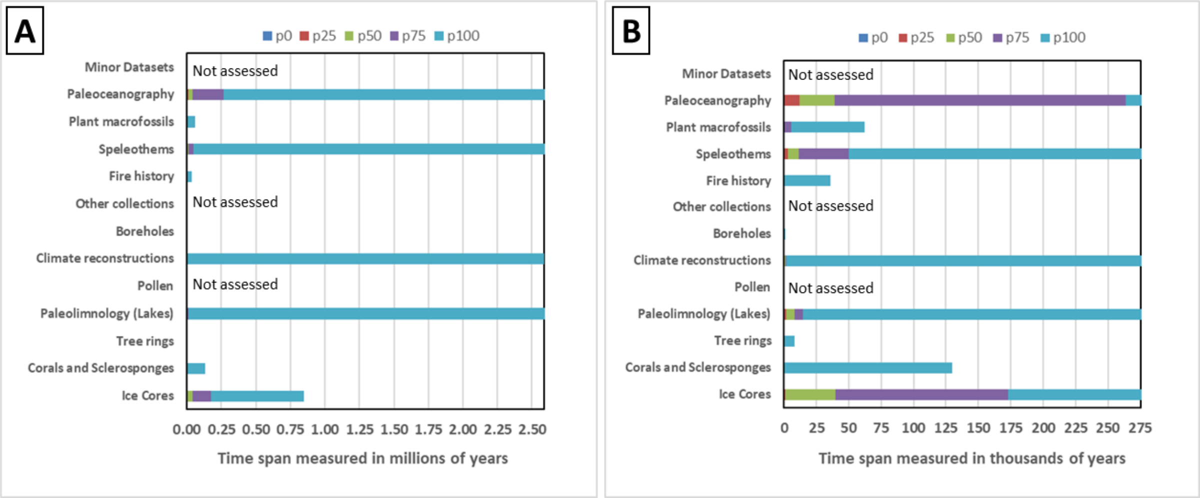

Figure 3.24. Stacked bars graph showing the percentiles p0, p25, p50, p75 and p100 per NOAA archive, based on all the time spans for all the studies within each archive. A) Temporal scale adjusted for the whole of the Quaternary period, B) Temporal scale adjusted for the last 275 Kyr.

3.2 Artic Data Center

The Artic Data Center (https://arcticdata.io/), funded by the National Science Foundation (NSF), is specialised in hosting software, code and data located or related to the Artic. In fact, any data created under the scope of the National Science Foundation Office of Polar Programs (NSF OPP) should be found in this repository. The site aims for having a good community established Findability, Accessibility, Interoperability, and Reusability ("FAIR") principles (https://www.dataone.org/fair/). Exceptionally, there are a few datasets located in Antarctica, only because the corresponding studies were related to both the Artic and Antarctica.

As per May-2022, there were 6,696 datasets openly available, resulting in 930,730 data files and 625 citations. The smaller number of citations compared to the number of datasets suggests that there are lot of datasets that have not been used in published articles, and they have the potential to be used in future research. The Artic Data Center also has a private section in which private datasets only are available for logged users.

A good summary of the history of the web portal can be found (https://arcticdata.io/history/). For instance, it was in the period 2015-2016 when the Artic Data Center performed a major data upload when thousands of data files were uploaded into the system.

The research on the Artic shows a noticeable proliferation in the last decades as shown in Figure 3.25, by compiling the dates in which the original data was collected.

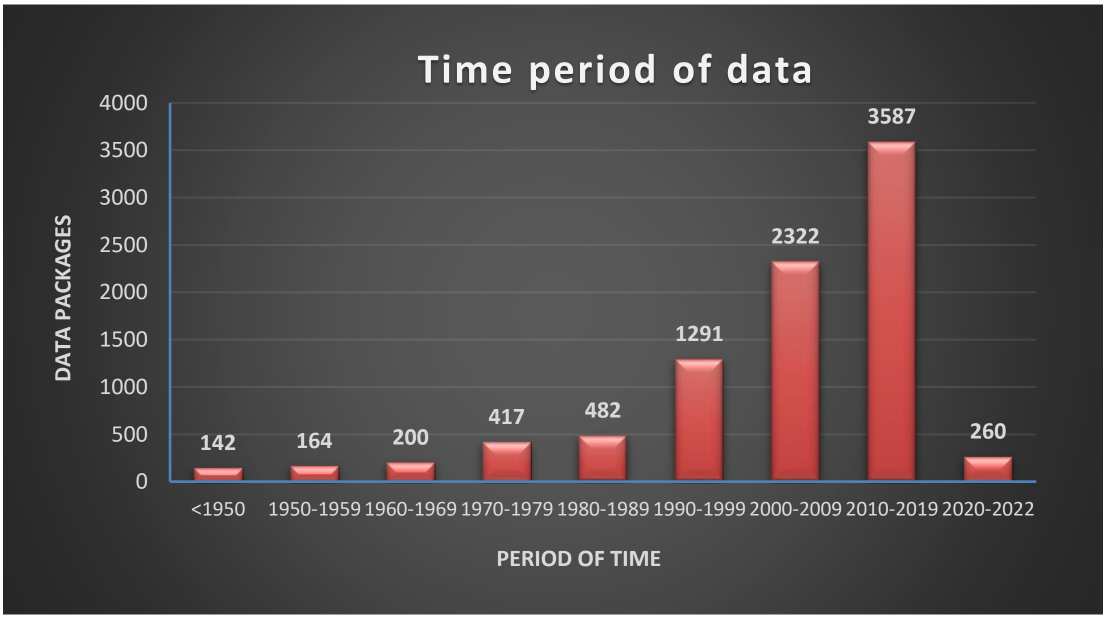

Figure 3.25. The years in which the data was collected, regardless of the upload date (source: Artic Data Center).

The data catalogue of the Artic Data Center (https://arcticdata.io/catalog/data) has a powerful search engine that allows the filtering of the datasets by "Data attribute", "Annotation", "Creator", "Year", "Identifier", "Taxon" and "Location" (Geographic region). However, the mapping capabilities of the Search engine do not allow the export in bulk of the spatial locations of the datasets outside the web map of the portal. The Artic data catalogue has been designed to display the geographic location of the queried datasets by the users inside the embedded web map. It is possible though, to examine the location of a dataset from the corresponding individual metadata page.

Each individual study has a comprehensive metadata page where the several aspects of the associated dataset/s are published. First, each dataset may be packaged with one or more data files. The information stored on each metadata page replicates the following structure of metadata categories: "General", "People and Associated Parties", "Geographic Region", "Temporal Coverage", "Project Information", "Methods & Sampling", "Data Table, Image, and Other Data Details", "Data Set Usage Rights", and "Access Control".

In regard to the exclusiveness of the datasets, it has been found that there are datasets that can be found in other online repositories hosting Artic data (e.g., Ice Cores category at NOAA). This is a characteristic of openly distributed and/or open datasets as their authors want to maximise the shareability of the data and the visibility of their work.

3.3 The Speleothem Isotopes Synthesis and Analysis (SISAL) database

The SISAL (Speleothem Isotopes Synthesis and Analysis) International Working Group (https://doi.org/10.5194/essd-12-2579-2020), has compiled over the years a database of isotopic data ($\delta^{18}O$ and $\delta^{13}C$) from speleothems and associated metadata, taken from previous paleoclimate studies. Its intended goals are to provide support for analysing past climate changes, correlating climate events between records, assessing climate periodicities, identifying potential triggers and evaluating climate model simulations (Comas-Bru et al., 2020). In its latest version (v2.0), the most notable changes are the addition of new age-depth models and their uncertainties. The first version (v1.0) of SISAL (Atsawawaranunt et al., 2018b) has been used so far in several regional reconstructions, such as in Quaternary journal published in 2018: https://www.mdpi.com/journal/quaternary/special_issues/speleothem_records_climate)

The main property of the SISAL database is that are structured data, implying that all of the records have the same fields or properties. This benefits the consistency of the archive, and it mainly avoids duplication of entities. By structuring the data into tabular form, the data is represented in one or more tables that consist of rows (records) and columns (attributes). The multiple tables are referenced one another by using keys, conforming a relational model (Figure 3.26). The "SITE" table incorporates the information at cave level and the "ENTITY" table incorporates the information at speleothem level; one site can have one or more entities. The "SAMPLE" table is perhaps the most important of all of them, as many other tables are linked to this one using the "sample_id" field. An important aspect of SISAL is that the chemical information and the temporal information corresponding to the same sample are stored in different tables. Thus, there is a "d18O" table for $\delta^{18}O$ measurements, and the so-called "d13C" table for $\delta^{13}C$ measurements, the "GAP" table for gaps, the "HIATUS" table for hiatuses, the "ORIGINAL CHRONOLOGY" table for the original time or age estimations, and the "SISAL CHRONOLOGY" table for the new age-depth models' estimations. For instance, for building a time-series on an entity based on all its available $\delta^{18}O$ records and their corresponding age-depth models, three tables would be required for that task: the "SAMPLE", the "d18O" and the "SISAL CHRONOLOGY" tables.

The tables can be managed and queried using Structured Query Language (SQL). The entire SISAL database can be downloaded from the online repository as a MySQL dump file (112 Megabytes), allowing the action of importing the whole database from any database management software. Alternatively, each table is available in comma-separated values (CSV) format files. Currently, the SISAL v2.0 (Comas-Bru et al., 2020) has 293 sites and 686 entities with samples (one cave can have several speleothems as entities, and each entity several samples). The geographic distribution of the 293 caves is represented in Figure 3.27.

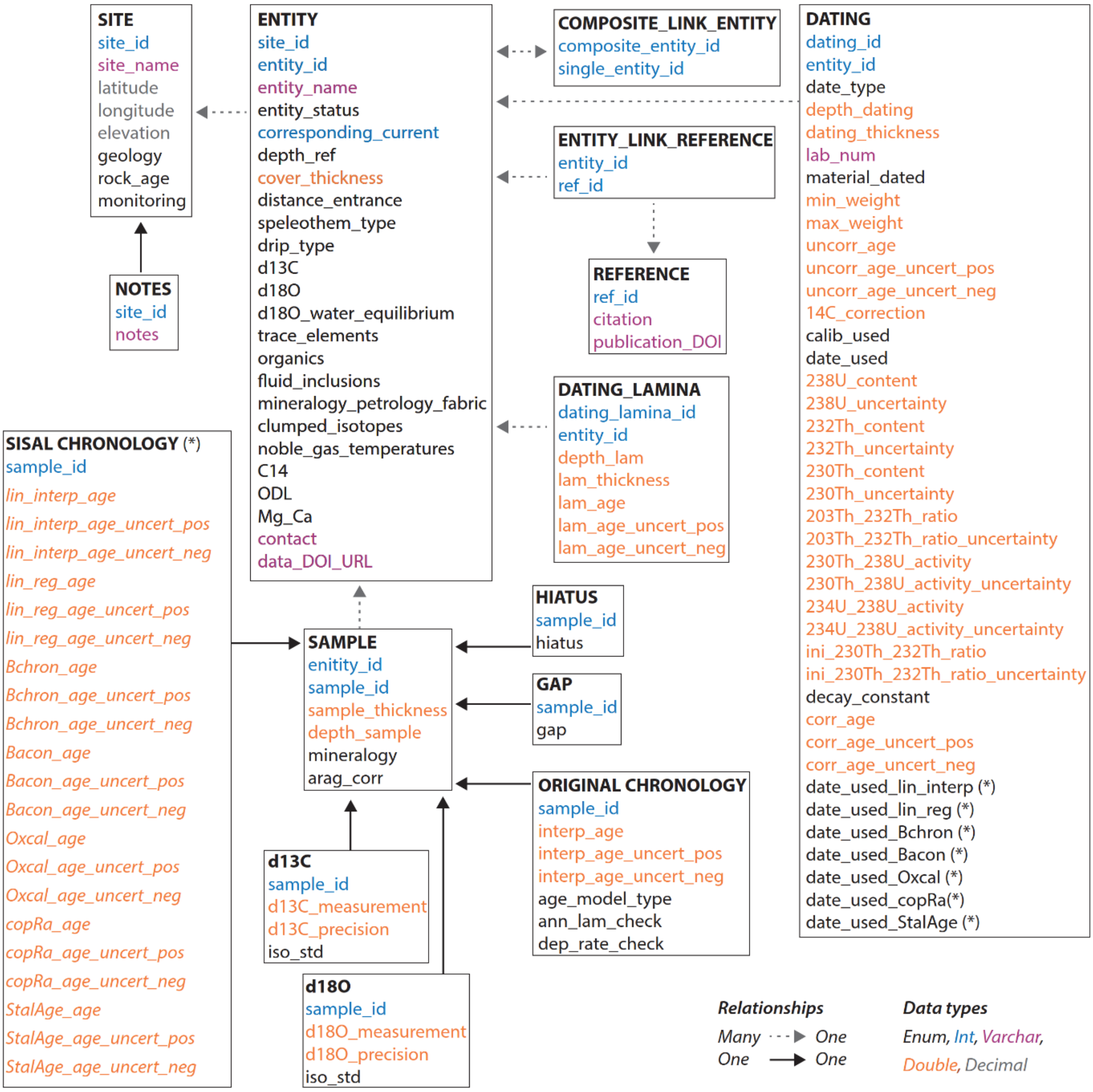

Figure 3.26. Structure of the SISAL database version 2 (from Comas-Bru et al., 2020).

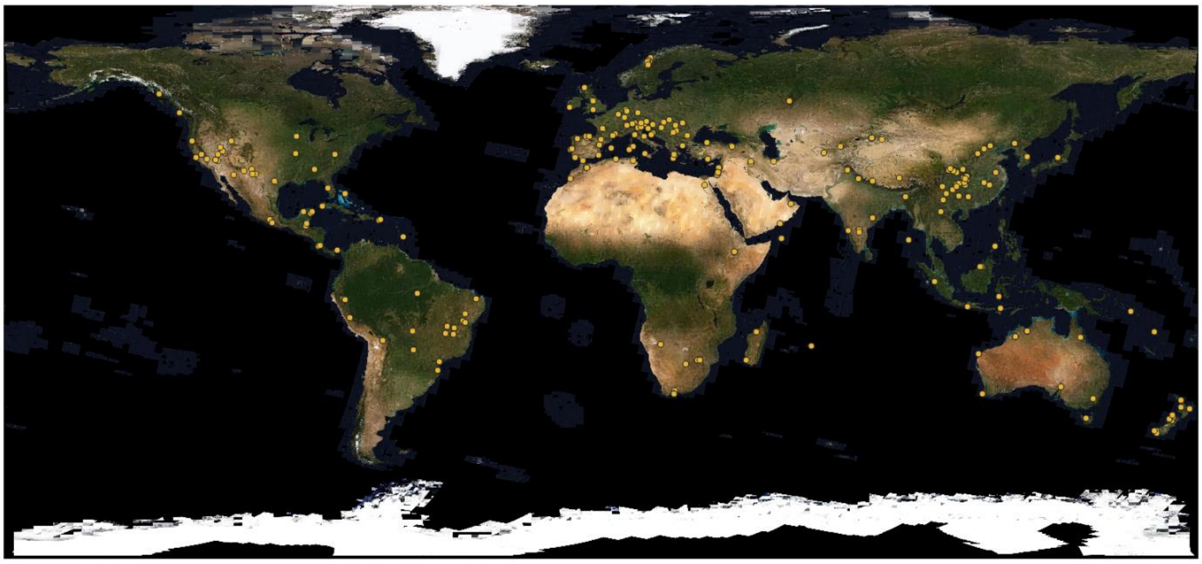

Figure 3.27. Geographic distribution of SISAL speleothems datasets (v.2.0) containing 293 caves (May-2022).

The temporal assessment on the SISAL samples (Figure 3.28) has revealed that most of the records are concentrated in the Upper Pleistocene and Holocene. Thus, when it comes to the conducted "latest age" assessment on the available chronologies, the values for the percentiles p25, p50 and p75, are 139, 6,001 and 47,155 cal. years BP, respectively. The "earliest age" values for the same percentiles are of 5,860, 13,904 and 82,279 cal. years BP, respectively. The values for the "latest age" and the "earliest age" determined a time span for the entities in the range of thousands to tens of thousands of years (Figure 3.28A). However, there are also speleothems with ages within the rest of the Pleistocene period, before the Upper Pleistocene (Figure 3.28B).

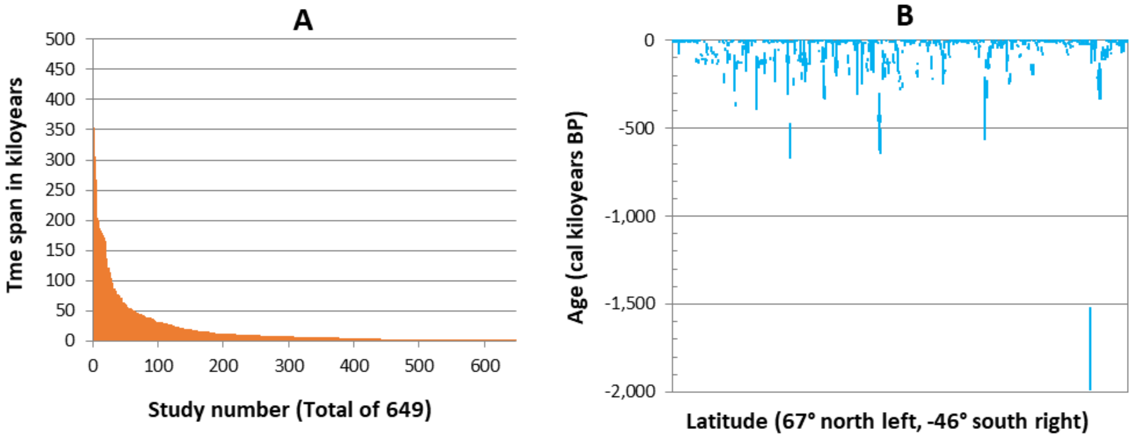

Figure 3.28. A) Time spans of all the 649 entities with starting and ending chronologies in the SISAL database, sorted from largest to smallest. B) Earliest year per entity in the SISAL database, sorted by latitude.

3.4 Agencia Estatal de Meteorología (AEMET)

The "Agencia Estatal de Meteorología" (AEMET) is the national meteorological service for Spain (http://www.aemet.es/en/portada). They have continually provided weather and climate services for more than 150 years.

The potentiality for paleoclimate research in using meteorological datasets from AEMET lies in five products. These products can be used for calibrating paleoclimate methodologies as some of them cover the entire 20th century, offering several decades of precipitation and temperature time series. The datasets are all based on observational data and have the following specifications: (A) optimised daily temperature long series for 22 locations (1850-2005); mostly > from 1893, (B) optimised daily precipitation long series for 66 locations (1850-2005), (C) gridded datasets (5x5 km) containing interpolated daily precipitation and temperature between 1951 and 2020, (D) gridded datasets (20x20 km) containing interpolated daily precipitation and temperature between 1971 and 2010, and (E) gridded datasets (50-60 km) containing interpolated daily precipitation and temperature between 1961-1990.The geographic location of the datasets A, B, C and D is illustrated in Figure 3.29. The corresponding time series have some differences amongst them because of their different catchment area and/or cell size. For example, when comparing the precipitation time series between the long series of the city of Granada (1850-2008), and the two gridded datasets 5x5km (1951-2016) and 20x20km (1971-2010), the graph shows some large divergence around 2010 (Figure 3.29D). Equivalent differences can be expected in other parts of the Iberian Peninsula, as well as for the temperature time series. However, the long series product is the most reliable dataset according to AEMET, as the gridded datasets incorporate a process of aggregation that may contain very heterogeneous values. There is no information available at AEMET for the geographic location of the grid for the 50x50 product.

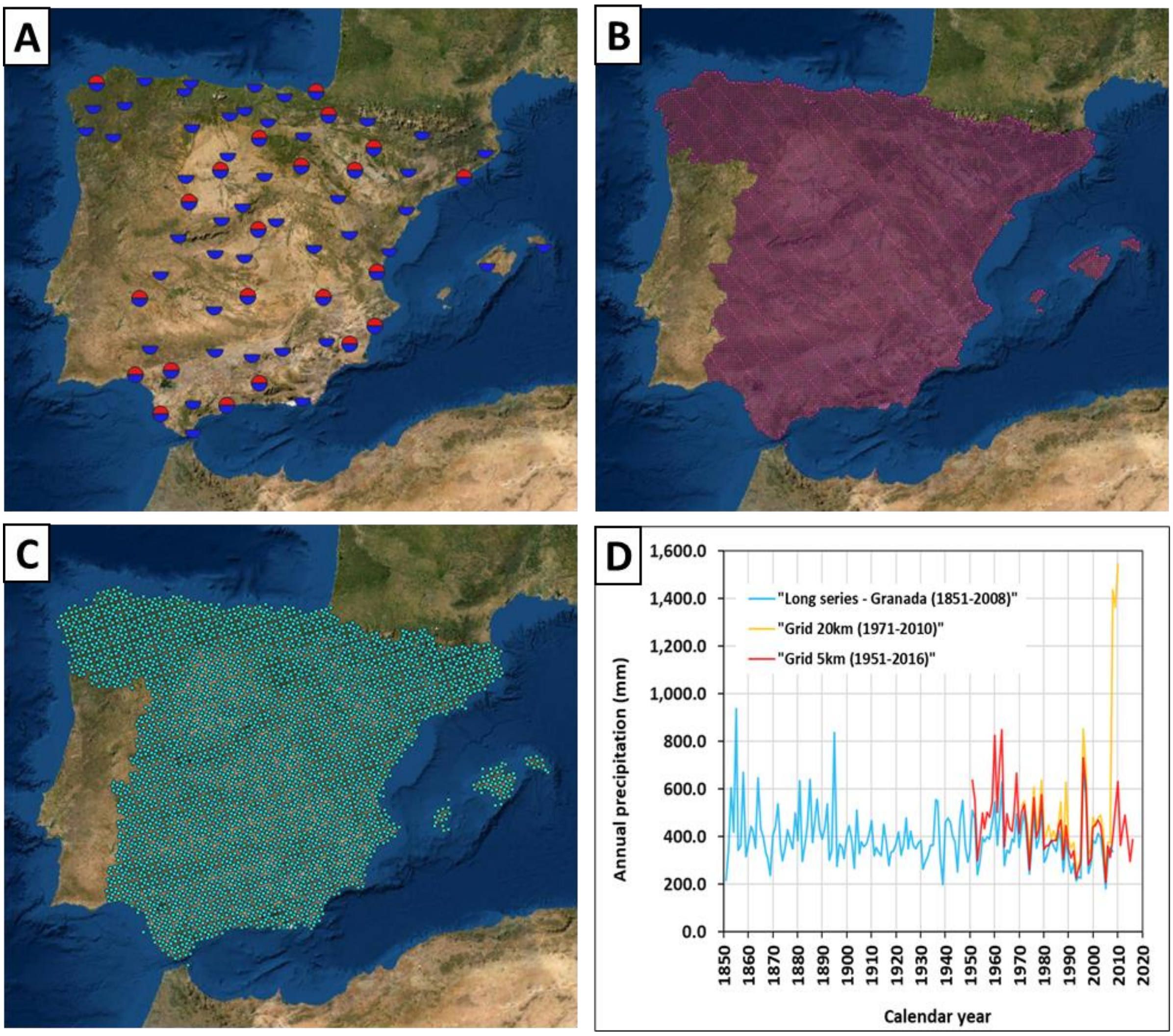

Figure 3.29. Snapshot of the AEMET historic climate datasets. Geographic location of: A) Optimised daily temperature series (RED) and precipitation (BLUE) series, B) 5x5 km gridded dataset and C) 20x20 km gridded dataset. D) Comparison of annual precipitation time series from datasets A, C and D for the location corresponding to the city of Granada.

3.5 Copernicus Climate Change Service

The Copernicus Climate Change Service (C3S) and its associated Climate Data Store (CDS) (https://cds.climate.copernicus.eu/) is an European Union initiative, which aims for providing combined climate data with latest science developments (e.g., modelling and/or supercomputing), aiming to be used as climate information for the research on recent past, present and near future. It covers climate states of Europe and worldwide.

The CDS toolbox (https://cds.climate.copernicus.eu/toolbox/doc/index.html) is aimed for providing technical support, computer power and ease of access to the CDS datasets. It has tutorials, guides, an application gallery, learning examples, a glossary, and an API section.

C3S is operated by the European Centre for Medium-Range Weather Forecasts (ECMWF) (https://www.ecmwf.int/) being an intergovernmental organisation funded by 35 states and acting as both research institute and operational service, amongst other research and learning activities. It is specialised in forecasting data, analysing Earth systems, and making climate predictions, but it also maintains an archive of meteorological datasets.

The access, usage and dissemination of Copernicus datasets are licensed by the European Union, but it is lawful for any scientific research as long as the corresponding attribution to the Copernicus programme is included. Additionally, some specific datasets available at the CDS web portal incorporate a citation and a DOI that should also be acknowledged. For accessing the data there is the pre-requisite for the user to create an account and to be logged into the system while querying and/or downloading the datasets. The access is also granted programmatically via API request by sending the corresponding API key attached to it.

The usefulness and potential of the C3S datasets has given good results by analysing atmosphere dynamics against aerosol deposition on the Greenland ice (see Chapter VIII. A case study using ice cores data: Approaching the Younger Dryas). Amongst the benefits of using C3S, one is the diverse range of global datasets covering different physical variables, environments, geographic areas, and temporal scenarios, as well as an extensive supporting documentation. On the other hand, the temporal coverage is limited to the 21st and 20th centuries. The conducted assessment revealed that, as in May-2022, there were 131 datasets available, and 75 of these have a global scope. A summary of the main stats for all the C3S categories of available datasets is presented in Table 3.2, and a brief description of the datasets is included in the Appendix 1.1.

For the download of the datasets, a system of queuing is in place, which allows the user to request datasets and manage the later download of the data at its own pace, once the datasets are ready, which can take from seconds to hours depending on the size of the datasets, but also on the number of live requests and/or other users' connections at the moment of the request. Each user has its personal area in the CDS portal under the name of "Your requests", where to take control of its previous or current requests.

For the same product (e.g., "ERA5 monthly averaged data on pressure levels from 1979 to present"), different variables can be available (e.g., geopotential, relative humidity, temperature, etc.), being the total size of the dataset much of an issue. Thus, for global datasets having several variables, a time dimension, a horizontal dimension and a vertical dimension, there are limitations imposed by the system on the size of the dataset that can be downloaded per request, which it forces the user to request smaller subsets of the dataset by amending the product type, the variables, the temporal interval, the geographical area and the data format of the request.

The datasets incorporate a comprehensive metadata (Overview section) consisting of the data description (data type, projection, horizontal coverage, horizontal resolution, temporal coverage, temporal resolution, file format, update frequency), list of main variables (name, units, description), and related variables if any. Furthermore, ECMWF provides with an extensive documentation regarding known issues which helps to understand the limitations, scope, and applicability of the data.

Another interesting feature of the CDS portal is the exposure of several metrics and statistics in the "Live" section (https://cds.climate.copernicus.eu/live/). These published figures are the number of registered users, running users, queued users, running requests, queued requests and daily downloads (in Terabytes) amongst other useful metrics.

ECMWF implements the supportive page C3S Copernicus Knowledge Base (CKB) (https://confluence.ecmwf.int/x/diwICQ), the C3S Forum (C-Forum) (https://confluence.ecmwf.int/x/iA80Dw) and the Support Portal (https://confluence.ecmwf.int/category/cd).

Furthermore, ECMWF is the author of the Python library "cdstoolbox", that has been designed to interact with the Copernicus datasets for producing bespoke data functionalities and visualizations within live applications. There are about 20 applications currently available at the CDS portal. Every application has the necessary documentation to understand how it works and what is trying to achieve, as well as the published source code. A summary of the categories of the available applications is presented in Table 3.3, and a brief description of the applications is included in the Appendix 1.2.

DATASETS		Variable domain								Spatial coverage		Temporal coverage			Sector									Provider			
	N. of datasets	Atmosphere (composition)	Atmosphere (surface)	Atmosphere (upper air)	Land (biosphere)	Land (cryosphere)	Land (hydrology)	Ocean (biochemistry)	Ocean (physics)	Europe	Global	Future	Past	Present	Agriculture	Biodiversity	Coastal regions	Disaster risk reduction	Energy	Health	Infrastructure	Tourism	Water management	Copernicus C3S	Copernicus CEMS	ESA CCI	EUMETSAT SAF
Climate indices	5	-	-	-	1	-	4	-	-	4	1	3	3	-	-	-	-	1	-	-	-	-	3	2	-	-	-
Climate projections	30	-	11	6	5	-	3	-	5	19	10	29	24	22	2	-	6	2	2	2	1	2	5	9	-	-	-
External Services	1	-	-	-	-	-	-	-	-	-	1	-	1	-	-	-	-	-	-	-	-	-	-	1	-	-	-
In-situ observations	11	1	7	3	-	1	1	-	-	3	7	1	11	1	1	-	-	-	-	-	1	-	-	1	-	-	-
Reanalysis	35	-	11	16	6	-	7	-	1	11	20	2	35	-	2	2	-	-	2	-	1	-	-	22	4	-	-
Satellite observations	36	4	4	5	5	5	5	1	9	3	29	1	36	12	-	-	1	-	-	-	-	-	-	11	-	2	4
Seasonal forecasts	10	-	-	-	-	-	4	-	-	3	7	7	8	3	-	-	-	-	-	-	-	-	2	8	2	-	-

Table 3.2. Summary table of the stats for available datasets at the Copernicus Climate Change Service (C3S) dated in May-2022.

APPLICATIONS		Variable domain								Spatial coverage		Temporal coverage			Sector									Provider			
	N. of datasets	Atmosphere (composition)	Atmosphere (surface)	Atmosphere (upper air)	Land (biosphere)	Land (cryosphere)	Land (hydrology)	Ocean (biochemistry)	Ocean (physics)	Europe	Global	Future	Past	Present	Agriculture	Biodiversity	Coastal regions	Disaster risk reduction	Energy	Health	Infrastructure	Tourism	Water management	Copernicus C3S	Copernicus CEMS	ESA CCI	EUMETSAT SAF
Climate projections	2	-	1	-	-	-	-	-	-	1	1	2	1	1	-	-	1	-	-	-	-	-	-	1	-	-	-
In-situ observations	1	-	-	-	-	1	-	-	-	-	1	-	1	-	-	-	-	-	-	-	-	-	-	-	-	-	-
Reanalysis	4	-	1	-	-	-	-	-	-	1	2	1	4	-	-	-	-	-	1	-	-	-	-	2	-	-	-
Satellite observations	4	-	1	-	-	1	1	-	-	-	4	-	4	1	-	-	-	-	-	-	-	-	-	1	-	1	-

Table 3.3. Summary table of the stats for the available applications at the Copernicus Climate Change Service (C3S) in May-2022.

4 Chapter IV. Methodology

During this research, a wide range of different methodologies has been developed, tested and applied to different scientific aspects. The methodologies exposed here can be considered as generic within the scope of the research plan, being mainly instrumental either for gathering the needed data or for gaining the required technical expertise and scientific knowledge. There is another group of more specific methodologies developed within the particular scope of each of the case studies that will be detailed in the corresponding chapters (see Chapters V, VI, VII and VIII).

The first group of the methodologies focuses on the NOAA datasets (subsection 4.1). The first part aims for describing the steps for downloading both the metadata and data files from all the different paleoclimate archives available at NOAA (subsection 4.1.1). The second part continues by presenting various developed scripts that are capable of translating the Tree Rings datasets (structured in .rwl files) into a more common data definition that will be later used in statistical and spectral analysis (subsection 4.1.2). The Tree Rings datasets represent an important part of the conducted research and they have been used in one of the case studies, therefore both generic and specific methodologies have been developed for this paleoclimate archive. The second and third groups of the methodology deepen into the extraction of time series from climate datasets containing physical variables. Specifically, the second group extracts climatic data using NetCDF global datasets (structured in .nc files) that have been previously downloaded from the Copernicus Climate Change Service (subsection 4.2). The third group describes the way to operate with meteorological and/or climatic datasets from AEMET, such as those related to precipitation and/or temperature (subsection 4.3). The fourth group contains the research made on the different spectral methods available for the research of paleoclimate time series. Two areas of spectral research have been developed; one is the investigation on the influence of different noise types (stochastic models) on the power spectra of simulated time series (subsection 4.4.1) and a second one specifically focused on the benefits of the Lomb-Scargle periodogram as spectral estimator (subsection 4.4.2). The fifth group presents the generation of insolation time series based on the program Earth Orbit v2.1, which is crucial for understanding the Quaternary climate evolution at orbital time scales (subsection 4.5). Finally, a novel Python code has been developed for the visualization of spectral analysis results from non-stationary time series, which helps with their analysis and interpretation (subsection 4.6).

4.1 NOAA datasets

4.1.1 NOAA datasets download process

The task of assessing the NOAA paleoclimate datasets required the development of a computer method for downloading the datasets from the NOAA paleoclimate archives. A semi-automatic approach has been followed, using created automation tasks in Python and manual methods. Over 8,636 studies containing in total 31,604 files were downloaded in 2016. The developed methodology can be divided in the following steps:

(1) For every paleoclimate archive (e.g., tree rings) the full table from the web page corresponding to all the studies organised by Title and Investigator (e.g., https://www.ncdc.noaa.gov/paleo-search/reports/all?dataTypeId=18&search=true), was copied (by doing mouse selection) and paste it as HTML into an Excel file sheet called "before macro". This action produced 8 rows of data per study (the web table contained 8 fields or columns per study in the NOAA website). The paste action produced that all of the data was inserted into one column. Before transposing the information back into 8 different columns, a manual check was conducted for ensuring that every study contained 8 rows as per the following fields: Title, Investigators, N_LAT, S_LAT, W_LON, E_LON, Earliest Year BP (CE) and Most Recent Year BP (CE).

(2) A second empty sheet called "after macro" was created for placing the results. This is the code of the created Excel macro:

```
Sub Transpose_HTML()
'
' Macro2 Macro
'
' Keyboard Shortcut: Ctrl+Shift+A
'
    ActiveCell.Range("A1:A8").Select
    Selection.Copy
    Sheets("after macro").Select
    Selection.PasteSpecial Paste:=xlPasteValues, Operation:=xlNone, SkipBlanks _
        :=False, Transpose:=True
    ActiveCell.Select
    Selection.PasteSpecial Paste:=xlPasteAll, Operation:=xlNone, SkipBlanks:= _
        False, Transpose:=True
    ActiveCell.Offset(1, 0).Range("A1").Select
    Sheets("before macro").Select
    ActiveCell.Offset(8, 0).Range("A1").Select
End Sub
```

Before running it, the active cell must be the very first cell at the top containing the hyperlink or link as Title.

(3) Having all the studies as rows in the sheet “after macro”, the next action aims for translating the titles as hyperlinks into readable URLs, for future reference and automation purposes. The created code for this Excel macro is:

```
Sub ExtractHL()
    Dim HL As Hyperlink
    For Each HL In ActiveSheet.Hyperlinks
    HL.Range.Offset(0, 1).Value = HL.Address
    Next
End Sub
```

Before running this second macro, the column containing all the hyperlinks must be copied in isolation to a new sheet, followed by the selection of the top cell of the list as the active cell. The URLs will be created by the macro in the next column, all records in one go.

(4) The last step is about gathering together the different columns created in the previous steps into one single sheet.

Once the hyperlinks have been extracted from the web, the automatic process for downloading the datasets from the NOAA archives can be pursued. These are the steps:

(1) A list in CSV format containing the links to the files must be created following this content structure:

```
id,study,Hyperlink
1,22315,https://www.ncdc.noaa.gov/paleo/study/22315
2,9957,https://www.ncdc.noaa.gov/paleo/study/9957
3,20085,https://www.ncdc.noaa.gov/paleo/study/20085
```

(2) In second place, a Python script was developed for looping trough the CSV file and download for each row the important metadata associated to each study (in XML format), plus any other dataset referenced within the xml file (*.txt, *.xls, etc.).

```
# -*- coding: utf-8 -*-

import os
import urllib.request
import random
import csv
from random import randint
from time import sleep
from urllib.parse import urlparse
from os.path import splitext, basename
```

```
url = "http://www1.ncdc.noaa.gov/pub/data/metadata/published/paleo/dif/xml/noaa-cave-"
input_f = r"00 INPUT speleotemas Datasets ALL.csv"
abspath = os.path.abspath(__file__)
root = os.path.dirname(abspath)
out = os.path.join(root, '01 OUTPUT speleotemas Datasets ALL.txt')

dictio = {}

with open(input_f, 'r') as csvinput:
    reader = csv.reader(csvinput)
    next(reader, None)  # skip the headers

    for row in reader:
        cadena = url + str(row[1]) + ".xml"
        archivo = row[1] + ".xml"
        delay = random.uniform(0.2, 0.8)
        sleep(delay)

        try:
            response = urllib.request.urlopen(cadena)
            print(response.getcode())
            if response.getcode() == 200:

                urllib.request.urlretrieve(cadena, archivo)
                print("\nFrom: " + cadena)
                print("To: " + archivo)
                print(" will be downloaded in " + str(delay) + " sec.2")
                file_path = os.path.join(root, archivo)
                with open(file_path) as fp:
                    for line in fp:
                        if "<URL>" in line:
                            to_write = line[line.find("<URL>")+5:line.find("</URL>")]
                            print(to_write)
                url_file = to_write
                disassembled = urlparse(url_file)
                filename, file_ext = splitext(basename(disassembled.path))
                archivo2 = os.path.join(root, row[1] + "_" + filename + file_ext)

                myfile = urllib.request.urlopen(to_write)
                with open(archivo2, 'wb') as output:
                    output.write(myfile.read())
                fila = str(row[1])+","+str(to_write)+","+str(archivo2)+"\n"
                dictio[row[1]] = fila

        except urllib.error.URLError as e:
            dictio[row[1]] = 404
            pass

output_w = open(out, 'w')
```

```
        output_w.write("Study,URL,File\n")
        for k, v in dictio.items():
            output_w.write(str(v))
        output_w.close()
```

For maintenance purposes and/or future upgrades, the base URL of the NOAA web site that is hard coded in the script is linked to a particular NOAA archive (e.g., speleothems) and must be checked periodically to ensure that future downloads are pointing to the right URL.

4.1.2 NOAA Tree rings datasets

The tree rings datasets downloaded from NOAA are natively built into several data formats (*.rwl, *.crn, *.txt, etc.). The most important ones are the raw ring width values that are encapsulated in each rwl file. Each file is specific to a site in which several trees are sampled, and generally the same tree is sampled twice. The rwl files follow the so-called "Tucson Decadal" format which contains a series of headers followed by rows having the core ID values with their 10 annual measurements per decade. Widths are usually expressed in units of .01mm or .001mm of the ring thickness, and the missing values are either 999 or -9999. To help with the interpretation of the datasets NOAA has published text files that are attached to each study and contain metadata and statistical analysis information.

The rwl files can be read in tree ring-related specific software and/or libraries for different programming languages (e.g., Matlab®, R, etc.). However, they have to be transformed to be used outside the dendrochronology domain, such as the spectral analysis. This research has developed a series of Python scripts that can interact with these rwl files and have the following three main goals: (1) extracting the basic information from the txt headers for all the available tree ring studies from NOAA, (2) grouping the datasets into sub-folders by tree species using the output from step 1, and (3) extracting the individual tree ring widths of each core from targeted datasets and writing the individual time series into CSV format.

The first developed Python code extracts some basic information within the txt file headers: Species information, Elevation, Beginning year, Ending year, Latitude and Longitude, and save the results into a CSV file. The code that has been run is:

```
# -*- coding: utf-8 -*-
import os
import csv
```

```
if __name__ == '__main__':
    path = r".\data"
    out_f = "tree_rings_summary.csv"

    cols = ['Species information    :',
            'Elevation              :',
            'Beginning year         :',
            'Ending year            :',
            'Latitude               :',
            'Longitude              :']
    with open(out_f, 'w', newline='') as csv_file:
        writer = csv.writer(csv_file, delimiter=',')
        headers = ["Study", "From", "Height", "To", "Lat", "Lon", "Species"]
        writer.writerow(headers)
        for dirname, dirnames, filenames in os.walk(path):
            for f in filenames:
                extension = os.path.splitext(f)[1][1:]
                if extension == "txt":
                    file_path = os.path.join(dirname, f)
                    record = []
                    with open(file_path, 'r') as openfile:
                        lines = [l for l in openfile if any(col for col in cols if col in l)]
                        record.append(f[0:f.find("_")])
                        for line in sorted(lines):
                            extract = line[line.find(":") + 1:].rstrip('\n').strip(' ')
                            record.append(extract)
                        writer.writerow(record)
```

Thanks to this code, new intel has been gathered regarding the metadata encapsulated within the txt files. For instance, the top 20 tree species sorted by their number of available rwl files are displayed in Figure 4.1.

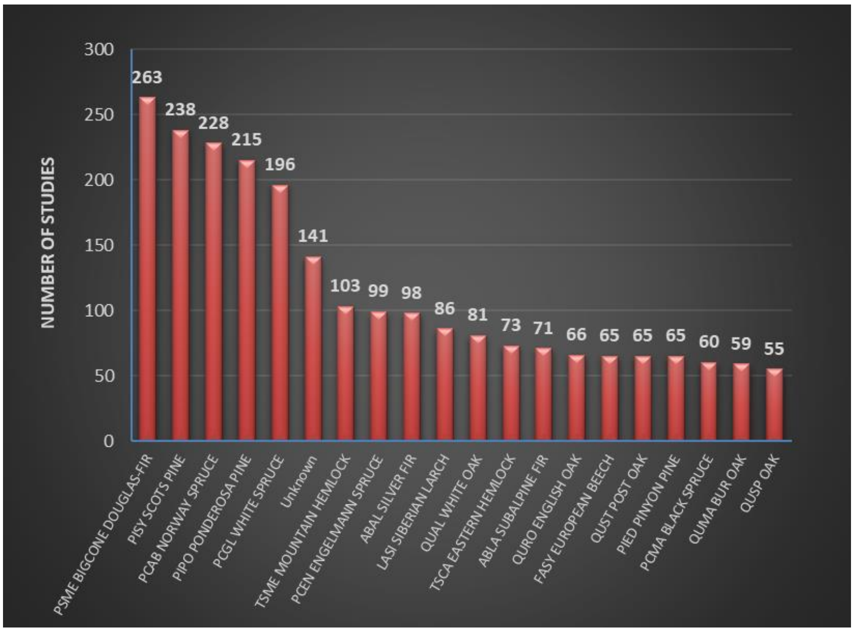

Figure 4.1. Top 20 species derived from the analysis on all the NOAA available Tree Rings metadata files.

The second script is capable to organise all the numerous downloaded files (~20,000 files in 2016) from the Tree Rings archive into sub-folders by species name. This is useful if for example, the research needs to focus on a particular tree species. A pre-requisite is the study number associated to each NOAA dataset to be appended to each filename in the initial download process. The code is:

```
# -*- coding: utf-8 -*-
import os
import csv
import shutil


if __name__ == '__main__':

    script_base = os.path.dirname(os.path.abspath(__file__)) + "\\data"

    myfiles = {}
    for dirname, dirnames, filenames in os.walk(script_base):
        for f in filenames:
            extension = os.path.splitext(f)[1][1:]
            if extension == "txt":
                txt_path = os.path.join(script_base, f)
                with open(txt_path) as openfile:
                    for line in openfile:
                        if "Species information    : " in line:
                            line = str(line.encode('utf-8').strip())
                            start = line.find(":") + 1
                            species = line[start:len(line)]
                            species2 = species.rstrip('\n')
                            species3 = species2.strip(' ')
                            species4 = species3.replace("'", "")
                            break
                myfiles[f[0:f.find("_")]] = species4

    for dirname, dirnames, filenames in os.walk(script_base):
        for f in filenames:
            initio = os.path.join(script_base, f)
            species = myfiles[f[0:f.find("_")]]
            target_folder = os.path.join(script_base, species)
            if not os.path.exists(target_folder):
                os.makedirs(target_folder)
            start_f = os.path.join(dirname, f)
            end_f = os.path.join(target_folder, f)
            shutil.move(start_f, end_f)
```

Finally, the third script extracts the width time series contained within the rwl file. This was validated using one single rwl file corresponding to the study number 4686 (species Abies Pinsapo or Spanish Fir) located in the southwest of Spain. The developed code is:

```
# -*- coding: utf-8 -*-
import os
import csv


def deter_study_number(filename):
    study_number = filename[0:filename.find("_")]
    return study_number


def deter_study_type(filename):
    """
    D Total Ring Density, E Earlywood Width, I Earlywood Density, L Latewood Width, N
    Minimum Density R Ring Width, T Latewood Density, X Maximum Density, P Latewood
    Percent
    """
    rwl_keys = ["d", "e", "i", "l", "n", "p", "t", "x"]
    exte = os.path.splitext(filename)[1]
    key_letter = filename[filename.find(exte) - 1:filename.find(exte)]
    if key_letter.lower() in rwl_keys:
        study_type = key_letter
    else:
        study_type = "v"
    return study_type


def rwl_read(rwl_path, filename):
    file_path = os.path.join(rwl_path, filename)
    # 4686_spai007e.rwl
    first_bit = deter_study_number(filename)
    second_bit = deter_study_type(filename)
    # 4686_e
    study_name = first_bit + "_" + second_bit
    count = 0  # lines
    serie_uniq = {}
    datafile = open(file_path, 'r')
    datareader = csv.reader(datafile)
    for row in datareader:
        # headers
        if count < 3:
            count += 1
            continue
        else:
        # E230301A1810   443  459  315  284  301  460  407  343  363  278
            series = row[0][:8].rstrip()
            year = int(row[0][8:12])
            new_row = ((row[0].replace(series, "")).replace(str(year), "")).lstrip()
            for elem in new_row.split():
```

```
                    # normal values (by default units are .01 mm)
                    if str(elem) != "999" and str(elem) != "9999" and str(elem) != "-999" and
str(elem) != "0":
                        serie_uniq[year] = str(elem)
                    # missing values or NULL values
                    if str(elem) == "-999" or str(elem) == "0":
                        serie_uniq[year] = "-999.25"
                    # 0.01mm (1/100th mm) -> 999 OR 0.001mm (microns) -> 9999
                    if str(elem) == "999" or str(elem) == "9999":
                        serie_uniq[year] = "-999.25"
                        # if they are in microns change to .01 mm
                        if str(elem) == "9999":
                            for yr, ring in serie_uniq.items():
                                serie_uniq[yr] = str(float(ring / 10))

                        # write to file
                        new_name = study_name + "-" + series
                        new_file = os.path.join(rwl_path, new_name + ".csv")

                        with open(new_file, 'w', newline='') as csv_file:
                            writer = csv.writer(csv_file, delimiter=',')
                            fila = []
                            for yr, ring in serie_uniq.items():
                                fila.append(str(yr))
                                fila.append(str(ring))
                                writer.writerow(fila)
                                fila = []
                        # Back to defaults
                        series = row[0][:8].rstrip()
                        serie_uniq = {}

                    year += 1
        datafile.close()



    if __name__ == '__main__':

        path = r".\data\ABPN SPANISH FIR"
        files_rwl = []
        for dirname, dirnames, filenames in os.walk(path):
            for f in filenames:
                extension = os.path.splitext(f)[1][1:]
                if extension == "rwl":
                    files_rwl.append(str(f))

        for rwl in files_rwl:
            rwl_read(path, rwl)
```

Thus, for the case of this dataset, 22 CSV files were generated, each file containing the tree-ring widths from each sampled core. In Figure 4.2 the width values of the 22 sampled cores are displayed (grey lines), together with the average curve (green line) and the number of samples (purple line) per calendar year. The obtained values were verified against the published metadata values for this dataset, to ensure the created code produced the expected results.

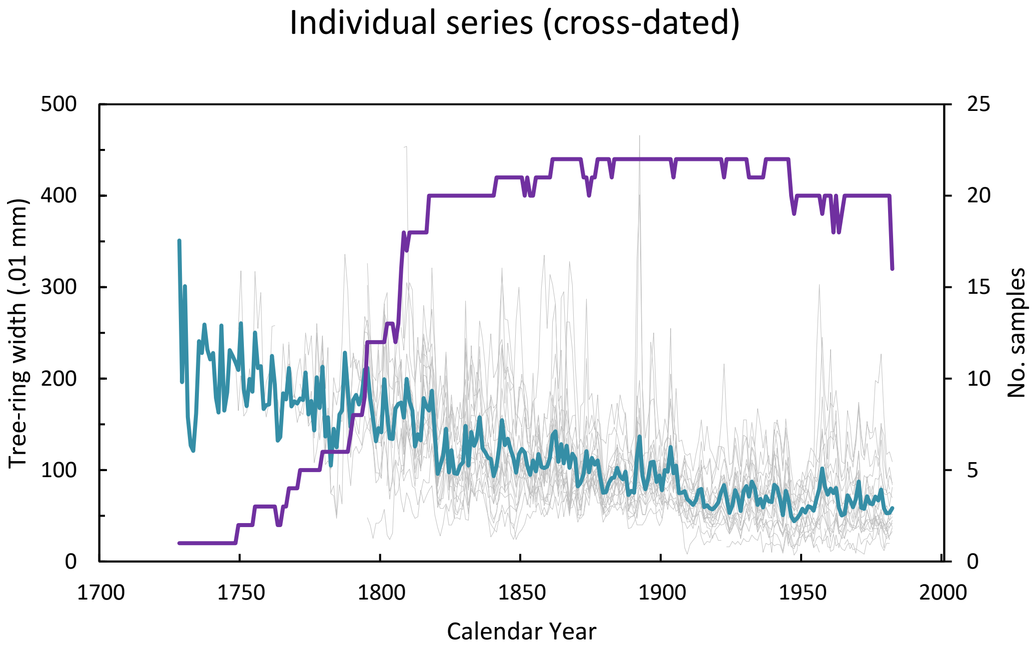

Figure 4.2. Tree-ring widths per calendar year extracted from a RWL file from a study located in SE Spain.

4.2 Copernicus datasets

Most of Copernicus datasets are distributed either in GRIB format (GRIdded Binary), especially designed for weather data, or in NetCDF format (network Common Data Format), widely used for array-oriented scientific data (https://www.unidata.ucar.edu/software/netcdf/). This research has focused solely on the usage of the NetCDF format. According to Unidata (https://www.unidata.ucar.edu/), the NetCDF format is characterised by being self-describing, portable, scalable, appendable, sharable, and archivable. A NetCDF file (*.nc) can be manipulated by using multiple freely available and/or licensed (commercial) software. This research used the computer program Matlab® for extracting time series containing meteorological data (see Chapter VIII). To illustrate the process of extracting data from a NetCDF file, the developed methodology has tested the data product named: "ERA5 monthly averaged data on pressure levels from 1979 to present" (Hersbach et al., 2019). This product is a global dataset of reanalysis having 4 product sub-types: "Monthly averaged reanalysis", "Monthly averaged ensemble members", "Monthly averaged reanalysis by hour of day" and "Monthly averaged ensemble members by hour of day". It contains 16 different physical variables: "Divergence", "Fraction of cloud cover", "Geopotential", "Ozone mass mixing ratio", "Potential vorticity", "Relative humidity", "Specific cloud ice water content", "Specific cloud liquid water content", "Specific humidity", "Specific rain water content", "Specific snow water content", "Temperature", "U-component of wind", "V-component of wind", "Vertical velocity" and "Vorticity (relative)". Horizontally, the gridded model uses a 0.25° x 0.25° cell size (less for the ensemble members: 0.5° x 0.5°). Vertically, it is interpolated for 37 different pressure levels ranging from 1,000 hPa (~ Earth surface) to 1 hPa (top of the stratosphere). Temporally, it covers the years 1979-2021, every month from January to December and 24 hours of choice (00:00-23:00). Regarding the geographical area, it is possible to download the whole available region or to specify a sub-region. Finally, the user can specify the file format, either GRIB or NetCDF.

The first step is to determine the specific parameters for the generation of the .nc file by the Climate Data Store service. This is because there are restrictions in place for downloading the data depending on its size (even certain combinations of parameters are blocked if the sub-dataset becomes too large). A valid subset of the data can be downloaded by for example selecting the following parameters: "Monthly averaged reanalysis" as sub-type, "Temperature" as variable, 1,000 hPa as pressure level, complete period 1979-2012 (00:00 for the hour reference) as time, whole available region as extent and NetCDF as file format. After a few minutes of queueing, a .nc file of 847.2 MB in size becomes available to be downloaded in the user's requests web area.

To test the methodology, two main operations as user cases were conducted for the purpose of extracting data from the whole downloaded dataset, one was to generate a ground air temperature time series for the whole period (1979-2012) at one specific location (e.g., cell over Mount Teide in Tenerife), and the second one was to generate a global dataset of ground air temperature for a fixed time (e.g., July-2003). Before conducting the coding operations in Matlab, it is important to mention that the downloaded dataset had dimensions of 1,440 cells (longitude) x 721 cells (latitude) x 408 steps (months), which can be retrieved from the .nc description inside the file.

In the fixed location case, it is required to translate the geographic coordinates of the location into the gridded model coordinates. The longitude is counted in the model starting at the Greenwich meridian; 0° corresponds to cell 1 and by moving eastwards we can reach cell 1440. The latitude is counted starting in the North pole; 90° corresponds to cell 1 and moving southwards to reach cell 721. Therefore, the Mount

Teide in Tenerife corresponds to the cell with coordinates (1374, 248) (Figure 4.3). The code in Matlab for extracting the temperature time series for this location is:

```
filename = 'global_temperature_1000hPa_1979_2012.nc';
nc = fullfile(cd, filename);
[filepath,name,ext] = fileparts(nc);
w = ncread(nc,'t',[1374 248 1], [1 1 408], [1 1 1]);
w = permute(w,[3 2 1]);
out_w = strcat('Tenerife_', name, '.csv');
w_csv = fullfile(filepath,out_w);
csvwrite(w_csv,w);
fclose('all');
```

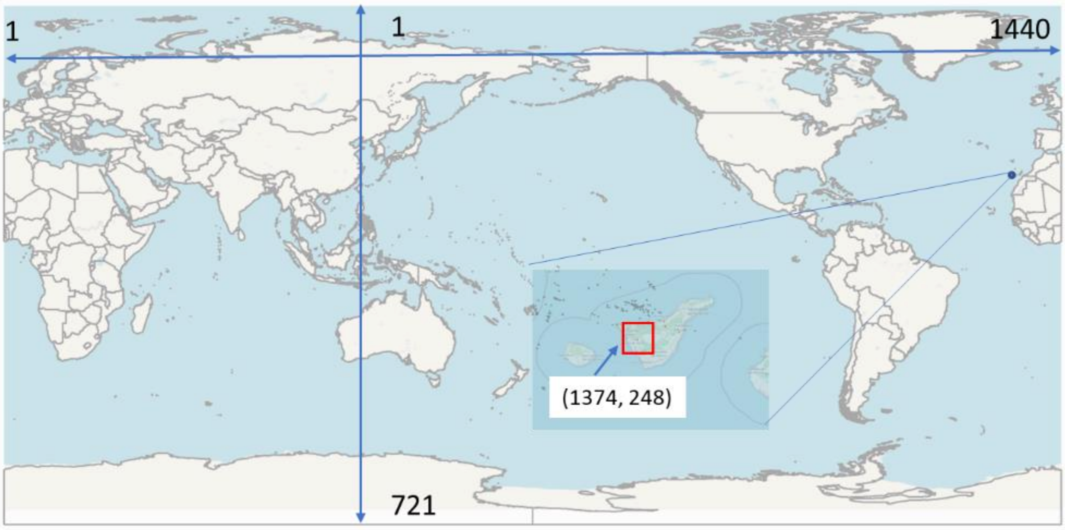

Figure 4.3. Schema of the grid orientation for the "ERA5 monthly averaged data on pressure levels from 1979 to present" dataset, and location of the cell corresponding to The Teide in the Tenerife island.

The extracted air temperature time series at ground level for the whole analysed period is shown in Figure 4.4.

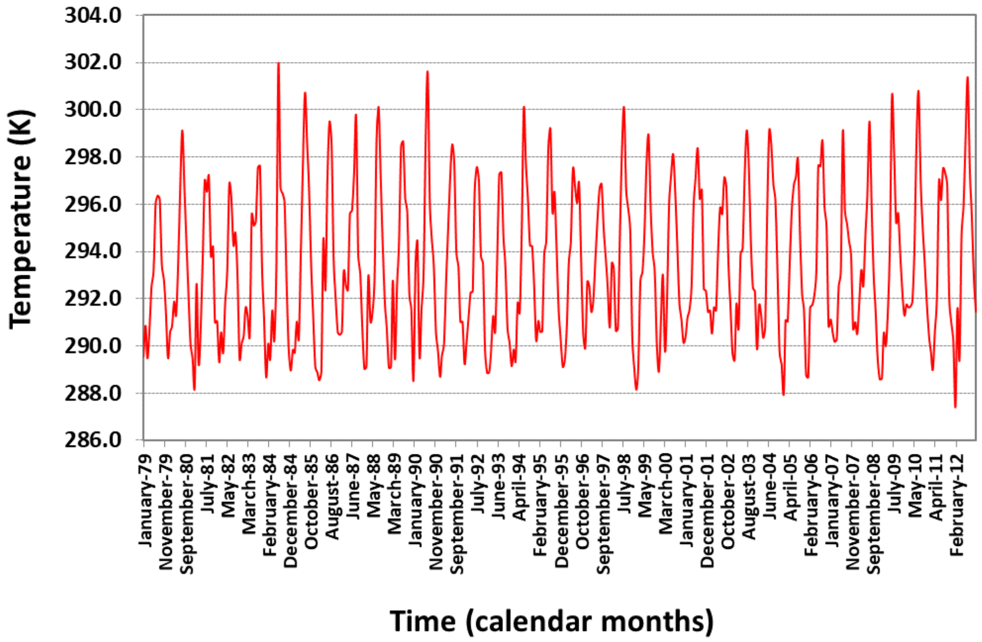

Figure 4.4. Air temperature time series at 1,000 hPa pressure level (Earth surface) between 1979 and 2012 for the cell (1374, 248) corresponding to the Mount Teide.

It is important to mention that because of the resolution of this dataset (0.25° x 0.25°), both the coast and the Mount Teide are within the same model cell, resulting in the same averaged temperature for both locations. Therefore, the extracted temperature time series should be taken with caution for regional and/or local studies and in other equivalent situations elsewhere.

In the user case of the selected fixed time, the key step is to lock the date to the value of July-2003, which corresponds to the time step 295 (number of months starting on Jan-1979), followed by the extraction of the associated temperature values for all the latitude and longitude values for that time step. The code is:

```
filename = 'temperature.nc';
nc = fullfile(cd, filename);
[filepath,name,ext] = fileparts(nc);
lon = ncread(nc,'longitude');
lat = ncread(nc,'latitude');
time_value = ncread(nc,'time',[295], [1]);
t = ncread(nc,'t',[1 1 295], [1440 721 1], [1 1 1]);
out_w = strcat('July2003_', name, '.nc');
w_nc = fullfile(filepath,out_w);
ncid = netcdf.create(w_nc,'NETCDF4');
```

```
netcdf.close(ncid);
nccreate(w_nc,'longitude','Dimensions',{'longitude',1440},'DataType','single');
ncwrite(w_nc,'longitude',lon);
ncwriteatt(w_nc,'longitude','units','degrees_east');
nccreate(w_nc,'latitude','Dimensions',{'latitude',721},'DataType','single');
ncwrite(w_nc,'latitude',lat);
ncwriteatt(w_nc,'latitude','units','degrees_north');
nccreate(w_nc,'time','Dimensions', {'time',1},'DataType','int32');
ncwrite(w_nc,'time',time_value);
ncwriteatt(w_nc,'time','units','hours since 1900-01-01 00:00:00.0');
nccreate(w_nc,'t','Dimensions',
{'longitude',1440,'latitude',721,'time',1},'DataType','double');
ncwrite(w_nc,'t',t);
ncwriteatt(w_nc,'t','units','K');
fclose('all');
```

The output file from the executed above code is in native .nc format and it can be plotted in any software with mapping capabilities (e.g., ArcGIS) as is shown in Figure 4.5.

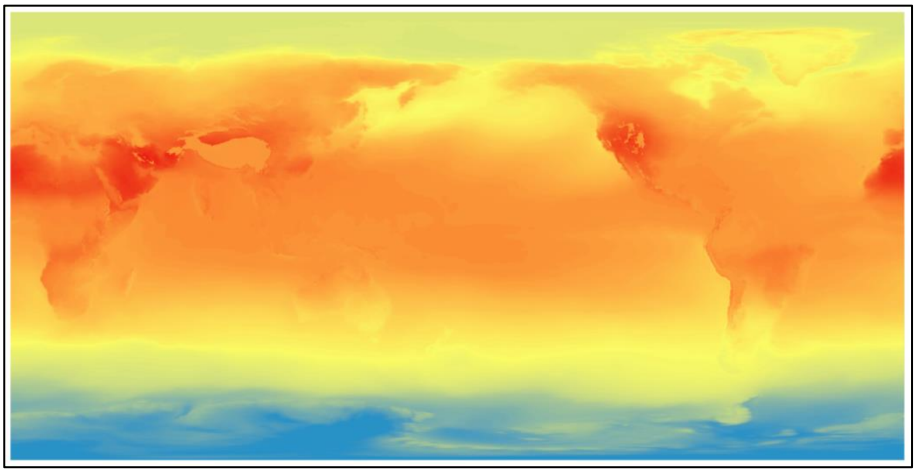

Figure 4.5. Global air temperature at 1,000 hPa pressure level (Earth surface) in July-2003.

4.3 AEMET gridded models

The handling of AEMET gridded models can be especially complex for the case of the gridded datasets of high resolution (5x5 km) which contains interpolated daily precipitation and temperature between 1951 and 2020. The 5x5 km grid is available at AEMET in ASCII format for the whole period and in NetCDF format (network Common Data Format) per decade (1951-1959, 1960-1969, etc.). This research has developed a Python code for extracting the data from the ASCII format file which is recommended as all the data are stored in one single file. This method is useful as the size of the txt files is too large for the majority of text editors (e.g., Notepad++). There is a total of 16,156 data points in this product and each point has an associated time series of 25,568 days (from Jan-1951 to Dec-2020). The guiding example aims for estimating the average precipitation and temperature by integrating 9 data points from the 5x5 km AEMET grid located near the city of Granada (Figure 4.6.).

Figure 4.6. AEMET gridded model of high resolution (5x5 km) and the location of the 9 data points (red points) for estimating the average precipitation and temperature for the period 1951-2020 near the city of Granada.

Apart from the input ASCCI files containing the data, the code has been designed to use three more input files for gaining more customization and becoming a more powerful tool; one is the list of IDs of data points to be used in the averaging process, the second is the list of the daily dates to be analysed (e.g., all dates from 1951 to 2020), and the third is the type of aggregation by specifying the so-called cut dates (e.g., monthly intervals as 31-March-2012, 30-April-2012, etc.). The code generates two types of outputs; one is the individual files –one per data point– containing the dates and the corresponding daily precipitation and/or temperature values (9 files in the example above), and the second are the two aggregated files, one for the averaged monthly precipitation and another for the averaged monthly temperature. The code is as follows:

```
import os
import csv
import statistics

data_file_pp = r".\pcp_red_SPAIN_1951-2020.txt"
data_file_tmin = r".\tmax_red_SPAIN_1951-2020.geo"
data_file_tmax = r".\tmin_red_SPAIN_1951-2020.geo"
output_path = r".\output"
file_location_ids = r".\points_selection.csv"
file_dates_to_do = r".\ALLdates.csv"
file_cut_dates_to_do = r".\cut_dates.csv"

def inputs_gathering(file_path):
    return_list = []
    with open(file_path, 'r') as f_csv:
        next(f_csv)  # skip headers
        mycsv = csv.reader(f_csv, delimiter=',')
```

```
        for row in mycsv:
            return_list.append(str(row[0]))
    return return_list

def data_extraction(file_path, column):
    loc = {}
    print("Extracting ID {} from {}".format(column, file_path))
    with open(file_path, 'rb') as infile:
        for line in infile:
            if line.strip():
                new_line = line.split()
                if str(new_line[0].decode('ascii')) in dates_to_do:
                    loc[str(new_line[0].decode('ascii'))] = new_line[int(column)]
    return loc

def data_manipulation(out_file, locp, loctmin, loctmax, tot_p, tot_t):
    with open(out_file, 'w') as data_f:
        t_avg_list = []
        pp = 0
        for k, v in sorted(locp.items()):
            if k not in cut_dates_to_do:
                pp += float(v)
                t_avg_list.append((float(loctmin[k]) + float(loctmax[k]))/2)
            else:
                pp += float(v)
                t_avg_list.append((float(loctmin[k]) + float(loctmax[k]))/2)
                t_avg = statistics.mean(t_avg_list)
                row = "    " + str(k) + "    " + str(pp) + "    " + str(t_avg) + "\n"
                data_f.write(row)
                if k in totals_p:
                    tot_p[k] += pp
                    tot_t[k] += t_avg
                else:
                    tot_p[k] = pp
                    tot_t[k] = t_avg
                pp = 0
                t_avg_list = []
    return tot_p, tot_t

def write_totals(file_path, dictio):
    with open(file_path, 'w') as avg_f:
        for key, value in dictio.items():
            fila = "    " + str(key) + "    " + str(value / counter) + "\n"
            avg_f.write(fila)

if __name__ == "__main__":

    location_ids = inputs_gathering(file_location_ids)
    dates_to_do = inputs_gathering(file_dates_to_do)
    cut_dates_to_do = inputs_gathering(file_cut_dates_to_do)
    totals_p = {}
```

```
    totals_t = {}
    counter = 0

    for a in location_ids:
        loc_p = data_extraction(data_file_pp, a)
        loc_tmin = data_extraction(data_file_tmin, a)
        loc_tmax = data_extraction(data_file_tmax, a)
        base_name = "monthly_" + str(a) + ".prn"
        out_f = os.path.join(output_path, base_name)
        totals_p, totals_t = data_manipulation(out_f, loc_p, loc_tmin, loc_tmax, totals_p,
totals_t)
        counter += 1

    avg_path_p = os.path.join(output_path, "PRECIPITATION_avg_9points.prn")
    write_totals(avg_path_p, totals_p)
    avg_path_t = os.path.join(output_path, "TEMPERATURE_avg_9points.prn")
    write_totals(avg_path_t, totals_t)
```

The precipitation time series and the temperature time series generated by this code have been plotted in Figure 4.7 and Figure 4.8 respectively, together with the AEMET optimised daily precipitation and temperature long series for the city of Granada for validation purposes.

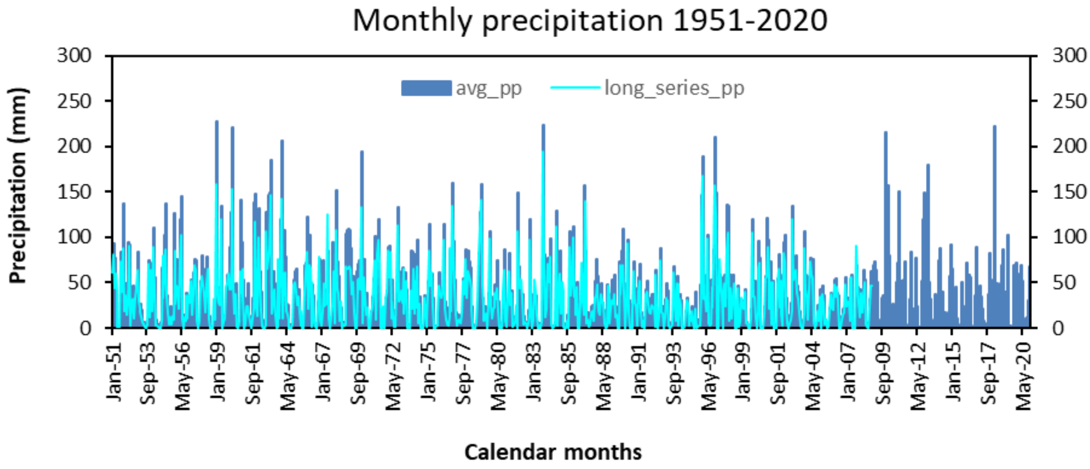

Figure 4.7. Averaged monthly precipitation from 9 contiguous cells from the AEMET gridded model 5x5 km between 1951 and 2020, compared to the AEMET optimised monthly long series product for the Granada time series (1951-2008).

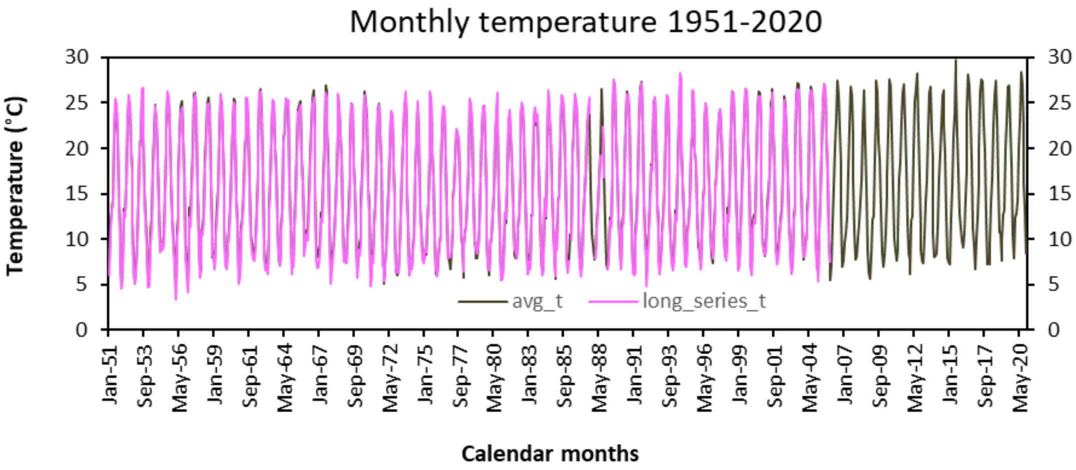

Figure 4.8. Averaged monthly temperature precipitation from 9 contiguous cells from the AEMET gridded model 5x5 km between 1951 and 2020, compared to the AEMET optimised monthly long series product for the Granada time series (1951-2005).

The above comparison speaks of a great similarity between the two AEMET products, with minor differences. To examine the development, creation, and update of the gridded 5x5 km dataset, as well as the details of the used interpolation methods, different research papers have been published (Herrera et al., 2012, 2016).

4.4 Spectral analysis

The spectral analysis has been used in this research as the tool for finding potential forcing mechanisms via estimating the spectrum of different paleoclimate time series. The formal mathematical discussions are beyond the scope of this research and have not been treated. Nonetheless, both the processing steps on the time series prior to the spectral analysis and the required statistical interpretations are always included. The appearance of significant spectral peaks in the power spectra does not guarantee the existence of an underlying oscillating system, as the significant periodicities could be the outcome of several physical processes producing repeated events within the climate system (Schwarzacher, 2000). In any case, there are plenty of cycles widely recognised over the years with a contrasted climate incidence (Rodríguez-Tovar, 2014) that may support the findings on this research. The simulated time series section (4.4.1) responds to the necessity of investigating the fluctuations that are common in the natural systems, produced by random or stochastic processes (Weedon, 2003). Particularly important to understand is how different mixtures of components and background noises, turn into different models of time series. Although there are multiple spectral estimators available (Trauth, 2021), it has been common practise in paleoclimate studies to adhere to a particular method of spectral estimation (Weedon, 2003). In this case the smoothed periodogram has been chosen. The Lomb-Scargle periodogram section explains the advantages of this spectral method and justifies its choice for the estimation of significant periodicities contained in the analysed climate time series with irregular sampling.

4.4.1 Simulated time series

The advantage of a simulated series is that the stochastic model is pre-determined and the influence of the input parameters on the output time series can be assessed (Pardo-Igúzquiza et al., 2000). This approach allows to investigate the detection of both low and high frequencies in the spectrum by applying different noise types (e.g., red and white noises), which have different stochastic models underneath. Additionally, it is possible to investigate different "signal-to-noise ratio" values (e.g., 0.5, 1 and 2) in the simulations. Although there was some previous indication that the power spectra of climate origin records should be tested against a red noise model (Weedon, 2003), on this occasion the simulated time series have used white and red noise models.

One of the most important global climate variability during the Quaternary is located in the millennial band, being the Quaternary climate paced by the Milankovitch cycles (mainly obliquity and precession) at orbital timescales (Milankovitch, 1941; Maslin, 2016). Higher frequency cycles –still within the millennial band– have had a notable persistence in the Holocene period such as the quasi periodic 1500 yr variability (Bond et al., 1995, 1997, 2001). This late well-known variability has not yet been unequivocally associated with a physical phenomenon; the 1500 yr cycle has been explained as being the product of oceanic internal forcing (Debret et al., 2007), internal variability of the climate system (Darby et al., 2012), and/or an artifact of arithmetic averaging (Obrochta et al., 2012). Nevertheless, the 1-2 kyr variability represents an significant global phenomenon to be investigated in the simulations.

To further implement with this practical approach, the program ESTOCAS (Pardo-Igúzquiza et al., 2000) has been applied for the analysis. ESTOCAS has been used in two steps. In the first step, seven time series have been combined into one by using the same stochastic model of a sinusoidal wave (*COS(w*t+phi)*). The program allows a maximum of 8 structures to be combined. The other parameters used the same integer value for the amplitude, and a different phase or random value on each case (between 0.0 and 2*PI). The periods of the seven combined structures have been 400 kyr, 110 kyr, 95 kyr, 41 kyr, 23 kyr, 19 kyr and 1 kyr, to match the Milankovitch cycles and the 1-2 kyr variability. The second step was simulating two noise structures: a Gaussian white noise (*mean m, variance v*), and an autoregressive process AR of order 1 (*p=1*) representing the red noise model. The length of the seven sinusoidal time series and the two noise time series had 2,500 data points, assuming a sampling of 0.4 kyr between consecutive records. The chosen sampling interval guarantees the detection of the sinusoidal wave corresponding to the highest simulated frequency (1 kyr) and the length of the whole series (2,500 data points) guarantees the detection of the longest frequency cycle (e.g., 400 kyr). In the first case, 2.5 data points are required to contain 1 kyr, and in the second case, the whole time series (1 Myr) contains 2.5 times the simulated 400 kyr. After the signal and the noise models have been obtained, the next step represents the integration of the signal time series (made of seven sinusoidal waves) and the two types of noise structures respectively, to match the targeted “signal-to-noise ratio” values of 0.5, 1.0 and 2.0, which will output six different time series (three per noise type). To accomplish it, the following formula must be used:

$$SNR = V / (A^2 * v)$$

SNR is the “signal-to-noise ratio” value, V is the variance of the signal time series, v is the variance of the noise time series and A is a constant value to be determined. By multiplying the simulated noise time series by the constant “A” the newly generated noise time series will have the chosen SNR incorporated. To generate the corresponding output, the whole signal time series is simply added to this new noise time-series or vice versa (value by value). In Figure 4.9 the different outputs of ESTOCAS are shown; A) seven sinusoids combined as signal and white noise time series, B) seven sinusoids combined as signal and red noise time series, C) combined signal-white noise for 3 different SNR of 0.5, 1.0 and 2.0, and D) combined signal-red noise for 3 different SNR of 0.5, 1.0 and 2.0.

Before estimating the power spectra of the simulated series another factor has been introduced which is the removal of certain number of values from the time series. The empirical time series does not usually follow regular sampling and can contain missing data. Thus, sub-series of the simulated time series on the following scenarios have been created by sampling at random: 50%, 25%, and 10% of the original simulated data. Thus, the number of time series to be estimated becomes 12 per noise model (4x3).

The computer program POWGRAF has been used for estimating the power spectra of the simulated time series (Pardo-Igúzquiza et al., 1994). The spectral estimator of choice in the program has been the smoothed periodogram (option 2), which uses in first instance the Fast Fourier Transform algorithm (Cooley and Tukey, 1965), followed by a smoothing process. The smoothing process has been the Hamming technique with 0.23, 0.54, 0.23 as the three coefficients (Yevjevich, 1972). This approach makes the smoothed periodogram a more reliable estimator than the periodogram without smoothing (Pardo-Igúzquiza et al., 1994). The analysed time series have been detrended before the spectral analysis, wherever the slope was statistically significant (3 cases out of 24). The generated output power spectra time series by the program have 0.5 as their maximum frequency value, considering that the sampling interval is of 0.4 kyr it implies that the maximum period to be estimated is 0.8 kyr.

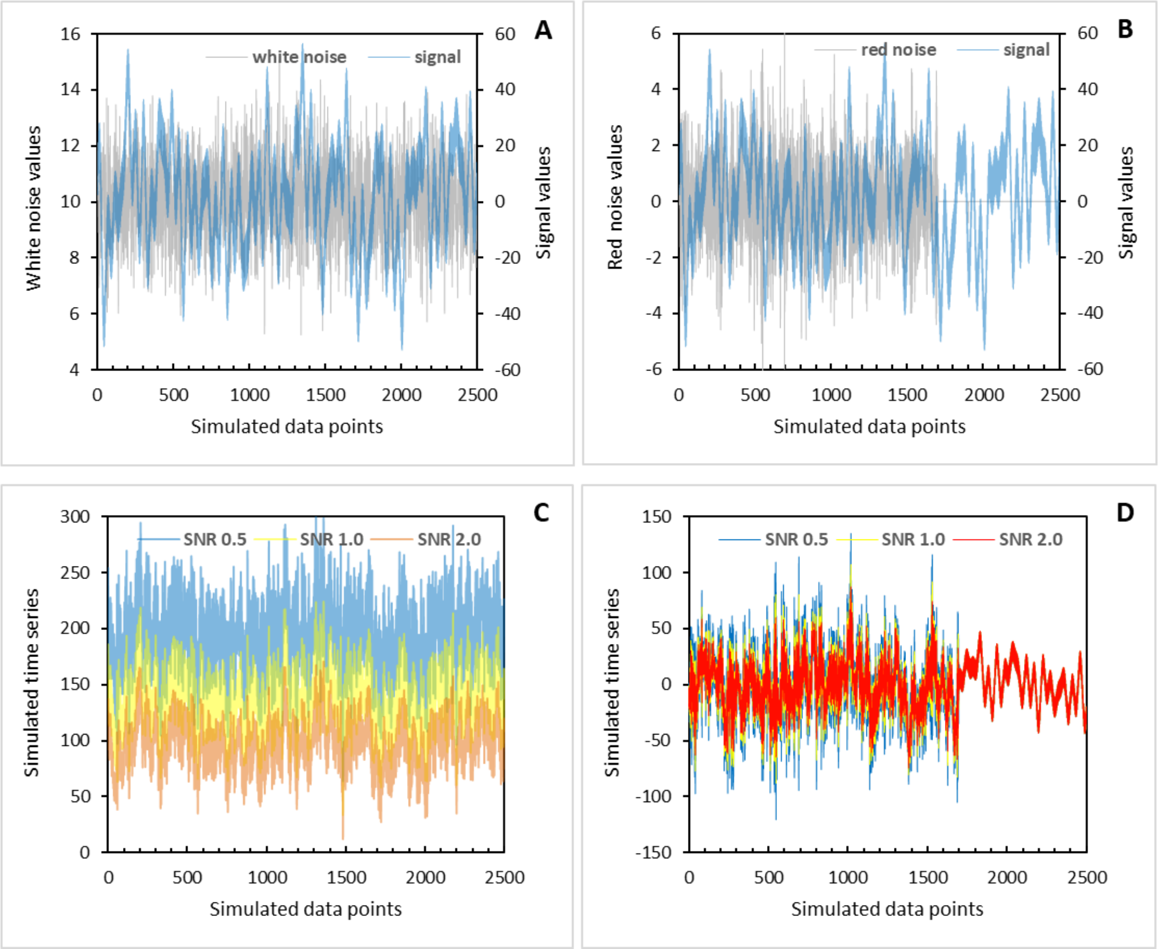

Figure 4.9. Simulated time series with ESTOCAS. A and C represents the white noise pipeline steps, and B and D represents the red noise pipeline steps.

The power spectra of the time series corresponding to the seven sinusoids (without any noise) using the smoothed periodogram reveals the following periodicities above the 95% of significance: 409.6, 109.2, 96.4, 41.0, 23.1, 19.3 and 1.2 kyr. These preliminary results support the usage of the smoothed periodogram as the spectral estimator for the generated sinusoids. The power spectra graphs of the simulated time series combined with a white noise model are presented in Figure 4.10. The graphs also include a green line depicting the confidence level of 95%. Each figure represents a specific combination of SNR and missing data. A summary of all the detected periodicities above 95% can be checked in Table 4.1.

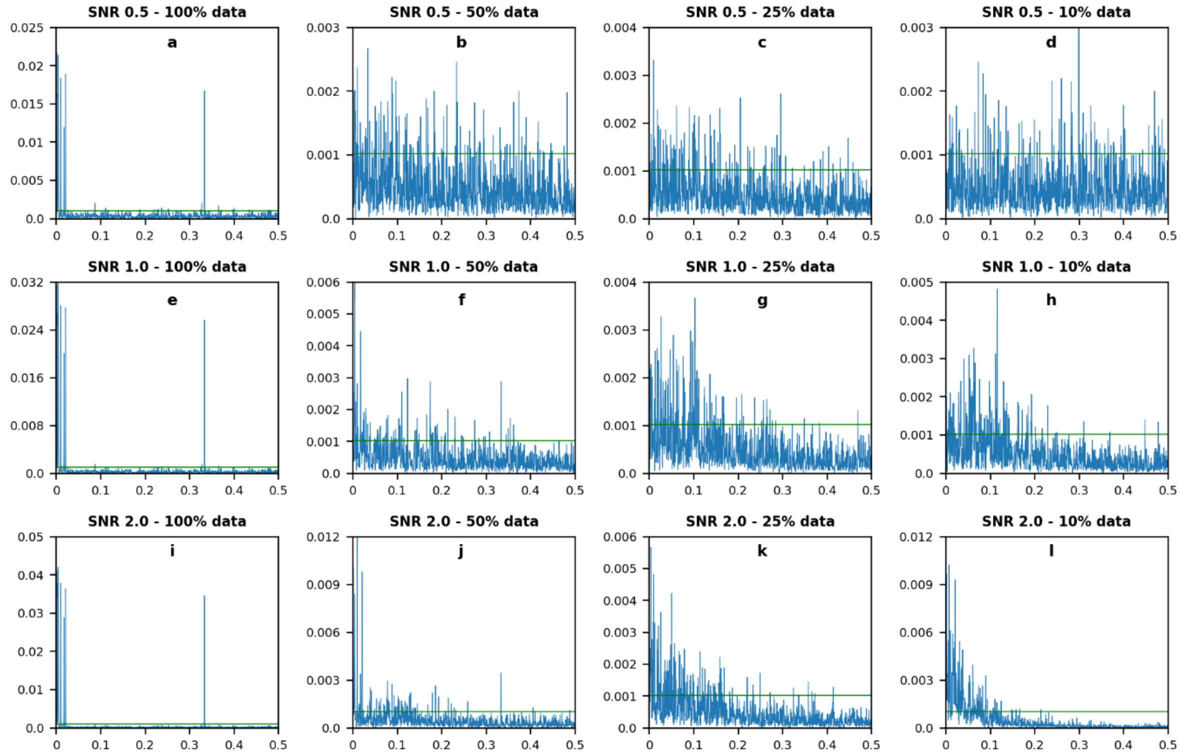

Figure 4.10. Power spectra from different simulations using WHITE noise while varying both signal-noise ratio (SNR) values and the percentage of missing data in the generated time series with the computer program POWGRAF. X axis measures frequency (cycles per time unit) considering a sampling interval of 0.4 kyr and Y axis measures power spectrum. Distribution of plots follows this structure: SNR of 0.5 (a, b, c and d), SNR of 1.0 (e, f, g and h), SNR of 2.0 (i, j, k and l), full dataset (a, e and i), 50% of dataset (b, f and j), 25% of dataset (c, g and k), and 10% of dataset (d, h and l). The input time series is formed by 7 sinusoidal waves (400, 110, 95, 41, 23, 19 and 1 kyr) spanning 2.5 Myr plus a noise wave using the gaussian white noise model. Green line represents the 95% of confidence level.

The most relevant aspects of the results using the white noise model are:

- The power spectra is much clearer in the time series corresponding to the simulations without any missing data or gaps (Figure 4.10 a, e, i), compared to the rest of the simulations with input time series that have missing data.
- The white noise adds a considerable number of additional peaks for both long- and short-range frequencies, although all of them are statistically significant above 95%. This can be observed predominantly for the simulated time series with gaps or missing data (Figure 4.10 b, c, d, f, g, h, j, k, l).

Simulation	Figure number	Periods of significant cycles (kyr) detected above 95% of ACL; rounded to integer values and duplicates removed.
SNR 0.5 – 100% data	**4.10.a**	**410, 205, 149, 109, 96, 41, 35, 23, 19, 15, 5, 4, 3, 2, 1**
SNR 0.5 – 50% data	**4.10.b**	**126, 78, 71, 47, 38, 35, 24, 22, 19, 18, 17, 15, 14, 12, 11, 9, 8, 7, 6, 5, 4, 3, 2, 1**
SNR 0.5 – 25% data	**4.10.c**	**410, 91, 78, 61, 42, 37, 29, 22, 20, 18, 16, 13, 12, 11, 10, 9, 8, 7, 6, 5, 4, 3, 2, 1**
SNR 0.5 – 10% data	**4.10.d**	**61, 46, 36, 30, 29, 27, 24, 17, 16, 14, 13, 11, 8, 7, 6, 5, 4, 3, 2, 1**
SNR 1.0 – 100% data	**4.10.e**	**410, 205, 149, 109, 96, 41, 35, 23, 19, 5, 4, 2, 1**
SNR 1.0 – 50% data	**4.10.f**	**410, 109, 96, 78, 61, 55, 41, 36, 24, 23, 21, 19, 17, 16, 14, 13, 12, 11, 10, 8, 7, 6, 5, 4, 3, 2, 1**
SNR 1.0 – 25% data	**4.10.g**	**328, 109, 91, 66, 36, 30, 28, 23, 20, 19, 16, 15, 14, 13, 12, 11, 10, 9, 8, 7, 6, 5, 4, 3, 2, 1**
SNR 1.0 – 10% data	**4.10.h**	**328, 109, 68, 63, 51, 41, 36, 32, 30, 26, 23, 22, 21, 18, 13, 12, 10, 9, 8, 7, 6, 5, 4, 3, 2, 1**
SNR 2.0 – 100% data	**4.10.i**	**410, 205, 149, 109, 96, 41, 35, 23, 19, 5, 1**
SNR 2.0 – 50% data	**4.10.j**	**410, 205, 149, 109, 71, 61, 41, 29, 28, 26, 23, 19, 17, 12, 11, 10, 8, 7, 6, 5, 4, 3, 2, 1**
SNR 2.0 – 25% data	**4.10.k**	**410, 182, 109, 82, 68, 55, 46, 41, 33, 23, 22, 21, 19, 18, 17, 16, 15, 13, 12, 11, 10, 9, 8, 7, 6, 5, 4, 3, 2, 1**
SNR 2.0 – 10% data	**4.10.l**	**410, 273, 126, 96, 82, 68, 55, 46, 41, 38, 32, 29, 25, 24, 23, 22, 21, 20, 19, 18, 17, 16, 15, 14, 13, 12, 11, 10, 9, 8, 7, 6, 5, 4, 3, 2**

Table 4.1. Summary table of the detected cycles in the simulated time series in the WHITE noise stochastic model.

In the red noise model scenarios (Figure 4.11), the results clearly differ from the white noise model. The summary with all the detected periodicities above 95% of significance is presented in Table 4.2. The main aspects of the results from the red noise simulations are:

- The power spectra of the underlying seven sinusoids waves are less affected by the red noise than in the white noise case. Therefore, it is possible to detect the seven sinusoids in the simulations even in the 50%, 25% and 10% of the missing data scenarios.
- The red noise adds a considerable number of additional peaks towards the longer frequencies, being the short frequencies less affected.

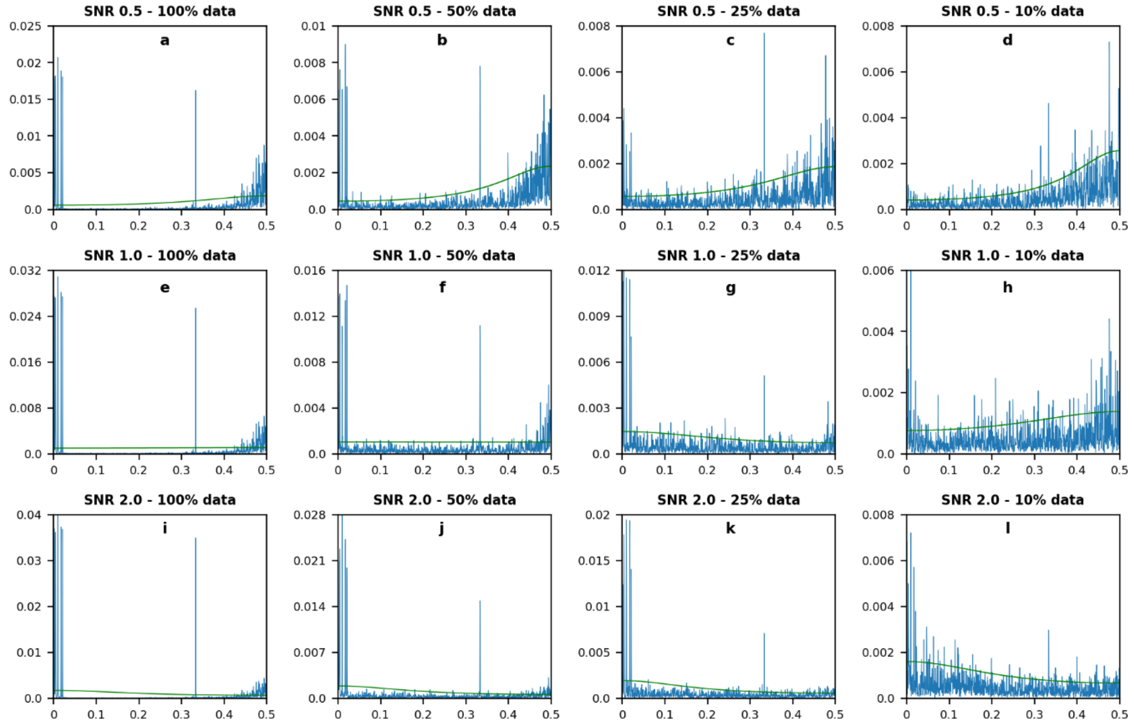

Figure 4.11. Power spectra from different simulations using RED noise while varying both signal-noise ratio (SNR) values and the percentage of missing data in the generated time series with the computer program POWGRAF. X axis measures frequency (cycles per time unit) considering a sampling interval of 0.4 kyr and Y axis measures power spectrum. Distribution of plots follows this structure: SNR of 0.5 (a, b, c and d), SNR of 1.0 (e, f, g and h), SNR of 2.0 (i, j, k and l), full dataset (a, e and i), 50% of dataset (b, f and j), 25% of dataset (c, g and k), and 10% of dataset (d, h and l). The input time series is formed by 7 sinusoidal waves (400, 110, 95, 41, 23, 19 and 1 kyr) spanning 2.5 Myr plus a noise wave using an autoregressive process AR(1) noise model. Green line represents the 95% of confidence level.

Simulation	Figure number	Period of significant cycles (kyr) detected above 95% of ACL; rounded to integer values and duplicates removed.
SNR 0.5 – 100% data	4.11.a	410, 96, 46, 41, 23, 19, 1
SNR 0.5 – 50% data	4.11.b	410, 96, 46, 41, 23, 20, 19, 17, 12, 10, 7, 4, 3, 2, 1
SNR 0.5 – 25% data	4.11.c	410, 96, 71, 51, 41, 23, 19, 13, 12, 10, 9, 7, 6, 5, 4, 3, 2, 1
SNR 0.5 – 10% data	4.11.d	819, 109, 91, 41, 26, 23, 19, 16, 13, 10, 9, 8, 7, 6, 5, 4, 3, 2, 1
SNR 1.0 – 100% data	4.11.e	410, 96, 41, 23, 19, 1
SNR 1.0 – 50% data	4.11.f	410, 164, 96, 41, 37, 23, 19, 9, 7, 6, 4, 3, 2, 1
SNR 1.0 – 25% data	4.11.g	410, 109, 41, 23, 19, 14, 12, 7, 5, 4, 3, 2, 1
SNR 1.0 – 10% data	4.11.h	410, 137, 117, 91, 50, 41, 33, 23, 19, 15, 13, 11, 9, 8, 5, 4, 3, 2, 1
SNR 2.0 – 100% data	4.11.i	410, 96, 41, 23, 19, 1
SNR 2.0 – 50% data	4.11.j	410, 109, 41, 23, 19, 3, 2, 1
SNR 2.0 – 25% data	4.11.k	410, 182, 96, 41, 30, 23, 19, 7, 3, 2, 1
SNR 2.0 – 10% data	4.11.l	410, 109, 78, 41, 23, 19, 17, 12, 10, 9, 8, 7, 6, 5, 4, 3, 2, 1

Table 4.2. Detected cycles in the simulated time series in the RED noise stochastic model.

4.4.2 Lomb-Scargle periodogram

The Lomb-Scargle periodogram (Lomb, 1976; Scargle, 1982; Press et al., 1992) is an excellent choice as spectral estimator in paleoclimate research, as the irregular sampling is commonly found in many available paleoclimate time series. To verify its performance and its results, the program SLOMBS has been used (Pardo-Igúzquiza and Rodríguez-Tovar, 2012). The main two features of SLOMBS are the implementation of the smoothed Lomb-Scargle periodogram and the incorporation of the permutation test to evaluate the statistical significance of the peaks (Tibshirani and Efron, 1993; Good, 2000; Pardo-Igúzquiza and Rodríguez-Tovar, 2000). The particularities of the Lomb-Scargle periodogram such as oversampling ratio of frequencies and smoothing of the estimated power spectrum, produces a loss in the degrees of freedom for evaluating the statistical significance. Therefore, a Montecarlo method such as the permutation test must be used to improve the identification of true spectral features. The same simulated time series generated in the signal-to-noise-ratio analysis (section 4.4.1) have been assessed using SLOMBS. The only adjustment has been converting the even sampling time series corresponding to the full datasets into uneven sampling: 95% of the original dataset. The rest of the time series representing the 50%, 25% and 10% of the original datasets remain the same for this example as they are valid time series to be tested using SLOMBS. The input parameters needed for running SLOMBS have been fixed as follows:

```
0.4             HIGHEST FREQUENCY TO EVALUATE (1 kyr)
2000            NUMBER OF FREQUENCIES IN THE INTERVAL
4000            NUMBER OF PERMUTATIONS
75654           INTEGER RANDOM NUMBER
2               0: NO SMOOTHING, 1 MEAN SMOOTHING, 2 LINEAR SMOOTHING
30              NUMBER OF SMOOTHING TERMS
```

The power spectra results from the white noise model analysis have been represented in Figure 4.12, together with the list of significant peaks above 99% of achieved confidence level (red line represents the estimated ACL in the secondary vertical axis). For the red noise model, the results have been plotted in Figure 4.13.

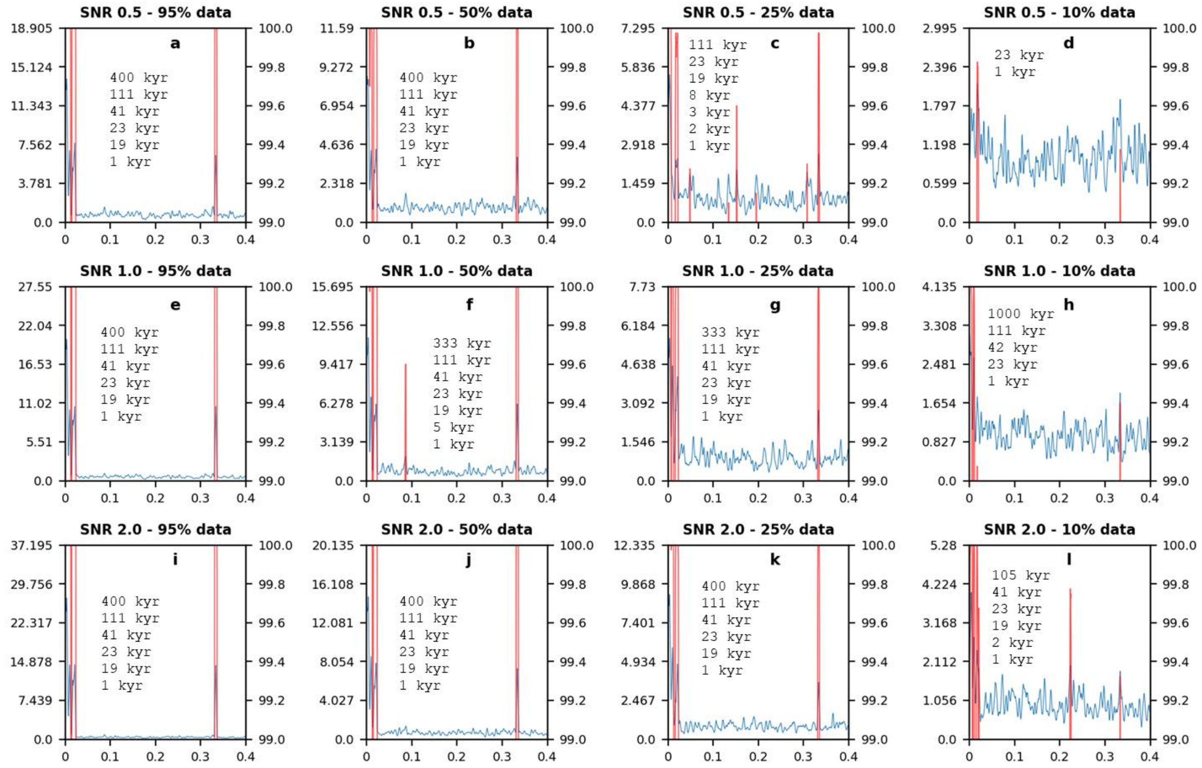

Figure 4.12. Power spectra from different simulations using WHITE noise while varying both signal-noise ratio (SNR) values and the percentage of missing data in the original time series with the computer program SLOMBS. X axis measures frequency (cycles per time unit) considering a sampling interval of 0.4 kyr, primary Y axis measures power spectrum and secondary Y axis measures achieved confidence level (ACL) above 99%. Distribution of plots follows this structure: SNR of 0.5 (a, b, c and d), SNR of 1.0 (e, f, g and h), SNR of 2.0 (i, j, k and l), 95% of datasets (a, e and i), 50% of dataset (b, f and j), 25% of dataset (c, g and k), and 10% of dataset (d, h and l). The input time series is formed by 7 sinusoidal waves (400, 110, 95, 41, 23, 19 and 1 kyr) spanning 2.5 Myr plus a noise wave using the gaussian white noise model.

The usage of SLOMBS for detecting spectral peaks in the simulated time series has proven to be more effective and accurate than in the previous smoothed periodogram model (section 4.5.1). The white model (Figure 4.12) and the red model (Figure 4.13) do not differ too much regarding the detection of spectral peaks. Thus, the Lomb-Scargle periodogram remains as a robust method to be applied in different underlying noise models in Paleoclimate research.

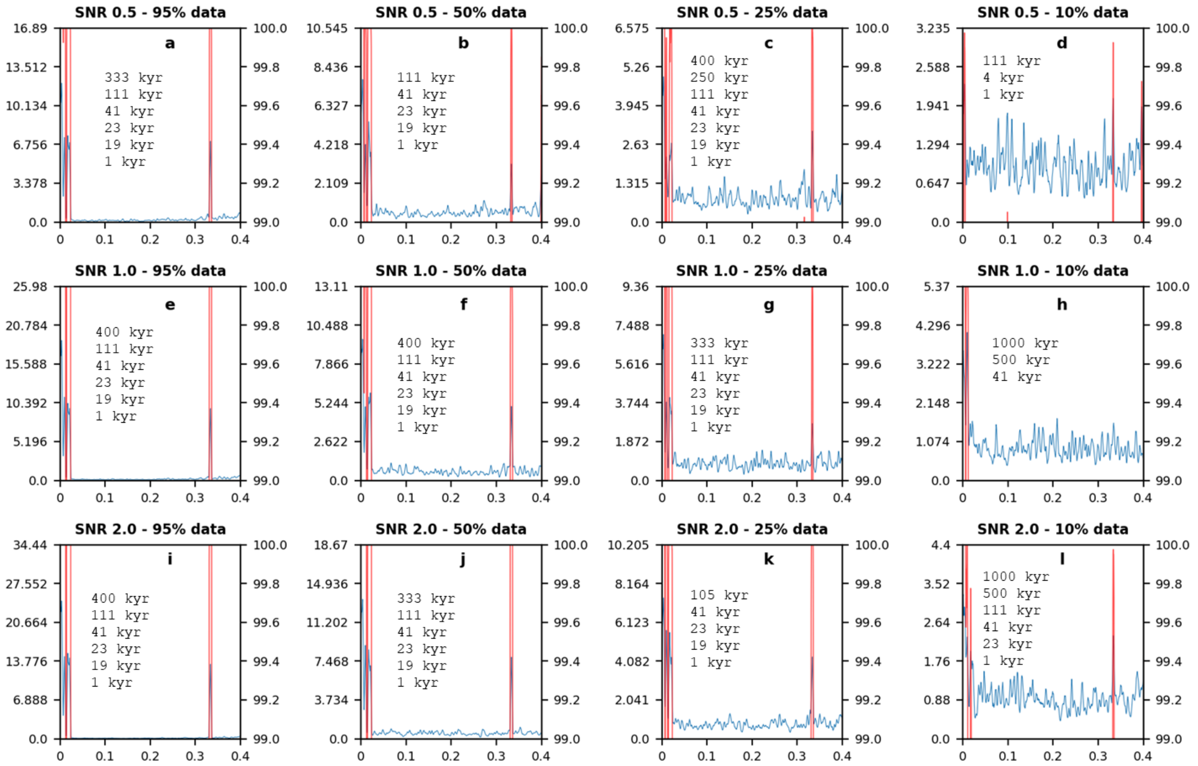

Figure 4.13. Power spectra from different simulations using RED noise while varying both signal-noise ratio (SNR) values and the percentage of missing data in the original time series with the computer program SLOMBS. X axis measures frequency (cycles per time unit) considering a sampling interval of 0.4 kyr, primary Y axis measures power spectrum and secondary Y axis measures achieved confidence level (ACL) above 99%. Distribution of plots follows this structure: SNR of 0.5 (a, b, c and d), SNR of 1.0 (e, f, g and h), SNR of 2.0 (i, j, k and l), 95% of datasets (a, e and i), 50% of dataset (b, f and j), 25% of dataset (c, g and k) and 10% of dataset (d, h and l). The input time series is formed by 7 sinusoidal waves (400, 110, 95, 41, 23, 19 and 1 kyr) spanning 2.5 Myr plus a noise wave using the gaussian white noise model. The input time series is formed by 7 sinusoidal waves (400, 110, 95, 41, 23, 19 and 1 kyr) spanning 2.5 Myr plus a noise wave using an autoregressive process AR(1) as the noise model.

4.5 Insolation estimates

The main purpose of the so-called astronomical solutions (e.g., Berger, 1978a, 1978b; Laskar et al., 2004) is to estimate the Earth's insolation quantities for a particular location/s and geological time interval/s. It is important to bear in mind that they are constrained by the validity time range of the derived equations, although this does not affect the Quaternary (< 2.5 Myr). In this research, the insolation patterns following the Milankovitch orbital parameters of precession, obliquity, and eccentricity (Milankovitch, 1941), when required, have been based on the solution proposed by Laskar et al. (2004), which is valid from 100 Myr before present to 20 Myr after present. As the calculation of the insolation values is a complex task, a good option is to use implemented analysis models such as Earth Orbit v2.1 (Kostadinov and Gilb, 2014). This model has been developed to be run under the computer program Matlab® (this research has used the version R2019b). The generation of insolation time series becomes a matter of minutes once the input parameters to the model are decided. Alternatively, the La2004 solution (as well as the La93 and the La2010) can be found available as a web-based application (http://vo.imcce.fr/insola/earth/online/earth/earth.html), but this online method lacks of the advantages of having graphical outputs and 3D visualization capabilities provided by the Earth Orbit v2.1 program.

To run the insolation estimates on Earth Orbit v2.1 there are a few input parameter/s that must be set, always depending on the research target (Figure 4.14). Thus, for the option of using the La2004 astronomical solution, there are three categories of parameters corresponding to the main three capabilities of the program that must be set to produce the different outputs. These groups of parameters are a) Milankovitch Orbital Parameters, b) calendar/date, Latitude and Insolation Options, and c) time Series (TS) & Insolation Plotting Options.

In the first group, the "year since present (J2000)" is required (expressed in kiloyears). It must be set between -100 Myr to +20 Myr (negative years for the past). It is 0 by default (referred to present day). This age will determine the values of eccentricity (dimensionless), obliquity of ecliptic (degrees) and precession/longitude of perihelion (degrees) to be applied. In the second group there are four parameters; a) the "month" and the "day" of the date for which the Earth's position is to be considered (e.g., 21st of June), b) the "fix calendar start date" which consists of two options: either equinox is fixed to be March 20th, or perihelion is fixed to be January 3rd. This second parameter indicates when the count of 365 days begins, c) the latitude on Earth expressed in degrees for which the insolation is estimated (negative degrees are in the southern hemisphere), and d) the total solar irradiance at 1 AU, which is 1,366 W/m^2 by default. The third group has two parameters, the start (e.g., past) and the end (e.g., present) of the insolation time series. Both are expressed in kiloyears, and again negative years are for the past.

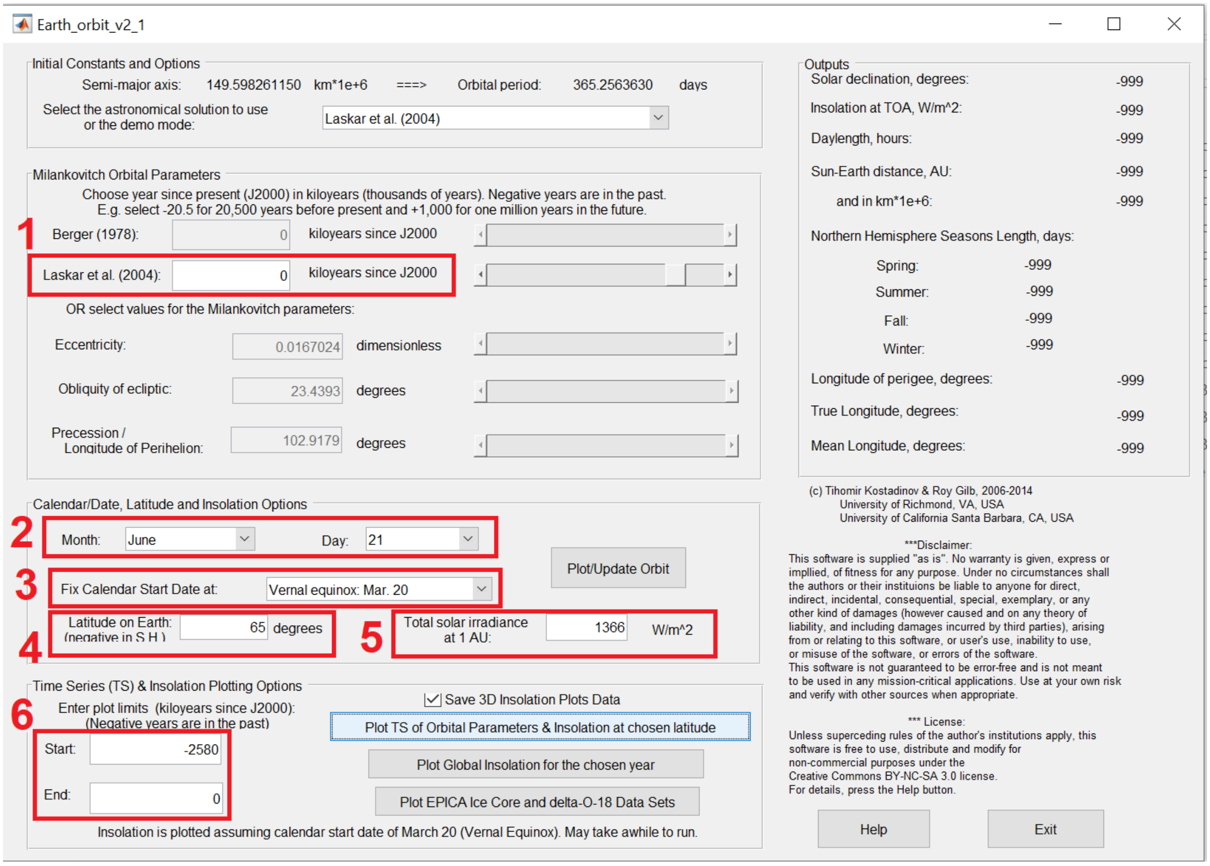
Earth_orbit_v2_1

Initial Constants and Options
Semi-major axis: 149.598261150 km*1e+6 ===> Orbital period: 365.2563630 days
Select the astronomical solution to use or the demo mode: Laskar et al. (2004)

Milankovitch Orbital Parameters
Choose year since present (J2000) in kiloyears (thousands of years). Negative years are in the past.
E.g. select -20.5 for 20,500 years before present and +1,000 for one million years in the future.
Berger (1978): 0 kiloyears since J2000
Laskar et al. (2004): 0 kiloyears since J2000
OR select values for the Milankovitch parameters:
Eccentricity: 0.0167024 dimensionless
Obliquity of ecliptic: 23.4393 degrees
Precession / Longitude of Perihelion: 102.9179 degrees

Calendar/Date, Latitude and Insolation Options
Month: June Day: 21
Fix Calendar Start Date at: Vernal equinox: Mar. 20
Latitude on Earth: (negative in S.H.) 65 degrees
Total solar irradiance at 1 AU: 1366 W/m^2

Time Series (TS) & Insolation Plotting Options
Enter plot limits (kiloyears since J2000): (Negative years are in the past)
Start: -2580
End: 0
☑ Save 3D Insolation Plots Data
Insolation is plotted assuming calendar start date of March 20 (Vernal Equinox). May take awhile to run.

Outputs
Solar declination, degrees: -999
Insolation at TOA, W/m^2: -999
Daylength, hours: -999
Sun-Earth distance, AU: -999
and in km*1e+6: -999
Northern Hemisphere Seasons Length, days:
Spring: -999
Summer: -999
Fall: -999
Winter: -999
Longitude of perigee, degrees: -999
True Longitude, degrees: -999
Mean Longitude, degrees: -999

(c) Tihomir Kostadinov & Roy Gilb, 2006-2014
University of Richmond, VA, USA
University of California Santa Barbara, CA, USA

***Disclaimer:
This software is supplied "as is". No warranty is given, express or impllied, of fitness for any purpose. Under no circumstances shall the authors or their instituions be liable to anyone for direct, indirect, incidental, consequential, special, exemplary, or any other kind of damages (however caused and on any theory of liability, and including damages incurred by third parties), arising from or relating to this software, or user's use, inability to use, or misuse of the software, or errors of the software.
This software is not guaranteed to be error-free and is not meant to be used in any mission-critical applications. Use at your own risk and verify with other sources when appropriate.

*** License:
Unless superceding rules of the author's institutions apply, this software is free to use, distribute and modify for non-commercial purposes under the Creative Commons BY-NC-SA 3.0 license.
For details, press the Help button.

Figure 4.14. Input parameters to the Earth Orbit v2.1 program using the La2004 astronomical solution.

The insolation time series and associated plots are generated when the "Plot TS of Orbital Parameters & Insolation at chosen latitude" button is pressed. The generated plots in memory can be saved from memory to disk in .fig format. The program allows saving the insolation time series for the chosen latitude in tabular form (.dat); 365 rows representing the 365 days of the year and "X" number of columns representing the time ticks at 1 kyr intervals for which the insolation is estimated (e.g., X=2,581 for the whole Quaternary period). However, the program does not provide with the eccentricity, obliquity, longitude of perihelion and climatic precession time series in numerical form directly, but indirectly in graphical form (Figure 4.15).

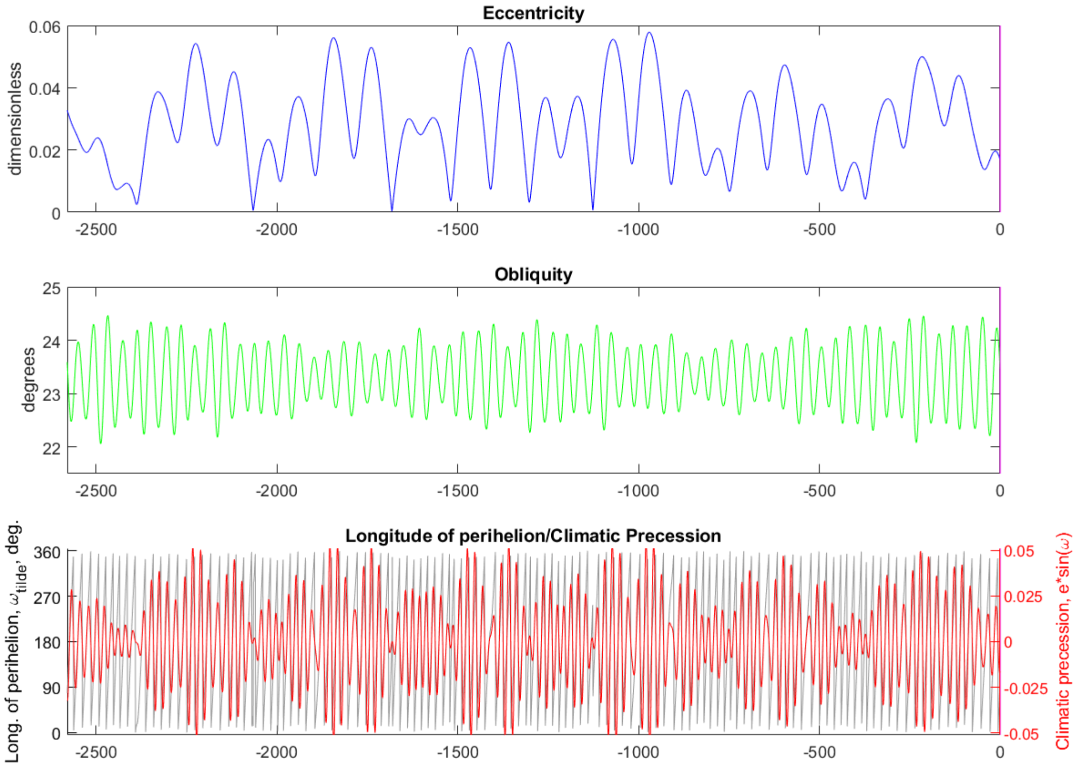

Figure 4.15. Time series of orbital parameters generated by the program as graphs for the whole of the Quaternary period.

To export the above graphs into numeric time series some coding must be run using the Matlab command line. For example, after saving the output graphs into the computer (e.g., "milankovitch_breakdown_3_graphs.fig") it is possible to extract the time series into a series of text files by running the following code:

```
fig=openfig('milankovitch_breakdown_3_graphs');
dataObjsX = findobj(fig,'-property','XData');
dataObjsY = findobj(fig,'-property','YData');
y1 = dataObjsY(1).YData;
y3 = dataObjsY(3).YData;
y5 = dataObjsY(5).YData;
y7 = dataObjsY(7).YData;
x1 = dataObjsX(1).XData;
A=[];
A(:,1)=x1;
A(:,2)=y1;
B=[];
B(:,1)=x1;
B(:,2)=y3;
C=[];
```

```
C(:,1)=x1;
C(:,2)=y5;
D=[];
D(:,1)=x1;
D(:,2)=y7;
dlmwrite('climate_precession.txt',A,',');
dlmwrite('long. of perihelion_precession.txt',B,',');
dlmwrite('obliquity_degrees.txt',C,',');
dlmwrite('eccentricy_dimensionless.txt',D,',');
```

Finally, by having the time series in numerical form, these can be represented or analysed using any other computer program (e.g., spectral analysis software). Overall, Earth Orbit v2.1 offers plenty of technical features, such as the 3D visualization of the Earth's orbit for a particular moment in time (Figure 4.16).

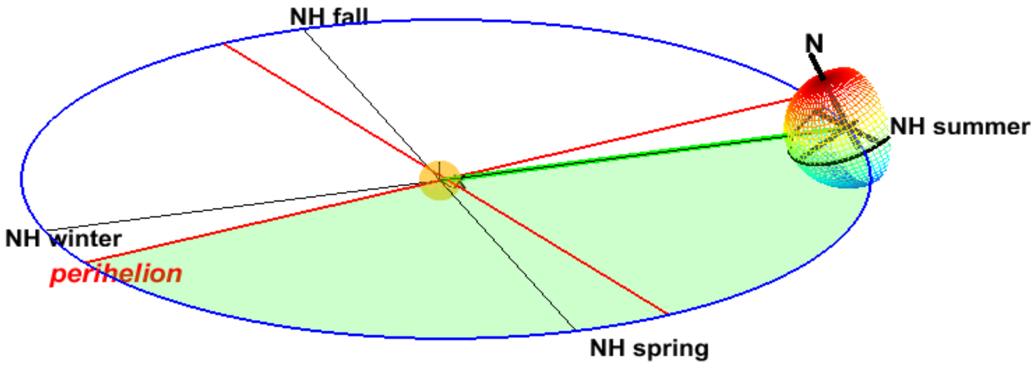

Figure 4.16. Plot orbit option in Earth Orbit v2.1 considering the Earth at the summer solstice (21st of June).

4.6 Case Study: Terrain methods on spectral analysis for paleoclimate interpretations: a novel visualization technique using Python (In press, *Computers & Geosciences*)

4.6.1 Introduction

Time series generated from paleoclimate records (i.e., ice cores, speleothems, etc.) often represent non-stationary physical processes. Therefore, the dominant cyclicities cannot be assumed to be constant. Because they vary over time, they are very sensitive to the time interval of choice for their analysis. Time-frequency analysis can deal with time-varying power spectra (evolutive spectral analysis in Berger et al., 1990), where the one-dimensional time series as input is transformed into a two-dimensional time-frequency representation. Advances in computing have led the wavelet transform (Torrence and Compo, 1998) to replace traditional techniques —e.g. short-time Fourier transform (STFT) and/or windowed Fourier transform (WFT) (see Welch, 1967) —in studies of the variability of series over time. Wavelet analysis may be applied to diverse fields, such as ecology (Cazelles et al., 2008), hydrology (Maheswaran et al., 2012), paleoecology (Sen et al., 2009), climate variability (Azuara et al., 2020) and astronomical forcing (Nie et al., 2008), among others.

One common characteristic of time series from paleoclimate proxies is uneven sampling, varying from quasi-regular to highly irregular intervals. This circumstance can be overcome by the usage of the Lomb–Scargle periodogram (Lomb, 1976; Scargle, 1982; Press et al., 1992), which can directly use uneven data. Initially, this was a deterrent for using wavelet and/or time-frequency analysis (Scargle, 1997; Sen et al., 2009). However, the validity of the wavelet transform to deal with unevenly spaced time series has been available (e.g., Foster, 1996), and can be applied in paleoclimate research (i.e., Witt and Schumann, 2005). Another past drawback of the wavelet transform is that it was deemed supportive of results from the qualitative standpoint, but quite often the lack of statistical significance tests limits the quantitative interpretation (Torrence and Compo, 1998), in part because of the complexity of the existing methods (Maraun et al., 2007). Luckily, latest developments such as the WAVEPAL python package (Lenoir and Crucifix, 2018a, 2018b) has addressed this issue by incorporating significance testing against a large choice of background processes. A further important and controversial aspect of wavelet implementation is the choice of the mother wavelet (Kirby, 2005; Maheswaran et al., 2012).

Amongst the software packages that exist today in the time-frequency domain for estimating and depicting the cyclicity and variability of paleoclimate time series, we cite here three sound examples for reference purposes. Thus, using MATLAB, the so-called Signal Processing Toolbox contains several spectral estimators within the time-frequency analysis section (https://www.mathworks.com/help/signal/time-frequency-analysis.html). One important estimator is the continuous wavelet transform, usually referred as cwt, that has been used for instance at describing the eastern African paleoclimate over the last ~620 kyr (Duesing et al., 2021), or for reconstructing modern high-resolution climate in the South China Sea (Zhao et al., 2021). On the other hand, the WAVELET python package (https://github.com/guillaumelenoir/WAVEPAL) is able to perform time-frequency analysis of irregularly sampled time series using the smoothed Morlet wavelet scalogram. The package requires python 2.x, and it has been applied for example to the study of the Mid- to Late-Holocene Mediterranean climate variability (Azuara et al., 2020), and the Indian Summer Monsoon variability (Reddy and Gandhi, 2022). Last but not least, the original wavelet analysis from Torrence and Compo (1998) is available in idl, fortran, python and MATLAB programming languages (http://atoc.colorado.edu/research/wavelets/).

All these time-frequency solutions incorporate the generation of the corresponding 2D plots of the results, but with the only graphical capabilities of using a color ramp together (in some cases) with the generation of contour lines for the significance levels. The present work may challenge the conceptual way by which the results from the above software packages are plotted. The framework where our proof of concept has been implemented is the group of non-evolutive spectral techniques, and one of the advantages of this approach is that the code can be easily tuned to work with spectral results from different non-evolutive spectral software packages, without requiring the learning transition to time-frequency techniques. Future developments may well be applied directly to time-frequency visualizations. This paper describes a novel visualization technique that improves the visual representation of those methods used in the time-frequency analysis. The code deals with the visualization challenge by importing hundreds to thousands of previously estimated power spectrum time series, as if they were terrain cross-sections, being each cross-section or transect representative of a unique moment in time. In geosciences, a cross-section is simply the intersection of a 3D entity with a plane. The goal is to stack the cross-sections from left to right, so they resemble a two-dimensional terrain elevation dataset from the visual point of view, therefore enhancing the spectral results when plotted against time and frequency. A terrain elevation model, also commonly referred as a Digital elevation Model or DEM, is no more than the representation of the topographic surface of the Earth, depicting ridges, valleys, etc.

Each spectral profile becomes this way a line of pixels as it would be contemplated like in a map (from above the ground). The terrain visualization methods that have been integrated in the proposed solution are the techniques known as color-relief, hillshade and slope. The color-relief typically uses a set of colours to differentiate elevation intervals. The hillshade uses an artificial source of light to project the shadows over the landscape based on the terrain variations. The slope is generated by using the gradient estimates of the terrain dataset to enhance steepness versus flatness. The code allows both a qualitative and quantitative analyses of the spectral results because the confidence levels generated by the spectral analysis technique of choice, can be imported into the visualization pipeline. Our method complements existing time-frequency spectral methods, such as the continuous wavelet analysis, because it allows the possibility of using traditional estimators of power spectrum, offering a quick and effective re-assessment of spectral results. This output when compared to those of paleoclimate time series produced by time-frequency domain visualizations, offers a higher resolution with greater scientific potential, that ultimately may justify their inclusion as a new developed feature in time-frequency methods.

4.6.2 Methodology

The code aims for the visualization of thousands of contiguous time series representing power spectra values, which are generated from spectral analysis techniques outside the time-frequency analysis domain (i.e., non-evolutive Lomb-Scargle periodogram), resulting in the type of visualization that one would expect from a time-frequency analysis, capable of analyzing the whole time series directly. There are three considerations of the visualization code to work: (1) the split of the original time series into smaller time series with some (and constant) degree of overlapping between consecutive time series, (2) the time window used for the split of the time series must be constant, and (3) the output files of the spectral technique of choice need to match the structure of two columns space-delimited, which will be used as the required input files to the visualization code. However, the presented code has the flexibility to be changed in future releases to meet any other requirements.

We have tested the code by using irregular time series, which is common in paleoclimate time series. The interpolation of the data should be avoided as it introduces bias (Schulz, M. and Stattegger, 1997; Rehfeld et al., 2011). Consequently it is recommended to use a spectral method that can deal with the uneven series directly, such as the Lomb-Scargle periodogram. This technique uses an oversampling ratio of frequencies and smoothing, which introduces a loss of degrees of freedom in the estimates because the neighboring frequencies are highly correlated in the estimated power spectrum (Press et al., 1992; Pardo-Igúzquiza and Rodríguez-Tovar, 2012). The program SLOMBS addresses these bias by using the permutation test to evaluate confidence levels, meaning that the Lomb-Scargle periodogram is calculated also for a large number (> 1,000) of random permutations of the time series.

In other words, the usage of SLOMBS is not a requirement for running the visualization code, but it has been used as the chosen case study to illustrate the capabilities of the code, but mainly because the time series to be analyzed are unevenly sampled. Other alternatives to deal with unevenly spaced time series can potentially be used with our code (i.e. REDFIT in Schulz and Mudelsee (2002)). In its current form, the proposed visualization code becomes not applicable to those time-frequency analysis software packages that do not need those three pre-requisites. However, there are a number of classical spectral techniques (Blackman-Tukey, Thompson multi-taper, etc.) that can greatly benefit from this new visualization technique.

The method is novel in that it assimilates the three dimensions of time-varying power spectra —time, period (or frequency) and power— in terms of the three dimensions of geographic space, respectively: longitude, latitude, and elevation. In geography, the longitude is the angular measurement east or west of the prime meridian (e.g. Greenwich meridian), whereas the latitude is the angular measurement north or south of the Earth's equator. The elevation is commonly defined as the height related to the sea level.

The power spectrum is treated as the terrain elevation (z axis) or the third geographic dimension. The association between time and longitude (x axis), and between period/frequency and latitude (y axis) is arbitrary, but the key lies in treating the power spectrum as a terrain magnitude. The popular technique of wavelet analysis likewise relies on this configuration of time in the x axis and period in the y axis. Python is the programming language of choice because of its readability (less verbose than other languages such as Java), and faster implementation (plenty of available material for learning and development resources), but more importantly it is the existence of the opencv-python (cv2) library allowing the handling of the terrain images its main advantage. Its growing usage in the geosciences is reflected by the number of papers referring to python in recent years (i.e., Computers & Geosciences: 30 studies during 2016, 28 during 2017, 30 during 2019, 29 during 2020, and 46 during 2021).

4.6.2.1 Terrain analysis.

Terrain analysis (Wilson and Gallant, 2000) has evolved rapidly since the advent of software and computers. The widespread development of digital elevation models

(DEMs) and Geographic Information Science (Longley et al., 2015) have made the features of terrain analysis accessible to users beyond the domain of geography. The code makes use of the slope, hillshading (or relief shading) and color mapping. These concepts will be introduced next.

Slope estimation can be achieved by calculation algorithms (Jones, 1998) including the so-called average maximum technique (Burrough and McDonell, 1998) used in ArcGIS software. Slope represents the maximum value among the differences between a cell's elevation and its neighbors' elevations; this inclination can be expressed in degrees or percent rise, hence between zero (flat surface) and 90 degrees (vertical surface).

The second feature, hillshading, is a visualization technique commonly applied to DEMs (Horn, 1981) that takes into account the effects upon a terrain of a pre-determined illumination source (e.g., sunlight). The parameters involved in hillshade calculation are the angle of the light source (best practice is to use 315 degrees clockwise from the north) and the light angle above the horizon (between 0 and 90 degrees, but typically 45 degrees). Similarly, slope maps can generally be converted into a shaded slope product by applying a colormap and some vertical exaggeration using GIS software (i.e., Global Mapper). Both the shading of the slope and the hillshading have the primary purpose of reproducing the natural topographic features more realistically.

Color mapping, in turn, is intended to enhance raster data through the application of a set of colors from a pre-determined artificial or natural color ramp (Darbyshire and Jenny, 2017). A further area of research surrounds the blending of different images into one (Kovesi et al., 2014). Thus, blending of the slope, hillshade and colormap can be a most striking way of presenting spectral analysis results.

In generating the slope, hillshade and color mapping for the visualization purposes of this study, we relied on the open-source (MIT license) tools of the GDAL geospatial library (https://gdal.org/). For the specific action of combining the different geospatial layers into the final blend, we used the python library “opencv-python”.

4.6.2.2 Spectral analysis.

Spectral analysis has a long history in paleoclimate research —particularly for Quaternary times— and an array of techniques and software are available today (Trauth, 2021). It is necessary to remind here that the usage of any spectral technique requires enough understanding of the involved physical phenomena as without a recognizable forcing mechanism, the mere detection of spectral peaks can be potentially derived from simple repetitions or bias introduced by the methodology itself, even when the detected frequencies are statistically significant. What we describe here resembles the overlapping segments feature of the time series in the spectrogram method, but our code is not bound by the Fourier-based methods of the spectrogram method. Moreover, it offers the possibility of displaying the results of any other underlying spectral technique, such as the maximum entropy spectral analysis (MESA) (Burg, 1967; Parzen, 1968) and/or the Lomb-Scargle periodogram (Lomb, 1976; Scargle, 1982) to cite a few.

Although one of the aims of the code is to transform non-evolutive spectral results into a "wavelet" form style, some thought is required before running it, as the code does produce the visualization, but not the required spectral time series as inputs that have to be generated independently of the code. Particularly important in our approach, it is deciding on the time window for dividing the original time series into fragments or fixed interval time series, because the window size determines the maximum frequency that can be evaluated on each transect. This "Nyquist frequency" (Shannon, 1948) is defined as twice the sampling frequency (Papoulis, 1984). For example, if we were to investigate the 11-year solar cycle, a maximum sampling of 5-6 years would represent that limit. The sampling ratio must therefore be smaller than the Nyquist limit. This rule of splitting the original time series into subseries to perform sub spectra analysis is known (i.e., Pardo-Igúzquiza and Rodríguez-Tovar, F.J., 2006), although it is not necessary in time-frequency methods (i.e., continuous wavelet analysis), to which our visualization code does not apply.

In the geosciences, uneven time series are common (Pardo-Igúzquiza and Rodríguez-Tovar, 2012). Thus, the required step of splitting the original time series (prior to spectral analysis) into fixed intervals will inevitably produce time series having a different number of records per generated series, only in the scenario of using uneven time series as input to the process. Although this is not a limitation for our code, it may stand as an issue for choosing the right spectral method. So, regardless of whether the original time series has regular or irregular sampling, this point must be addressed when deciding which spectral analysis method is best to use. It is mandatory that the number of estimated frequencies on each output file from the spectral method be the same, because this number represents the Y-axis dimension of the visualization. Here, the code was tested on multiple regular (containing the same number of frequencies) time series representing power spectra, all obtained from the spectral analysis conducted on multiple uneven time series pre-defined with overlapping fixed intervals.

Another point to be underlined in any spectral analysis interpretation is the separation of the significant cyclicities from the noise introduced by the methodology itself. This can be achieved by running either standard statistical tests or computer-intensive permutation tests (Pardo-Igúzquiza and Rodríguez-Tovar, 2000). Having introduced this factor into the code, we have enabled the usage of a second input file —per time series file— that contains the achieved confidence level (ACL), ranging from 0 to 100 (or from 0.0 to 1.0). Typically, scientific validity is secured when confidence levels exceed the values of 90%, 95%, or 99%. The code adopts this information as the threshold between the displayed power spectrum values and the no-data values.

Even though the code can deal with different non-evolutive spectral techniques, it has been developed for operating with the output files produced by SLOMBS computer software (Pardo-Igúzquiza and Rodríguez-Tovar, 2012), which uses the Lomb-Scargle periodogram (Pardo-Igúzquiza and Rodríguez-Tovar, 2012, 2013, 2015; Pardo-Igúzquiza and Dowd, 2020). SLOMBS was integrated by means of the Monte Carlo permutation test to evaluate the significance of the registered spectral peaks, and it adjusts the statistical significance by smoothing the periodogram. This procedure has been applied in cyclostratigraphic analyses of time series from core and outcrop data, as it permits characterization of cyclic variations mainly related to climate changes at different ranges. Significant peaks in spectral analysis have thereby been recognized, involving cycles having cyclicities longer than those of the Milankovitch band (Hernández-Molina et al., 2016), or cycles precisely from the Milankovitch frequency band (Duran et al., 2013; Vegas et al., 2013; Cantalejo and Pickering, 2015; Hernández-Molina et al., 2016; Lofi et al., 2016; Rodríguez-Tovar et al., 2016), cycles belonging to the sub-Milankovitch frequency band at millennial- to centennial-scale cyclicities (Vegas et al., 2013; Jiménez-Espejo et al., 2014; Rodrigo-Gámiz et al., 2014, 2018), and even in the range of cycles per year (Duran et al., 2013; Morgan et al., 2017).

4.6.3 Python code

The flow of the program is described in Figure 4.17. In addition to the main steps (points 1 to 4), some previous actions need to be considered (Figure 4.18). Thus, before running the code, which takes less than a minute on a modern computer (using ~2,000 input files representing one time series each), the input files must be created. They consist primarily of time series files containing both the inputs (step 1-2 in Figure 4.18) and the outputs (step 3-4 in Figure 4.18) of each spectral analysis performed on every transect that was split from the original time series. Additionally, template files are provided with the code (color templates). In our case the software was tested using as input the results of the program SLOMBS (Pardo-Igúzquiza and Rodríguez-Tovar, 2012). It is possible to use other software and/or classical spectral methods, excluding time-frequency methods, as long as the output file extensions and the structure of the output data files match those of SLOMBS (step 4 in Figure 4.18): .prn, .LOM and .ACL for the file extensions of the input data, power spectra and achieved confidence levels, respectively, each containing two space-delimited columns. Thus, for every time series or transect three files are needed. One is the time series containing the time and the values of the physical variable to be analyzed in the spectral analysis (.prn); the second file is the output with the Lomb–Scargle spectrum results (.LOM), which contains the frequencies and the Lomb–Scargle periodogram values; and the third file holds the evaluated frequencies and the corresponding achieved confidence level results (.ACL).

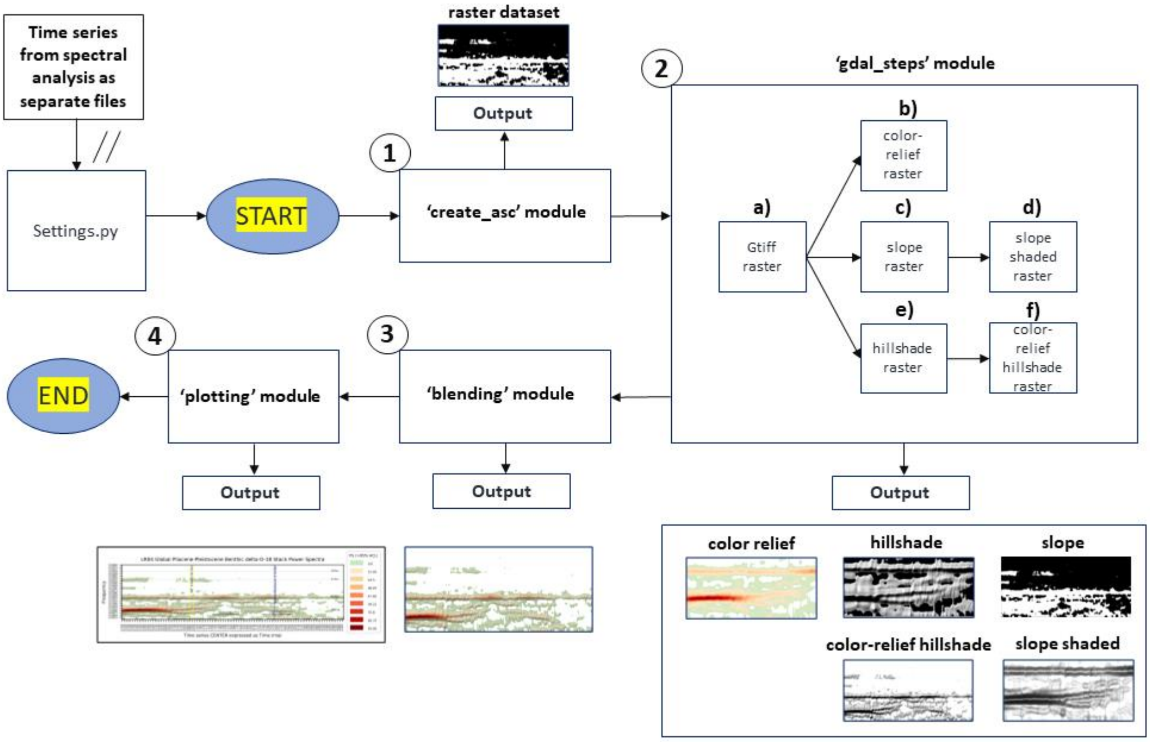

Figure 4.17. Code flowchart. Prior to running the code one must have the spectral results ready and the configuration parameters set. See text for explanation.

As the visualization code recreates a typical time-frequency analysis visualization by using several individual data files that are stacked together, it was necessary to split the original time series into smaller —but constant— intervals prior to the spectral analysis (step 2 in Figure 4.18). The spectral analysis is then carried out after the split and before running the visualization code. The decision on how to split the original dataset into sub-intervals may affect the shape of the output raster generated by the code, since the number of pixels in the x-axis of the visualization represents the number of analysed time series or input files, while the number of pixels in the y-axis reflects the number of evaluated frequencies during the spectral analysis, which is assumed to remain constant on every spectral analysis run. These two facets (number of time series and number of analysed frequencies) must be balanced in order that the output raster will have legible dimensions. The best visual results are obtained when the output raster is rectangular, implying that the number of time series becomes larger than the number of analysed frequencies. Also, the percentage of overlapping between consecutive time series positively affects the resolution of the visualization, given that the program uses the mean of each time series interval, or center point, for placing every transect in the corresponding time value of the x-axis. Therefore, the larger the overlap of time series, the smaller the time differences between consecutive pixels across the x-axis. The sampling of the original dataset can be uneven before the split, but each new time subseries should be created using the same constant time window. The chosen time window for creating each transect is constant to avoid introducing any temporal heterogeneity along the x-axis. Using this way, the derived interpretation on the estimated power spectra between consecutive transects is considered to be based on the same time interval. A good recommendation is also to separate the subseries by small time steps (i.e., one time step of the original series) to increase the resolution at detecting time-frequency changes in the visualization. This approach does not require to interpolate any values, but to use the same original time series in the new time subseries. All the input data files must be placed in the folder specified for this purpose in the settings file.

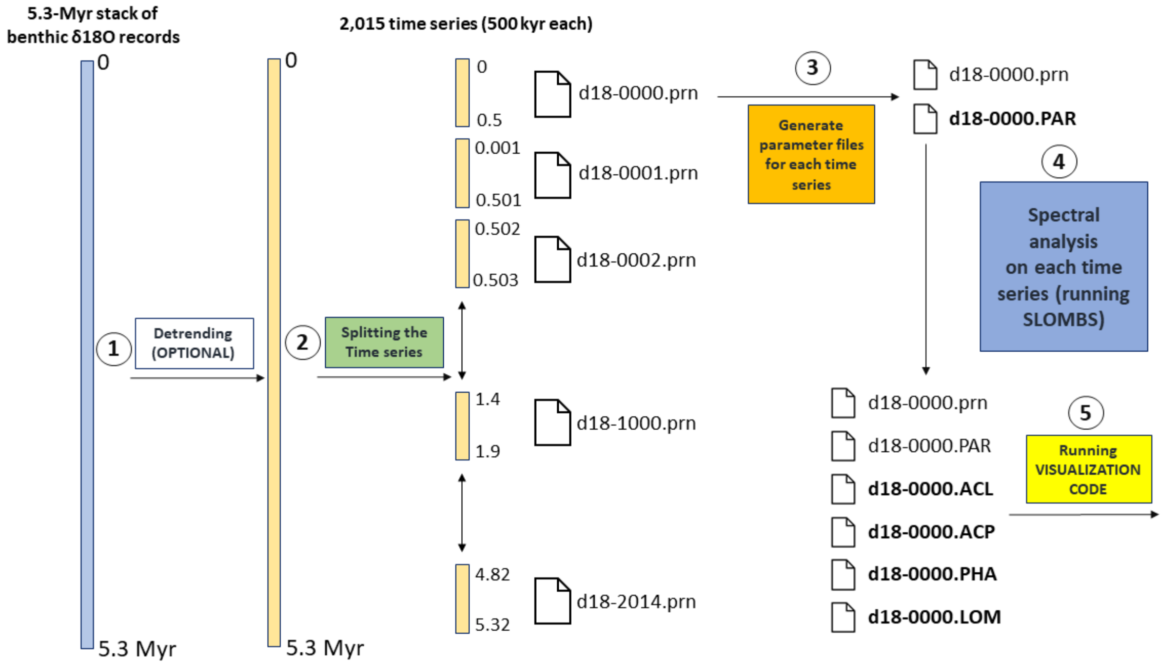

Figure 4.18. Sketch of previous actions prior to the spectral analysis, describing the split of the original paleoclimate time series and the output files of the spectral analysis, before running the visualization code.

Once the input data to the code is in place, a few configuration parameters must be set in the settings.py file before running the code (all these parameters can be found in Appendix 2.1). When the code is run, the first module (step 1 in Figure 4.17) "create_asc" reads all the .prn, .LOM and .ACL input files and generates a 2-D raster file formed by columns (time) and rows (frequencies) in ASCII-format raster (.asc file extension). Just after the .asc file is generated, a projection file .prj is created, where the coordinate system properties are given, so the data becomes spatially enabled. The geographic projection is hard-coded into the projection file, meaning that there is no need for the user to deal with it; the British National Grid (BNG) projection (EPSG:27700) is the one we selected to enable the geographic features. The template could be changed to host any other projected coordinate system, but there is no evidence that by doing so the visualization will be improved. Thus, in the BNG every pixel translates into 1 meter over the Earth's surface as per the linear unit of this projected coordinated system.

The second module (step 2 in Figure 4.17) "gdal_steps", is responsible for generating different raster files to be later blended and used as part of the visualization. The module owes its name to the usage of GDAL (Geospatial Data Abstraction Library) tools, a pre-requisite that needs to be installed in the computer where the code is going to be run. An important aspect of the designed pipeline using GDAL is that the size of the raster images (matrices) along the process remains unchangeable. So, for instance, if the pipeline is run using an input matrix formed by 500 pixels (representing frequencies) and 2,015 pixels (representing time), all the subsequent color, slope and hillshade images will have these dimensions.

The first raster file to be created by the module is, in fact, the translation of the .asc file into GeoTIFF format (.tif) (a in step 2 of Figure 4.17). The reason behind this transformation is that the spatial properties are preserved within the file itself, which is more efficient, reliable and convenient for the following steps of the pipeline. Once the data is translated into a .tif format, the program will use this file to generate six different output files: the color-relief from the data (b in step 2 of Figure 4.17), the slope from the data (c in step 2 of Figure 4.17), the color-relief from the slope (d in step 2 of Figure 4.17), the hillshade from the data (e in step 2 of Figure 4.17), and the color-relief from the hillshade (f in step 2 of Figure 4.17). For all these steps, the GDAL tool "gdaldem" is used, being designed to deal with DEMs (https://gdal.org/programs/gdaldem.html).

In detail, the first output or color-relief raster is generated using the provided file as the default color template (.clr), based on a sequential list of nine RGB colors. The color template is configurable, and there is no further requirement, except for the usage of three colors as a minimum: white for the no-data values (i.e., -999), one for the lowest power spectra value and one for the maximum value. Based on our experience the higher the number of colors provided the clearer the visualization (e.g., nine). The structure of the template consists of the power spectra values, followed by the pixel value (0-255) of the red, green and blue bands, respectively. The output file is a 3-band RGB raster file representing the data by means of the color-ramp provided. The second file is the slope raster, whose values can vary between 0.0 and 90.0 degrees and are stored as a floating-point raster file. The third file to be generated is the color-relief, or shaded slope, from the slope raster, and it relies on a basic color ramp of black (0, 0, 0) for vertical or high slope, and white (255, 255, 255) for flat surfaces. This color ramp is also a file (.txt) available in the "templates" folder. The fourth file is the hillshade. The fifth file is the color-relief, or shaded hillshade, from the hillshade raster, using another color ramp which converts the black no-data background of the original hillshade into white. Thus, the latest transformed hillshade can use the dark color just for the darkest areas that receive less or zero light from the source.

The third module (step 3 in Figure 4.17) of the program, the "blending" module, uses the opencv-python library to merge the color, the slope shaded and the hillshade shaded raster files into a single file. To this end, the color image and the slope shaded are blended first, and the resulting image is then blended with the hillshade raster file. By default, the color image has a weight of 1, and the slope shaded image has a weight of 0.1, followed by the hillshade image with a weight of 0.4. In this context the weight coefficient is equivalent to opacity. These coefficients can be configured in the settings file.

The fourth and last module of the program (step 4 in Figure 4.17) is the "plotting" module. It adds optional graphic features such as axes, ticks, labels, titles, and vertical/horizontal lines. This module uses the python library matplotlib; and although it enhances the final plot around the blended raster file, it does not alter or modify the blended raster produced in step 3, which remains as a separate file in the "output" folder.

4.6.4 Case study

4.6.4.1 Orbital forcing and Pleistocene glaciation

The Pleistocene (0.01–2.58 Ma) comprises most of the Quaternary period's history, and it offers numerous examples as potential case studies to test our code. It is characterized by the occurrence of glacial and interglacial periods provoking both global ice volume increases and decreases, as well as the associated sea level oscillations. The Pleistocene climate has been and is still being researched and debated widely.

The current paradigm to explain the alternations between cold glacial periods and warmer interglacial periods was first theorized by Milutin Milanković (1941) (see also Maslin, 2016, for a review on this subject). He postulated that reductions of the solar irradiation reaching the Earth's surface —hence the term orbital forcing— during summer at the latitude of 65 °N, could potentially lead to an ice age. Today we refer to the Milankovitch cycles in the geological record as the precession, obliquity, and eccentricity cycles. Precession is the combined movement of the Earth's axial precession and the Earth's apsidal precession; the first one (clockwise) is the absolute movement of the Earth's rotation axis describing a cone in space (one cycle takes about 26 kyr) and the second one (counterclockwise) is the precession of the Earth's orbit or the precession of the line connecting the apsides of Sun and Earth (one cycle takes about 112 kyr). Obliquity is the variation (tilt) of the Earth's axis of rotation; though its current value is about 23.44 degrees, it can oscillate between roughly 22.1 and 24.5 degrees. Eccentricity is the change in shape of the Earth's orbit from a perfect circle. The length of these astronomical cycles may vary (Rodríguez-Tovar, 2014): between 19 and 24 kyr for precession (extremes at 14 and 28 kyr), around 41 kyr for obliquity (extremes at 28 and 54 kyr) and between 100 and 400 kyr for eccentricity.

A few decades after the initial theory was formulated, researchers were able to test and link the paleoclimate record with the insolation input (Hays et al., 1976; Imbrie et al., 1992), including the exposure of further scientific issues. The visual representation of some of these issues will be the target of our case study. We selected the "100 kyr problem" (Raymo et al., 2003), the "Milankovitch 41 kyr problem" (Raymo et al., 2003), the "eccentricity myth" (Maslin et al., 2005) and the "late Pliocene-early Pleistocene 100 kyr problem" (Nie et al., 2008) to show the utility of our code at presenting a clearer picture of the variations in insolation input over time. Although research on the Pleistocene climate has progressed since those pioneer works, the issues remain largely unresolved, as we explain below. Yet, the visualization code relies on the quality of the dataset to be analyzed using spectral analysis.

All four of these issues are interrelated. Assuming that the occurrence of glacial-interglacial periods is controlled primarily by changes in the Earth's orbital parameters (Hays et al., 1976) and that both the 23 kyr (precession) and 41 kyr (obliquity) cycles were found to be direct responses (linear) to high-latitude summer insolation forcing (Imbrie et al., 1992), the "100 kyr problem" is the absence of an astronomical (Milankovitch) explanation for the observed 100 kyr cyclicity of the glacial-interglacial cycles after 0.8 Ma (Raymo et al., 2003). It has been suggested that this 100 kyr cyclicity was caused by internal mechanisms operating within the climate system (Imbrie et al., 1992). For example, the timing of the terminations of the 100 kyr glacial periods was successfully modelled by astronomical variations and CO2 concentrations (Berger et al., 1999). Precisely, the "eccentricity myth" represents the view that the "100 kyr problem" is in fact an artifact of spectral analysis, and therefore it is unlikely that the astronomical eccentricity cycle is the main driver of the observed 100 kyr glacial-interglacial periods in the Pleistocene. In turn, the "Milankovitch 41 kyr problem" evokes the fact that the global ice volume between 0.8 and 3 Ma varied predominantly at the 41 kyr obliquity period, without substantial evidence for the 23 kyr precession period. These two different orbital forcing scenarios —the "100-kyr world" and the "41-kyr world"— are separated by the Mid-Pleistocene transition (MPT), implying a change in the dominant frequency and mean ice volume, but also a higher contrast between warm and cold periods (Maslin and Ridgwell, 2005). Finally, the "late Pliocene-early Pleistocene 100 kyr problem" (Nie et al., 2008), refers to the amplitude and phasing mismatch between eccentricity and the ice volume, as well as other paleoclimatic proxy records, between 1 and 3 Ma.

Recent research suggests that obliquity still dominates the "100-kyr world", the sequence of interglacials simply being the deglaciation response when a certain summer insolation threshold was exceeded, which did not happen in every obliquity cycle (Tzedakis et al., 2017). The importance of obliquity in the pacing of the Pleistocene glacial terminations during the "100-kyr world" has been corroborated in speleothems (Bajo et al., 2020). Overall, the causes for the MPT, which changed the cyclicity of the glacial cycles from 41 kyr to 100 kyr, is still under scrutiny (Berends et al., 2021). Furthermore, it is now predicted that the influence of Milankovitch cycles on Earth's climate may be delayed (Maslin, 2016) or even future suppressed in the context of current climate change (Caccamo and Magazù, 2021).

4.6.4.2 Implementation and results.

Three different time series were used to illustrate the code capabilities with regard to these paleoclimate issues. One is the 5.3-Myr stack of benthic δ^{18}O records (Figure 4.19a, b), known as the "LR04" stack, built from 57 global sites, and orbitally tuned (Lisiecki and Raymo, 2005). Also, a second version of the "LR04" stack but untuned (Lisiecki, 2010) has been used for testing with a different spectral resolution (reducing the number of evaluated frequencies in the y-axis). The third is the computed mean daily insolation on the 21st of June at 65 °N, and for the same period and time intervals of those in the "LR04" stack (Figure 4.19d, e), which was obtained using the La2004 orbital solution (Laskar et al., 2004). The insolation dataset was generated to match the irregular time units of the LR04 stack dataset so all the visualizations can be compared along the x-axis (time).

As the primary objective of the case study is to illustrate the evolution of the Milankovitch cycles during the Pleistocene, as well as over the late Pliocene and Pliocene-Pleistocene limit, the choice of these datasets is well aligned to our goal.

The first step was to identify the Milankovitch cycles in two of the original time series. The estimation of the Lomb-Scargle periodogram was conducted on both the entire "LR04" stack dataset (Figure 4.19c) and the entire daily insolation dataset (Figure 4.19f), to test the assumption of stationarity and the detection capabilities of the spectral method over the last 5 Myr. No detrending was applied to the original time series prior to spectral analysis. This resulted in positive detection of the obliquity and precession Milankovitch cycles for the tuned "LR04" stack and the insolation datasets. For the aforementioned 100 kyr cycle during the Pleistocene it was only detected in the "LR04" stack dataset, all above the 95% level of achieved confidence (using the permutation test as the chosen Monte Carlo evaluation method).

The second step was the split of the time series into smaller time series for all three datasets. It was decided to use a moving window of 500 kyr —with one sampling record or step of separation (varying in the original series between 1 and 5 kyr) between consecutive time series— to generate 2,015 fixed interval time series from the original datasets. This interval enables the potential detection of cycles in the astronomical band (19-100 kyr) on every transect or each fixed interval where the stationary assumption was made at orbital time scales. A conservative strategy was adopted for the cycle identification, whereby the detection limit set was one-fifth of the length of the series, granting the detection of 100 kyr cyclicity, and below, on each of the 500 kyr windows generated.

These shorter time series contain the original values; no detrending or transformation was performed based on our previous results on the entire series. The achieved detection of the Milankovitch cycles (Figures 4.19, 4.20, 4.21) granted the aimed visualization capabilities of our code. However, one alternative is applying some type of detrending on the original time series and perform the spectral analysis on the resulting time series. For example, applying a moving average technique for smoothing the time series, may enhance the frequencies in the lowest part of the spectrum. If the user is interested in the highest frequencies of the spectrum, a possibility is subtracting the smoothed time series to the original time series, and perform the spectral analysis on the obtained residuals.

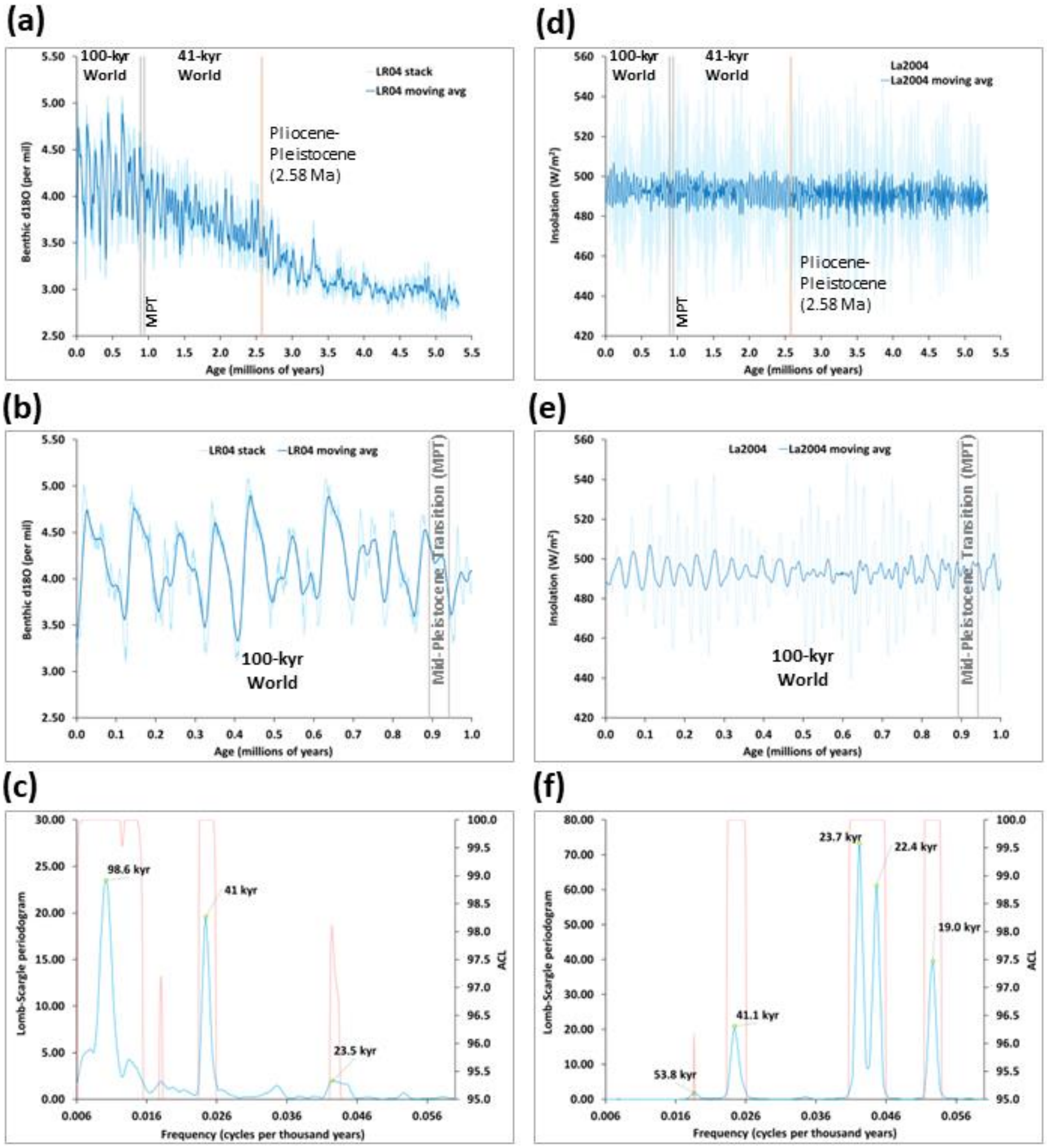

Figure 4.19. Time series visualization and Lomb-Scargle spectral results on two datasets: a-c) orbitally tuned “LR04” stack time series of benthic δ^{18}O records (Lisiecki and Raymo, 2005); d-f) mean daily insolation on June 21 at 65 °N using La2004 orbital solution (Laskar et al., 2004).

For visualization purposes, the center or middle point of the time subseries was considered the value to be represented in the x-axis (time axis) as per our methodology. Given that all tested datasets have time units expressed in kyr and all have the same uneven sampling (varying between 1 kyr and 5 kyr), the visualization will inevitably have more resolution towards the left of the image, and less to the right. As the visualization does not perform any interpolation between transects along the x-axis, the time ticks in the x-axis unequivocally reflects this heterogeneity. The total number of time series analyzed was identical for all datasets, being 2,015 each (6,045 total). The input parameters for every run of SLOMBS were the same for the tuned "LR04" and insolation datasets: 0.06 as the highest frequency to evaluate (~16.6 kyr), 500 as the number of frequencies in the interval, 5,000 as the number of permutations, and 30 as the number of smoothing terms (linear smoothing). For the untuned "LR04" dataset, we introduced the changes of setting a value of 250 as the number of frequencies to evaluate and a value of 2,500 as the number of permutations. The aim was to assess the visualization output by reducing the resolution along the y-axis, but also to test the detection of Milankovitch cycles on the untuned version of the "LR04" stack.

The number of smoothing terms was chosen to allow a neater detection of the main signals, while limiting the appearance of less prominent spectral peaks. The run on every time subseries generated a .LOM extension file (Lomb-Scargle spectrum) and an .ACL extension file (Achieved confidence level) that are inputs to the visualization code. Based on these parameters, the output images had a width of 2,015 pixels and a height of 500 pixels for the tuned "LR04" stack and insolation datasets, and a width of 2,015 pixels and a height of 250 pixels for the untuned "LR04" stack version. After spectral analysis on the 6,045 (3 x 2,015) time series was completed, the visualization code was run four times to produce the four visualizations: "Summer insolation at 65 °N on June 21 Power Spectra" without restrictions on the minimum ACL parameter (Figure 4.20a); the same visualization but imposing a minimum value of ACL (above 95%) for displaying the power spectrum (Figure 4.20b); the orbitally tuned "LR04 Global Pliocene-Pleistocene Benthic δ^{18}O Stack Power Spectra" imposing a minimum value of ACL (above 95%) for displaying the power spectrum (Figure 4.20c); and the untuned "LR04 Global Pliocene-Pleistocene Benthic δ^{18}O Stack Power Spectra imposing a minimum value of ACL (above 95%) for displaying the power spectrum (Figure 4.20d).

The generation of the image with no minimum ACL requirement (Figure 4.20a) was to prove that the code can effectively suppress any undesired achieved confidence levels and/or to deal with multiple scenarios on this regard (from 0 to 100%). Any power spectra below the set threshold is represented using the white color (Figure 4.20b, c, d).

Focusing on the visualization results with the minimum requirement of 95% of ACL, the insolation plot (Figure 4.20b) contains a strong signal in the precession band (19-23 kyr), followed by obliquity (41 kyr). There is no record of the low-eccentricity signal in the power spectrum for the estimated Earth's received insolation, which was known to be weak (Imbrie et al., 1992), although it could have been targeted by the usage of a specific band-pass filter (Nie et al., 2008) to enhance its detection.

The results for the orbitally tuned "LR04" stack power spectra (Figure 4.20c) clearly delineate a strong 100 kyr cyclicity for most of the last 1 Myr, and a strong obliquity signal at 41 kyr for the last 5 Myr. The precession signal is very weak in the tuned "LR04" time series. In the same benthic stack, two intervals are well identified in the visualization in the 100 kyr band: one with a strong response to forcing (at 2.3-3.0 Ma) and another having a weak response (at 1.3-1.8 Ma). These intervals were previously identified (Nie et al., 2008). The paleoclimate frameworks referred to as the "100 kyr problem", the "Milankovitch 41 kyr problem", the "eccentricity myth" and the "late Pliocene-early Pleistocene 100 kyr problem" have been included for visual reference in Figure 4.20c.

The plot of the untuned "LR04" stack (Figure 4.20d) has on purpose less resolution in the y-axis (250 pixels). This translates into the display of more blurred features and becoming generally less sharp than the tuned dataset version (500 pixels). In any case, the two datasets display almost identical spectral bands around the 100 and 41 kyr cyclicities.

The dominance of the 100 kyr band is clearly visible after approximately 0.69 Ma in both tuned and untuned "LR04" versions. Furthermore, the high resolution of the tuned "LR04" stack allows two new graphical features to be introduced in the paleoclimate discussion, which are less evident in the lower resolution dataset. One feature around the 100 kyr band consists of a broad bimodal characteristic between roughly 0.69 and 1.13 Ma, crossing the MPT boundary (Figure 4.20c). Less evident is a second similar feature in the Pliocene, although this time the Y-shaped characteristic looks inverted. The second feature is located roughly between 1.82 and 2.58 Ma (both features have been drawn as black lines in Figure 4.20c). To put these two visual findings by our code into context, we have brought together two published plots that use the same stack and for the last 2.5 Ma (referred as "LR05" in Thakur et al. (2013)); one using the continuous wavelet transform (Figure 4.21a) and the other one using the synchrosqueezing time-periodicity decomposition (Figure 4.21b). The synchrosqueezing method has given satisfactory results in the time-frequency domain using seismic data (i.e., Wang et al., 2014). In the Figure 4.21a and b, the first Y-shaped feature of the 100 kyr band (~0.69-1.13 Ma) can be identified in a similar position to those from our visualization. However, it is the continuous wavelet transform method where this is more evident (Figure 4.21a), as the synchrosqueezing method display many other similar ridges. The second feature (~1.82-2.58) is not evident in these two plots. The granularity of the referred two methods does not allow a better visual analysis, because of the chosen grayscale color to display the results and poor resolution of the graphical output.

Research on Plio-Pleistocene climate evolution using a flexible change point detection algorithm with sinusoidal models (Ruggieri et al., 2009) postulated that important regime changes can be obtained at 0.78 Ma and 2.7 Ma in the "LR04" dataset, being the other relevant change points at 1.03, 1.2 and 2.45 Ma. All these ages are close to, or within, the depicted Y-shaped features in our visualization. On this regard, if considering that the suppression of the 100-kyr glacial cycles during the "41-kyr world" is caused by strong precession forcing disrupting the internal carbon-cycle responses and/or climate feedbacks (Lisiecki, 2010), the existence of the Y-shaped features can potentially expose the timings where these regime changes gradually shift from one state to another. In another similar context, looking at a detailed work on insolation forcing leading to interglacials (Tzedakis et al., 2017), the timings of the Y-shaped features at 0.69, 1.13, 1.82 and 2.58 Ma closely match the age values of insolation maximum described at 0.694, 1.115, 1.811 and 2.59 Ma, that have been categorised in the study as reaching interglacial thresholds. There are, however, some other relatively close peaks in caloric summer insolation in the study, that are associated with continued interglacial or interstadial status.

These findings show the potential benefits of applying the exposed visualization method on top of spectral analysis using paleoclimate time series. Yet, the paleoclimate origin and/or forcing mechanism of these new features are beyond the scope of this paper. To further test the usefulness of the proposed visualization on this and/or other aspects of the Quaternary climate research, we recommend expanding its usage using different spectral methods and other paleoclimate time series.

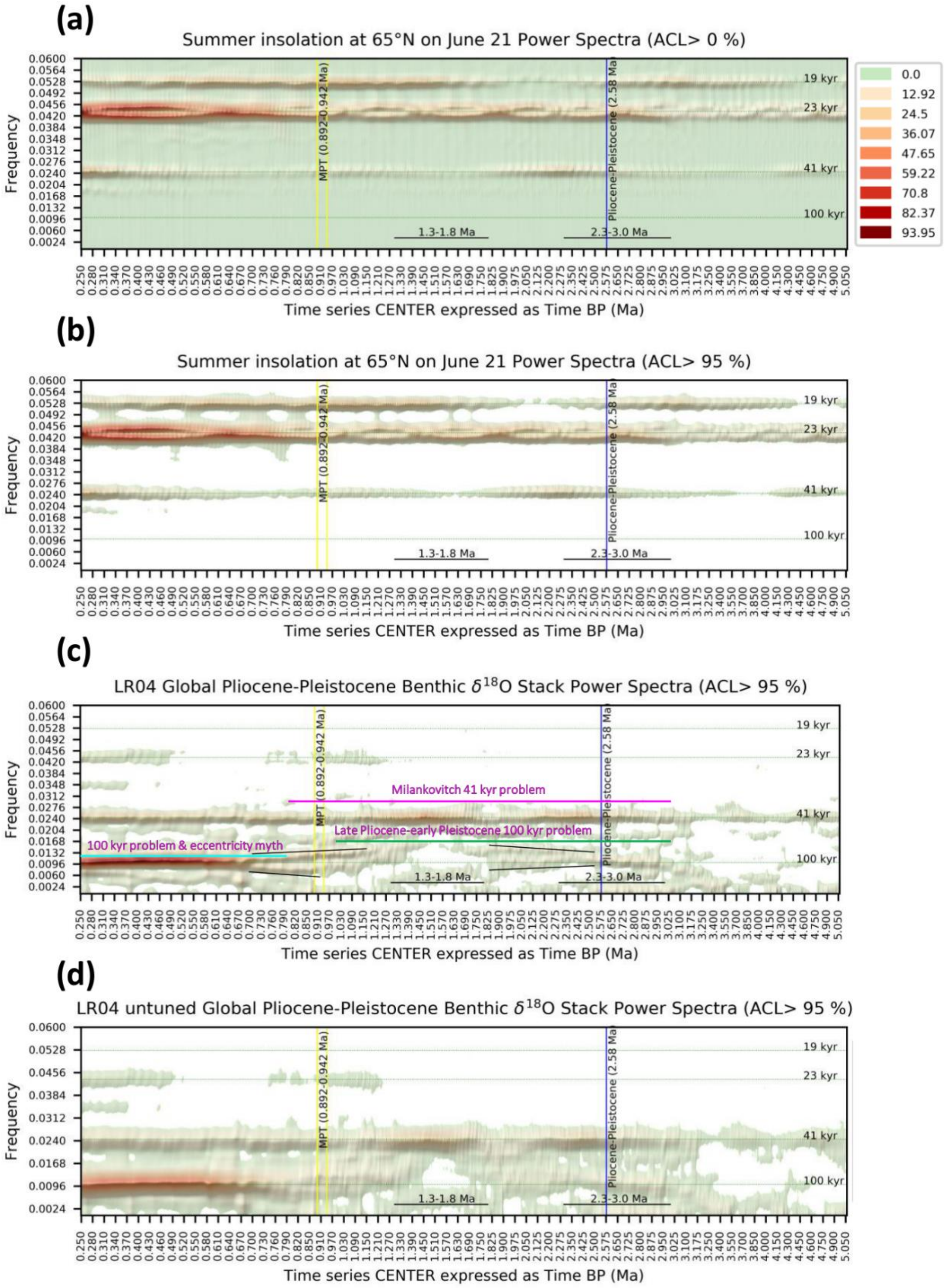

Figure 4.20. Visualization outputs from the python code. a) Summer insolation at 65 °N on June 21 Power Spectra without restrictions on the minimum ACL parameter; b) Summer insolation at 65 °N on June 21 Power Spectra imposing a minimum value of ACL above 95%; c) Orbitally tuned LR04 Global Pliocene-Pleistocene Benthic δ^{18}O Stack Power Spectra imposing a minimum value of ACL above 95%; d) Untuned LR04 Global Pliocene-Pleistocene Benthic δ^{18}O Stack Power Spectra imposing a minimum value of ACL above 95%.

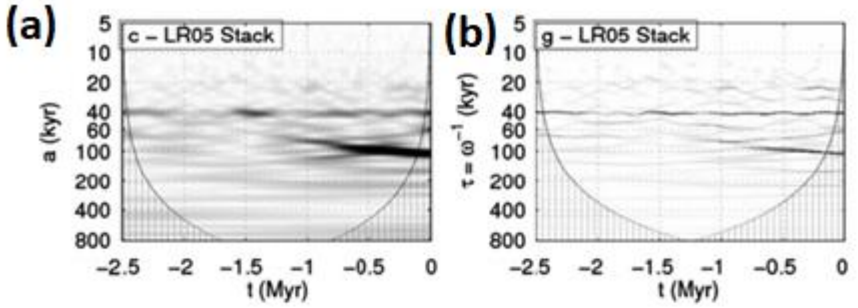

Figure 4.21. Visualization outputs from other spectral techniques. a) The LR04 stack using continuous wavelet transform (LR05 in Thakur et al., 2013); b) The LR04 stack using synchrosqueezing time-periodicity decomposition (LR05 in Thakur et al., 2013).

4.6.5 Conclusions

The code developed and described here was successfully applied on a major paleoclimate issue: the Pleistocene glaciations. The obtained high-resolution visualization of the Milankovitch cycles across the last 5 Myr validates our novel approach. The potential of the code ultimately relies on the resolution of the time series used, as well as on the capabilities of the chosen spectral analysis technique, but the code alone can improve and refine previous visualizations and their associated interpretations. We also consider this code useful for validating the results derived from time-frequency techniques, such as the wavelet, helping to refine and/or calibrate them, thus providing for more accurate results and derived interpretations.

The python code, hosted in the GitHub platform, guarantees easy access and future updates, while enabling research collaboration.

4.6.6 Code availability

Name of the code: spectral-analysis-visualization-method (MIT license). Code developer: José Sanchez-Morales (josesanmor@correo.ugr.es; jose.chez.morales@gmail.com)

Hardware requirements: Any platform where GDAL utilities are installed (https://gdal.org/)

Software required: Python 3 with numpy (v1.21.2), matplotlib (v3.1.2) and opencv-python (v4.6.0). Program language: Tested with python 3.7.0 on Windows 10. Program size: ~400 KB (without data samples).

The source code is available for downloading at the link: https://github.com/jose-sanchez-morales/spectral-analysis-visualization-method

5-8 Results

This Thesis has selected the paleoclimate archives of tree-rings, speleothems, and ice-cores for researching into three paleoclimate aspects of the Quaternary climate. Additionally, modern climate variability in southern Spain and derived from meteorological time series, has been used for studying decadal teleconnections between this region and distant climate modes of variability such as the North Atlantic Oscillation (NAO) and the Mediterranean Oscillation (MO).

Chapter V: A case study using meteorological data. It contains the published chapter of the book: Theory and Applications of Time Series Analysis (Sánchez-Morales et al., 2019b).

Chapter VI: A case study using tree-ring data. It contains the published scientific paper featuring climate variability on a local scale using tree rings (Sánchez-Morales et al., 2019a). The paleoclimate proxies of early-wood tree width and wood tree-ring density are suitable variables to reconstruct climate conditions at annual resolution for the Earth's most recent period (i.e., past few centuries), and therefore have been used as case study for investigating the Sierra de las Nieves karst massif climate evolution since 1,728 AD.

Chapter VII: A case study using speleothems data: Global climate changes through the Holocene (In prep. *The Holocene*). In regard to the speleothems, the global distribution of $\delta^{18}O$ records at millennial scale during the Holocene period, allowed the investigation of the evolution of regional climates, including their associated cyclical phenomena, and their integration and interpretation from a global perspective.

Chapter VIII: A case study using ice cores data: Approaching the Younger Dryas (Submitted to *Paleoceanography and Paleoclimatology*). One of the most intriguing facets of the Quaternary period since the Last Glacial Period, is the occurrence of cold periods lasting from one to several millennia and having abrupt onsets. In particular, this fourth case analyses the most recent one of these cold spells, the so-called Younger Dryas which just precedes the current warm Holocene period. The interest of this climate event is that it may be triggered by a catastrophic event as opposed to similar cold events caused by long term climatic variability. The fact that the Younger Dryas has been best documented in the Greenland ice, it makes the datasets generated from ice-cores the best paleoclimate proxies to study its origin, and therefore have been incorporated in the research.

5 Chapter V. A case study using meteorological data

Spatial Distribution of Climatic Cycles in Andalusia (Southern Spain)

J. Sánchez-Morales, E. Pardo-Igúzquiza and F. J. Rodríguez-Tovar

Abstract Several climatic cycles in Andalusia (southern Spain) have been identified by using precipitation and temperature data from most of the twentieth and the early twenty-first centuries at 707 meteorological stations. Some of the cycles detected had been recognized in previous studies, such as the 3-year cycle and the 7/8-year cycle, which were the most common periodicities across the study area. Spectral analysis was used for statistical analysis. The power spectrum estimator used is the smoothed Lomb–Scargle periodogram. The results reveal very interesting spatial patterns that had not been seen before in previous climatic studies, which illustrate a combined and complex influence of the North Atlantic Oscillation and the Mediterranean Oscillation. In general, the precipitation record studied presents better results than the temperature record, which offers less clarity in assessing climatic variability in Andalusia. Nevertheless, most of the cycles identified in the precipitation record were detected in the temperature record as well.

Keywords Power spectrum · Climate · North Atlantic Oscillation · Mediterranean Oscillation · Andalusia · Spain

---

J. Sánchez-Morales (✉) · F. J. Rodríguez-Tovar
Universidad de Granada, Avd. Fuentenueva s/n, 18071 Granada, Spain
e-mail: josesanmor@correo.ugr.es; jose.chez.morales@gmail.com

F. J. Rodríguez-Tovar
e-mail: fjrtovar@ugr.es

E. Pardo-Igúzquiza
Instituto Geológico y Minero de España, Ríos Rosas 23, 28003 Madrid, Spain
e-mail: e.pardo@igme.es

O. Valenzuela et al. (eds.), *Theory and Applications of Time Series Analysis*,
Contributions to Statistics, https://doi.org/10.1007/978-3-030-26036-1_17

Spatial Distribution of Climatic Cycles in Andalusia (Southern Spain)

José Sánchez-Morales[a], Eulogio Pardo-Igúzquiza[b], Francisco Javier Rodríguez-Tovar[a]

(a) Departamento de Estratigrafía y Paleontología, Facultad de Ciencias, Universidad de Granada. Campus Fuentenueva s/n, 18002 Granada (Spain)

(b) Instituto Geológico y Minero de España (IGME), Ríos Rosas, 23, 28003 Madrid (Spain)

E-mail addresses: josesanmor@correo.ugr.es (J. Sánchez-Morales), e.pardo@igme.es (E. Pardo-Igúzquiza), fjrtovar@ugr.es (F.J. Rodríguez-Tovar).

Published in:

Sánchez-Morales, J., Pardo-Igúzquiza, E. and Rodríguez-Tovar, F.J., 2019. Spatial distribution of climatic cycles in Andalusia (Southern Spain). In: Valenzuela, O., Rojas, F., Pomares, H., and Rojas, I. (Eds.), Theory and Applications of Time Series Analysis, Elsevier, pp. 243–255. https://doi.org/10.1007/978-3-030-26036-1

ABSTRACT

Several climatic cycles in Andalusia (southern Spain) have been identified by using precipitation and temperature data from most of the twentieth and the early twenty-first centuries at 707 meteorological stations. Some of the cycles detected had been recognized in previous studies, such as the 3-year cycle and the 7/8-year cycle, which were the most common periodicities across the study area. Spectral analysis was used for statistical analysis. The power spectrum estimator used is the smoothed Lomb–Scargle periodogram. The results reveal very interesting spatial patterns that had not been seen before in previous climatic studies, which illustrate a combined and complex influence of the North Atlantic Oscillation and the Mediterranean Oscillation. In general, the precipitation record studied presents better results than the temperature record, which offers less clarity in assessing climatic variability in Andalusia. Nevertheless, most of the cycles identified in the precipitation record were detected in the temperature record as well.

Keywords: Power spectrum, Climate, North Atlantic Oscillation, Mediterranean Oscillation, Andalusia, Spain.

5.1 Introduction

Andalusia (southern Spain) is a region characterized by huge climatic contrasts, i.e., the 'Sierra de Grazalema' in the southwest is the wettest place on the entire Iberian Peninsula with average rainfall of over 2,000 mm/year, whereas the 'Desierto de Tabernas' in the southeast is considered the driest place in Continental Europe with less than 150 mm/year on average. The influence of both the Atlantic Ocean and Mediterranean Sea on this area of 87,597 km^2, plus the presence of the Betic Cordillera with altitudes above 3,000 m.s.l. (meters above sea level), make this region unique from a climatic point of view and very interesting for analysing the evolution of climate from past to present times, especially during the most recent periods. Thus, Andalusia could be seen as a natural laboratory for the study of climatic changes from past to present.

Climatic studies from the region of Andalusia are frequent and focus on a variety of aspects. Thus, several statistical techniques and methodologies have been used, i.e., principal component analysis (Esteban-Parra et al., 1998), empirical orthogonal function (Rodrigo et al., 1999), innovative missing values estimator (Ramos-Calzado et al., 2008), non-instrumental climate reconstruction (Rodrigo et al., 2012), and gridded dataset and combined indices evolution (Fernández-Montes and Rodrigo, 2015), amongst many others.

The causes of climate variability in Andalusia at annual, inter-annual, decadal, and multi-decadal time scales are generally associated with diverse phenomena, involving several climatic subsystems, revealing the interactions between atmosphere and ocean (Esteban-Parra et al., 1998; Rodrigo et al., 1999, Ramos-Calzado et al., 2008; Rodrigo et al., 2012; Fernández-Montes and Rodrigo, 2015). In some cases, a cyclic pattern in climatic variability has been interpreted. The identification of climatic cycles in Andalusia by means of spectral analysis has been carried out in previous studies, although the method differed according to the specific study (Rodrigo et al., 2000; Luque-Espinar et al., 2008). On this basis, this study examines climatic evolution during the 20th and 21st centuries in Andalusia, based on the spectral analysis of data from different climatic proxies, in order to evaluate the cyclic nature of said evolution, and to interpret the processes involved.

5.2 Methodology

This study uses spectral analysis as a statistical technique to evaluate the importance of the frequencies associated with precipitation and temperature time series in Andalusia (see meteorological datasets below). The power spectrum estimator used is the smoothed Lomb-Scargle periodogram (Lomb, 1976; Scargle, 1982; Pardo-Igúzquiza and

Rodríguez-Tovar, 2012), which works directly with uneven time series, such as the annual precipitation and/or annual temperature series in the study area. The technique evaluates the statistical significance of the peaks using the Monte Carlo permutation test, as neighbouring frequencies are highly correlated, and then it adjusts statistical significance by smoothing the periodogram (Pardo-Igúzquiza and Rodríguez-Tovar, 2012). Linear smoothing with three terms was applied to the raw periodogram. The output consists of the Lomb-Scargle spectrum, the achieved confidence level spectrum, the mean spectrum of permutations and the phase spectrum.

The parameters required have been optimized for dealing with the annual precipitation and/or temperature time series in the study area, and for achieving the intended goal of capturing climatic cycles with a duration just above the sampling interval (i.e., biannual oscillation). Thus, 0.5 has been used as the highest frequency to evaluate, 200 as the number of frequencies in the interval, 2,000 as the number of permutations, 75,654 as the random seed, three as the number of smoothing terms and linear smoothing was enabled. To illustrate the above process, the output of this methodology from one of the precipitation stations is presented below (Figure 5.1).

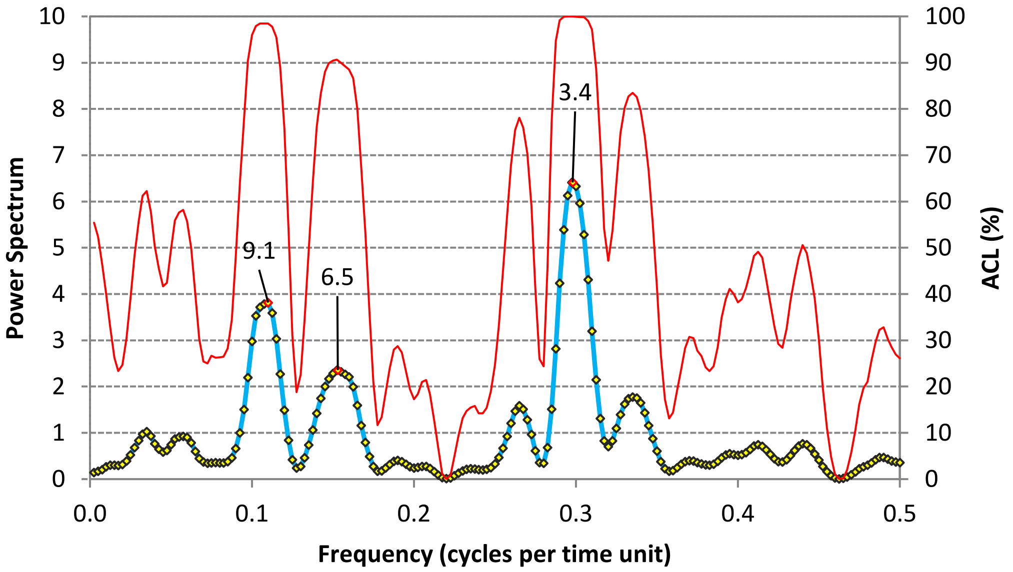

Figure 5.1. Example of power spectrum for annual precipitation at station P6289, and associated peaks of 9.1, 6.5 and 3.4 years above Achieved Confidence Level (ACL) of 90%, by using the smoothed Lomb–Scargle periodogram.

5.3 Meteorological datasets

The precipitation and temperature data were collected from two different sources and named chguadalquivir (www.chguadalquivir.es) and aemet (www.aemet.es). The sources differ from each other with regard to the sampling interval; datasets from chguadalquivir were available monthly and covered the period from 1951 to 1987, whereas datasets from aemet were available daily, and covered the period from 1901 to 2012. There were 1,574 precipitation station and 526 temperature station datasets from chguadalquivir, spread across the entire study area. There were 595 precipitation station and 282 temperature station datasets from aemet, all located in the eastern half of the study area.

For a better comparison, all the datasets have been converted into annual datasets. As a first step, the daily datasets were summarized into monthly datasets; only months with a minimum of 25 days of precipitation measurements and/or a minimum of 20 days of temperature measurements were considered. Then, to convert the monthly datasets into annual datasets, only complete years and/or years that had 12 months of measurements were used. A second level of filtering was also carried out in which precipitation stations with less than a total of 20 years of records and temperature stations with less than a total 10 years of records were excluded from the analysis. It was not a requirement for that total amount of years with records to be consecutive, as this spectral analysis methodology can deal with uneven series. Upon combining the two data sources, a comparison method was established to see which one had more years of information for the same station, as various stations were in both data sources. If the length of the series in years was the same in both sources, preference was given to the dataset from aemet, which was originally compiled daily.

The filtering process produced 547 precipitation stations and 160 temperature stations, a total of 707 meteorological datasets to be analysed (Figure 5.2).

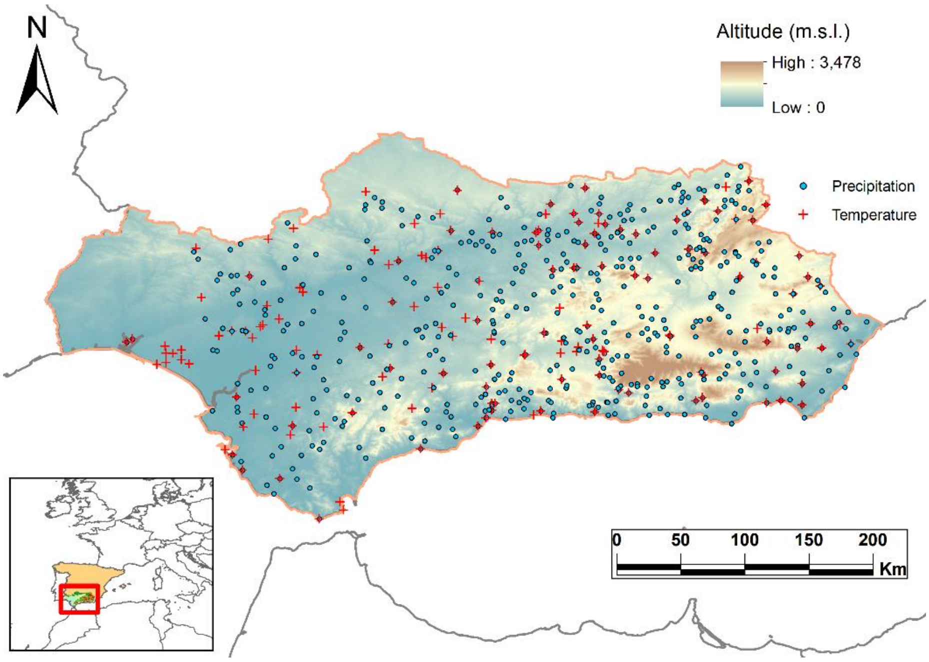

Figure 5.2. Distribution of the meteorological stations selected for the spectral analysis.

5.4 Results

The spectral analysis carried out on the 707 datasets detected 1,751 significant peaks in the precipitation datasets (Figure 5.3) and 466 significant peaks in the temperature datasets (Figure 5.4), all above or equal to 90% of ACL. All the cycles detected for the same meteorological variable have been plotted in the same diagram.

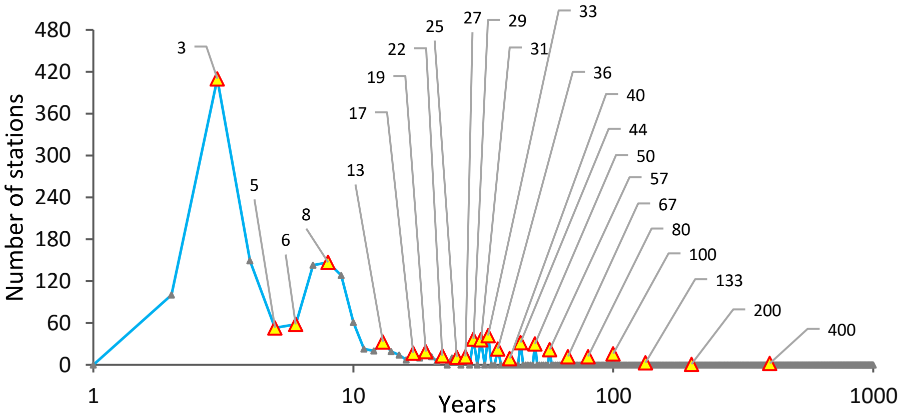

Figure 5.3. Diagram containing all the precipitation cycles in the study area and the number of stations in which the cycles were detected (yellow triangles represent the value of the cycle in years).

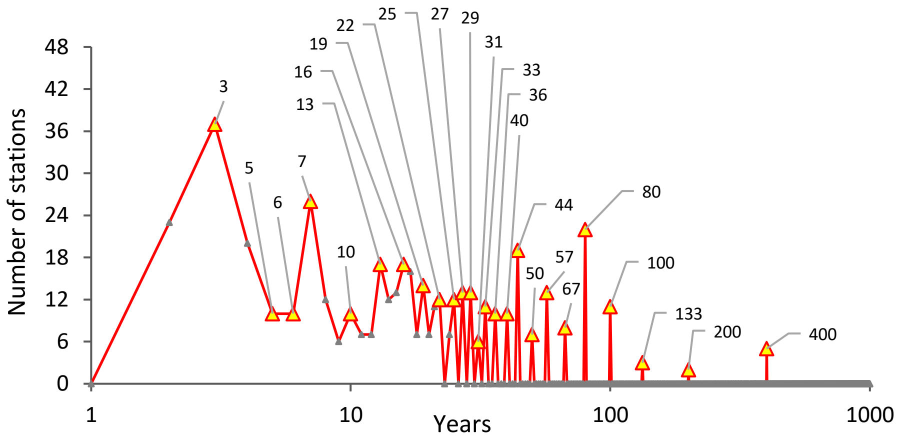

Figure 5.4. Diagram containing all the temperature cycles in the study area and the number of stations in which the cycles were detected (yellow triangles for the values of the cycle in years).

The number of cycles detected is lower in the temperature record than in the precipitation record, but it is very remarkable that both temperature and precipitation variables show signals at the same frequencies. The 3-year cycle and the 7/8-year cycle were the most frequently detected, and show the highest significance. Thus, a detailed analysis of cycles at both 3 years and 7/8 years has been conducted.

All precipitation (344) and temperature (28) stations showing peaks between frequency values of 0.4 (2.5 years) and 0.29 (3.5 years) have been collected and plotted on a map to see their spatial distribution (Figure 5.5). The same output has been conducted for the 7/8-year cycle by isolating all peaks between 0.154 (6.5 years) and 0.118 (8.5 years), 223 precipitation stations and 23 temperature stations (Figure 5.6).

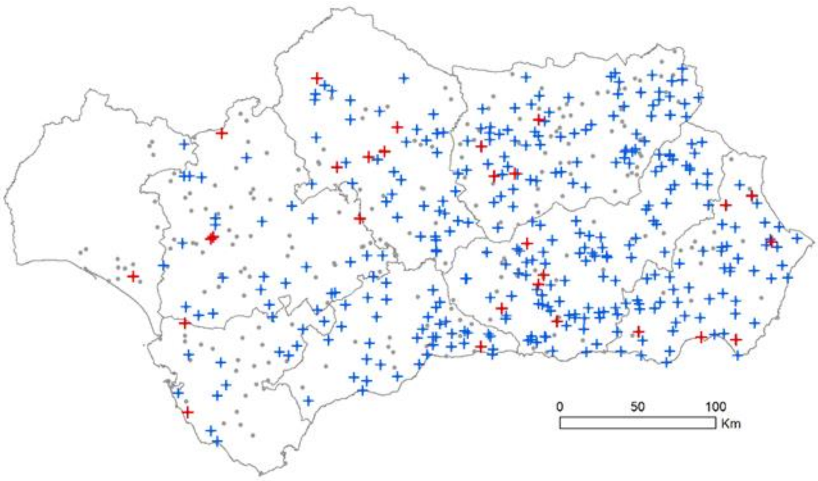

Figure 5.5. Spatial distribution of all precipitation and temperature stations in which the 3-year cycle was detected (crosses in blue for precipitation and red for temperature) above 90% of ACL, and all the other stations used for the analysis (points in grey).

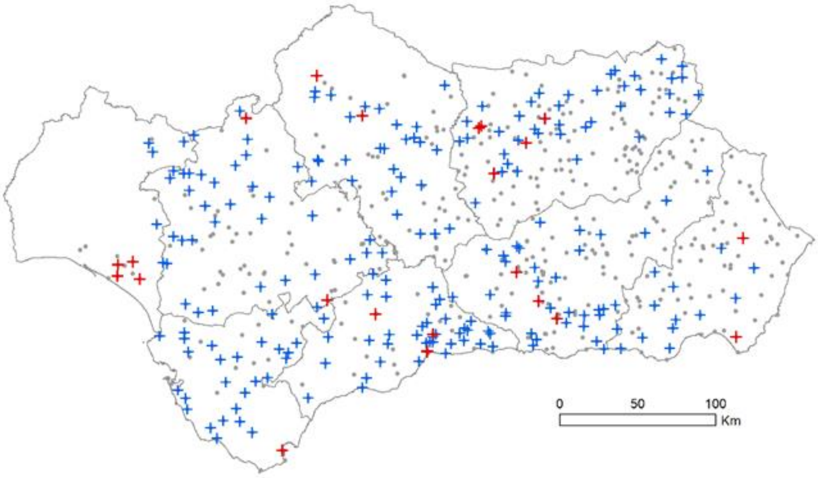

Figure 5.6. Spatial distribution of all precipitation and temperature stations in which the 7/8-year cycle was detected (crosses in blue for precipitation and red for temperature) above 90% of ACL, and all the other stations used for the analysis (points in grey).

Overall (Figures 5.5, 5.6), the spatial distribution of temperature observed does not show any geographical predominance of one cycle over the other, as opposed to the maps showing the precipitation cycles observed, where a general trend can be inferred. In the latter, there are more 3-year cycles in the east and more 7/8-year cycles in the west. The two cycles have been combined into one map by using all the precipitation stations in which the two cycles were detected together (Figure 5.7). This process was based on a preliminary selection of stations in which at least one of the two cycles must be present at each station; if both cycles were detected in the same station, the cycle with more power spectrum was the one counted for that station. Thus, 423 precipitation stations resulting from the aforementioned conditions have been analysed. About 261 precipitation stations show predominance of the 3-year cycle and 162 precipitation stations show predominance of the 7/8-year cycle. This process was followed by an interpolation process in which the 'Inverse Distance Weighting' technique was applied. The parameters were '2' for the power and '5' for the maximum number of neighbours.

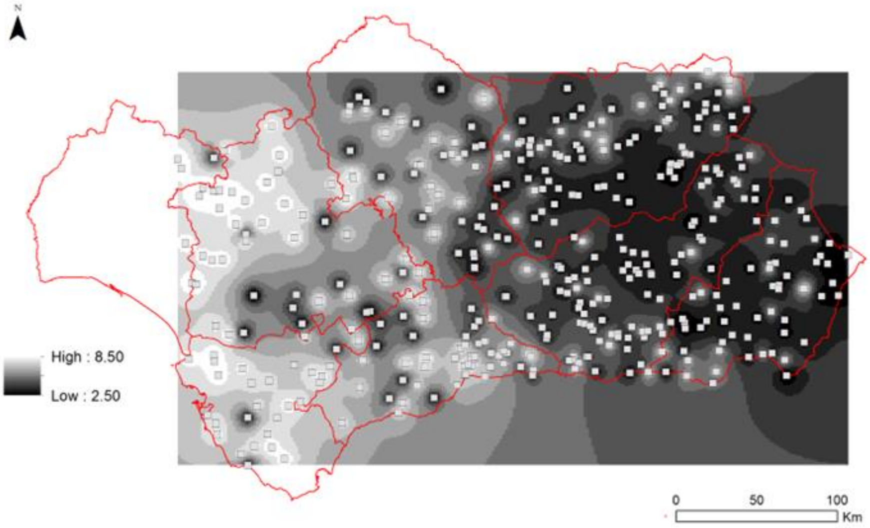

Figure 5.7. Spatial interpolation on 423 precipitation stations showing the geographical influence in Andalusia on the 3-year cycle and the 7/8 year cycle. Values from 2.50 to 8.50 in years.

5.5 Interpretation

The causes of climate variability in Andalusia from annual to multi-decadal time scales have generally been associated with Atlantic Ocean phenomena: large scale circulation features of Western Europe and the Atlantic Ocean (Esteban-Parra et al., 1998), alternation of zonal circulation and meridional circulation in the Atlantic that shifts the Azores High (Rodrigo et al., 1999), persistency and displacement of the Azores High (Ramos-Calzado et al., 2008), and changes in North Atlantic Oscillation (NAO) phases (Rodrigo et al., 2012). However, Eastern Andalusia is less influenced by Atlantic air masses and climate variability there is also influenced by Mediterranean Sea dynamics (Fernández-Montes and Rodrigo, 2015).

Previous studies applying spectral analysis to climatic datasets reveal cyclic climatic variability in the range of two to 250 years, but mainly located in the range of two to 11 years. Thus, a study on rainfall variability in Southern Spain found (Rodrigo et al., 2000) peaks above 95% significance at 2.1, 3.5, 7-9, 16.7 and 250 years, and a previous study on hydraulic heads across the Vega de Granada aquifer (Luque-Espinar et al., 2008) found a decadal cycle (peaks between 8 and 11 years) and a 3.2-year cycle, amongst others.

The power spectrum has been estimated for both North Atlantic Oscillation and Mediterranean Oscillation indexes (MOI) (Figures 5.8, 5.9). The NAO index is available at daily resolution (Climate Prediction Center, 2018) from 1950 to 2017. The MOI has two versions (Climatic Research Unit, 2018), 'Algiers-Cairo' (MOAC) and 'Israel-Gibraltar' (MOIG), both from 1948 to 2016 at daily resolution. The NAO and MOIG indexes have been analysed by using annual series.

The NAO index has significant periodicities at 50, 13.7, 2.7, 2.5 and 2.1 years, and the MOIG index at 7.8, 6.5, 4.1, 3.4, 2.4 and 2.1 years, all above 90% of ACL.

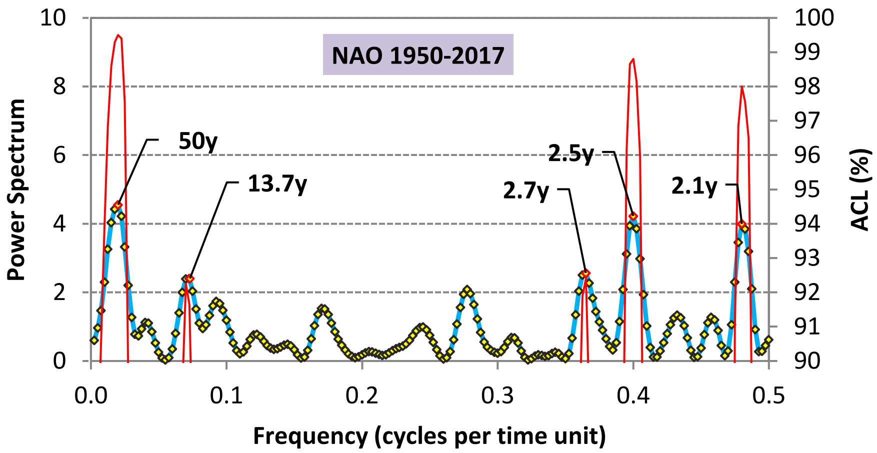

Figure 5.8. Power spectrum of the NAO index using annual records derived from the original dataset, and associated peaks of 50, 13.7, 2.7, 2.5 and 2.1 years above ACL of 90%, by using the smoothed Lomb–Scargle periodogram.

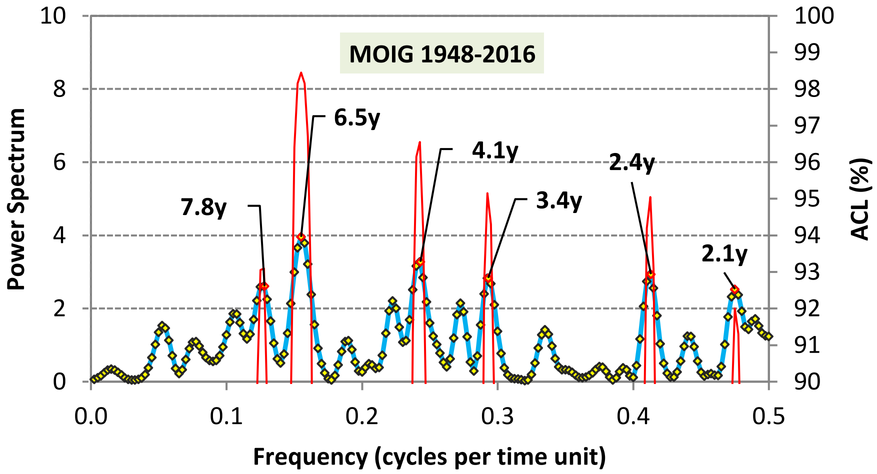

Figure 5.9. Power spectrum of the MOIG index using annual records derived from the original dataset, and associated peaks of 7.8, 6.5, 4.1, 3.4, 2.4 and 2.1 years above ACL of 90%, by using the smoothed Lomb–Scargle periodogram.

A second exercise has been conducted to assess the correlation between all the monthly series from the 707 stations (547 precipitation stations and 160 temperature stations) and the NAO and MO indexes. The geographical influence of both oscillations has been assessed (Figures 5.10-5.13). The NAO correlation for precipitation (Figure 5.10) is low; it tends to be more negative towards the west (-0.343) and zero or slightly positive towards the east (0.067). The NAO and temperature correlation (Figure 5.11) is less clear, with values between -0.214 and 0.240. The MOIG and precipitation correlation (Figure 5.12) is greater in value (from -0.16 to -0.76) than with the NAO and is always negative; it shows a pattern of being more negative towards the west (-0.753) and less negative towards the east (-0.240). The correlation between MOIG and temperature (Figure 5.13) is always positive, with values between 0.386 and 0.643, and it is equally distributed across the study area.

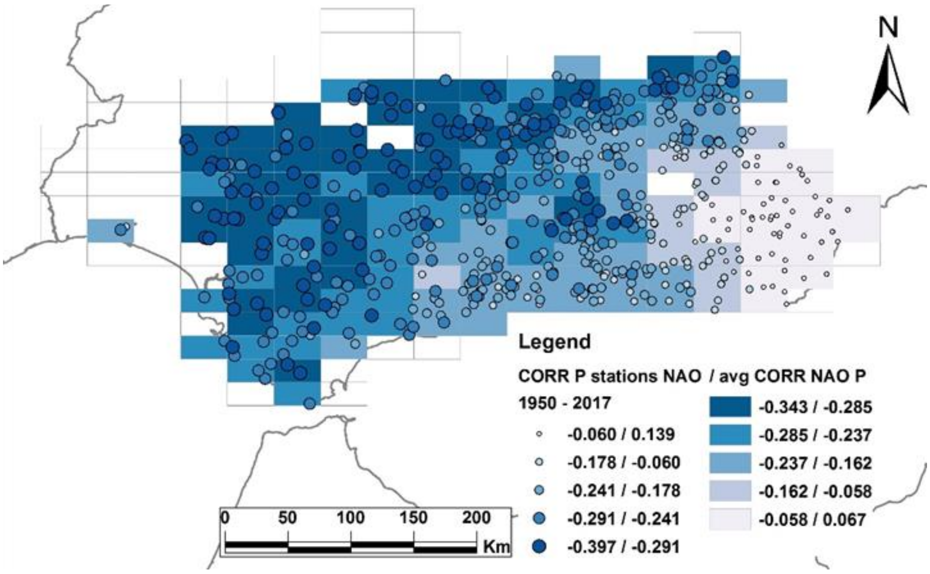

Figure 5.10. Correlation coefficients between the NAO index monthly values (1950 – 2017) and the monthly values of the 547 precipitation stations. The rectangles represent the average value for that particular area.

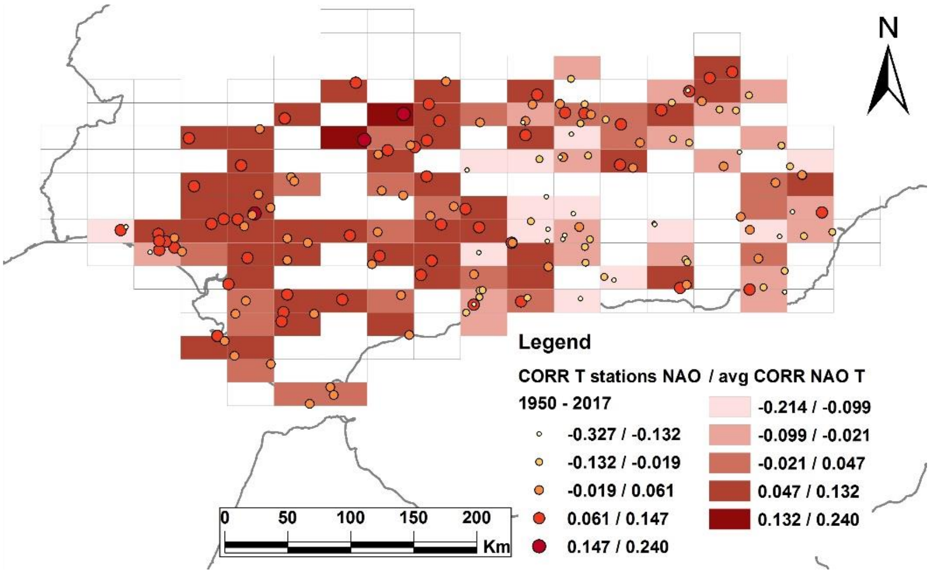

Figure 5.11. Correlation coefficients between the NAO index monthly values (1950 – 2017) and the monthly values of the 160 temperature stations. The rectangles represent the average value for that particular area.

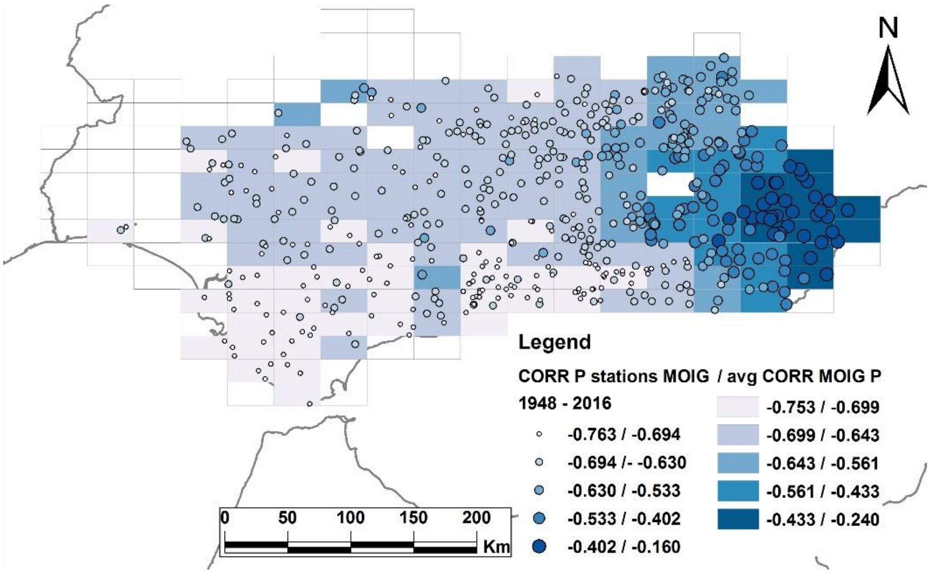

Figure 5.12. Correlation coefficients between the MOIG index monthly values (1948 – 2016) and the monthly values of the 547 precipitation stations. The rectangles represent the average value for that particular area.

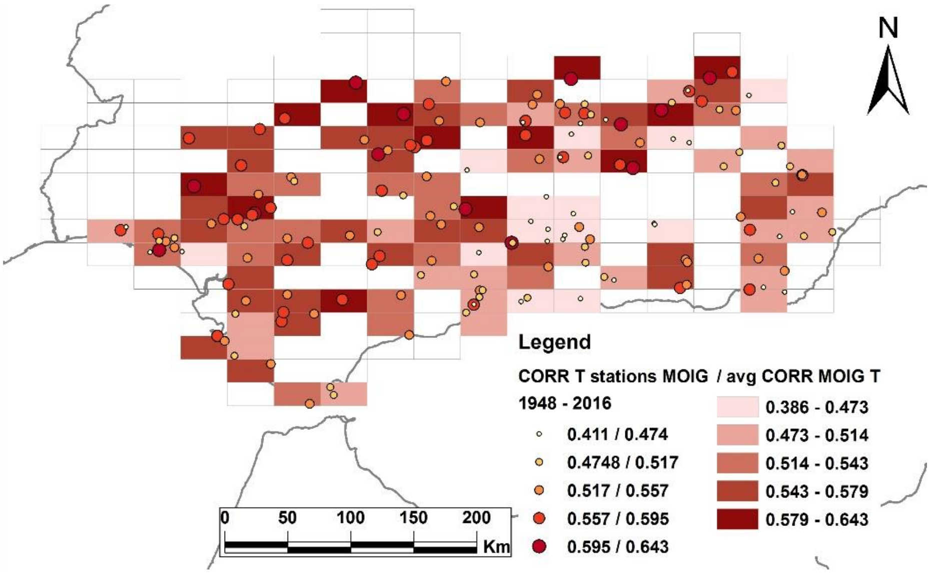

Figure 5.13. Correlation coefficients between the MOIG index monthly values (1948 – 2016) and the monthly values of the 160 temperature stations. The rectangles represent the average value for that particular area.

The most significant frequencies associated with both the NAO and MOIG indexes have been combined, as have the power spectra frequencies detected above 90% of ACL (Figures 5.14, 5.15). Certain precipitation and temperature frequency values match some of the frequencies associated with NAO and MOIG quite well.

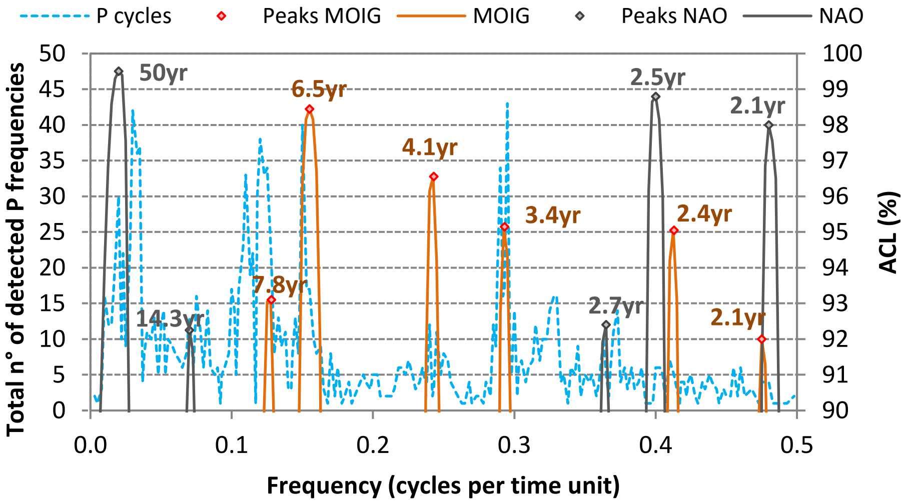

Figure 5.14. Histogram of frequencies detected above ACL 90% from all precipitation stations, together with the most significant frequencies of the NAO and MOIG indexes.

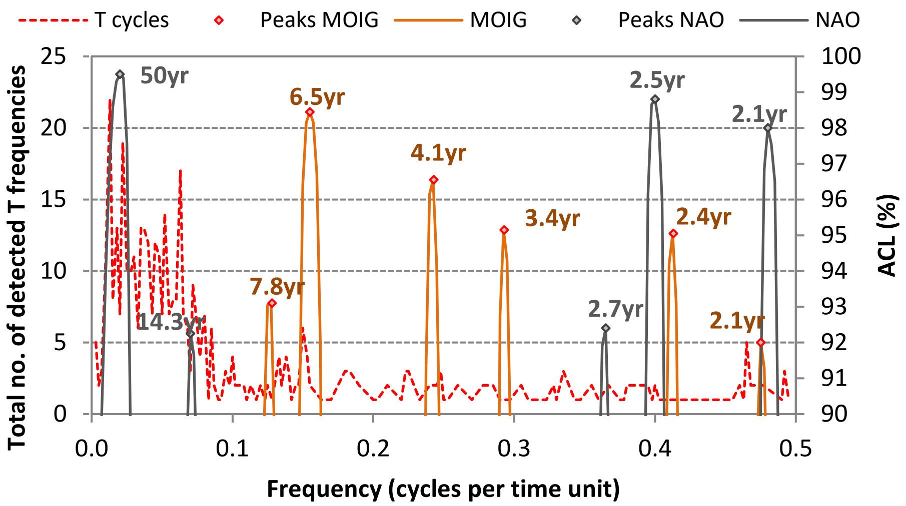

Figure 5.15. Histogram of frequencies detected above ACL 90% from all temperature stations, together with the most significant frequencies of the NAO and MOIG indexes.

Particularly interesting are the precipitation cycles that correspond to the MOIG cycles of 3.4, 6.5 and 7.8 years, and to the NAO cycles of 2.1, 2.7, 14.3 and 50 years. The match between the temperature cycles recorded and the NAO and MOIG cycles is less clear than the precipitation comparison.

Other cycles detected in the study area, which were also above 90% of ACL, could be tentatively associated with other climatic phenomena (Table 5.1; See Rodríguez-Tovar (2014) for a review).

Table 5.1. Tentative correlation between the other cycles detected above 90% ACL and other well-known cycles, including the number of precipitation (P) and temperature (T) stations where said cycles were detected.

Cycle value in years	Cycle	P	T
10/11	Sunspot cycles of 11 years	84	17
17	Southern Oscillation Index (SOI)	17	16
19	Lunisolar cycle	19	14
20-25	Hale Cycle	51	49

5.6 Conclusions

Spectral analysis of precipitation and temperature time series from a considerable number of meteorological stations (707 locations) distributed across southern Spain in the region of Andalusia has allowed for the characterization of the spatial variability of the two most frequent cycles in the study region: a 7/8-year cycle and a 3-year cycle. The length of time over which data was collected at the stations analysed was relatively short (in most cases less than 50 years, but always more than 20 years for precipitation and 10 years for temperature) and therefore the focus of this research has been the high-frequency cycles. Many other periodicities greater than 10 years have been found with an ACL higher than 90%, but they are less abundant. Initially it was thought that the western part of the study area might be more influenced by the climatic activity derived from the North Atlantic Oscillation (NAO), manifesting as a cycle in the range from 7 to 8 years. On the other hand, the eastern part of the study area was hypothesized to be more influenced by the Mediterranean Oscillation (MO), represented by a 3-year cycle. However, the correlation values calculated across the study area between the meteorological variables on the one hand, and the NAO and MOIG indexes on the other, plus the spectral analysis conducted, show that the Mediterranean Oscillation may play a greater role in the region than the North Atlantic Oscillation. Thus, the 7/8-year cycle may correspond to the 6.5- and 7.8-year cycles detected in the MOIG index, and the 3-year cycle may be associated with the 3.4-year cycle detected in the MOIG index, and with the 2.7- and 2.5-year cycles detected in the NAO index. The explanation of how these two climatic phenomena interact with one another is outside the scope of this paper and more research is needed. Nevertheless, these results can help meteorologists and climatologists to better understand how weather and climate works in the southern Iberian Peninsula.

Acknowledgement

This work has been supported by research project CGL2015-71510-R from the Spanish Ministry for the Economy, Industry and Competitiveness.

6 Chapter VI. A case study using tree-ring data

A new method for reconstructing past-climate trends using tree-ring data and kernel smoothing

José Sánchez-Morales[a], Eulogio Pardo-Igúzquiza[b], Francisco Javier Rodríguez-Tovar[a], Peter A. Dowd[c]

(a) Departamento de Estratigrafía y Paleontología, Facultad de Ciencias, Universidad de Granada. Campus Fuentenueva s/n, 18002 Granada (Spain)

(b) Instituto Geológico y Minero de España (IGME), Ríos Rosas, 23, 28003 Madrid (Spain)

(c) Faculty of Engineering, Computer and Mathematical Sciences, The University of Adelaide (Australia)

E-mail addresses: josesanmor@correo.ugr.es (J. Sánchez-Morales), e.pardo@igme.es (E. Pardo-Igúzquiza), fjrtovar@ugr.es (F.J. Rodríguez-Tovar), peter.dowd@adelaide.edu.au (P.A. Dowd).

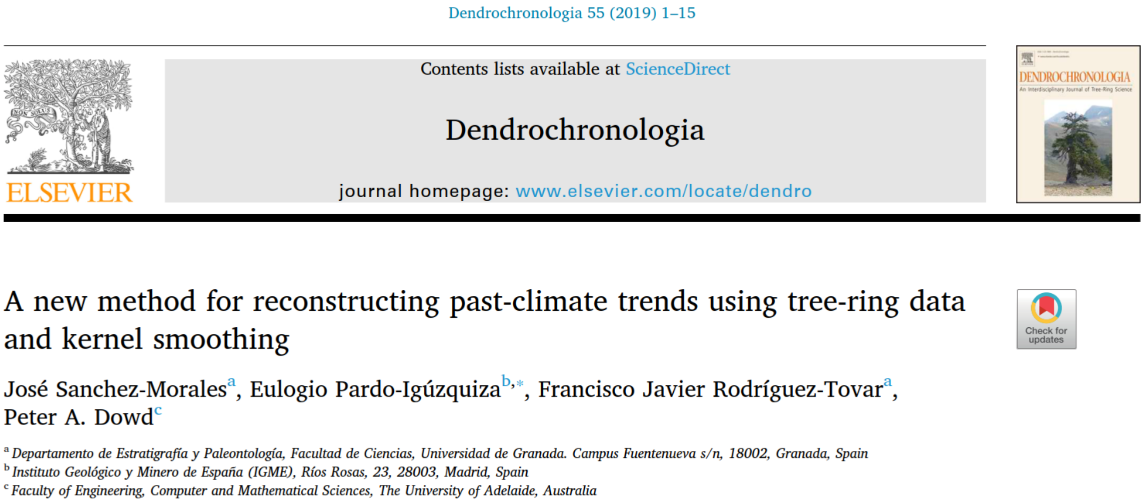

Dendrochronologia 55 (2019) 1–15

Contents lists available at ScienceDirect

Dendrochronologia

journal homepage: www.elsevier.com/locate/dendro

A new method for reconstructing past-climate trends using tree-ring data and kernel smoothing

José Sanchez-Morales[a], Eulogio Pardo-Igúzquiza[b,*], Francisco Javier Rodríguez-Tovar[a], Peter A. Dowd[c]

[a] Departamento de Estratigrafía y Paleontología, Facultad de Ciencias, Universidad de Granada. Campus Fuentenueva s/n, 18002, Granada, Spain
[b] Instituto Geológico y Minero de España (IGME), Ríos Rosas, 23, 28003, Madrid, Spain
[c] Faculty of Engineering, Computer and Mathematical Sciences, The University of Adelaide, Australia

Published in:

Dendrochronologia (2.691; JCR Impact factor), 2019

v. 55, p. 1–15 https://doi.org/10.1016/j.dendro.2019.03.002

ABSTRACT

Mediterranean high-relief karst areas are very vulnerable to changes in temporal patterns of precipitation and temperature. Understanding climate change in these areas requires current climate trends to be assessed within the context of the variability of rainfall and temperature trends in the recent past. A major difficulty is that the instrumental record in these high-relief areas is very limited and the use of data from paleoclimatic proxies, such as tree-ring data, is required to infer past climate variability. Furthermore, for complex relationships between tree-ring data and climatic variables, it is almost impossible to infer past inter-annual variations in temperature or precipitation, and the inference is limited to the reconstruction of low-frequency variability (i.e., the trend). To do so, in this work, we propose a new method based on detecting trends (by kernel smoothing) in tree variables that show maximum correlation with the trends (also estimated by kernel smoothing) of climate variables. This enables a standard regression framework to be established to reconstruct past climate. We have used tree-ring proxy data from *Abies pinsapo* to evaluate past climate trends in the Sierra de las Nieves karst massif in Southern Spain. The analysis has found that during the last three hundred years the smoothed mean annual rainfall steadily decreased until the beginning of the 20th century and thereafter it remained more or less constant until the end of the century. On the other hand, the smoothed mean annual temperature has steadily increased since the beginning of the 18th century until recent times. These trends are also suggested by the climate projections for the latter part of the current 21st century. As the study area is a high-relief karst massif of significant hydrologic and ecologic interest, the implications of these trends should be taken into account when formulating effective action plans to mitigate the impact of climate change.

Keywords: Dendro-climatological analysis, Kernel smoothing, Abies pinsapo, Climatic change, Rainfall, Temperature, Southern Spain.

6.1 Introduction

Climate change affects the biodiversity and geodiversity of many vulnerable areas. This is especially so in areas of high-relief Mediterranean karst massifs where very specific present-day ecosystems have been established by adapting to local climate variables at high elevation (Lindner et al., 2010; Loáiciga et al., 2000). Present-day ecosystems are the result not only of current conditions but also of past climate. In this context, the analysis of historical climate data, especially those of the recent past (i.e., last few centuries), provides a better understanding of current climate change and its effects. Thus, the reconstruction of past climates is of paramount importance because it allows the current precipitation and temperature trends to be placed in historical perspective. Is the 20th century warming abrupt and exceptional? This question can only be answered by taking into account of the magnitude of past climate variability. In addition, the association of forcing factors with past climate change helps us to understand why climate changes and the types of change that can be expected in the near future. Again, to do so requires an assessment of past climate variability.

There have always been fluctuations in climate and it is of particular interest to assess local climate variability in terms of rainfall and temperature. However, past instrumental meteorological data are scarce, especially in these high-altitude areas; instrumental measurements of climate variables, such as rainfall and temperature, are usually limited to meteorological stations in towns in the nearby valleys. In these cases, other climate proxies must be used to reconstruct past climate variability. Among the available climate proxies, assuming that a yearly resolution is adequate, the most suitable method is the use of tree rings (i.e., Schweingruber, 1987; Speer, 2010; Stoffel et al., 2010; Wimmer and Vetter, 1999). Rainfall, as a measure of water availability, and temperature, are two climate variables that significantly affect tree growth features (i.e., Źywiec et al., 2017). Thus, tree-ring parameters can be used as a valuable proxy to obtain information on past rainfall and temperature (Cook and Kairiukstis, 1989). In general, the most commonly used tree-ring parameters are the tree-ring widths and densitometric measurements (Grudd, 2008; Kirdyanov et al., 2008). Three steps are required to use these two variables in paleoclimate reconstruction: (1) standardization of the tree-ring measurements, (2) calibration of standardized tree-ring measurements against instrumental records and (3) using a statistical procedure (e.g., statistical regression) to conduct the reconstruction.

Measurements of all variables include noise originating from various sources including other environmental variables that affect growth (e.g., availability of light, competition with neighbouring trees, soil nutrients, forest fires, insect attacks). Additionally, some tree-ring variables, such as tree-ring width, are affected by a growth trend in the tree and must be standardized (Fritts, 1976; Cook and Kairiukstis, 1989). This systematic change can be modelled and removed from the original time series to provide a variable that changes only with environmental factors. One of several detrending methods is used depending on the form of the trend in the growth of the tree. Usually, there is a declining growth trend in normally growing trees that can be approximated by a negative exponential curve (Helama et al., 2016). Other tree-ring variables, such as density, do not need this standardization.

In the second step, the correlation between the chronology and the instrumental climate data is used to find a statistical relationship that can be used to transform tree-ring data into estimates of paleoclimate data. However, this classical framework of dendroclimatological analysis may be complicated when the relationship between the tree-ring variables and the paleoclimate records is complex and far from a simple linear relationship for which paleoclimate data can be reconstructed from standard regression techniques. In this work we present an application of statistical techniques to reconstruct past climate variability based on finding the trends in the tree variables that have the maximum correlation with the trends in the climate variables and then establishing a standard regression framework.

6.2 Methodology

The most common tree-ring variables used for extracting paleoclimatic information are tree-ring width series (early wood tree-ring width, late wood tree-ring width and total tree-ring width) and ring density series (minimum tree-ring wood density, maximum tree ring wood density and mean tree ring wood density) (Büntgen et al., 2010; Esper et al., 2015; Fritts, 1976; Grudd, 2008).

The workflow of the methodology is given in **Figure 6.1**, in which there are three main step-wise problems to be solved: (1) standardisation (Helama et al., 2004), (2) calibration and (3) reconstruction (Fritts et al., 1971). Standardisation is required because some tree-ring variables, such as tree ring width variables, have a biological trend (i.e., an ageing trend in tree growth which is independent of climate) that must be removed (Bontemps and Esper, 2011). The most commonly used standardisation method is Regional Curve Standardisation (RCS) (Briffa et al., 1992) because it has the ability to preserve low frequency (i.e., generally multi-centennial) climatic fluctuations (Helama et al., 2016). The RCS method has been reported to retain more low-frequency signal than methods based on individual tree detrending (Melvin and Briffa, 2008). Although other methods are available (e.g., cubic smoothing splines (SPL) which model the high frequency variation better), the RCS standardisation tracks the low-frequency trends more robustly (Wilson et al., 2005). In other cases, more sophisticated statistical modelling provides similar long-term chronologies as the RCS method (Bontents and Esper, 2011). For all these reasons, we have used the RCS method in this work to standardise tree-ring width variables.

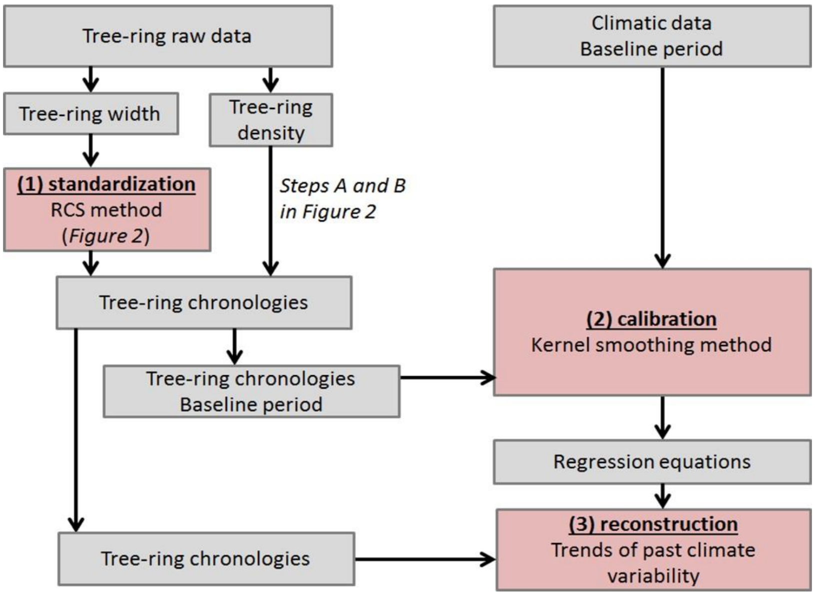

Figure 6.1. Workflow for the proposed methodology. Tree-ring raw data (width and density) are available for a long period. Some of this period overlaps the climate data for the so-called baseline period and the inference of past climate is done for the time with tree-ring data before the baseline period. The first step is to obtain the tree-ring chronologies that will require standardisation of the tree ring width variables (as explained in the main text). The second step is calibration in order to infer a regression relationship between trends of tree-ring variables and climate variables that will be used in the third step of reconstruction to infer past climate variability in the trends.

For a given study area, a number of radial tree-ring series (raw or original time series) are obtained from the same or different trees and these are used to determine the width and density variables. For each width variable, the RCS method comprises the following steps (Figure 6.2):

i) Align the raw series of a site by biological year (starting at year 1). This step A in **Figure 6.2**. The biological year, or cambial age, is the ring number from the pith (Spicer and Gartner, 2001). The raw time series of the variable aligned by biological year are denoted by:

$\{v_{ik};\ i = 1,\ldots, n_k;\ k = 1,\ldots,N\}$

n_k: number of tree-rings of the k-thm series.

N: total number of tree-ring series at the same site from the same or different trees. Note that because no all the series have the same number of tree-rings each series has its own length and for each biological year there may be a different number of series n_{ik}.

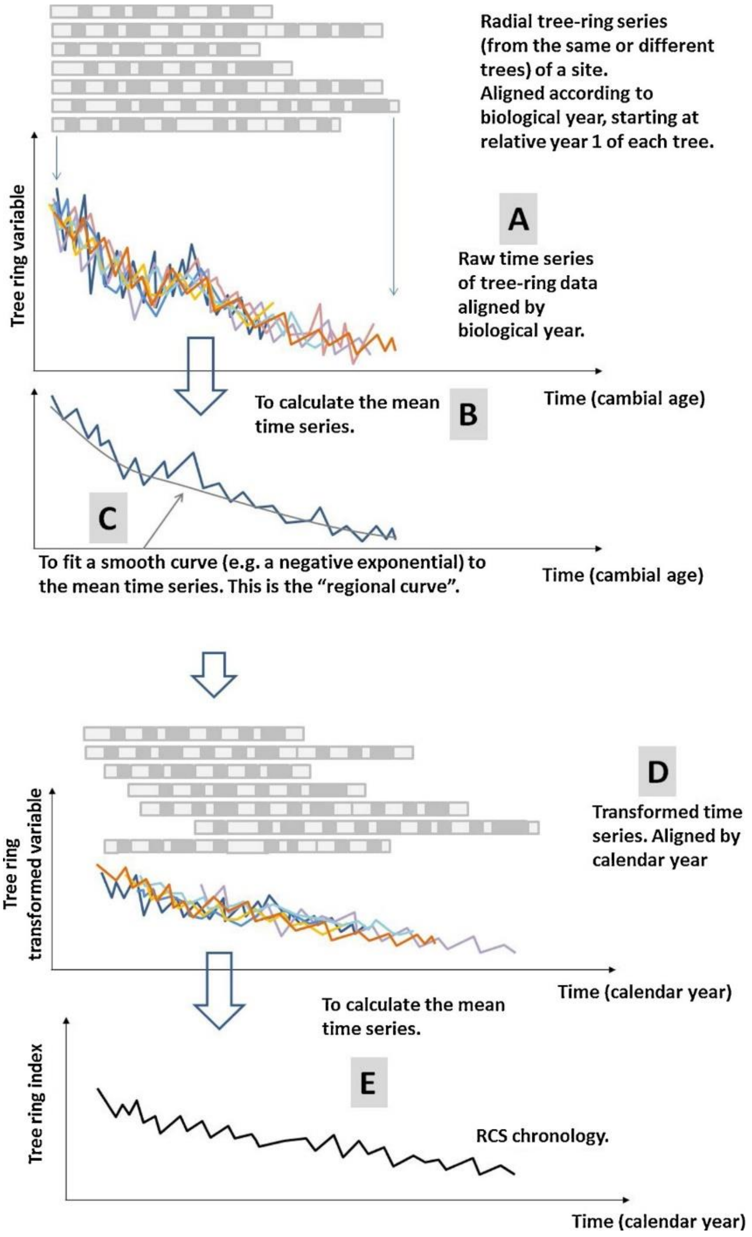

Figure 6.2. Steps for calculating the RCS chronology of a site. A. The radial raw tree ring series are aligned by biological year. B. The mean time series is calculated from the aligned time series. C. A negative exponential is fitted to the mean time series to obtain the RCS curve. D. Each raw time series is divided by the RCS curve to obtain the transformed time series. The transformed time series are aligned. E. The mean of the transformed time series is calculated, and this constitutes the final RCS chronology.

- Compute the mean series $\{\bar{v}_i$, i = 1, …, $n_{max}\}$. This is step B in Figure 6.2.

$$\{\bar{v}_i = \frac{1}{m_i}\sum_{k=1}^{m_i} v_{ik}\}.$$

Where m_i is the number of times series for the i-thm biological year.

- Fit a smooth mathematical function, to the mean time series to obtain the so-called regional curve (RC); this is step C in Figure 6.2. For example, a negative exponential curve:

$$\bar{v}_i = \beta e^{-\infty i}$$

Where ∞ and β are the parameters obtained by a least squares fitting of the equation to the mean time series $\{\bar{v}_i$, i = 1, …, $n_{max}\}$.

- Divide each raw time series by the RC curve values. This is a standardisation to obtain the time series of tree-ring index

$$I_{ik} = \frac{v_{ik}}{\bar{v}_i}\ ;\ \text{ip} = 1, \ldots, n_k;\ \text{k} = 1, \ldots, \text{N}$$

- Return the time series of tree-ring index to the calendar year. These are called the transformed series. This step D in Figure 6.2.
- Calculate the mean of the transformed series, called the RCS site chronology (step E in Figure 6.2):

$$\bar{I}_J = \frac{1}{l_j}\sum_{k=1}^{l_j} I_{jk}$$

Where l_j is the number of time series for the calendar year j.

When dealing with tree-ring density variables, the raw chronologies are obtained by applying Eq. (5) to the raw variables as the biological growth trend is not present in these variables.

The second stepwise problem is calibration. In this second step, RCS chronologies (or raw chronologies for ring-density variables) must be correlated with instrumental rainfall and temperature data (Fritts, 1976; Esper et al., 2002). This step is easily solved, by standard statistical regression, if there is a high correlation (for example, an absolute value of correlation larger than 0.8) between the tree-ring variable and the instrumental climatological variable (temperature or precipitation). However, in many cases the relationship between the variables is complex and is not clear from simple regression graphs. This may be because the noise in the tree-ring chronologies hide the climatic signal. Thus, rather than trying to reconstruct precise values of past rainfall and temperature it is more appropriate to evaluate long term trends (i.e., low frequency variation) in the past variability of rainfall and temperature. One possible approach is to smooth the time series of both tree-ring variables and climate variables using a moving window smoother with the bandwidth chosen to maximise the correlation between the smoothed time series of tree-ring chronologies and climate variables. One form of kernel smoothing (Ghosh, 2018) for trend estimation is the simple moving average (SMA). Given a time series of n data $\{\bar{I}_1, \bar{I}_2, \dots, \bar{I}_n\}$ the trend is the new time series $\{\bar{T}_1, \bar{T}_2, \dots, \bar{T}_n\}$ in which each value is calculated from the original series by the SMA with a bandwidth of M values defined as:

$$\bar{T}_j = \frac{I_{j-M/2} + I_{j-\frac{M}{2}+1} + \dots + I_{j+\frac{M}{2}-1} + I_{j+M/2}}{M+1}$$

A statistical relationship between tree-ring variables and climate variables is established from the smoothed time series (or trend), and the smoothed times series of rainfall and of temperature can be reconstructed together with their variability by standard linear regression:

$$\bar{C}_j = \infty + \beta T_j$$

Where $\bar{C}_j$ is the reconstructed trend of the climate variable (rainfall or temperature) for year j based on the trend of the tree-ring variable $\bar{T}_j$. ∞ and β are the regression coefficients estimated in the calibration step.

6.3 Case study

The study area is the Sierra de las Nieves karst massif in the province of Málaga, Southern Spain (Figure 6.3). This is a high-relief karst area of significant hydrological and ecological value that is likely to be very vulnerable to climate change (Pardo-Igúzquiza et al., 2015). The area is a Natural Park and, since 1995, a UNESCO Biosphere Reserve. There are no instrumental meteorological records in the vicinity of this area that are longer than a few decades (Pardo-Igúzquiza et al., 2012). Thus, proxy data must be used for past climate reconstructions. In particular, there are public domain tree-ring data obtained for a larger study of the entire Iberian Peninsula (Braker and Schweingruber, 1984). The data are used by the second author in Briffa et al. (1988) as part of a network across Europe used to reconstruct summer temperature patterns for the period 1750–1800 using maximum latewood density chronologies of coniferous trees. The results of Briffa et al. (1988) are synoptic for Europe and they are not comparable with the results of the present study where we focus on climate variability on a local scale. This is needed in the Sierra de las Nieves in order to understand past climate change and variability which will help understand the current trends and will allow the park environmental managers to plan actions against the impact of possible climate change on the water resources and the biodiversity of the Sierra de las Nieves Natural Park.

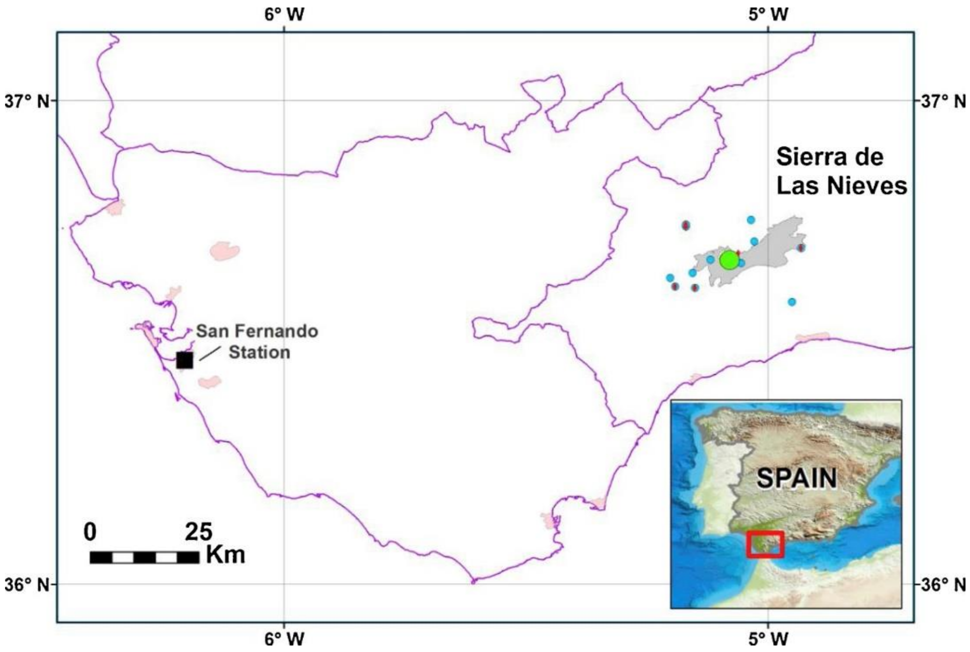

Figure 6.3. Location of the study area in the Sierra de las Nieves karst aquifer (southern Spain) and location of the San Fernando station. The green point represents the location of *Abies pinsapo* series used in this research and the other points around it represent the locations of local meteorological stations (For interpretation of the references to colour in this figure legend, the reader is referred to the web version of this article).

The original data (including both raw tree-ring widths and raw tree ring wood density data) are available from the International Tree-Ring Data Bank and the National Oceanic and Atmospheric Administration. The series of tree-ring data are from *Abies pinsapo* at an altitude of 1650 m (Braker and Schweingruber, 1984). Abies pinsapo is a circum-Mediterranean tree that is found only in the mountain ranges of Southern Iberia and Northern Morocco (Linares and Carreira, 2009; Linares et al., 2009; Quézel et al., 1999).

Abies pinsapo has a limited area of distribution at five sites, three in southern Spain and two in the north of Morocco (Esteban et al., 2010). The sites in Spain are located in the Serranía de Ronda, which is in the high mountain ranges of the westernmost part of the Betic Cordillera, and they span the provinces of Málaga and Cádiz (Fernández-Cancio et al., 2007; Esteban et al., 2010). *Abies pinsapo* occurs in hyper-wet Mediterranean climates, with an annual precipitation between 1000 and 3000mm, but with a dry summer season from June to September (Fernández-Cancio et al., 2007) and it is adequate for dendroclimatology studies (Fuster, 2007).

There are six tree-ring proxies available in the study area. Three proxies are tree-ring width variables (early wood width index, late wood width index and total width index) and the other three are ring density variables (minimum, maximum and mean tree-ring wood density). The RCS methodology was applied to the tree-ring width variables to obtain the RCS chronologies. The raw chronologies were used for the density variables. As an example, Figure 6.4 shows the chronologies of early wood width index (Figure 6.4A) and mean wood density (Figure 6.4B). The chronologies were obtained using a number of series that range from one (for the first 21 years) to 22. As the instrumental record in the area is very short (covering only the last few decades), the longest time series, San Fernando (Figure 6.4), was chosen even though this meteorological station is 100 km to the west of the tree-ring data location and with an elevation close to sea level. Nevertheless, the San Fernando annual time series for rainfall and temperature are well correlated with the mean time series calculated from the stations around Sierra de las Nieves. Both locations belong to the same climatic area and the altitudinal differences imply more rainfall and lower temperature because of the increase in altitude from sea level to the height of the Sierra de las Nieves. However, the trends are the same for the regional area that comprises both locations.

For the San Fernando station there are continuous monthly and annual records of rainfall and temperature from 1870 to the present. Ten climatic variables were processed: total annual rainfall, spring rainfall, summer rainfall, autumn rainfall, winter rainfall, mean annual temperature, mean spring temperature, mean summer temperature, mean autumn temperature, and mean winter temperature. The period from 1870 to 1982 was used for calibration purposes; there are no tree ring data available after 1982.

The calibration data are chosen to cover the time span in which the tree-ring data and the instrumental data overlap. As there are six tree ring variables and ten climate variables, there are 60 possible combinations (pairs) of tree-ring variables and climate variables. Figure 6.4 shows two of those combinations. Figure 6.4A shows the relationship between the early wood width index and yearly rainfall and Figure 6.4B shows the relationship between mean wood density and mean annual temperature.

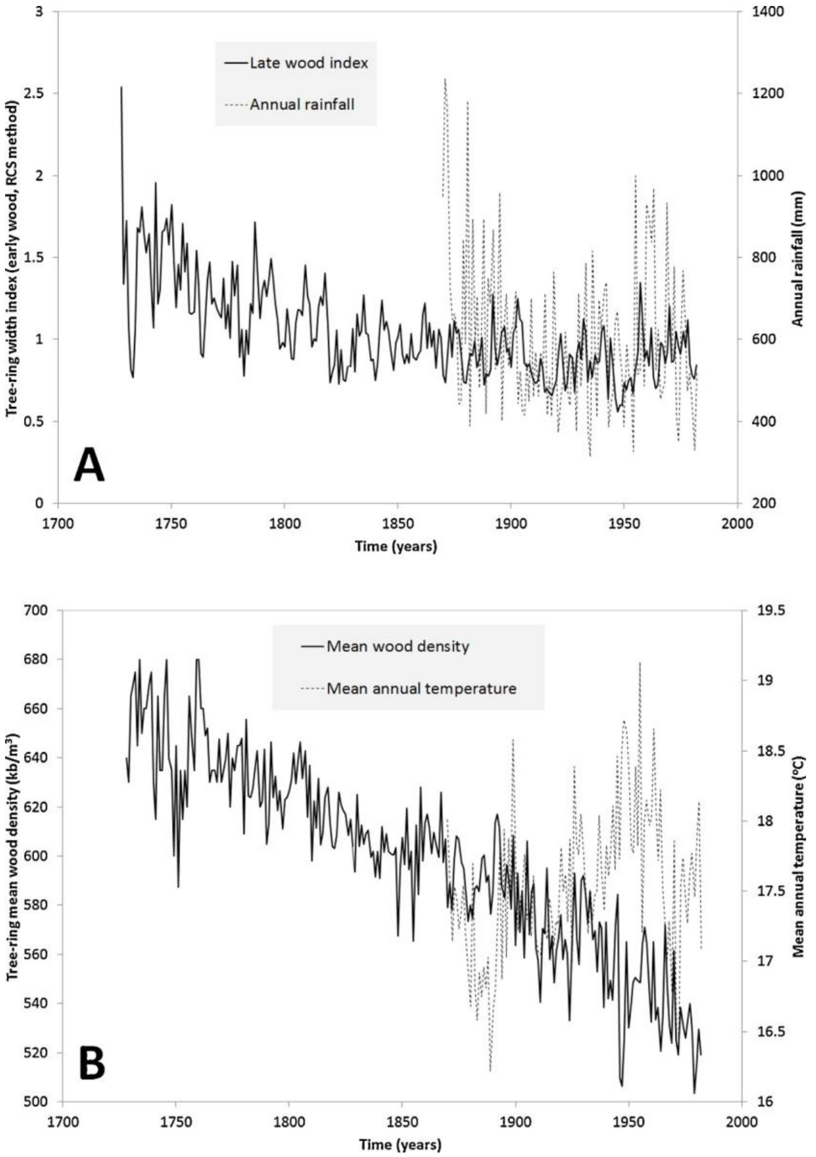

Figure 6.4. A: Time series of RCS index of early wood tree-ring width and annual rainfall at San Fernando station. B: Raw mean tree-ring wood density and mean annual temperature at San Fernando station.

The relationships in Figure 6.4 are complex and there is no simple correlation between the time series. In fact, the linear correlation between the tree-ring variables and the climate variables is negligible as can be seen in Table 6.1. Detecting any relationship requires a robust procedure, in the sense of finding statistical relationships between means (i.e., trends or low-frequency variability) rather than between the actual data as in Figure 6.4. This can be done by using a moving window running mean applied to every series used in the calibration period, as described in the methodology section. In this smoothing, the bandwidth is selected so as to maximise the correlation between each tree-ring variable and each climate variable for the calibration period of 1870-1982.

	Rainfall year	Rainfall winter	Rainfall spring	Rainfall summer	Rainfall autumn	Temp. year	Temp. winter	Temp. spring	Temp. summer	Temp. autumn
EARLY WOOD WIDTH	**0.03**	**−0.07**	**−0.1**	**0.17**	**0.04**	**−0.07**	**0.01**	**0.01**	**−0.06**	**−0.11**
LATE WOOD WIDTH	**0.05**	**0.06**	**−0.1**	**0.12**	**0.17**	**0.18**	**0.21**	**0.22**	**0.06**	**0.05**
ANNUAL WOOD WIDTH	**0.02**	**−0.03**	**−0.14**	**0.18**	**0.08**	**0.05**	**0.12**	**0.12**	**0**	**−0.03**
MINIMUM WOOD DENSITY	**−0.01**	**−0.06**	**0.07**	**−0.23**	**0.05**	**0**	**−0.14**	**0.04**	**0.05**	**−0.01**
MAXIMUM WOOD DENSITY	**0.07**	**−0.14**	**0.06**	**0.09**	**0.16**	**−0.22**	**−0.22**	**−0.04**	**−0.16**	**−0.18**
MEAN WOOD DENSITY	**0.06**	**−0.14**	**0.07**	**0.04**	**0.16**	**−0.21**	**−0.24**	**−0.03**	**−0.15**	**−0.18**

Table 6.1. Correlation coefficients between the tree-ring variables and the climate variables.

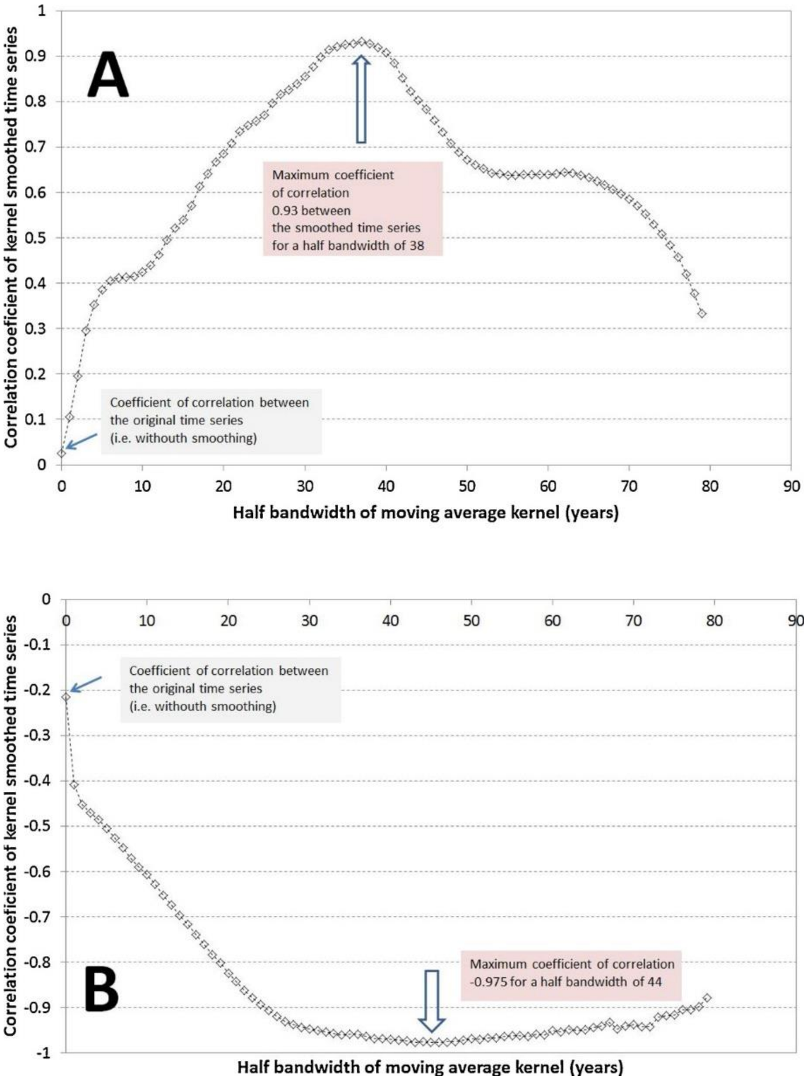

Figure 6.5. Reconstruction of rainfall. A: Correlation coefficient between the smoothed early wood tree-ring width and smoothed yearly rainfall as a function of the semibandwidth that defines the amount of smoothing. B: Correlation coefficient between the smoothed mean tree-ring wood density and smoothed yearly mean temperature as a function of the semi-bandwidth that defines the amount of smoothing.

A

	Rainfall year	Rainfall winter	Rainfall spring	Rainfall summer	Rainfall autumn	Temp.year	Temp.winter	Temp.spring	Temp.summer	Temp.autumn
EARLYWOODWIDTH	0.93	0.69	0.83	−0.59	0.81	−0.75	−0.69	−0.74	−0.95	−0.79
LATEWOODWIDTH	−0.78	0.73	−0.89	0.85	−0.88	0.91	0.94	0.92	0.88	0.89
ANNUALWOODWIDTH	−0.69	0.86	−0.81	0.82	−0.79	0.83	0.87	0.83	0.79	0.8
MINIMUMWOODDENSITY	0.9	−0.44	0.97	−0.95	0.96	−0.96	−0.99	−0.95	−0.93	−0.95
MAXIMUMWOODDENSITY	0.91	−0.46	0.98	−0.9	0.97	−0.98	−1	−0.97	−0.95	−0.96
MEANWOODDENSITY	0.91	−0.46	0.98	−0.91	0.97	−0.98	−1	−0.97	−0.95	−0.96

B

	Rainfall year	Rainfall winter	Rainfall spring	Rainfall summer	Rainfall autumn	Temp.year	Temp.winter	Temp.spring	Temp.summer	Temp.autumn
EARLYWOODWIDTH	38	80	34	35	38	65	38	65	80	33
LATEWOODWIDTH	54	34	54	53	49	49	49	44	50	54
ANNUALWOODWIDTH	54	35	49	53	49	49	49	48	48	49
MINIMUMWOODDENSITY	55	42	46	68	50	46	75	41	46	46
MAXIMUMWOODDENSITY	54	44	56	80	48	46	57	42	46	51
MEANWOODDENSITY	54	44	56	80	48	44	41	42	44	49

Table 6.2. A: Maximum correlation coefficient between the smoothed tree-ring variables and the smoothed climate variables. B: Values of the semi-bandwidth (in years) for which the maximum correlation between the smoothed series is reached.

The maximum correlation coefficients are given in Table 6.2A and the optimal semiband width for rainfall is given in Table 6.2B. It can be seen that, in most cases, very high correlation coefficients are achieved provided a smoothing kernel with a large enough bandwidth is used. The optimal cases are those with a high correlation coefficient and a short bandwidth. The case of early wood tree-ring width and yearly rainfall with an optimal bandwidth of 38 is shown in Figure 6.5A. With respect to temperature, Figure 6.5B shows the correlation coefficient between mean wood density and mean annual temperature as a function of the bandwidth that defines the amount of smoothing; the maximum correlation coefficient is -0.975 (Table 6.2). For rainfall, the smoothed time series is given in Figure 6.6A and the linear relationship between both is given in Figure 6.6B. Both time series (Figure 6.6A) show a similar pattern with a minimum annual rainfall between 1920 and 1950 when the tree rings have minimum widths. The linear relationship in Figure 6.6B is statistically significant with a very low p-value, with relatively low dispersion around the straight line and a relatively high coefficient of determination.

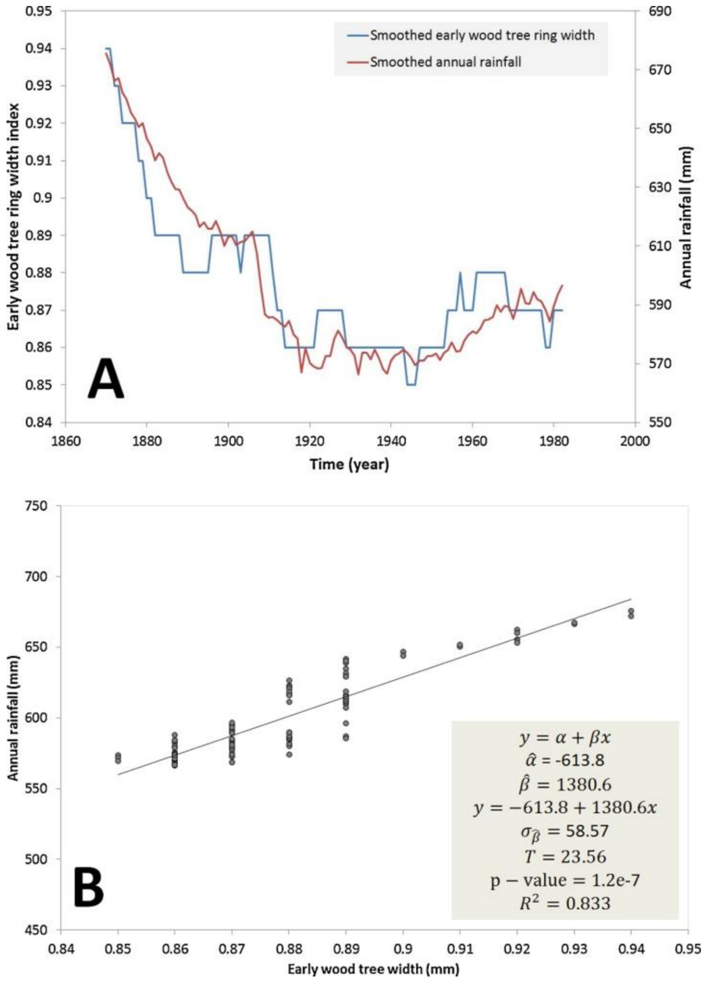

Figure 6.6. Reconstruction of precipitation. A: Smoothed time series for the maximum achieved correlation coefficient in Figure 6.5. B: linear regression between the smoothed tree-ring and climate time series in A. The figure shows the estimates of the regression parameters: intercept (∞) and slope (β), the standard deviation of the estimate of slope, the t-statistic, the p-value, and the coefficient of determination R^2. The low p-value (< 0.01) indicates the statistical significance of the linear relationship.

For temperature, Figure 6.7A shows the smoothed time series for mean wood density and for mean annual temperature for the maximum correlation coefficient of -0.975. Both time series in Figure 6.7A show similar patterns with a clear linear trend of increasing temperature and decreasing mean wood density. The linear relationship between mean annual temperature and mean wood density is evident in Figure 6.7B. The linear regression in Figure 6.7B is statistically significant with a very low p-value, with relatively little dispersion around the straight line and a high coefficient of determination.

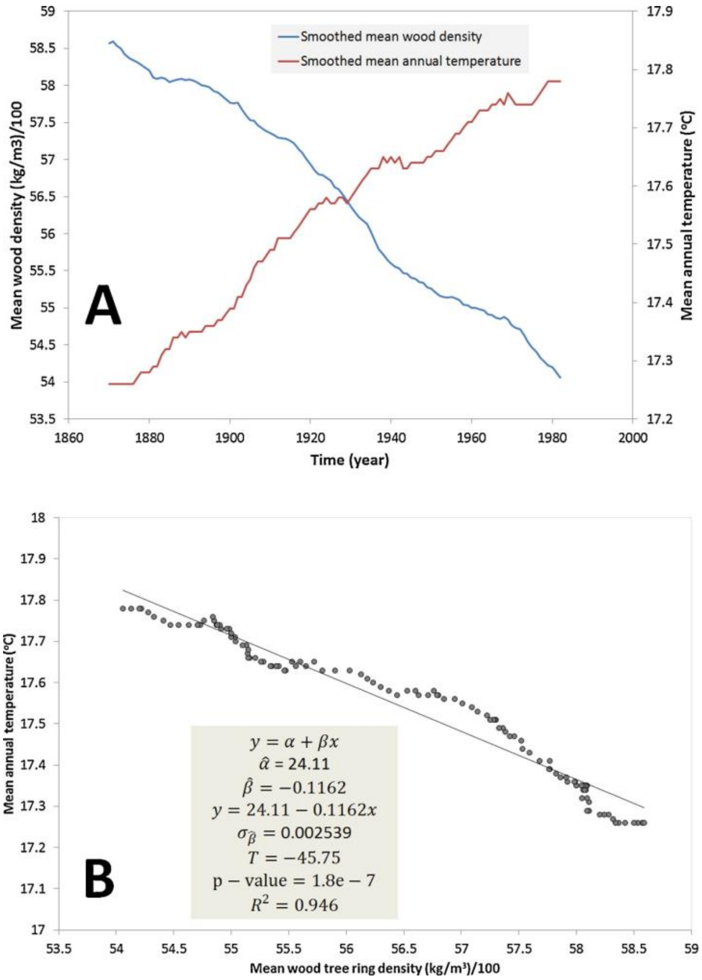

Figure 6.7. A: Smoothed time series for the maximum achieved correlation coefficient in Figure 6.9. B: linear regression between the smoothed tree-ring and climate time series in A. The figure shows the estimates of the regression parameters: intercept (∞) and slope (β), the standard deviation of the estimate of slope, the t-statistic, the p-value, and the coefficient of determination R^2. The low p-value (< 0.01) indicates the statistical significance of the linear relationship.

Some significant additional information was obtained by applying moving window running means to the complete 1728–1982 early wood time series (Figure 6.8A). The running means in Figure 6.8A show that the early wood tree-ring width decreased from 1728 to 1920, reached a minimum and stabilised over the period 1920 to 1950, and then began to increase. Applying the linear relationship in Figure 6.6B to the smoothed time series in Figure 6.8A, gives the time series shown in Figure 6.9A. It should be noted that in Figure 6.9A, the inferred past rainfall is not yearly rainfall but the smoothed yearly rainfall within a semi-bandwidth of 38 years. In other words, we are making inferences about the rainfall trend rather than the individual yearly rainfall, which is probably impossible to estimate with any acceptable measure of accuracy.

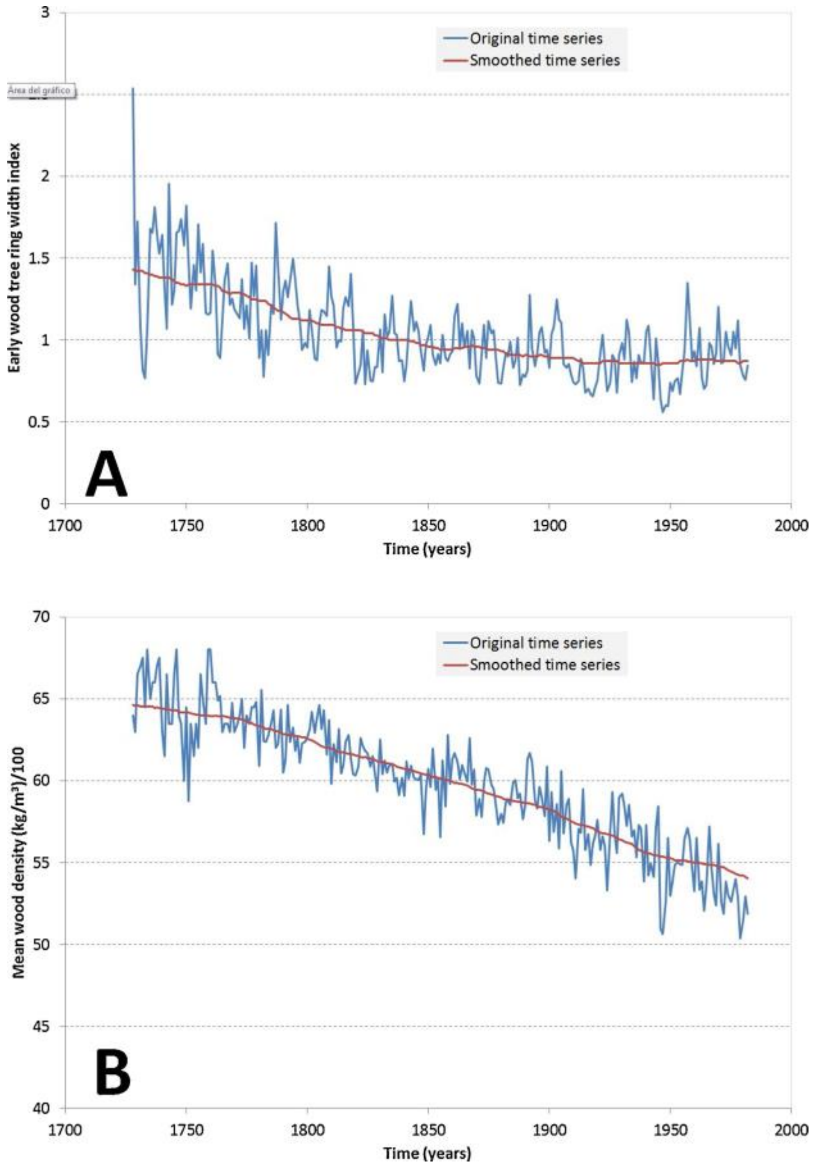

Figure 6.8. A: Original early wood tree-ring width index and moving average trend for the period 1728–1982. The semi-bandwidth (44 years) that maximises the correlation with yearly rainfall has been used. B: Original mean tree-ring wood density and moving average trend for the period 1728–1982. The semi-bandwidth (48 years) that maximises the correlation with mean annual temperature has been used.

The same for temperature; additional significant information is obtained by applying moving window running means to the complete 1728–1982 mean wood density time series (Figure 6.8B). There is a systematic decrease in mean wood tree ring density from 1728 to 1982. Applying the linear relationship in Figure 6.7B to the smoothed time series in Figure 6.8B generates the time series shown in Figure 6.9B. It should be noted again that in Figure 6.9B, the past temperature inference is not mean annual temperature but the smoothed mean annual temperature with a semiband width of 44 years. In other words, we are making inferences about the trend of the mean annual temperature. It is clear from this analysis that the temperature has been increasing with two changes of slope and faster increases in 1772 and in 1900. It should be noted that the results reported here refer to a particular location. The results will be different for averages over larger areas with a smoothing of local temporal variations in temperature. Thus, the particular values given here are not comparable with those reported by other authors for the whole of the northern hemisphere (Mann and Bradley, 1999), although the general trends are compatible.

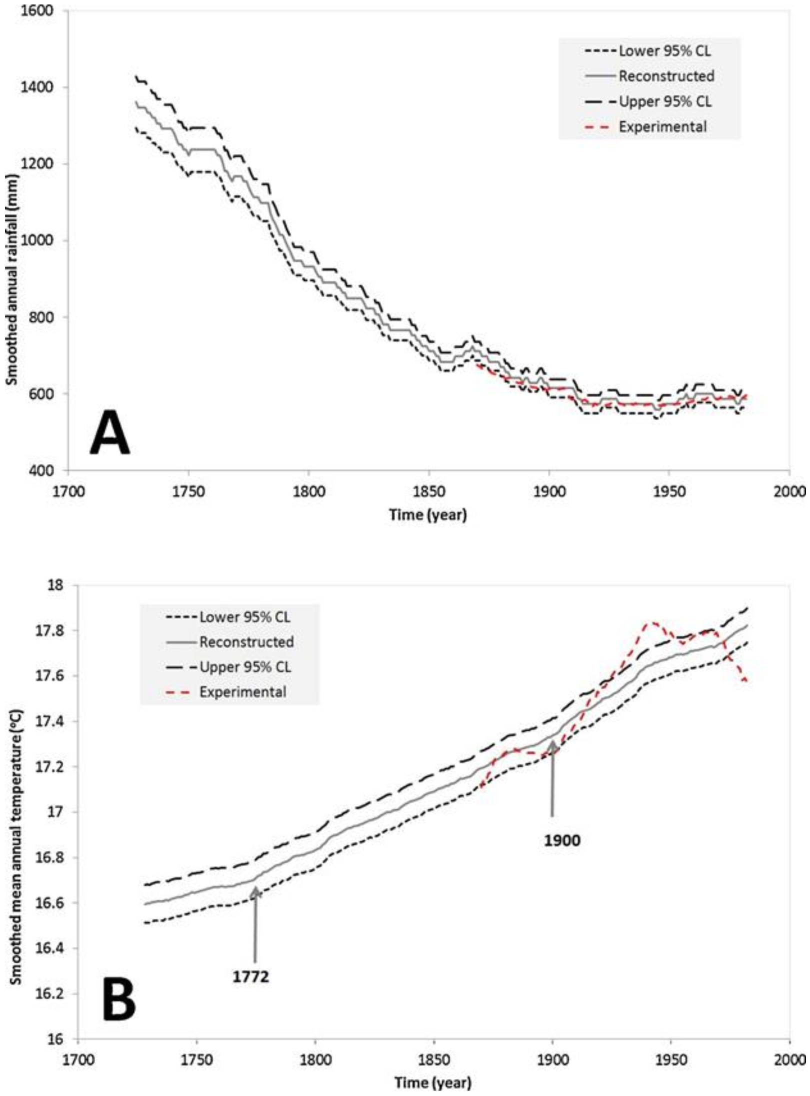

Figure 6.9. A: Linear reconstruction of the trend of yearly rainfall for the period 1728–1982 using standard linear regression. The dashed line represents the experimental values for the calibration period. B: Linear reconstruction of the trend of mean annual temperature for the period 1728–1982 using standard linear regression. The dashed line represents the experimental values for the calibration period.

These observations for the annual rainfall and the mean annual temperature at San Fernando station can be extrapolated to the study area in Sierra de las Nieves. This is because there is a good linear correlation between values recorded at the San Fernando stations and those recorded at stations in the study area (Sierra de las Nieves). This relationship was obtained by calculating mean time series of rainfall and temperature for the stations around the Sierra de las Nieves but which have data for the last decades only. The major differences between the San Fernando and the Sierra de las Nieves time series are that mean annual rainfall in the study area is 513 mm higher than at San Fernando and the variance is almost four times larger (Figure 6.10A); the mean temperature is 7 °C lower in the study area than at San Fernando station but the variance in temperature is almost one-third less than the temperature at San Fernando station (Figure 6.11A). Particular time series of annual rainfall and temperature can readily be obtained from a stochastic weather generator using the means and variances. However, this is outside the scope of the present work. Figure 6.10B and Figure 6.11B show the statistically significant (very low p-value) relationships between the rainfall and temperature at San Fernando station and Sierra de las Nieves with differences due to the difference in altitude.

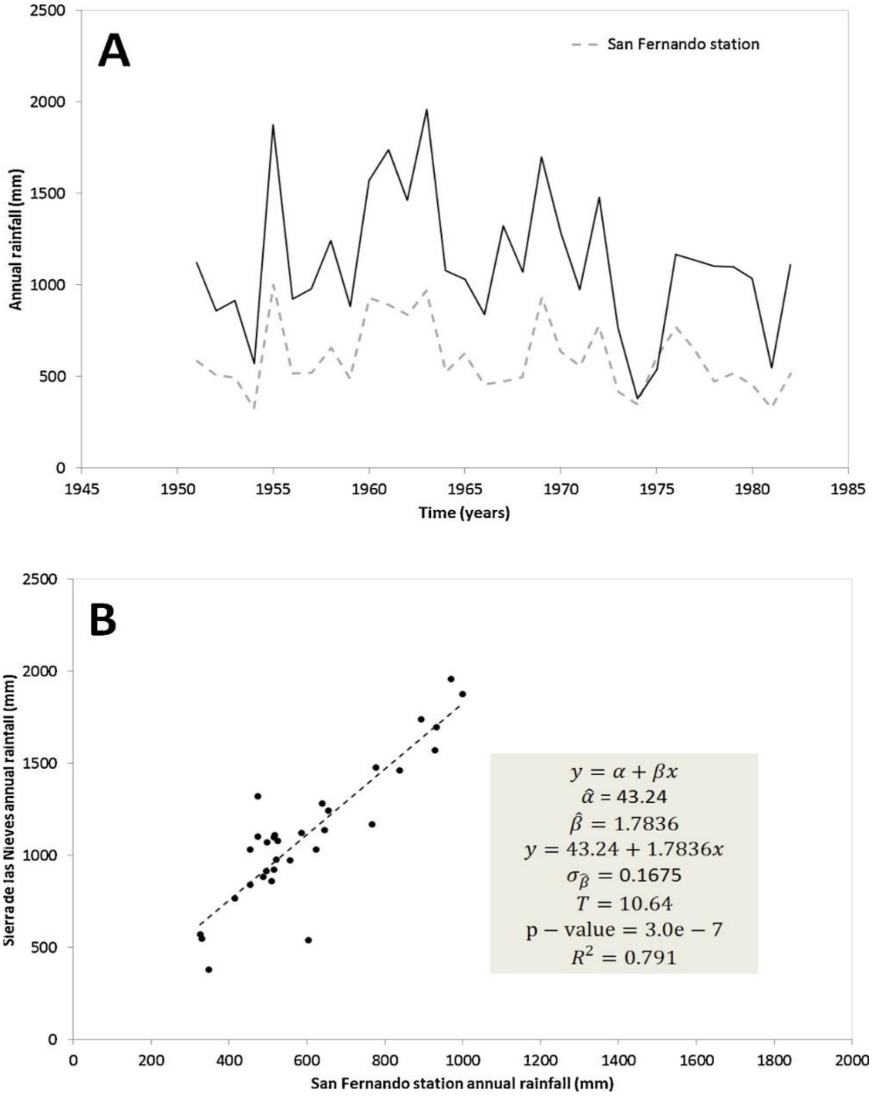

Figure 6.10. A. Reconstruction of rainfall at Sierra de las Nieves from the correlation between nearby meteorological stations and San Fernando station. B: linear regression used in the reconstruction. The figure shows the estimates of the regression parameters: intercept (∞) and slope (β), the standard deviation of the estimate of slope, the t-statistic, the p-value, and the coefficient of determination R^2. The low p-value (<0.01) indicates the statistical significance of the linear relationship.

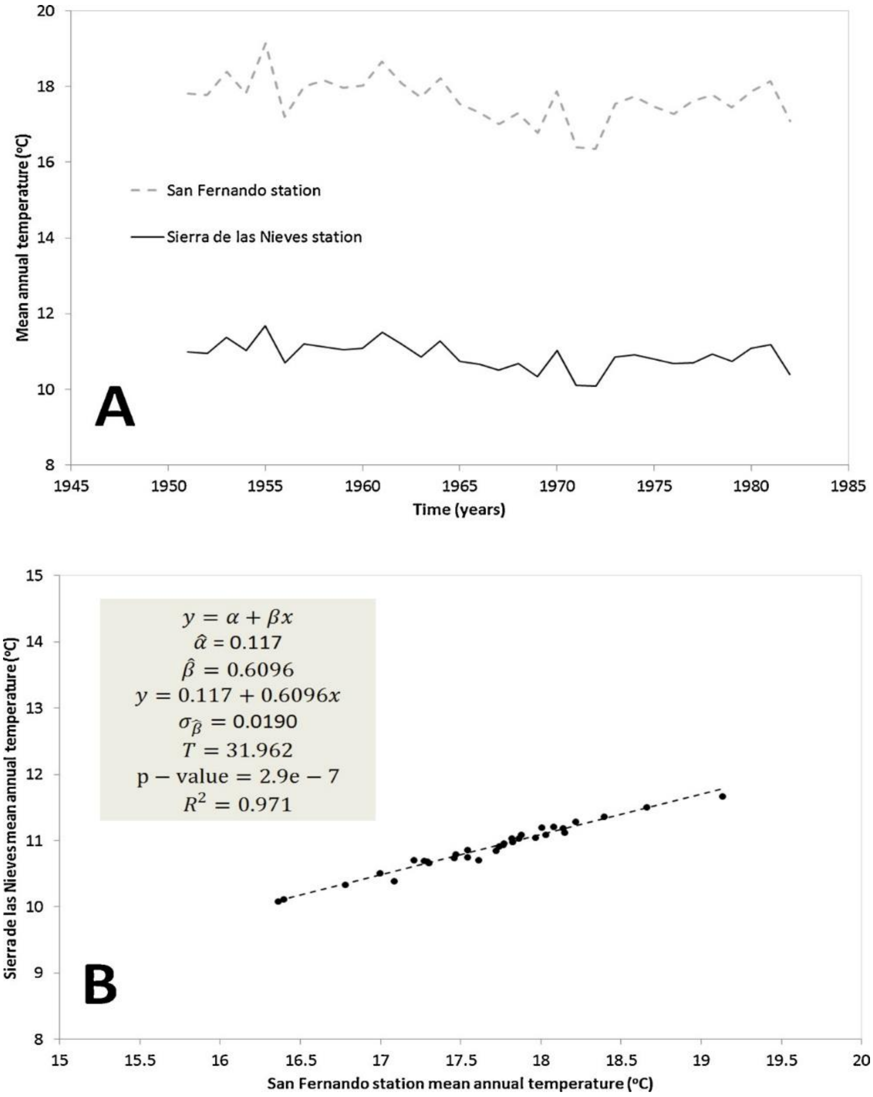

Figure 6.11. A. Reconstruction of temperature at Sierra de las Nieves from the correlation between nearby meteorological stations and San Fernando station. B: linear regression used in the reconstruction. The figure shows the estimates of the regression parameters: intercept (∞) and slope (β), the standard deviation of the estimate of slope, the t-statistic, the p-value, and the coefficient of determination R^2. The low p-value (< 0.01) indicates the statistical significance of the linear relationship.

6.4 Discussion

For the purpose of illustrating the methodology presented here we have used only the early wood tree-ring width, mean tree-ring wood density, annual rainfall and mean annual temperature. However, in practice, all combinations of tree and climate variables can be included depending on the purpose of the study. For example, if winter rainfall and mean spring temperature are variables of interest, they could be derived from appropriate correlated tree-ring variables. In the work presented here we have used early wood tree-ring width to infer past trends in rainfall and mean tree-ring wood density to infer past trends in mean temperature. Rainfall and temperature influence tree-ring variables but not in the same way and they are not the only climate variables that influence tree-ring variables. The results for the mean reconstructed averages of yearly rainfall and mean yearly temperature show that rainfall has been decreasing since 1728 (the lower time limit imposed by the tree-ring data) to a minimum around 1930 and since then it has been increasing to the levels of the 19th century. There has been an increase in temperature since 1728 with a greater rate of increase in 1772 and around 1900.

Perhaps the most difficult part of a paleoclimatic reconstruction is the validation of the results. With respect to temperature, the trend of our reconstruction is consistent with the results of Mann and Bradley (1999) as represented in Figure 6.12A - keeping in mind that we are performing the reconstruction at a particular location while Mann and Bradley (1999) give trends for the entire northern hemisphere. With respect to rainfall, Rodrigo (2007) reconstructed flooding at Seville from documental records. Figure 6.12B shows a moving average for the period covered in Rodrigo (2007) from which it can be seen that the results are consistent with higher rainfall in the past and a decrease until the beginning of the 20th century.

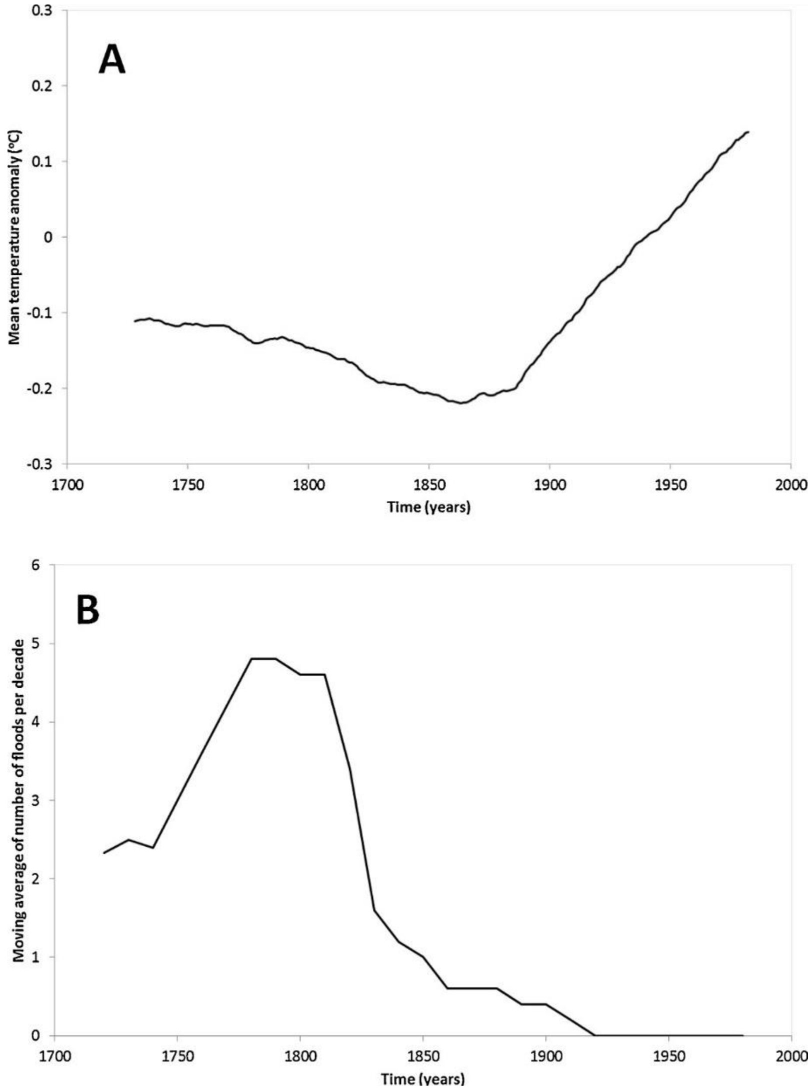

Figure 6.12. A. Trend of northern hemisphere temperature modified from Mann and Bradley (1999). B. Trend of flooding in the Guadalquivir River in Seville modified from Rodrigo (2007a).

6.5 Conclusions

The work presented here addresses the problem of climate modelling and prediction when there are very few instrumental measurements of climate variables and it is thus not possible to reconstruct exact time series. A statistical approach is proposed for cases in which there is a complex relationship between climate variability and tree-ring features for a particular period and a specific location. The procedure has been demonstrated by application to the Sierra de las Nieves karst aquifer, a high-relief Mediterranean karst area in which there are complex climate relationships, but instrumental data are scarce. This problem has been addressed by statistical analysis of tree-ring data from *Abies Pinsapo*. These data were used to evaluate current climate variability (trends) of rainfall and temperature and the manner in which the climate has evolved from the past. The correlation between instrumental and proxy variables is complex and only revealed when a large averaging is applied to the available data to extract correlations and trends from those data. In the proposed methodology, time series are smoothed by a moving window running mean for which the band-widths are chosen so as to maximise the absolute value of the correlation coefficient between the resulting tree-ring, and climate, time series. Although better results could be obtained with longer time series, any inference about past climate is a useful contribution to the assessment of current climate variability.

Acknowledgements

Funding for this research was provided by Projects CGL2015-71510-R and CGL2015-66835-P (Secretaría de Estado de I+D+I, Spain), Research Group RNM-178 (Junta de Andalucía), and Scientific Excellence Unit UCE-2016-05 (Universidad de Granada).

7 Chapter VII. A case study using speleothems data: Global climate changes through the Holocene (In prep. *The Holocene*)

7.1 Introduction

Speleothems are natural mineral deposits created in caves within the unsaturated zone of carbonate rocks. They are excellent continental paleoclimate archives, as they can potentially register the climate signal at a remarkably high resolution and over a wide range of time scales: from sub-decadal to annual, and up to orbital variability (hundreds of thousands of years). They sometimes show banded growth (annual and/or seasonal) that can be dated (i.e., U-Th dating) as per their measurable isotopic signal (Walker at al., 2018). Such features make speleothems sound representatives of the internal cave environment, the external hydroclimate conditions, the supra-climate, and the karst system processes. Stalagmites —growing upward— may be preferable for the study of carbonate formations, their interpretation being less complex (Fairchild and Baker, 2012). Of special interest in the application of speleothems in paleoclimate studies is the analysis of $\delta^{18}O$ records as paleoclimate proxies.

The $\delta^{18}O$ records from speleothems are the result of multiple factors and processes operating in the ocean, atmosphere, soil zone, epikarst and cave system, and therefore their usage for reconstructing past temperatures and precipitation become complex (Lachniet, 2009). For instance, speleothems do not directly record precipitation as opposed to ice cores, because both referred chemical species undergo fractionation by cave-internal processes (Bühler et al., 2022).

A recent global isotope-enabled simulation using hundreds of speleothems from 193 caves (Comas-Bru et al., 2019) indicated that the observed disparities and/or uncertainties between speleothem records and hydroclimate variability may be attributed to site-specific controls. However, considering that past climate variability at orbital timescales has been recognised in speleothems, the usage of time series from stalagmites at longer timescales is recommended for validating paleoclimate model simulations (i.e., over decadal), reducing the influence of local processes which act as low-pass filters of the paleoclimate signal in the speleothem formation (Clemens et al., 2018). Although paleoclimate reconstructions in certain regions, such as in China, are yet to be fully achieved (Zhang et al., 2019), the discrepancies found between speleothem $\delta^{18}O$ records and reconstructed past precipitation tend to increase at centennial and shorter timescales. There is some consensus on the impact that controlling factors behind regional precipitation and other cave related variables have on the speleothem δ^{18}O records; yet recent work suggests that when cave records do not reflect the volume of rainfall amount, they might instead point to variations in large-scale circulation patterns and moisture sources (Yang et al., 2016; Hu et al., 2019; Lachniet, 2020).

Numerous studies have attempted to reconstruct/interpret past precipitation and climate based on speleothems, at local to regional scales, and seasonal to millennial scales (e.g., Lachniet, 2020). The use of paleoproxies (δ^{18}O, δ^{13}C) from speleothems is on the rise in global studies and model simulations. However, most studies analyse speleothems pertaining to local/regional areas or short stratigraphic intervals. Against this background, the present research offers a meta-analysis of δ^{18}O time series from five continents through the entire Holocene, to approach their geographical and stratigraphical similitudes and differences associated with climatic variations and other forcing processes. This case study presents a new means of looking at oxygen time series from speleothems for studying the Holocene paleoclimate evolution.

7.2 Materials and methods

This work is based on a collection of δ^{18}O time-series from speleothems previously published. In an attempt to reveal the climate signal recorded in speleothems at geological time scales, a process for collecting significant paleoclimate studies' datasets was conducted (Table 7.1). The aim here is neither to validate or replicate the original work, but rather combine, use, and interpret the data as time series capturing different versions of the global paleoclimate by looking at their similarities and differences.

7.2.1 SISAL database

The SISAL (Speleothem Isotopes Synthesis and Analysis) international working group (http://dx.doi.org/10.17864/1947.256) has compiled, over the years, a database of speleothems and associated data from previous research studies (Atsawawaranunt et al., 2018a). One main purpose of SISAL was to validate present and future isotope-enabled models (Comas-Bru et al., 2019). In the present research, version 2.0 of SISAL was used (Comas-Bru et al., 2020). This version contains time-series from more than 290 caves across the globe, including associated metadata. The speleothems from SISAL were screened first by taking into account the main criteria of the δ^{18}O time series to cover the Holocene period (0–11,700 years BP), or at least a considerable portion of it (~10 kyr). For example, the speleothems "048" (South-Africa) and "117" (Japan), reach back as far as 10,110 and 10,006 years BP respectively (Table 7.1), but they have been selected as the only alternative in the database for those regions. This has also further limited the secondary requirement of datasets evenly distributed across continents, by also considering that the karst is not equally distributed either. In view of such criteria, 24 $\delta^{18}O$ datasets were selected. The location of the 24 selected datasets is shown in Figure 7.1, including their SISAL code.

In regard to the chronology of the selected time series, this research relies on the dating and calibration of the original (published) datasets, which was conducted in most cases by using the Vienna-PDB standard ("Material and $\delta^{18}O$ std" column in Table 7.1.).

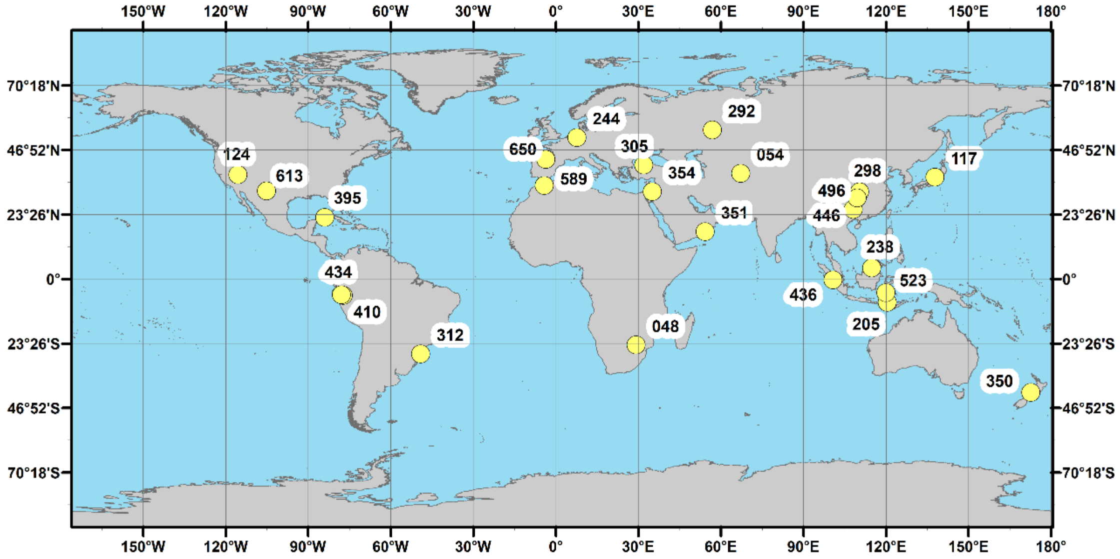

Figure 7.1. Global location of the 24 studied speleothems. Numbers refer to SISAL* entity code.

Table 7.1. General features of the 24 selected speleothems for this study. * SISAL = Speleothem Isotope Synthesis and AnaLysis; ** Data < 11,700 years BP; *** BP = 1950 AD

SISAL* entity code	Entity name and type	Site name (cave)	Lat. (°N)	Long. (°E)	Data pairs**	From (years BP***)	To (years BP***)	Sampling avg.	Material and δ¹⁸O std	Citation
48	T8 (stalagmite)	Cold Air	-24.00	29.18	997	-48.00	10,110.00	10.20	Aragonite (PDB)	Holmgren et al. (2003)
54	TON-2 (stalagmite)	Tonnel'naya	38.40	67.23	334	-58.12	11,670.46	35.22	Calcite (Vienna-PDB)	Cheng et al. (2016a)
117	FG01 (stalagmite)	Fukugaguchi	36.99	137.80	963	-52.80	10,006.43	10.46	Calcite (Vienna-PDB)	Sone et al. (2013)
124	LC-1 (stalagmite)	Leviathan	37.89	-115.58	236	-60.00	11,690.00	50.00	Calcite (Vienna-PDB)	Lachniet et al. (2014)
205	LR06-B3_2009 (stalagmite)	Liang Luar	-8.53	120.43	159	-39.30	10,699.90	67.97	Calcite (Vienna-PDB)	Griffiths et al. (2009)
238	BA03_decadal (stalagmite)	Bukit Assam	4.03	114.80	812	-44.66	11,678.16	14.46	Calcite (Vienna-PDB)	Chen et al. (2016)
244	BuStack (composite)	Bunker	51.37	7.66	2,677	-57.40	10,723.50	4.03	Calcite (Vienna-PDB)	Fohlmeister et al. (2012)
292	KC-Composite (composite)	Kinderlinskaya	54.15	56.85	932	-50.00	11,674.00	12.59	Calcite (Vienna-PDB)	Baker et al. (2017)
298	SB-43 (stalagmite)	Sanbao	31.67	110.43	432	70.27	11,686.69	26.95	Calcite (Vienna-PDB)	Dong et al. (2010
305	SO-1 (stalagmite)	Sofular	41.42	31.93	2,285	-56.00	11,696.00	5.15	Calcite (Vienna-PDB)	Fleitmann et al. (2009)
312	BT-2 (stalagmite)	Botuverá	-27.22	-49.16	103	-55.00	11,634.36	114.60	Calcite (Vienna-PDB)	Cruz et al. (2005)
350	MD3 (flowstone)	Nettlebed	-41.23	172.68	77	114.84	11,597.26	151.09	Calcite (PDB)	Hellstrom et al. (1998)
351	Q5 (stalagmite)	Qunf	17.17	54.30	1,412	308.00	10,558.00	7.26	Calcite (Vienna-PDB)	Fleitmann et al. (2007)
354	Soreq-composite (composite)	Soreq	31.76	35.02	782	0.00	11,680.00	14.96	Calcite (Vienna-PDB)	Grant et al. (2012)
395	CP (stalagmite)	Dos Anas	22.38	-83.97	973	61.00	11,699.80	11.97	Aragonite (Vienna-PDB)	Fensterer et al. (2013)
410	ELC_composite (composite)	El Condor	-5.93	-77.30	163	290.00	11,540.00	69.44	Calcite (Vienna-PDB)	Cheng et al. (2013)
434	Sha-composite (composite)	Shatuca	-5.70	-77.90	1,770	-34.47	10,601.86	6.01	Aragonite (Vienna-PDB)	Bustamante et al. (2016)
436	TA12-2 (stalagmite)	Tangga	-0.36	100.76	745	159.00	11,690.00	15.50	Aragonite (Vienna-PDB)	Wurtzel et al. (2018)
446	D4_2005 (stalagmite)	Dongge	25.28	108.08	743	-16.50	11,689.19	15.78	Calcite (Vienna-PDB)	Dykoski et al. (2005)
496	LH-2 (stalagmite)	Lianhua	29.48	109.53	742	51.00	11,639.00	15.64	Aragonite (Vienna-PDB)	Zhang et al. (2013)
523	GB09-03 (stalagmite)	Gempa Bumi	-5.00	120.00	226	30.00	11,680.00	51.78	Calcite (Vienna-PDB)	Krause et al. (2019)
589	Cha1 (stalagmite)	Chaara	33.96	-4.25	1,573	-50.94	11,621.83	7.43	Aragonite (Vienna-PDB)	Ait-Brahim et al. (2019)
613	PP1 (stalagmite)	Pink Panther	32.00	-105.20	660	-15.00	11,687.00	17.76	Calcite (Vienna-PDB)	Asmerom et al. (2007)
650	GAR-01_drill (stalagmite)	La Garma	43.43	-3.67	320	-26.40	11,671.40	36.67	Calcite (Vienna-PDB)	Baldini et al. (2015)

7.2.2 Methodology for δ^{18}O trend evaluation and comparison

To estimate the trend of each proxy time-series and establish the evolution of speleothems throughout the Holocene from a climatic point of view, a three-step methodology was developed (Figure 7.2). It was aimed for calculating the maximum and/or minimum distance between time series by means of a scoring system. The overall correlation between speleothem time series is variable (Figure 7.2d and Table 7.2) which allows the implementation of the referred three-step system. The process begins by generating a moving-average for each speleothem time-series with the purpose of smoothing the general trend (semi-bandwidth of 1,000 years; t-1,000, t+1,000). Each resulting time series is divided into 1,000-year intervals, or ten equal periods for the Holocene (Figure 7.2a). To homogenize the start of the 24 time-series at the beginning of the Holocene, values between 10,000 years BP and 11,700 years BP were discarded, as some speleothems fall short in age for that period. Each interval is then compared with the next interval of the same time-series (i.e., 0-1,000 years vs. 1,000-2,000 years; as "k" and "l" in Figure 7.2a), making a total of nine comparisons per speleothem (Figure 7.2b). The linear trend is evaluated and defined as increasing (+1), decreasing (-1) or stationary (0).

A zero (0) is assigned if the two consecutive intervals (k, l) cross each other in the analysed time series (the minimum of the first time series being larger than the maximum of the second time series), hence resulting in a stationary comparison as the two means are indistinguishable. If the minimum is smaller than the maximum, a minus one (-1) is assigned if the average of the preceding sub-period (k) is likewise higher than the average of the following sub-period (l). A positive one (1) is assigned if the average of the following sub-period (l) is higher than the average of the preceding sub-period (k).

In a third step (Figure 7.2c), the similarity of the trend of both time-series is compared, interval to interval, according to a scoring look-up table that assigns a high score or three to a perfect coincidence (-1,-1), (0,0) or (1,1); a medium score or two for a non-perfect coincidence (-1,0), (0,-1), (1,0) or (0,1); and a low score or one for opposite trends (-1,1) or (1,-1). The final score (=13) corresponds to two time-series with highly dissimilar trends as made evident, in this case, in the plot of the time-series. This methodology has reasonably good agreement with the Pearson's r analysis, which has been used to validate this novel scoring system, by calculating the correlation coefficients over the entire length of the time-series for all speleothems (Figure 7.2d).

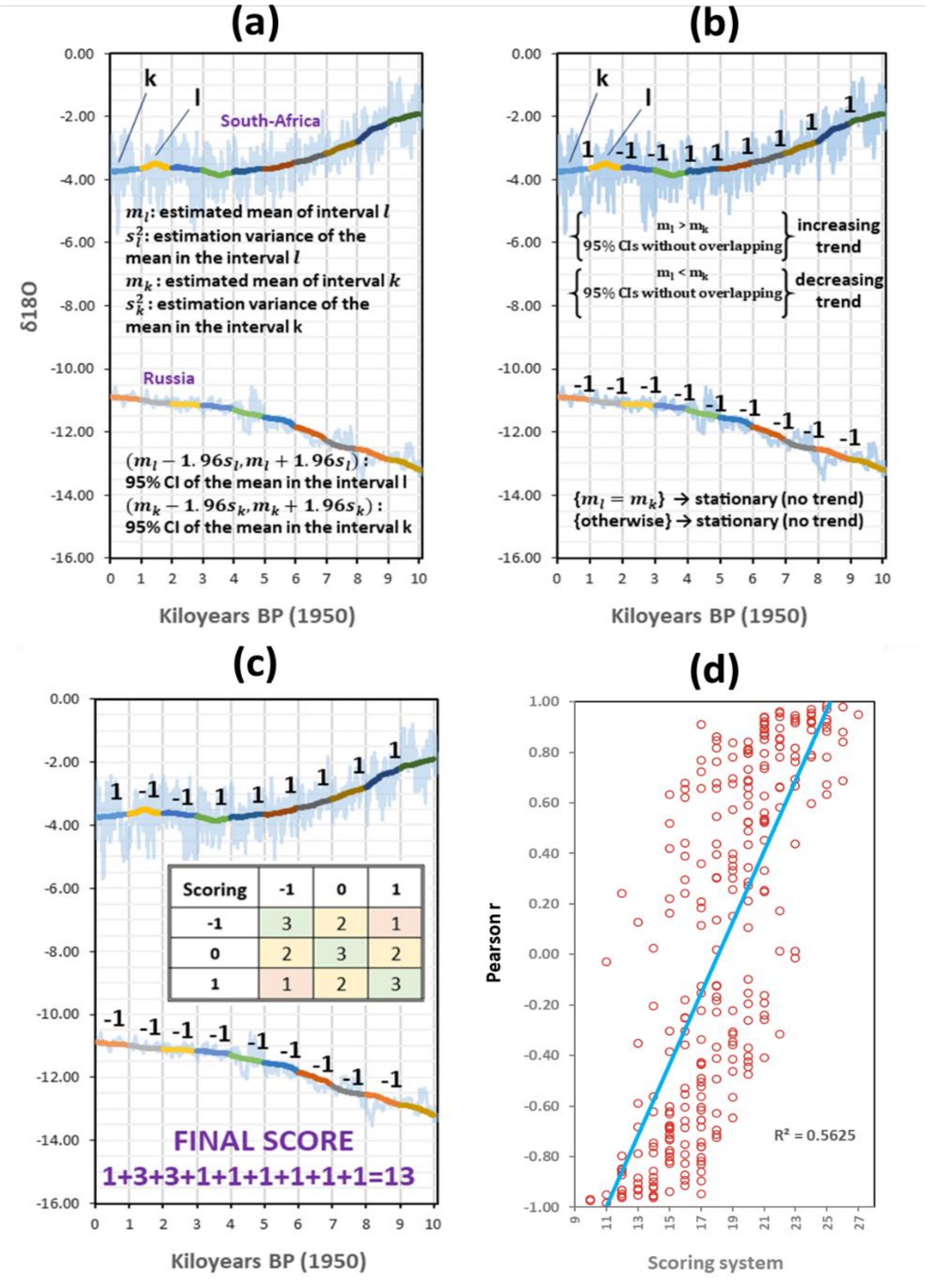

Scoring	-1	0	1
-1	3	2	1
0	2	3	2
1	1	2	3

Figure 7.2. Methodology for δ^{18}O trend evaluation and comparison: (a), (b) and (c). The time-series from speleothems "048" (South-Africa) and "292" (Russia) are divided into intervals of 1,000 years each (a). For each pair of consecutive intervals, the linear trend is evaluated and defined as increasing (+1), decreasing (-1) or stationary (0); the stationary trend (no trend) is defined when the slope of the fitted line is not statistically different from zero (b). The similarity of the trend of both time-series is compared interval to interval according to a scoring look-up table that assigns a high score of 3 to a perfect coincidence (-1,-1), (0,0) or (1,1), a medium score of 2 for not a perfect coincidence (-1,0), (0,-1), (1,0) and (0,1), and a low score of 1 for opposite trends (-1,1) and (1,-1). The final score (13) corresponds to two time-series with highly dissimilar trends as is evident, in this case, in the graph of the time-series (c). Pairs of data (Pearson r coefficients vs. scoring system) for each pair of oxygen time series being compared (24 speleothems) (d).

Table 7.2. Trend analysis results showing the scores between each pair of analysed time series.

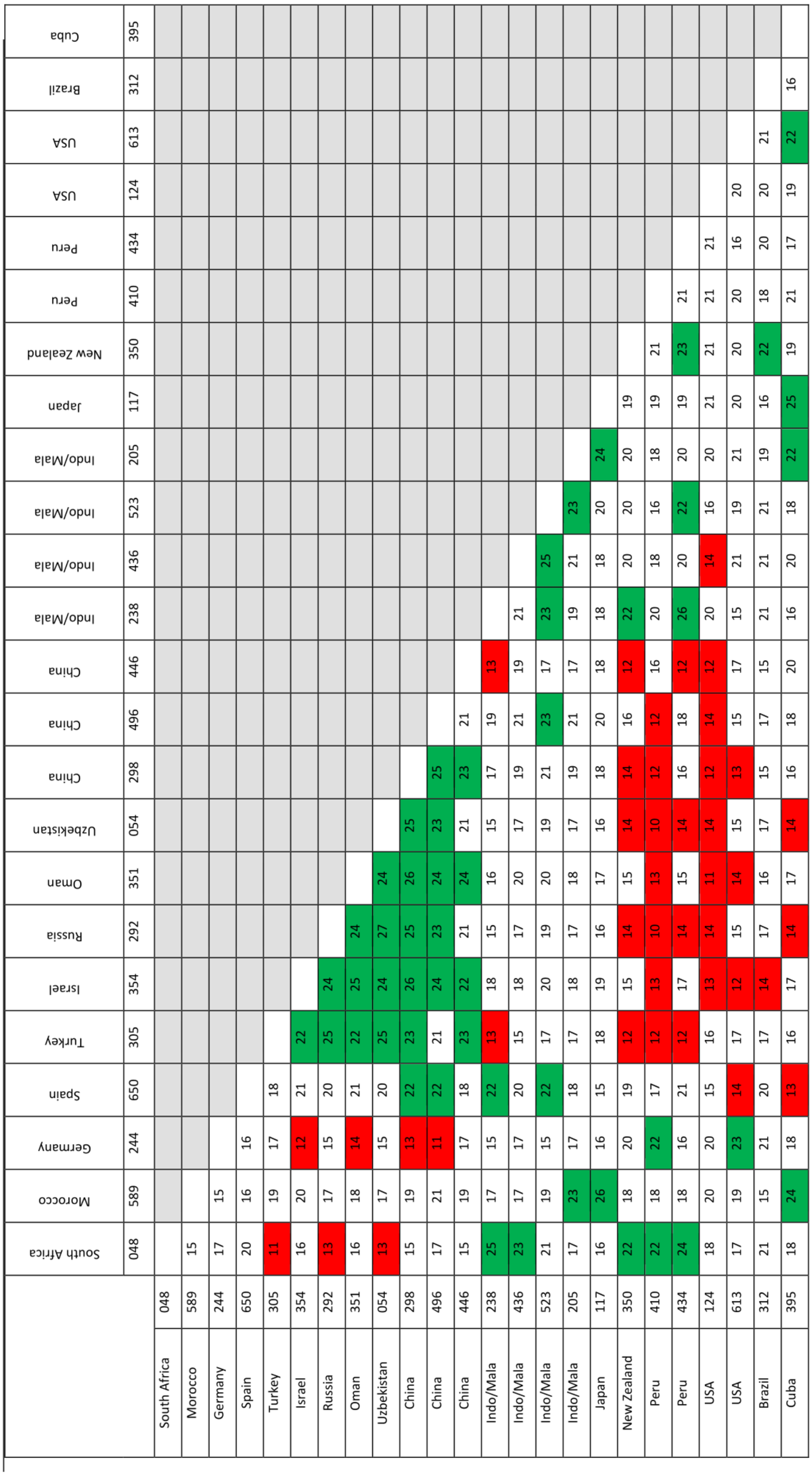

		South Africa	Morocco	Germany	Spain	Turkey	Israel	Russia	Oman	Uzbekistan	China	China	China	Indo/Mala	Indo/Mala	Indo/Mala	Indo/Mala	Japan	New Zealand	Peru	Peru	USA	USA	Brazil	Cuba
		048	589	244	650	305	354	292	351	054	298	496	446	238	436	523	205	117	350	410	434	124	613	312	395
South Africa	048																								
Morocco	589	15																							
Germany	244	17	15																						
Spain	650	20	16	16																					
Turkey	305	11	19	17	18																				
Israel	354	16	20	12	21	22																			
Russia	292	13	17	15	20	25	24																		
Oman	351	16	18	14	21	22	25	24																	
Uzbekistan	054	13	17	15	20	25	24	27	24																
China	298	15	19	13	22	23	26	25	26	25															
China	496	17	21	11	22	21	24	23	24	23	25														
China	446	15	19	17	18	23	22	21	24	21	23	21													
Indo/Mala	238	25	17	15	22	13	18	15	16	15	17	19	13												
Indo/Mala	436	23	17	17	20	15	18	17	20	17	19	21	19	21											
Indo/Mala	523	21	19	15	22	17	20	19	20	19	21	23	17	23	25										
Indo/Mala	205	17	23	17	18	17	18	17	18	17	19	21	17	19	21	23									
Japan	117	16	26	16	15	18	19	16	17	16	18	20	18	18	18	20	24								
New Zealand	350	22	18	20	19	12	15	14	15	14	14	16	12	22	20	20	20	19							
Peru	410	22	18	22	17	12	13	10	13	10	12	12	16	20	18	16	18	19	21						
Peru	434	24	18	16	21	12	17	14	15	14	16	18	12	26	20	22	20	19	23	21					
USA	124	18	20	20	15	16	13	14	11	14	12	14	12	20	14	16	20	21	21	21	21				
USA	613	17	19	23	14	17	12	15	14	15	13	15	17	15	21	19	21	20	20	20	16	20			
Brazil	312	21	15	21	20	17	14	17	16	17	15	17	15	21	21	21	19	16	22	18	20	20	21		
Cuba	395	18	24	18	13	16	17	14	17	14	16	18	20	16	20	18	22	25	19	21	17	19	22	16	

7.2.3 Orbital forcing and insolation calculations

The insolation over the last 13-ka (2,000 years AD – 11,000 years BC) was estimated for the surface location of the 24 selected speleothems, hence not only covering the Holocene but overlapping the Upper Pleistocene for better boundary conditions. The published software model Earth Orbit v2.1 (Kostadinov and Gilb, 2014), capable of implementing the Laskar orbital solution (Laskar et al., 2004), was chosen in view of its simplicity and well-validated results. The Laskar orbital solution incorporates orbital eccentricity, obliquity, and precession cycles, all of which are needed at geological timescales. The length of the so-called Milankovitch cycles (Milankovitch, 1941) in the geological record is widely recognized (i.e., Rodríguez-Tovar, 2014; Maslin, 2016): Precession has a length of 19 and 24 kyr (extremes at 14 and 28 kyr), obliquity about 41 kyr (extremes at 28 and 54 kyr) and eccentricity of 100 and 400 kyr.

The Earth Orbit model was run once per speleothem. The most relevant input parameter is the value of the latitude of the cave for which the insolation time-series is to be obtained. This is somewhat of a generalisation, because the catchment area of the registered climate signal in the cave could be representative of a much broader geographic area, and also local and/or regional terrain features might obscure the insolation input. The rest of the input parameters of the model were kept constant for all speleothems: start date was 2000 years AD (year 0 in the software), end date 13,000 years BP (or 11,000 years BC), fix calendar start date at March-20th (vernal equinox), and total solar irradiance at 1 AU (1,366 W/m^2). For each input latitude, the model calculates the associated daily insolation over a year (365 days), starting on March 20th (Vernal Equinox), and for 13 specific dates: 2000 AD, 1000 AD, 0 AD, 1000 BC, 2000 BC, 3000 BC, 4000 BC, 5000 BC, 6000 BC, 7000 BC, 8000 BC, 9000 BC and 10,000 BC.

Using these data points, it was further interpolated the corresponding insolation curves for every month and for every analysed cave location. This process is illustrated for the dataset “523” located in SE Asia (Indonesia; latitude = -5 degrees); the insolation curves broken down by calendar month are represented for this location and the Holocene period using the 14 x 12 insolation data points (Figure 7.3a), followed by the interpolated curves and the $\delta^{18}O$ time-series (Figure 7.3b) for which the degree of correlation is to be obtained in a later step.

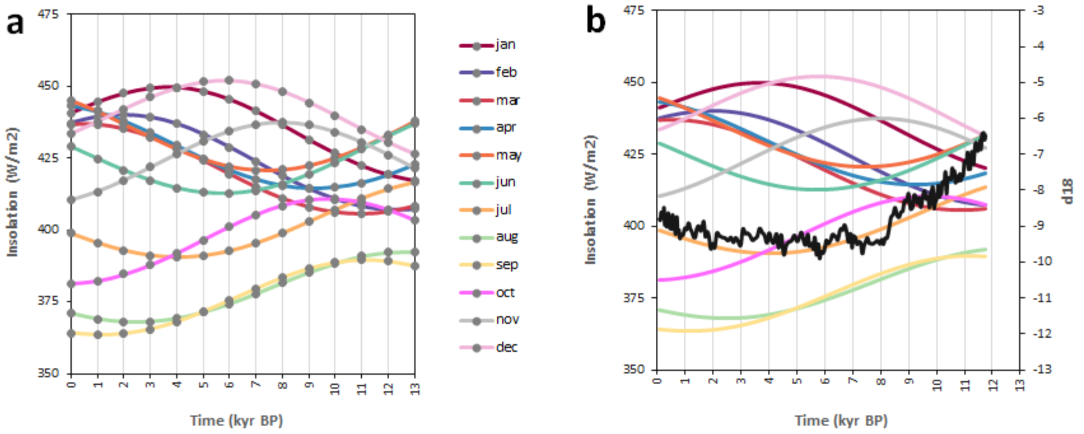

Figure 7.3. Methodology for estimating the theoretical monthly insolation curves: (a) and (b). The monthly insolation curves for the location of speleothem "523" in Indonesia (latitude of -5 degrees) were estimated for the last 13 ka (a). The comparison between the estimated monthly insolation curves and the corresponding $\delta^{18}O$ time-series for speleothem "523" best correlates to the insolation curve of July (b).

7.2.4 Spectral analysis technique

The Lomb-Scargle periodogram (Lomb, 1976; Scargle, 1982) was the underlying spectral analysis technique used, having a proven record of bespoken geological case studies (Jiménez-Moreno et al., 2007; Rodríguez-Tovar et al., 2010; Rodrigo-Gámiz et al., 2014). To assess the significance of the registered spectral peaks, a Monte Carlo permutation test was used, as the neighbouring frequencies are known to be highly correlated (Pardo-Igúzquiza and Rodríguez-Tovar, 2000, 2011, 2012). Thus, the significant frequencies obtained can be considered as primary and not spurious peaks derived from the applied methodology. One computer program provides an estimate of the Lomb–Scargle periodogram plus an estimate of the phase spectrum: SLOMBS (Pardo-Igúzquiza and Rodríguez-Tovar, 2012). This software also evaluates the statistical significance of the peaks determined by the Monte Carlo permutation test and offers the option of adjusting statistical significance by smoothing the periodogram. The second software to be used is CSLOMBS (Pardo-Igúzquiza and Rodríguez-Tovar, 2012), that estimates the smoothed Lomb–Scargle cross-periodogram, the squared coherence spectrum and the phase spectrum.

The implemented spectral analysis made use of the residuals obtained by subtracting the corresponding moving-average from the original $\delta^{18}O$ time-series (semi-bandwidth of 1,000 years) that had been previously calculated on each speleothem. Then, as a second step, the resulting time-series were resampled into a common sampling time interval of 20 years to speed up the spectral calculations and to facilitate any stacking process. In Figure 7.4 the original time series and the moving-average time-series for each speleothem are displayed.

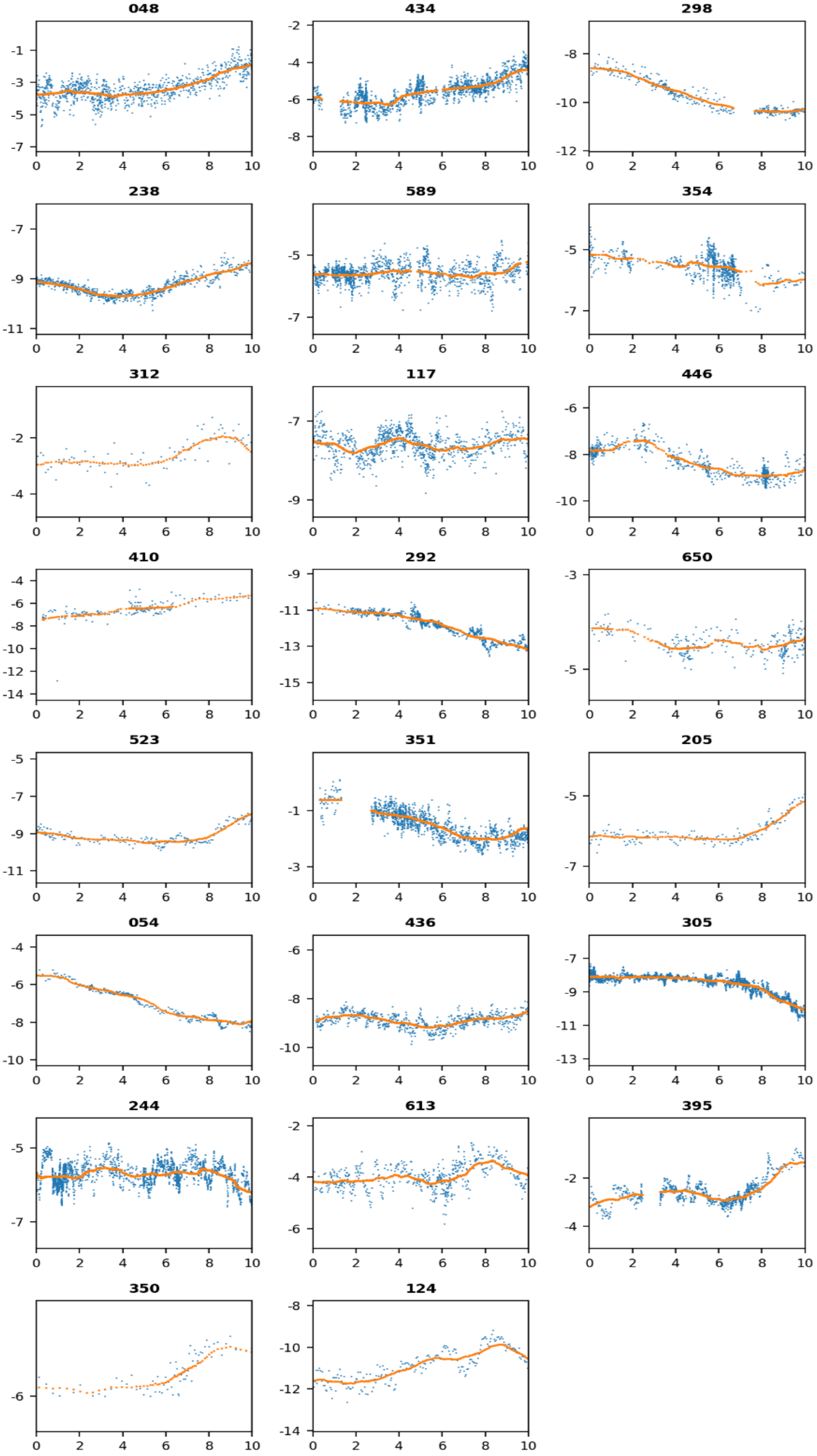

Figure 7.4. Original δ^{18}O time series for all 24 selected speleothems and their estimated moving-average time series using a semi-bandwidth of 1,000 years for the last 10 ka.

7.3 Results

7.3.1 δ^{18}O trend results

The δ^{18}O trend results (Present as 1950 AD – c. 10 ka) are summarized in Table 7.2. For illustrative purposes it was decided that scores higher than 21 —indicative of a strong similarity between the δ^{18}O time series— could be coloured in green; scores smaller than 15, indicating a strong dissimilarity between the speleothems, could be coloured in red. The scores between 15 and 21 are not displayed in the figures. The strongest similarity was found between speleothem "292" located in Russia and speleothem "054" from Uzbekistan, with a similarity score of 27. Precisely the strongest dissimilarity was seen between these two speleothems and speleothem "410" located in Peru, with a similarity score of 10 in both cases. Under the same global analysis, four speleothems show a substantial number of dissimilarities with other speleothems: speleothem "292" in Russia and "054" in Uzbekistan diverge with six speleothems each; speleothem "410" in Peru diverges with seven speleothems; and speleothem "124" in USA diverges with eight speleothems.

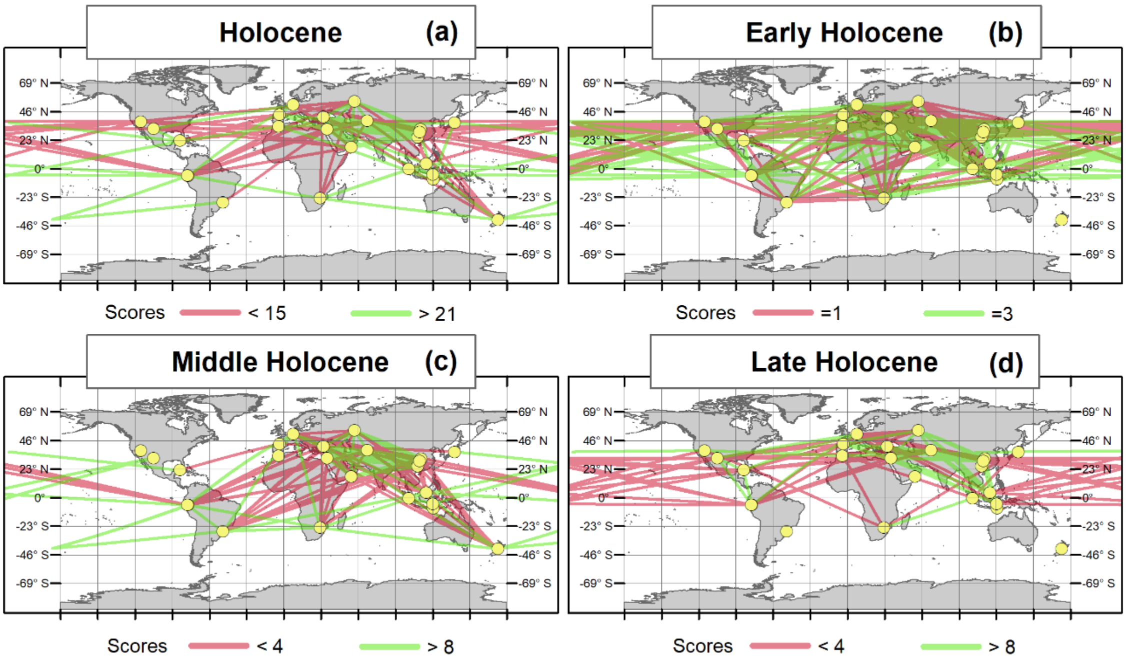

Figure 7.5. Spatial distribution of the most extreme connection lines between the 24 analysed speleothems and derived from the trend analysis. Holocene (0-10 ka) (a) showing scores > 21 (similarity) and scores < 15 (dissimilarity). Early Holocene (8-10 ka) (b) showing scores of 3 (similarity) and scores of 1 (dissimilarity). Middle Holocene (4-8 ka) (c) and Late Holocene (0-4 ka) (d) showing scores > 8 (similarity) and scores < 4 (dissimilarity).

To better visualize the results, the trends with the highest and lowest scores are plotted as lines connecting the relevant pairs of speleothems (Figure 7.5). These lines were obtained for the Holocene as well as for the adjusted correspondence between the δ^{18}O series (0–10 ka) and the three boundaries of the Holocene (11.6 ka, 8.2 ka and 4.2 ka; Walker et al., 2018) that have been slightly adjusted into three sub-divisions; Early Holocene (c. 8–10 ka), the Middle Holocene (c. 4-8 ka) and the Late Holocene (c. 0-4 ka).

On the Holocene map (Figure 7.5a), the lines follow the same colour scheme as in Table 7.2 (15/21 for red/green lines respectively). For the Holocene sub-periods, the previous colour scheme was modified, however: the Late Holocene (Figure 7.5d) and the Middle Holocene (Figure 7.5c) —comprising four series each of 1 ka (three comparisons within) — use a score of four for the red lines (dissimilarity) and a score of eight for the green lines (similarity). Because the Early Holocene (Figure 7.5b) comprises only 2 ka in this study (two intervals allowing a single comparison), a simplification was applied; the red lines indicate a score of one, the green lines a score of three. The breakdown between similarity and/or dissimilarity lines quite clearly illustrates the contrast in the climate response across the Holocene and its sub-periods.

7.3.2 Climatic response to insolation forcing

The correlation coefficients between every speleothem's time-series and each one of the calculated monthly insolation curves derived from the location of the speleothem were estimated. This gave 12 correlation values per speleothem, to be used for generating one curve per speleothem, thus a total of 24 curves (Figure 7.6a).

The curves generated from the correlation coefficient values show two distinctive patterns of correlation. The first group encases a group of lines whose correlation is the strongest in the summer months (boreal; June - September), followed by the autumn months, and is the lowest (negative) in the winter and spring months (red lines in Figure 7.6a). Because of that, this group has been denoted as the “summer” group, and there are speleothems from both hemispheres in this categorization. The other group of speleothems is represented by the so-called “winter” group, which shows opposite behaviour —the correlation is negative— during the summer and autumn (boreal), yet positive during winter and spring (blue lines in Figure 7.6a).

The geographical distribution of these groups is plotted in Figure 7.6b. The nine speleothems within the “winter” group are exclusively in the northern hemisphere and are distributed across Eurasia, whereas the “summer” group comprises 15 speleothems located in America, Africa, Western Europe, SE Asia, and Oceania. To further represent the two groups, the stack of the differences with respect to the mean (residuals) for each group was estimated (Figure 7.6c), generated as the average of the 20-year (resampled) $\delta^{18}O$ residuals time-series from each speleothem. For the purpose of the cross-spectral analysis, the "winter" group (512 pairs of data; 320–10,540 years BP) was truncated to match the lower limit of 10,000 years of the "summer" group (486 pairs of data; 300–10,000 years BP). These two stacked time series representing the "summer" and the "winter" groups have their largest correlation (negative) when applying smoothing by means of an optimal semi-bandwidth of 1,000 years (r=-0.55), overall depicting an opposite behaviour. The Figure 7.6c also represents these moving average smoothed curves.

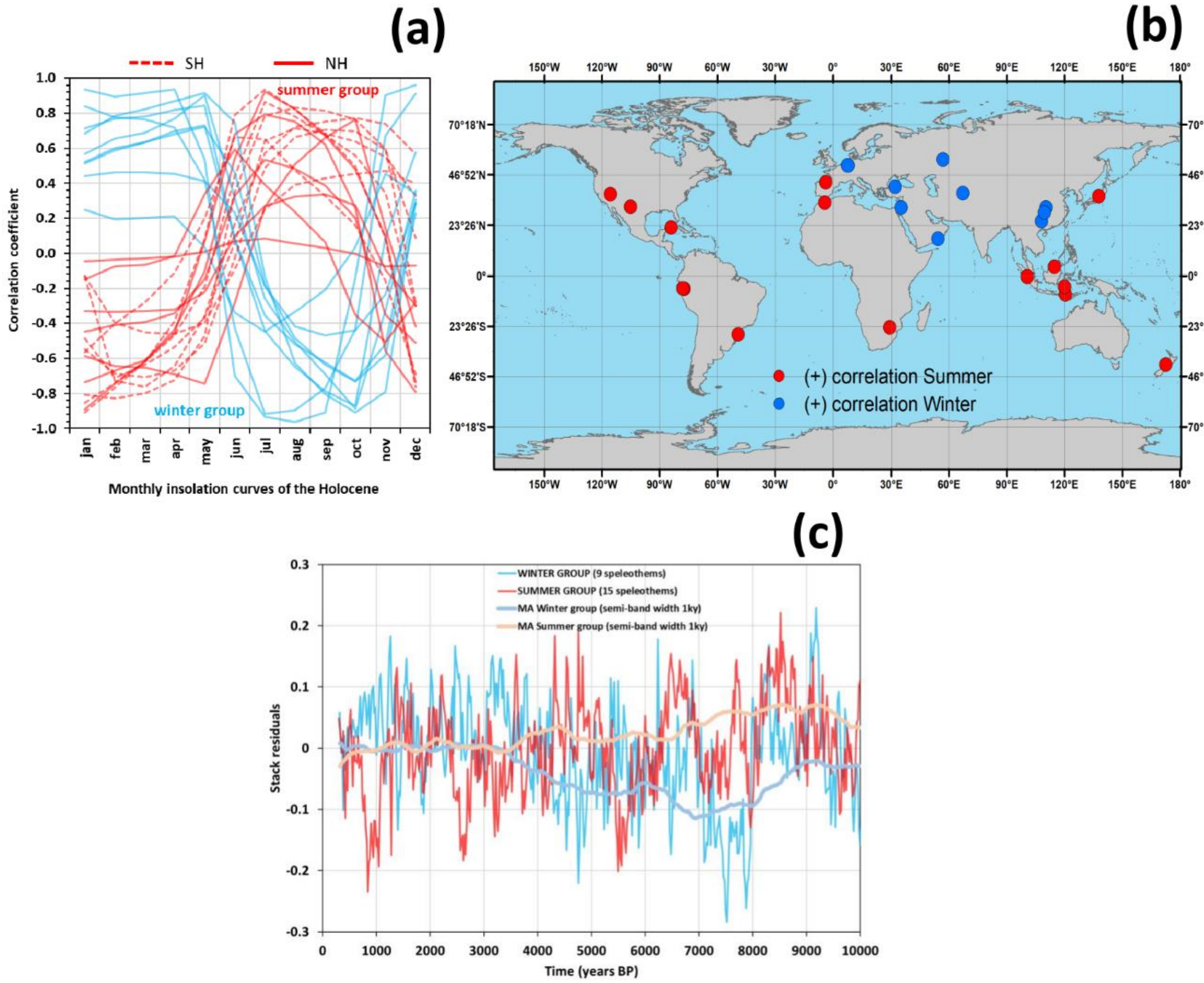

Figure 7.6. Response to radiative forcing studied in 24 speleothems. Generated curves (1 per speleothem) using the 12 correlation coefficient values obtained when correlating the 12 monthly insolation curves for the location of each speleothem with the corresponding $\delta^{18}O$ time-series (a). Geographical distribution of the correlation groups; in blue those speleothems of the "winter" group or negatively correlated with the summer months, and in red those speleothems within the "summer" group or positively correlated with the summer months (b). Stacked $\delta^{18}O$ residuals as time-series from the "winter" and "summer" groups resampled at 20-year interval, including the smoothed time series using a semi-band width of 1,000 years (c).

7.3.3 Estimated Lomb–Scargle power spectrum

The first result is an estimation of the Lomb–Scargle periodogram for the "summer" group and the "winter" group, separately. Using SLOMBS, the estimated Lomb-Scargle power spectrum for the "summer" group (15 speleothems) is given in Figure 7.7a, with the estimated confidence level in Figure 7.7c; the power spectrum for the "winter" group (9 speleothems) is given in Figure 7.7b, with the estimated confidence level shown in Figure 7.7d. Spectral analysis revealed a series of statistically significant spectral frequencies amongst the 1,000 frequencies evaluated per group (from 0.01, or 100-year period, to 0.00001, or 100,000-year period).

However, cycles above the 3.3-ka period were not considered, as this period marks the limit of one-third of the length of the Holocene time-series (c. 10 ka). The "summer" group had significant periodicities at 2222, 1695, 885, 781, 592 and 418 years, all above 99% of confidence. In turn, the "winter" group periodicities are identified at 2778, 1389, 952, 730, 505, 435 and 377 years. They are all statistically significant, above 99% of achieved confidence level (obtained using 10,000 random permutations and 20 smoothing terms). Some of these frequencies were likewise detected for the individual speleothems, such as the 1389-year cycle in Japan (speleothem "117") or the 2,222-year cycle in both Malaysia (speleothem "238") and China (speleothem "298"). A detailed summary of all the significant frequencies found on the 24 individual speleothems when estimating the Lomb-Scargle power spectrum is included in the Appendix 3.1.

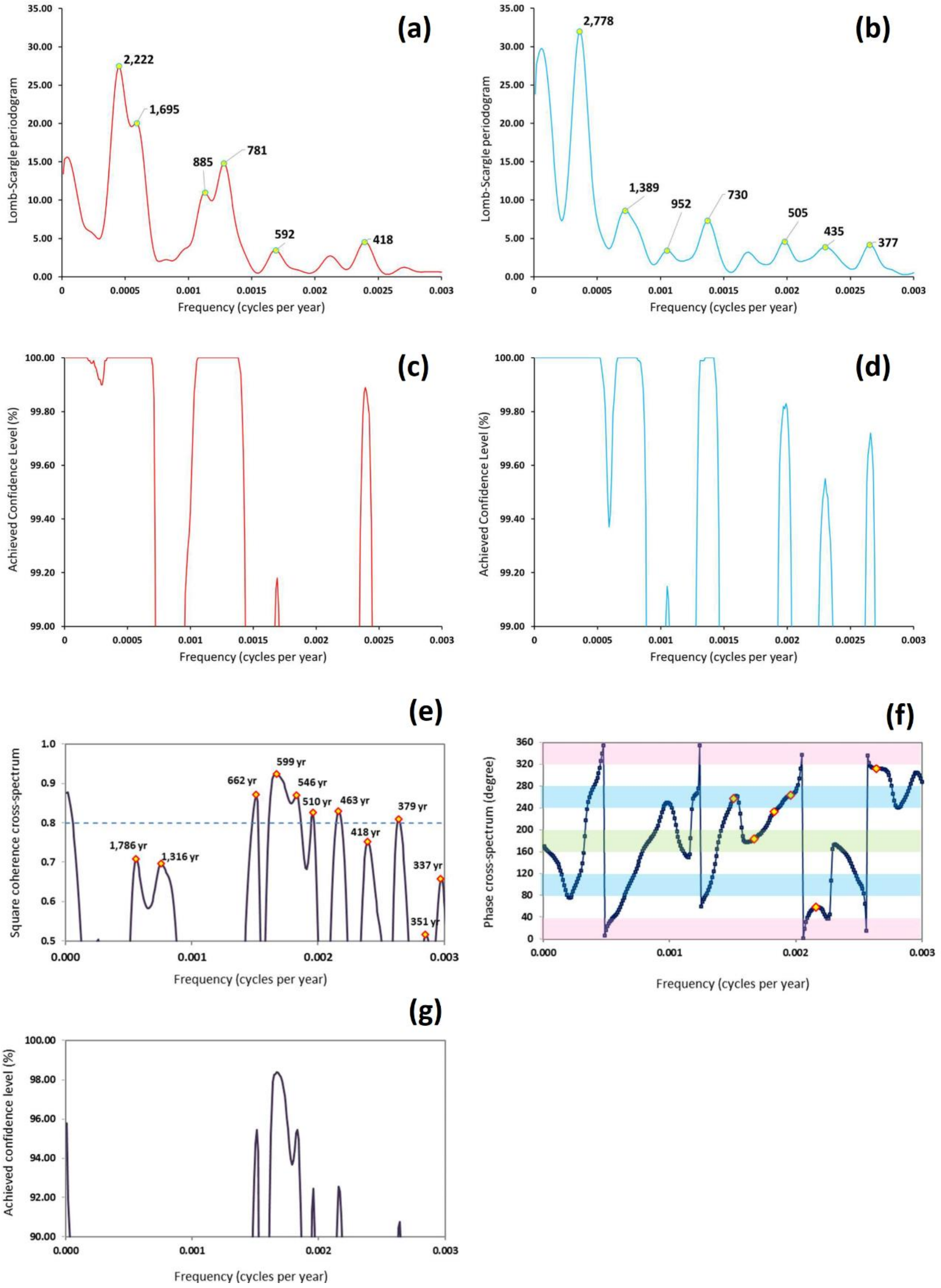

Figure 7.7. Estimated Lomb–Scargle periodogram for the "summer" time-series (a). Estimated Lomb-Scargle periodogram for the "winter" time-series (b). Estimated confidence level of the power spectrum for the "summer" time-series (c). Estimated confidence level of the power spectrum for the "winter" time-series (d). Smoothed Lomb–Scargle squared coherence cross-spectrum between the "winter" and the "summer" time-series (e). Smoothed Lomb–Scargle phase cross-spectrum marking the position of the periodicities: 662, 599, 546, 510, 463 and 379 years (f). Achieved confidence level for the estimated squared coherence (g).

7.3.4 Estimated Lomb–Scargle cross-spectrum

The cross-spectra between the “winter” and the “summer” time-series were estimated with a focus on the centennial to millennial timescales (frequencies being inversely proportional to the periodicities). This research identified several spectral peaks, with periods of 1786, 1316, 662, 599, 546, 510, 463, 418, 379, 351 and 337 years, as evidenced in the smoothed Lomb-Scargle squared coherence cross-spectrum (Figure 7.7e). However, only the periodicities of 662, 599, 546, 510, 463 and 379 are statistically significant above 90% of confidence (Figure 7.7g). Furthermore, the frequencies in the millennial timescale band are slightly less coherent (<0.8) than the centennial group when looking at the estimated coherence results. For instance, the 1786- and 1316-year cycles around the 1,500 ± 500 years periodicity have 0.7 of coherence. Particularly important are the periodicities located at 599 and 463 years, which show great coherence. In the phase cross-spectrum graph (Figure 7.7f) it is seen that the 1,786- and 1,316-year cycles are out of phase in the two groups. Their phase differences of 39 and 142 degrees respectively theoretically translate into a time shift of 196 years for the 1,786-year cycle, and of 520 years for the 1,316-year cycle. The 599- and 463-year cycles are also out of phase, and have respective associated time shifts of 305 and 75 years. All these estimations may include the age uncertainties derived from the original time series used in this study.

7.4 Discussion

7.4.1 δ^{18}O stack trend: Latitudinal analysis through the Holocene

The estimated global δ^{18}O evolution for the Holocene (Figure 7.5a) derived from the trend analysis (Table 7.2) was further divided into the Early (Figure 7.5b), Middle Holocene (Figure 7.5c) and the Late Holocene (Figure 7.5d).

The Early Holocene (>8 ka) shows a great density of lines (score=3), indicating high similarity between the speleothems, depicting a recognisable latitudinal band crossing the Pacific Ocean, the South Atlantic and the Indian Ocean (Figure 7.5b). However, red lines are also present further North (i.e., between North America and China), evidencing greater dissimilarity (score=1) between speleothems within the Northern hemisphere as well as between the two hemispheres. Also important is the incipient area of similarity (green lines) between speleothems within Eurasia that is consolidated during the Middle Holocene. A similar latitude contrast was previously explained as the combined mechanism of the deglaciation of the Laurentide Ice sheet (LIS) and its cooling effect in the surrounding regions, while at the same time high latitudes were reaching a maximum insolation period during the Holocene (Renseen et al., 2012). This could explain the discrepancy observed between higher and lower latitudes in this period, except for the Eurasian region.

In the Middle Holocene (Figure 7.5c), some important climate features can be underlined. One is the existence of a region across the Pacific Ocean marked by several lines depicting similarity, except between one speleothem from Peru and the Chinese speleothems. There is also a huge contrast between southern hemisphere speleothems and those located in Eurasia, as evidenced by many red lines converging from South America, Africa, SE Asia, and New Zealand to main Eurasia. This finding contradicts the general stabilization and/or homogenization during the Middle Holocene, driven by the warm Holocene Thermal Maximum (HTM) and occurring between ~7 ka and ~4.2 ka (Wanner et al., 2011). The Eurasian region seems to initiate the build-up of its climate identity on this period, as it is evidenced by the presence of multitude of green lines within the region. There are further confluences of similarities: a latitudinal band in the Southern Ocean connecting the southernmost speleothems, as well as some green lines crossing the North Atlantic, and the Indian Ocean, that could ultimately be ascribed to the general context of climate convergence in this period.

The so-called 4.2 ka transition marks the separation between the Middle and the Upper/Late subseries/sub epochs in the Holocene. This global and detectable reorganisation of climate is detectable in speleothems, and in fact, the global stratotype for the Middle to Late Holocene was defined using speleothems from the Mawmluh Cave in northern India (Walker et al., 2018). The Late Holocene evidences a weakening or departure from wetter to drier conditions in the monsoon areas (Zhang et al., 2013). The Late Holocene (Figure 7.5d) —marked by the 4.2 ka transition (Walker et al., 2018)— shows a significant increase in the number of similarities and dissimilarities, not observed previously during the Middle Holocene. The most evident similarities would be those observed within the Eurasia speleothems, continuing with their individualized climate identity initiated during the Middle Holocene. In contrast, the strongest dissimilarity is observed across the Pacific Ocean, represented by a large density of red lines, suggesting a heterogenous incidence of the El Niño–Southern Oscillation (ENSO) over both sides of the Pacific. The observed change evidences a global reorganisation of both atmosphere and oceans that it was accelerated after 4.2 ka.

7.4.2 Solar forcing: The “summer” and “winter” group speleothems

The importance of orbital variations and solar variability in the global climate changes of the Holocene has been previously highlighted (e.g., Mayewski et al., 2004). Discernment of two groups of speleothems, the so-called “summer” and “winter” groups (Figure 7.6a), is based on the specific climate response ($\delta^{18}O$) to the estimated monthly insolation curves for the Holocene. It has been estimated (Renssen et al., 2012) that the maximum positive insolation anomaly for the last 9 ka shifts, from June in the northern hemisphere to October in the southern hemisphere on most of the continents. This indicates that the best correlation for the δ^{18}O time-series would occur with the insolation curve of the month having the largest insolation anomaly, as it has been suggested by Renssen.

Starting with the "summer" group (15 speleothems), its eight speleothems within the tropics (six in the southern hemisphere and two in the northern hemisphere) have their best correlation with the insolation curves from June to September. At mid-latitudes for the "summer" group, the two speleothems in the southern hemisphere correlate well to October-November insolation curves, whereas the five speleothems in the northern hemisphere have their best fit to June-October. The results for the "summer" group match the predictions of the cited modelling work (Renssen et al., 2012): the Holocene maximum warming driven by the Holocene Thermal Maximum (HTM) occurring during July-August at northern hemisphere mid-latitudes and the tropics, and during September-October at southern hemisphere mid-latitudes. However, the nine speleothems of the "winter" group located in Eurasia (Figure 7.6b) reveal a different pattern, lagging six months behind the correlation curves of the "summer" group. In detail, there are six speleothems in this group that best correlate to March-May insolation curves: China (3), Uzbekistan (1), Oman (1) and Israel (1). In turn, there are three speleothems within the "winter" group that best correlate to November-December insolation curves: Russia (1), Turkey (1) and Germany (1). At any rate, both sub-groups share a prominent negative correlation with the summer months.

It is not surprising that the plotted curves of the residuals for both groups have a significant negative correlation, as illustrated by the two smoothed moving average time series (semi-bandwidth of 1,000 years) and r=-0.55, especially during the Early and Middle Holocene (Figure 7.6c). This differentiation may reveal that other factors apart from the solar forcing are equally important during the Holocene. Previous works have identified a similar out-of-phase in the effective moisture between speleothems in Eurasia, interpreted as a consequence of teleconnections with cold events in the North Atlantic (Wang et al., 2005; Dykoski et al., 2005), combinations of dominant temperature effect, a moisture source control in the Urals (Baker et al., 2017), and some incidence of latitude climate perturbations, such as the Atlantic meridional overturning circulation (AMOC) or the Artic sea ice conditions (Kaboth-Bahr et al., 2021).

7.4.3 Spectral variability: millennial to centennial climate forcing

Observed cycles in the spectral analyses conducted on the δ^{18}O time-series of the speleothems for the "summer" and the "winter" groups appear to fit well with previously identified climate-related periodicities with the appropriate level of caution regarding age uncertainties (Table 7.3).

The "summer" group reveals significant frequencies in the spectral analysis (Figure 7.7a, c), that can be related with known cycles. In the millennial timescale, the 2,222-year cycle roughly matches the 2,400-year Hallstatt cycle (Vasiliev and Dergachev, 2002). This cycle has been identified in the cosmogenic radionuclide ^{14}C from trees and in the ^{10}Be from ice-cores and linked to long-term solar activity (Usoskin et al. 2016), and it has also been tentatively linked to the motion of the Sun (Charvátová, 2000). The 1,695-year cycle most likely represents the ~1,470-year (±500) (Bond et al. 1993, 1997, 2001; Broecker 1994). The "Bond" cycles are associated with cold periods in which the migration of cold and/or iced waters from the Nordic and Labrador seas into the North-Atlantic was enhanced. However, the 1,695-year cycle could be the expression of a composite cycle: 1,000- and 2,000-year, as alternatively proposed regarding the "Bond" cycles (Obrochta et al., 2012).

The detected centennial band frequencies are located at: 885, 781, 592 and 418 years. In the centennial band, periodicities between 900 and 1,000 years and between 400 and 550 years are found in the Holocene (Hall et al., 2004). The 885-year cycle could be interpreted as the ~900-year oscillation in relation to negative salinity anomalies in the North Atlantic (Schulz and Paul, 2002). The 781-year cycle could be the same 800-year cycle previously detected in Irish trees and explained as atmospheric circulation changes in the North Atlantic produced by non-linear reactions to the input of solar activity (Turney et al., 2005). The 592-year cycle certainly matches the 590-year cycle found in lake sediments of southwestern Alaska and pointing to a climate linkage between subpolar regions of the North Atlantic and North Pacific (Hu et al., 2003). Besides, the 592-year cycle is not far from the 550-year oscillation detected in deep-sea sediment cores and associated with cyclical variations in North Atlantic Deep Water (NADW) circulation, ultimately coherent with fluctuations in atmospheric conditions over Greenland (Chapman and Shackleton, 2000). The 418-year cycle found would match a fundamental 420-year cycle, identified as an important fundamental oscillation when analysing atmospheric ^{14}C in trees and linked to Sun activity (Stuiver and Braziunas, 1989). The "summer" group has demonstrated a close linkage to climate-related oscillations occurring in both atmosphere and ocean during the Holocene.

The "winter" group reveals similar significant spectral frequencies in the millennial to centennial timescale band (Figure 7.7b, d). Thus, the observed 2,778-year cycle could correspond to the same quasi 2,600-year cycle previously detected in Greenland ice and linked to atmospheric circulation (O'Brien et al., 1995). Still, it might ultimately be ascribed to the same ~2,400-year Hallstatt cycle (Vasiliev and Dergachev, 2002) as previously interpreted for the "summer" group. The second cycle identified, the 1,389-

year cycle, may match the "Bond" cycle detected in the "summer" group. In the literature, centennial frequencies such as the ones found in this research are commonly placed in the Holocene (Hall et al., 2004). Regarding the centennial variability found in the $\delta^{18}O$ time-series from the "winter" group, the 952-year cycle may correspond with a cycle of 950 years previously found in sequences from lake sediments in southwestern Alaska (Hu et al, 2003) and linked to solar-ocean driven forces. Another similar cycle of 1,000 years exists in relation to the NADW circulation variability in the North-Atlantic (Chapman and Shackleton, 2000). The 730-year cycle resembles a 725-year cycle found in sediments from Lake Edward in Africa (Russell and Johnson, 2005) and explained as a feature of tropical climate variability in regions affected by periodical Intertropical Convergence Zone (ITCZ) migrations. The 505-year cycle may correspond with the ~500-year cycle found in sediment cores from the northern Red Sea and Black Sea (Lamy et al., 2006) and originated from the Arctic Oscillation/North Atlantic Oscillation atmospheric variability driven by solar forcing. The 435-year cycle corresponds with a 434-year cycle obtained in organic sediments from Lake Titicaca in South America (Baker et al., 2005) and proposed as being highly related to the periodicity of the North Atlantic SSTs. Regarding the 377-year cycle, to date there is not a conclusive interpretation of a similar one, although a periodicity of 373 years has recently been found in marine sediments in the western Mediterranean (Rodrigo-Gámiz et al., 2018).

7.4.4 Combined spectral analysis between the "summer" and the "winter" groups

There are some noteworthy similarities in the results of the individual spectral analysis for both groups. The 505-year and 435-year cycles of the "winter" group and the 592-year and 418-year bear correspondence with the important 550-year cycle of the North Atlantic region (Risebrobakken et al., 2003). Less clear is the identification of the 1,000-year cycle in relation to the NADW circulation in both groups (Chapman and Shackleton, 2000), especially in the case of the "winter" group's 952-year cycle detected; the 885-year and the 781-year cycles of the "summer" group are further off the mark. On the millennial timescale, the ~2400-year cycle and the ~1,500-year one are well represented in both groups, resembling the 2,778-year and 1389-year cycles in the "winter" group, and 2,222-year and 1,695-year cycles in the "summer" group. This supports the argument that even if the primary source behind the oscillation is clear (i.e., solar forcing), the response of the ocean-atmosphere and subsequent systems would cascade down into different cyclical variations of the same forcing.

To further investigate the cycles obtained for both groups, cross-spectral analysis was conducted between the "summer" and "winter" groups. The squared coherence spectrum results reveal significant frequency cycles of high coherence (above 0.8), indicating the existence of several shared oscillations for both groups of speleothems. The cycles seen in the square coherence cross-spectrum higher than 0.8 are those in the centennial timescale (Figure 7.7e), with an achieved confidence, in most cases, above 90%. Although the “winter” and “summer” groups still share some coherence (~0.7) around the 1,500-year cycle in the form of two cycles (1,786-year and 1,316-year), the achieved confidence level for the millennial band is below 90% (Figure 7.7g). All centennial timescale periodicities oscillate around the 400–550-year band, which is quite common in several proxies during the Holocene, as mentioned above. Yet despite their similar periodicity, some of these cycles have an associated shift between the groups: red bands show an in-phase spectrum, blue bands show the intermediate phase, and the green band marks out-of-phase (Figure 7.7f). This shift can be explained by the fact that these two speleothem groups display a quite different response to solar forcing, resulting in different mechanisms and feedbacks that are not aligned in time.

Detected cycles (years)			Known cycles (years)	References
“Summer” group	“Winter” group	Cross spectral summer & winter (above 0.8 coherence)		
-	2,778	-	2,600	O'Brien et al. (1995)
2,222	-	-	2,400	Usoskin et al. (2016); Vasiliev and Dergachev (2002); Charvátová (2000)
1,695	1,389	-	1,500	Bond et al. (1993, 1997, 2001); Broecker (1994)
			1,000 & 2,000	Obrochta et al. (2012)
-	952	-	1,000	Chapman and Shackleton (2000)
			950	Hu et al. (2003)
885	-	-	900	Schulz and Paul (2002)
781	-	-	800	Turney et al. (2005)
-	730	662	725	Russell and Johnson (2005)
592	-	599, 546	590	Hu et al. (2003)
			550	Chapman and Shackleton (2000)
-	505	510, 463	500	Lamy et al. (2006)
418	-	-	420	Stuiver and Braziunas (1989)
-	435	-	434	Baker et al. (2005)
-	377	379	373	Rodrigo-Gámiz et al. (2018)

Table 7.3. Summary of detected periodicities and their match with known cycles.

7.5 Conclusions

The meta-analysis presented here, of 24 speleothems located worldwide, has deepened the understanding of the Holocene period at a global scale. The Early Holocene is marked by an important, homogeneous, and recognisable latitudinal climate signal in most of the speleothems. The Middle Holocene was characterized by reduced homogeneity and greater differences between the hemispheres, as well as manifesting an individualization of the climate signal recorded in speleothems of Eurasia towards greater homogeneity. In the Late Holocene, the speleothems from Eurasia continued to depict a characteristic $\delta^{18}O$ evolution from the rest of the continents, while those around the Pacific Ocean showing an increasing higher contrast. The analysis of the insolation input vs. climate signal response reveals a singular but consistent correlation between the estimated monthly insolation and speleothem $\delta^{18}O$ curves. A "winter" group —defined for the oxygen curves of the speleothems located in Eurasia— presents a negative correlation during the estimated insolation for the summer months (boreal), but positive during the winter months (boreal). That same climate response is of the opposite sign in the oxygen curves from the rest of speleothems worldwide, hence the so-called "summer" group. This phenomenon is shared by all the speleothems analysed from Eurasia, indicating that, despite climatic differences among Eurasian sub-regions (i.e., between Central Asia vs. South-East Asia), there is a common response to insolation at orbital timescales that is influenced by the dynamics of distant climate regions such as the North Atlantic, and more generally by the Westerlies in the affected latitudes. Spectral analysis results come to identify important cycles in both the millennial and centennial bands, linked to either solar and/or North-Atlantic activities, operating in the "winter" and "summer" group. The fact that only some cycles in the centennial band were recognised in the cross-spectral analysis for both groups would indicate a non-shared millennial scale variability that is distinctive, linked to the differentiation and climate evolution in each group during the Holocene. The possible involvement of other teleconnections would require further investigation using a multi-proxy approach with equivalent or even higher resolutions. Future studies should aim to delimit the geographical extent of this important differentiation, while identifying the ocean and atmosphere mechanisms ultimately responsible for the depicted climate evolution and derived from the oxygen time series.

8 Chapter VIII. A case study using ice cores data: Approaching the Younger Dryas (Submitted to *Paleoceanography and Paleoclimatology*)

8.1 Introduction

The Younger Dryas (YD) is a very distinctive cold period of the Earth's climatic recent past. It has been identified globally in both marine and terrestrial environments, initiated in the northern hemisphere, and propagated to the southern hemisphere, and it is under lot of scrutiny to determine its origin. The YD onset occurred at 12,870 ± 30 BP in the North-Atlantic (Cheng et al., 2020). In Greenland, the YD onset is recognisable in the ice records (Rasmussen et al., 2014), and coincides well with the Greenland stadial GS-1 which starts at 12,896 ±138 a b2k, after the Bølling-Allerød (BA) warm period, and ends at 11,703 ±99 a b2k, before the Holocene period. Although the YD has been profusely studied (see review in Carlson, 2013; Cheng et al., 2020), some of its facets are still controversial. Strong debate surrounds the triggering mechanisms of the YD-associated climate changes and the return to glacial conditions for about 1,300 years.

8.1.1 Younger Dryas theories

Four categories of theories are mainly discussed on the origin of the YD: a) Dansgaard-Oeschger (D-O) variability, b) freshwater forcing, c) volcanic eruptions, and d) extra-terrestrial impact.

8.1.1.1 Dansgaard-Oeschger variability

The so-called D-O events (Bond et al., 1993; Dansgaard et al., 1993) were abrupt variations in the Greenland temperature record during the last glacial period that usually started with a sharp increase in temperature, leading to a warm interstadial in a few years or decades, followed by a gradual decrease lasting a few centuries to a millennium towards the final drop or cold stadial. The YD was considered to be sharing the main characteristics of the other 24 known D-O events (Broecker et al., 2010). However, recent work on the 19 D-O oscillations prior to the BA/YD cold reversal (Li and Born, 2019) pointed that the coupled atmosphere-ice-ocean dynamics could produce these climatic events, but the YD was excluded by alternatively proposing that it would be related to a variation in freshwater input to the ocean. More recently it has been suggested that the underlying mechanisms of the YD could be different from D-O events

(Cheng et al., 2020). The AMOC continues to be considered the most likely driver of the DO cycles (Broecker et al., 1985; Menviel et al., 2020). Precisely, the YD cold period has been explained by the hysteresis of the AMOC (Broecker et al., 2006, 2010; Li and Born, 2019). The AMOC comprises a network of currents in the Atlantic Ocean transporting warm surface waters from the tropics into the North Atlantic (NA); in turn, denser and colder waters sink and move southwards until they eventually return to the surface.

8.1.1.2 Freshwater forcing

The capping of the NA by the addition of melted freshwater has been profusely studied as the triggering mechanism capable of producing the cold response at the start of the YD. Thus, this mechanism has been invoked in conjunction with rapid deglaciation events, potentially responsible for the massive release of freshwater: the drainage of Lake Agassiz through the St. Lawrence rivers into the NA (Broecker et al., 1989); a combined meltwater/iceberg discharge into the Arctic Ocean (Tarasov et al., 2005); or else from the Lake Agassiz via the Mackenzie River system (Murton et al., 2010). Indicative could be that the flow strength of the Labrador current seemed to be stronger during the YD than during the preceding Heinrich event 1 (HE1), based on the sortable silt in the sediment used as proxy (Li and Piper, 2015). A wide range of freshwater discharges and associated timings has been proposed: 0.31 Sv (1 Sverdrup (Sv) equals 1,000,000 m^3 s^{-1}) over 300 years (Goldstein et al., 2003), 5 Sv over 3 years (Renssen et al., 2018) and 0.30 Sv for 1 year (Murton et al., 2010), the last two via the Mackenzie river. Still, the timings involved in these proposals contradict the duration of a recently discovered much longer 400-year lag between precursor changes in North Atlantic Deep Water (NADW) formation and abrupt lagged temperature responses in Greenland ice-cores (Muschitiello et al., 2019). The addition of meltwater to the oceans from ice sheets may not be a trigger of cold periods by a weak AMOC, but rather a mechanism coeval to warming periods such as the Bølling period (Deschamps et al., 2012). Alternative theories propose the existence of large tabular icebergs floating in the Arctic Ocean and later released through the Fram Strait, starting at around 13.4-13.1 ka BP, as the origin of the freshwater needed to trigger changes in the NADW formation areas and hence the YD (Moore, 2005). Another study suggests the conjunction of shifting atmospheric fronts, sea ice distribution, and wind patterns and intensities to explain the sea level rise of some 6 m in the YD (Abdul et al., 2016), as none of the two largest meltwater post-glacial pulses actually occurred during the YD. Similarly, the YD contributed to a limited sea level rise in comparison with the last 35 thousand years of deglaciation events (Lambeck et al., 2014).

8.1.1.3 Volcanic cooling

A volcanic trigger for the YD onset was recently hypothesised (Baldini et al., 2018). The study interpreted that a large sulfate spike in the GISP2 ice-core located close to the start of the YD cooling in Greenland (GS-1); 12.846 ± 138 ka BP in the GICC05 time-scale (Rasmussen et al., 2014), is the imprint of the Laacher See eruption (LSE) in Central Europe; 12.880 ± 0.04 ka BP (estimated by varved lake sequences). The theory explicitly invoked other additional positive feedback mechanisms (i.e., AMOC weakening) to deal with the short residence time of 1-3 years for the sulphur aerosol, but also because the hydroclimatic response of the YD over Central Europe lagged behind the LSE events by 170-200 years. Recent bipolar synchronization at the GS-1/YD onset has identified four acidity spikes (Svensson et al., 2020), from which the earliest is the referred spike by Baldini (2018), but the authors associated this spike with low-latitude eruptions, and not with the LSE (Svensson et al., 2020). New research using fossil trees (Reinig et al., 2020, 2021) has re-defined the calibrated age of the LSE events from the previous estimated age of 12.880 ka BP to 13.006 ± 0.009 ka BP, that is 126 years older than previously accepted. The immediate consequence is that the time window for the new LSE signature in the Greenland ice would have to occur between 13.015 ka and 12.975 ka BP, therefore excluding the bipolar sulfur anomaly at 12.870 ka BP that was later used in the 2018 theory. Secondly, it implies that the YD cooling was synchronous over Greenland and Europe. A recent volcanic reconstruction using sulphate deposition simulations and four ice-cores (Abbott et al., 2021), two in Greenland and two in Antarctica, proposes two volcanic simulated events at 12.994 ± 0.140 ka and 12.980 ± 0.140 ka BP (GICC05) as potential candidates yet to be found in the Greenland ice record.

Outside the Greenland ice sheet, a recent geochemical study used osmium ratios ($^{187}Os/^{188}Os$) and highly siderophile elements contained in sediments from the Hall's cave in Texas (USA) for supporting a volcanic origin of the YD (Sun et al., 2020). The study emphasised that low osmium ratios (un-radiogenic) must be present in the analysed sediments together with high HSE concentrations, for claiming an extra-terrestrial origin. It was pointed that many YD locations supporting the Younger Dryas Impact Hypothesis (YDIH) (see below) do not contain consistent low osmium ratios and have more radiogenic values instead, such as in the Hall's cave. However, it was also acknowledged that low osmium ratios, or derived from un-radiogenic sources, were reported in a previous research when analysing the YD boundary at Melrose, Pennsylvania (Wu et al., 2013). The LSE in Central Europe is mentioned as a viable candidate for explaining the obtained results. The lateral variability of HSE concentrations found at the same stratigraphic levels in the Hall's cave (i.e., different Platinum concentrations reported at 13.08 ka BP), complicates the extrapolation of these results to other locations potentially affected by volcanic emissions (Sweatman, 2021).

8.1.1.4 Extra-terrestrial impact

The interest to understand the YD has increased in the last years, after the proposal of one of the most striking theories to interpret the YD, the so-called Younger Dryas Impact Hypothesis: a comet or a fragment of a comet impacted the Earth over North America, either as an atmospheric airburst or as a ground impact with no lasting crater, at the onset of the YD (Firestone et al., 2007). Various geochemical markers in different sites in North-America would be compatible with the cosmic impact, holding evidence including magnetic microspherules and grains, nanodiamonds, iridium, and fullerenes containing extraterrestrial helium, in addition to indicators of associated wildfires and/or biomass burning (Firestone et al., 2007). In the wake of the initial proposal of the impact hypothesis, several supportive papers including new forms of evidence have been published (Melott et al., 2010; Petaev et al., 2013; Kinzie et al, 2014; Kennett et al, 2015; Moore et al., 2017), including a Platinum spike (Petaev et al., 2013), the supporting update using ice-cores and terrestrial data (Wolbach et al., 2018a, 2018b), as well as a recently published endorsing review (Sweatman, 2021). Nonetheless, the theory is still mired in strong criticism and/or scepticism (Pinter et al., 2011; Holliday et al, 2014; Van Hoesel et al., 2014; Cheng et al., 2020).

8.1.2 The sodium aerosol

Studies on aerosol sodium and atmosphere parametrization using ice-core records is a well-developed line of research, with recent/undergoing work in the Greenland/Artic (Iizuka et al., 2018; Schüpbach et al., 2018; Sakerin et al., 2020; Erhardt et al, 2022) as well as in the Southern Ocean/Antarctica (Mayewski et al., 2017; Thomas et al., 2022). Sodium has traditionally been considered as an important glacio-chemical species (Mayewski et al., 1997) and a sea-salt transport proxy (De Angelis et al., 1997) peaking in winter (Legrand and Mayewski, 1997, Erhardt et al, 2022). The presence of sodium spikes at the YD onset was previously attributed to major atmospheric reorganizations (Mayewski et al., 1993), and its deposition recorded in the GISP2 core intrinsically reflected global changes in the northern hemisphere in a well-mixed atmosphere (Mayewski et al., 1997). Recent work also suggests that the interannual sodium variability of inland Greenland would be linked to large-scale atmospheric circulation patterns and not to the sea ice volume or the Artic sea ice dynamics (Rhodes et al., 2018).

The sodium in the form of sea salt aerosol is formed in the sea surface, and it is controlled by three main parameters: wind speed, atmospheric relative humidity, and the sea surface temperature (SST) (Thomas et al., 2022). The sodium has been proposed as a proxy for relative wind speed at source as larger transport distances required higher wind speed (Mayewski et al., 1997). Regarding its transport, modern studies have modelled that sodium particles are highly affected by wet deposition in route (Schüpbach et al., 2018), and implies that a larger loss exists when winds bring the aerosol from open ocean regions, which are affected by a higher precipitation, than when the aerosol has its origin in the sea-ice regions.

The research of atmospheric paths to Greenland in modern times reflects the linkage of aerosols with large scale atmosphere dynamics. Previous research on modelled air-mass trajectories over the Summit area in Greenland between 1946 and 1989 (Kahl et al., 1997), stated that 67% of the modelled 10-days trajectories at 500 hPa level during winter, had their origin in westerly winds reaching back Asia and/or Europe (longer transport), and 47% from North-America in the summer (shorter transport). At 700 hPa the same trajectories moved first over the North-Atlantic before reaching the Summit area from the south. Further north in the North Greenland Eemian Ice Drilling area (NEEM) area, another modelled work on back-trajectories (Schüpbach et al., 2018), found that an important proportion of the marine aerosol is transported from the open North-Atlantic and adjacent basins, with a mean transport time of 5.7±1 days for the sodium, whereas the remaining part would be originated from salt deposited in the sea-ice, especially during winter and/or glacial times (Schüpbach et al., 2018). In the SE Dome region, the air-mass at upper elevations (1,000 and 1,500 m agl) has been found to be originated from a broader region than at lower elevations (0 and 500 m agl), and includes distant regions such as Eastern Canada, Europe, Russia, and North-Atlantic Ocean (Iizuka et al., 2018). In regard to the past atmosphere, the study of aerosols has revealed the importance of transport distances during glacial times (Schüpbach et al., 2018). For instance, it was proposed that transport times were more likely to be determined by larger transport distances, due to the larger extension of the continental Laurentide ice cap and the associated multiyear sea ice coverage over the North Atlantic.

This research reveals the spectral relationship between modern three wind variables as wind speed, wind azimuth and wind vertical velocity derived from ERA5 data (1950-2006), and sodium concentration from two ice-cores in Greenland: NEGIS and Summit07. Then it analyses the evolution of the sodium variability (power spectra) around the YD onset, evidencing the YD atmosphere imprint recorded in the Greenland ice. The existence of high-resolution sodium time series recently published (Sneed et al., 2017) offers new information to apply spectral techniques, allowing the study of sodium sub-decadal variability and the estimation of significant periods, evidencing wind-related changes in Greenland associated to the YD onset. This work aims for recognising that changes in the atmosphere were present at the start of the YD. The evidenced wind-related changes integrate YD onset features, including the Pt spike, strengthening the existing debate amongst the YD competing theories.

8.2 Regional setting

This research is based on data from Greenland (Figure 8.1). Greenland ice-cores are widely recognized as exceptional sources of paleoclimate data because of their very continuous and extended record, the high-resolution yearly sampling, the existence of measurable glaciochemical proxies, and the absence of human alteration.

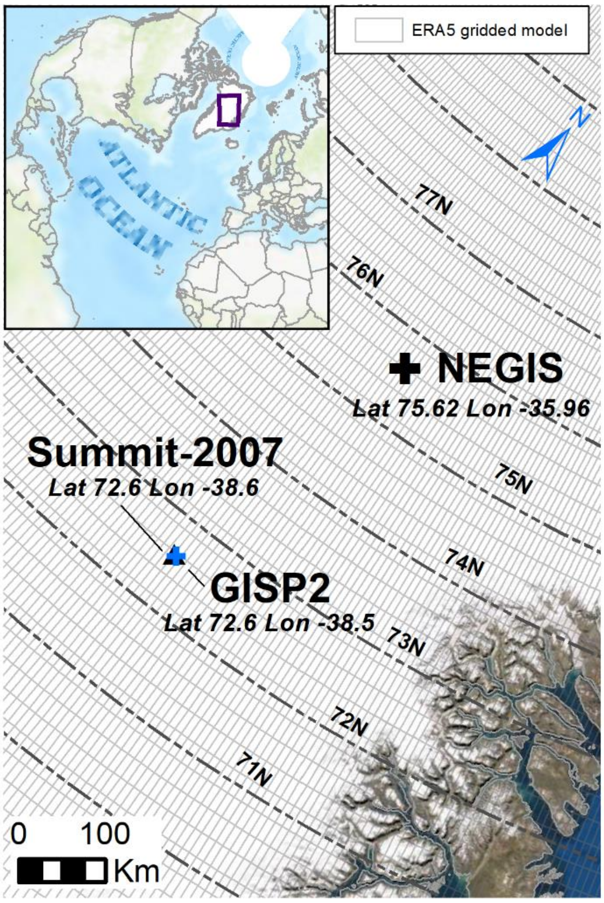

Figure 8.1. Geographic location of NEGIS, Summit07 and GISP2 ice-cores, including the ERA5 gridded model.

Previous work in the NEEM region in Greenland has shown the limitations of reconstructing atmospheric variability by using one single ice-core (Gfeller et al., 2014), but according to the research 60% of variability can be captured using one single core. To date, the absence of high resolution ice-core datasets involving the YD does not allow replicate coring as the study suggested for optimum results, but the detailed studied core offers enough representativeness to make some conclusions on the subject.

One of the most important widely studied deep ice-cores available is the Greenland Ice Sheet Project 2 (GISP2) which was drilled in Central Greenland (72.6°N, 38.5°W) at 3,200 meters above sea level (masl). It is used here to investigate the YD onset, as sodium time-series have been recently published at very high resolution for this interval (Sneed et al., 2017).

The source of the sodium data for modern times used in this research came from the Summit07 ice-core (Zhai et al., 2021) and from the Northeast Greenland Ice Stream (NEGIS) (Vallelonga et al., 2014). The NEGIS borehole site has an altitude of 2,702 masl (75.623°N, 35.96°W), some 350 km away from the location of both GISP2 (72.6ºN, 38.5ºW) and Summit07 (72.6ºN, 38.6ºW) which share roughly the same location and therefore, same altitude.

8.3 Materials and methods

This research uses open data that is fully available to the scientific community. The sodium data comes from different data repositories. Thus, the Artic Data Center (ADC) has been the source for two datasets; sodium data from the Summit07 ice-core for modern times (Zhai et al., 2021) and sodium data from the GISP2 ice-core for the YD onset period (Sneed et al., 2017). The National Oceanic and Atmospheric Administration (NOAA) has provided with the NEGIS sodium record for modern times (Vallelonga et al., 2014). Also, the original low-resolution sodium time series from the GISP2 ice-core (Mayewski et al., 1997) has been used for adding some context into the visualization of the data. Likewise, the platinum dataset comes from the original paper published by Petaev et al. (2013). In regard to the wind variables' datasets, the u and v components (for estimating the wind speed and the wind azimuth) and the vertical velocity, correspond to the 5th generation (ERA5) of re-analysis, available at the Copernicus Climate Change Service (Hersbach et al., 2019; Bell et al., 2020).

8.3.1 Sodium samples from Greenland

The main requirement for the usage of sodium time series was having high resolution; for modern times this enables the comparison with wind data (ERA5) at seasonal level, and for the YD onset it allows the identification of cycles with periods below 7 years. The reason for the later requirement is that when using spectral analysis, the maximum frequency that is possible to investigate is always limited by twice the sampling resolution (known as the Nyquist rate). That means that the original GISP2 sampling for the glacio-chemical species around the YD (~3.5 years) (Mayewski et al., 1993, 1997), represented a technical limit for the estimation of cycles having periods below twice 3.5 years. By using the recently published ultra-high resolution sodium series from GISP2 (Sneed et al., 2017) it is possible to overcome this known drawback, allowing the estimation of frequencies between the annual cycle (1 year) and 7 years of period.

The various sodium concentration datasets used in this research have not been re-processed from the original ones, with the only conversion of averaging the measurements from continuous sampling into monthly level. Therefore, NEGIS and YD time series have been averaged, while keeping the Summit07 at yearly resolution and the low-resolution GISP2 at original sampling (multiyear), the later just used for reference purposes. The three modern time series for the sodium: NEGIS, Summit07 and GISP2 are displayed together (Figure 8.2a). The original units have been kept in the same axis as they are equivalent. The low-resolution sodium time series from GISP2 (Mayewski et al., 1997) were published in micrograms/kilogram (ppb) using ion chromatography (IC). The high-resolution modern NEGIS sodium record (Vallelonga et al., 2014) was expressed in ppbw (ng/g) using optical absorption spectroscopy (OAS). The sodium data recently published at yearly level from Summit07 (Zhai et al., 2021) are in µg/L using continuous flow analysis with ion chromatography system (CFA-IC). On the other hand, the YD ultra-high-resolution time series for the sodium (Sneed et al., 2017) are expressed as thousands of counts per second (cps) using the technique known as LA-ICP-MS. This dataset is compared against the low-resolution time series from GISP2 (Mayewski et al., 1997) and the platinum time series from same GISP2 (Petaev et al., 2013), using normalised units (Figure 8.2b). For reference purposes, the $\delta^{18}O$ curves for NGRIP and GISP2 ice-cores expressed as per mil deviations relative to the mean 1850-2000 CE (Badgeley et al., 2020) have been included as they are a proxy for temperature reconstructions.

The NEGIS sodium record represents the continuous detection of sodium impurities in the ice at seasonal sampling, with a core chronology precision of ± 1 year using volcanic strata (Vallelonga et al., 2014). There is a total of 62,844 measurements from 3.306 to 66.149 meters depth, covering a time span of ~400 years (1,607-2,004 AD). For the Summit07, the depth-age model was built using concentration profiles of calcium and magnesium (Geng et al., 2014) and the dataset contains 235 measurements at yearly level (1,772-2,006 AD). The YD sodium dataset contains 166,431 measurements of sodium from 1,710.2 to 1,718.9 meters depth and the time span of the section goes from 12,823.5 to 13,040.4 years BP (1950), expressed using the GISP2 Meese/Sowers time-scale (Figure 8.2b). One important aspect of this dataset is that there are four disconnected sections with continuous measurements, referred as YD-A, YD-B, YD-C and YD-D (Figure 8.2b), therefore the analysis in between the intervals has not been conducted because this data is not available.

The applied time scale when handling ice-cores' data can potentially lead to inaccuracies and/or misinterpretations. However, both the publicly available Pt and sodium time series for the YD period used in this research were published using the same GISP2 chronology, which around the time of the YD onset is accurate and coincides well in any case with the GICC05 time scale (Svensson et al., 2006; Seierstad et al., 2014).

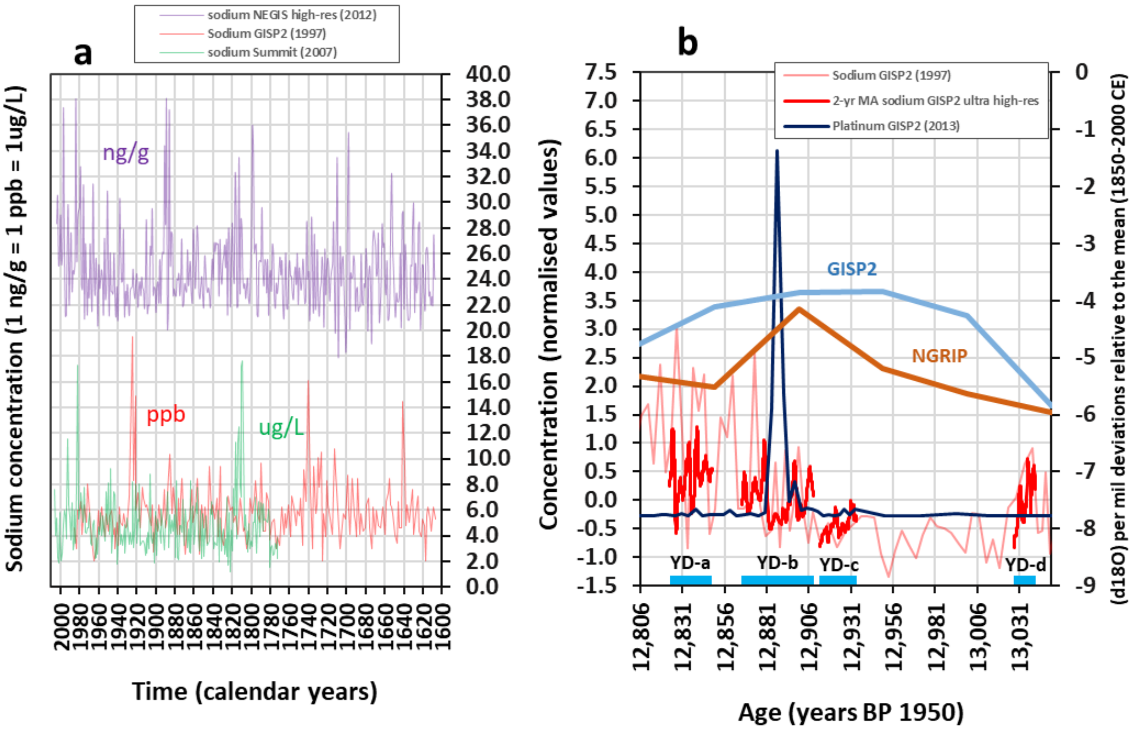

Figure 8.2. Comparison between modern NEGIS, Summit07 and GISP2 sodium records for the last 400 years (a). Comparison between the normalised Pt series (Petaev et al. 2013) and different sodium records around the YD onset: low-resolution from GISP2 (Mayewski et al., 1997) and ultra-high res from GISP2 (Sneed et al., 2017) which is available for the denoted periods YD-a, YD-b, YD-c and YD-c, and expressed as the 2-year moving average. The δ^{18}O curves for NGRIP and GISP2 ice-cores (Badgeley et al., 2020) represent an approximation to the start of the YD temperature drop (b).

8.3.2 ERA5 datasets and wind variables

The global dataset "ERA5 monthly averaged data on pressure levels from 1979 to present" from the fifth generation of re-analysis (Hersbach et al., 2019) has been used together with the ERA5 dataset available for the 1950-1978 period which exists today as preliminary version (Bell et al., 2020). Both ERA5 datasets have 16 variables each for 37 different pressure levels, from 1 hPa up in the atmosphere to 1,000 hPa at surface level. The global data grid has dimensions of 1440 x 721 x 12 x 37, respectively corresponding to longitude, latitude, month, and pressure level. Each cell size in the grid represents an extent of 0.25 x 0.25 degrees. The three variables of reference which have the highest interest to this research were: "u" (u component of wind), "v" (v component of wind) and "w" (vertical velocity). The "u" and "v" variables have been transformed into wind azimuth and wind speed. Two cells from ERA5, one for NEGIS and one for Summit07, have been used by selecting the grid cells that overlap the location of these two ice-cores.

The first step was to extract from the Copernicus Climate Change Service the corresponding time series of wind variables that overlaps the sodium period available for both ice-cores. The software MATLAB has been used for this extraction procedure on the downloaded .nc files. The NEGIS sodium record, available at higher resolution than Summit07, has been analysed covering the ERA5 dataset between 1979 and 2003 (295 pairs of data per pressure level). The Summit07 sodium record, available at yearly level (56 years), has been compared with the two ERA5 datasets; 1950-1978 (preliminary) and 1979-2006, that have been averaged annually. A detailed analysis using the NEGIS sodium record and the ERA5 dataset (Jan-1979 to Dec-2003), has been conducted for investigating the relationship between sodium and wind-blowing direction (azimuth) and wind speed by taking into account all the 37 pressure levels (Figure 8.3).

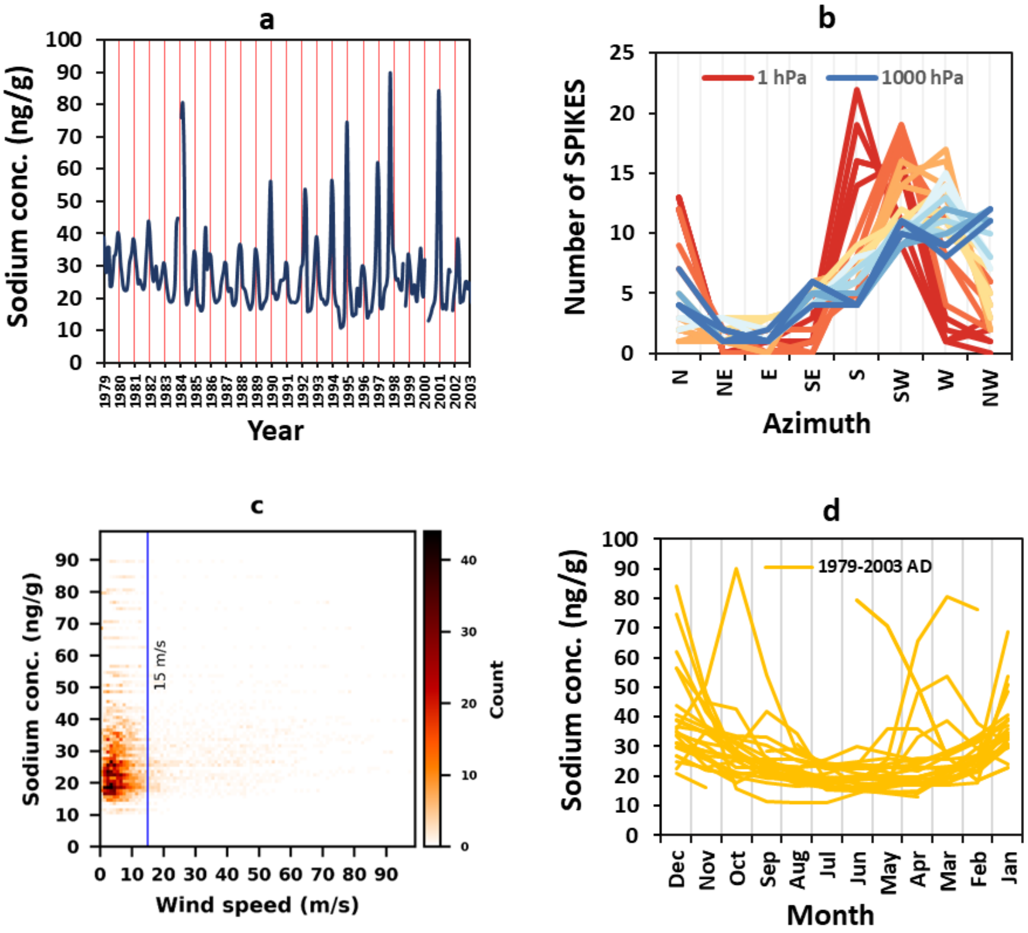

Figure 8.3. Different analyses on NEGIS sodium record from 1979 to 2003: Time series depicting spikes of sodium every winter (a), pairs of number of sodium spikes in averaged monthly data and wind-blowing azimuth (ERA5) translated into cardinal points and for all 37 pressure levels (b), bi-dimensional histogram using averaged monthly concentration data and wind speed (ERA5) (c), time series representing the sodium concentration per month and the annual seasonality (d).

As a complement to the cross-spectral analysis using both NEGIS and Summit07 sodium records, the correlation of the ERA5 variables wind speed, wind azimuth and vertical velocity at monthly level with the corresponding sodium record of NEGIS (1979-2003) and Summit07 (1950-2006) have been estimated. For the wind speed (Figure 8.4b, f) the generated 2-year trend represents the p25 (using all pressure levels) or lower altitude wind speed values. For the wind azimuth (Figure 8.4c, g), it has been followed the approach that assigns the p75 to the anticyclonic or descending air masses, and the p25 to the cyclonic or ascending air masses (Thomas et al., 2022), and the 2-year trend represents in this case the difference in wind azimuth between the p75 and the p25 levels. For the wind vertical velocity (Figure 8.4d, h), the 2-year trend represents the p75 (descending).

8.3.3 Spectral methods

Respect to the modern data the identification of any shared cyclical signal between the modern sodium recorded at NEGIS and Summit07 ice-cores and the present day wind-related variables in the atmosphere by cross spectral analysis has been approached (Figure 8.4a, e). The cross spectral analysis between the three different ERA5 wind variables and the two time series serves the purpose of revealing the significant frequencies at 37 different pressure levels from the surface up to the top of the atmosphere. This CPU-Intensive analysis involved the run of 222 cross spectral analyses (3 variables x 2 cores x 37 pressure levels), covering a time span of 25 years for the NEGIS dataset (295 months) and 57 years for the Summit07 dataset. For each analysis, the smoothed Lomb–Scargle cross-periodogram, the squared coherence spectrum, the phase spectrum, and the estimated significance level, have been calculated (Pardo-Igúzquiza and Rodríguez-Tovar, 2012). All the physical units have been kept as this does not affect the results; azimuth in degrees (clockwise from north), speed in meters per second, vertical velocity in Pascal per second, sodium from NEGIS in ng/g and sodium from Summit07 in µg/L. For mapping the relationship between sodium and wind variables at different pressure levels a threshold of 90% of achieved confidence level in the estimated Lomb–Scargle cross-periodogram, and a minimum value of 0.8 in the squared coherence, without any restrictions in the phase spectrum, have been introduced. The cycles above periods larger than half of the length of the analysed time series have not been considered (Figure 8.4).

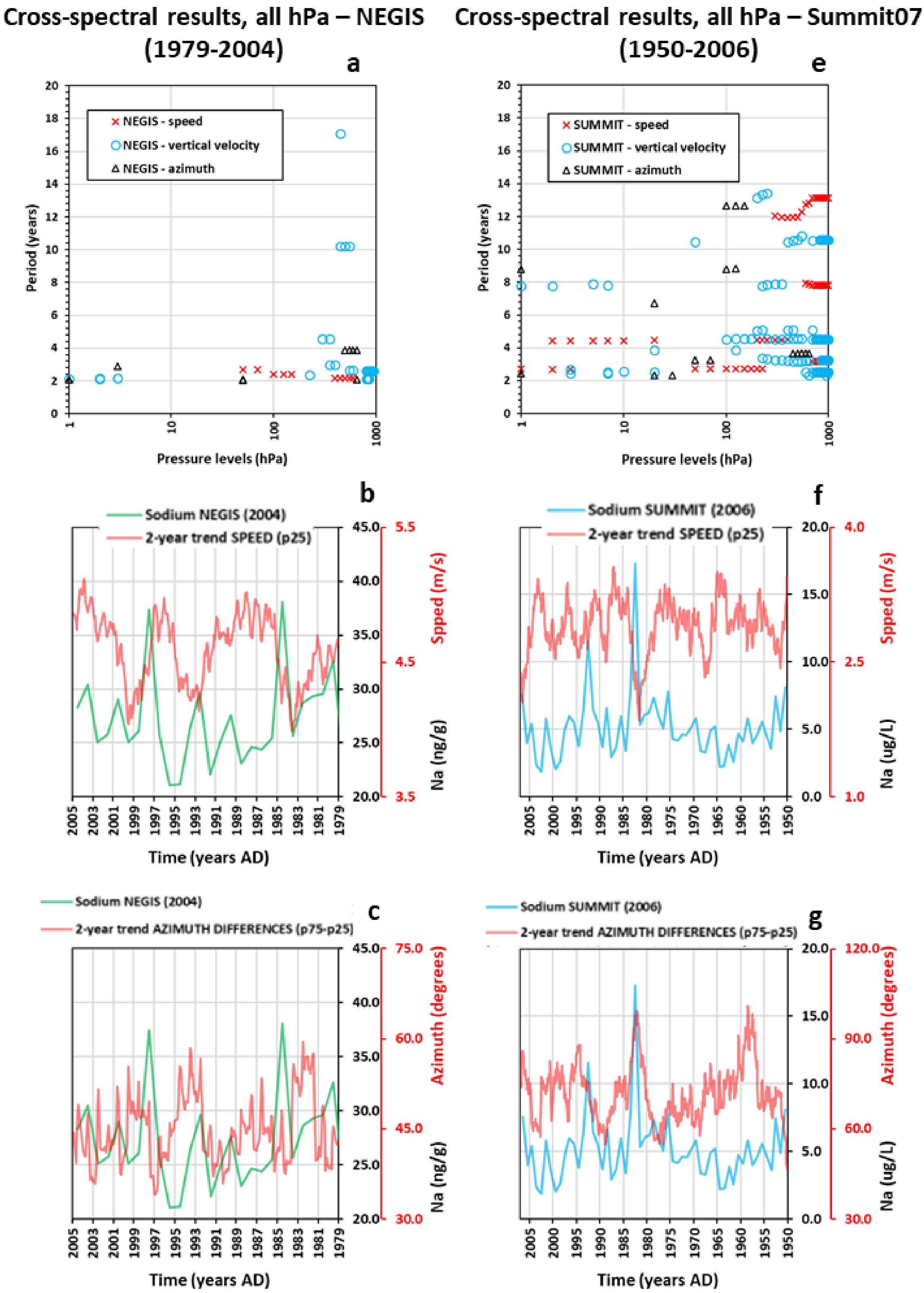
Cross-spectral results, all hPa – NEGIS (1979-2004)
a
NEGIS - speed
NEGIS - vertical velocity
NEGIS - azimuth
Period (years)
0
2
4
6
8
10
12
14
16
18
20
1
10
100
1000
Pressure levels (hPa)
Cross-spectral results, all hPa – Summit07 (1950-2006)
e
SUMMIT - speed
SUMMIT - vertical velocity
SUMMIT - azimuth
Period (years)
Pressure levels (hPa)
b
Sodium NEGIS (2004)
2-year trend SPEED (p25)
45.0
40.0
35.0
30.0
25.0
20.0
5.5
4.5
3.5
Spped (m/s)
Na (ng/g)
2005
2003
2001
1999
1997
1995
1993
1991
1989
1987
1985
1983
1981
1979
Time (years AD)
f
Sodium SUMMIT (2006)
2-year trend SPEED (p25)
20.0
15.0
10.0
5.0
0.0
4.0
2.5
1.0
Spped (m/s)
Na (ug/L)
2005
2000
1995
1990
1985
1980
1975
1970
1965
1960
1955
1950
Time (years AD)
c
Sodium NEGIS (2004)
2-year trend AZIMUTH DIFFERENCES (p75-p25)
45.0
40.0
35.0
30.0
25.0
20.0
75.0
60.0
45.0
30.0
Azimuth (degrees)
Na (ng/g)
Time (years AD)
g
Sodium SUMMIT (2006)
2-year trend AZIMUTH DIFFERENCES (p75-p25)
20.0
15.0
10.0
5.0
0.0
120.0
90.0
60.0
30.0
Azimuth (degrees)
Na (ug/L)
Time (years AD)

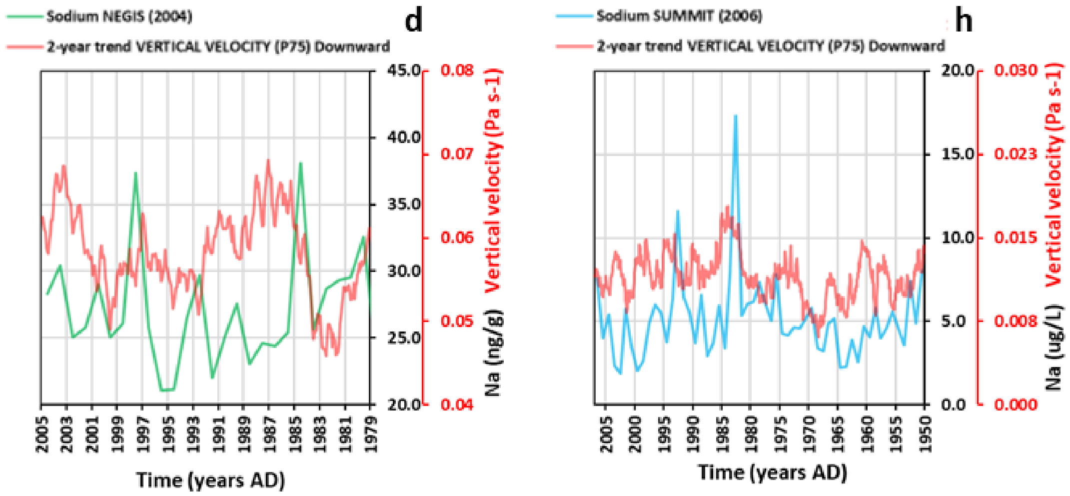

Figure 8.4. Cross-spectral results between wind-related variables (ERA5) and sodium records: NEGIS from 1979 to 2004 (a) and Summit07 from 1950 to 2006 (e). Markers represent the period (in years) of the significant frequencies obtained in the Lomb-Scargle cross-spectrum analysis, using monthly averaged (NEGIS) and annually averaged (Summit07) data for 37 pressure levels. Comparison of wind speed and sodium time series; NEGIS (b) and Summit07 (f). Comparison of wind azimuth and sodium time series; NEGIS (c) and Summit07 (g). Comparison of vertical velocity and sodium time series; NEGIS (d) and Summit07 (h).

The obtained frequencies in the cross-spectral analysis maps the temporal scale of the processes and/or the involved periodicities highly correlated with the sodium deposition, including its vertical variations in the atmosphere at different pressure levels. The collected range of significant frequencies obtained in modern times represents a framework that the sodium variability found in the YD can be compared against. The assumption is that the sodium variability during the YD onset is also representative of the same wind-related variables in the atmosphere, as analysed for modern times.

In regard to the spectral analysis applied to the YD sodium time series (Sneed et al., 2017), the Lomb-Scargle periodogram (Lomb, 1976; Scargle, 1982) has been estimated, as well as the estimated significance level. The Lomb-Scargle periodogram is also suitable for the study of time series consistent of irregular sampling intervals (Jiménez-Moreno et al., 2007; Rodríguez-Tovar et al., 2010; Pardo-Igúzquiza and Rodríguez-Tovar, 2011, 2012), or averaged from irregular time series such as the sodium time series for the YD onset period. Individual spectral analysis on sodium sub-series were conducted using the available time intervals, as the sodium data was published for four transects that have been called YD-A, YD-B, YD-C and YD-D (the data in between these intervals does not exist).

The methodology has been the novel visualization technique exposed in Chapter 4.6. Thus, the produced moving sub-series partially overlap on purpose, being the results from each individual spectral analysis circumscribed to the central age or middle point of the analysed time sub-series. Each pixel as a column of data in the Figure 8.6 represents a single individual spectral analysis. Prior to the spectral analysis four processing steps on each transect of data were conducted: a) the published and continuous sodium time series were averaged at monthly level, b) a smoothing within a semi-bandwidth of 1 year (2-year trend) has been estimated from the previously monthly averaged time series, c) the 2-year trend is removed from the time series for reducing the effect of the seasonality and enhancing the interannual variability for maximizing the identification of cyclical patterns, and d) the four transects have been divided into 38, 81, 58 and 35 time series respectively. The length of these shorter time series is of 22, 22, 16 and 10 years. The time separation between these consecutive time series has been of 0.083 years for transects YD-A, YD-C and YD-D and of 0.25 years for transect YD-B (Figure 8.6). The minimum achieved confidence level has been on this occasion of 95%. As a conservative strategy respect to the cycle identification, only those cycles that may appear more than once in the analysed interval have been considered. Thus, the detection limit has been imposed as one-third of the length of the series, being 7.3 years for the intervals YD-A and YD-B, 5.3 years for YD-C, 3.5 years for the YD-D. Therefore, the identification of the periods above time limits was not addressed.

In both the modern and the YD data, the usage of spectral analysis (Weedon, 2003) overcomes the noise associated to inter-annual and seasonal representativeness of aerosol proxies deposited in the ice identified by Gfeller et al. (2014). The Lomb–Scargle periodogram is estimated by using an oversampling ratio of frequencies, therefore for assessing the statistical significance of the registered spectral peaks, a Monte Carlo permutation test was used, to deal with the known issue of highly correlated neighbouring frequencies introduced by the oversampling of frequencies (Press et al., 1992), and secondly, smoothing the periodogram, in order to obtain clearer and more robust estimates (Pardo-Igúzquiza and Rodríguez-Tovar, 2000, 2011, 2012; Rodrigo-Gámiz et al., 2014; Sánchez-Morales et al., 2019b). This Monte Carlo procedure takes into account the high correlation between the estimated power spectrum of neighbouring frequencies introduced by the oversampling and performs smoothing in order to obtain consistent estimations. The use of Monte Carlo supports that the significant frequencies obtained can be considered as primary and not spurious peaks derived from the applied methodology.

Two computer programs implement the methods indicated: SLOMBS and CSLOMBS (Pardo-Igúzquiza and Rodríguez-Tovar, 2012). SLOMBS was used in the individual spectral analysis for the YD period, and CSLOMBS was used for the cross-spectrum analysis for modern times. These two software tools evaluate the statistical significance of the peaks determined by the Monte Carlo permutation test and incorporate the option of adjusting the statistical significance by smoothing the periodogram. A summary of all the parameters used in both the SLOMBS and CSLOMBS programs can be found in the Appendix 4.1.

8.4 Results

8.4.1 Wind variables analysis and NEGIS

A total number of 48 sodium concentration spikes in the NEGIS ice-core have been counted across 295 months, including both large and minor spikes, between 1979 and 2003 using averaged values at monthly level (Figure 8.3a). These sodium spikes when compared with the ERA5 wind azimuth time series reveal the predominance of three main wind blowing directions: south at high-pressure levels, south-west at medium-pressure levels, and west at low-pressure levels (Figure 8.3b). The obtained wind azimuth pattern would describe an anticlockwise gyre towards ascending altitudes. The 10,952 pairs of data formed by monthly wind speed values (1979-2003) and monthly NEGIS sodium concentrations for all the 37 pressure levels have been represented in a bi-dimensional histogram (Figure 8.3c). The density of data shows that the sodium-speed data pairs are mainly located at wind speed values below a threshold of ~15 m/s. Regarding the seasonality of the sodium at NEGIS, the results show the well-established fact that is the sodium peaking in winter (Figure 8.3d).

8.4.2 Cross-spectrum analysis between sodium and wind variables at different pressure levels

The time span of the analysed time series for the cross spectral analysis is shorter for the averaged monthly NEGIS sodium record (25 years) than for the yearly Summit07 sodium record (57 years). The analysis of the three variables (wind speed, wind azimuth and vertical velocity) has revealed significant cross-cycles (confidence>90% and coherence>0.8) at multi-annual scale for different pressure levels (Figure 8.4a, e).

Most of the obtained significant cross cycles are located towards the 1,000 hPa pressure level (or near to the ice surface) (Figure 8.4a, e). The length of the time series was of 295 months and 56 years for NEGIS and Summit07, respectively. Most of the obtained cycles have periods below 15 years. For NEGIS, the analysis between sodium and the wind azimuth (black triangles in Figure 8.4a), indicates that the direction of the wind is correlated at different pressure levels and has periods between 2 and 4 years with a cluster of frequencies around 500 hPa. For Summit07, the same ~2-4 years of period has been identified as a significant band too, and further, there are cross-cycles with periods longer than 5 years; ~7, ~9 and ~13 years (Figure 8.4e). Some of these longer period cycles are concentrated near the 100 hPa pressure level. The sodium and wind speed cross-spectrum analysis for NEGIS (red crosses in Figure 8.4a) reveals significant periodicities at ~2 years. In this case these are located around the 100 and 500 hPa levels. For Summit07, two bands at ~2 years and at ~5 years periods are present for different pressure levels. Longer in period are two clusters of cycles at ~8 and ~12 years that have been obtained for altitudes lower than 350 hPa (Figure 8.4e). The cross-spectrum analysis on vertical velocities and NEGIS (blue circles in Figure 8.4a), reveals significant cycles predominantly at lower altitudes than 225 hPa. Four distinctive period bands were identified, at ~2-3, 5, 10 and 17 years. For Summit07, the cross-cycles in relation with the vertical velocity show numerous significant periodicities at different pressure levels, but mainly found at altitudes below the 100 hPa level. The periods that have been identified are ~2-5, 8, 10-11 and 13 years (Figure 8.4e).

These cross spectral results have been verified by direct comparison between the sodium and the ERA5 time series for different pressure levels scenarios (see Materials and Methods). Thus, the 2-year trend of the p25 (lower speed values) time series for the wind speed is highly correlated with the sodium spikes of 1984 for NEGIS (Figure 8.4b) and with the 1982 spike for Summit07 (Figure 8.4f). For the wind azimuth the 2-year trend of the differential drifting of the air masses (p75 minus p25) is well correlated in the NEGIS for the winters of 1984 and 1997 (Figure 8.4c). Same analysis for the Summit07 reveals the same strong correlation for the winter of 1982 in this case (Figure 8.4g). The 2-year trend of the vertical velocity (p75) representing the anticyclonic or descending air masses in relation to the NEGIS has a relatively significant increase in value from ~0.05 Pa/s-1 to ~0.07 Pa/s-1 for the winter of 1984 (Figure 8.4d). The winter of 1997 shows a weaker association. Similarly, for the Summit07, the winter of 1982 coincides with an increase in vertical velocity from ~0.011 Pa/s-1 to ~0.016 Pa/s-1 (Figure 8.4h). The other sodium spikes have a less evident association with the vertical velocity.

8.4.3 Platinum anomaly and GISP2 ultra-high resolution time series

A Platinum (Pt) anomaly was previously identified in the GISP2 at the YD onset (Petaev et al., 2013). The published Pt time series is compared to the ultra-high resolution sodium series from GISP2 (Figure 8.2b, Figure 8.5d, Figure 8.6). Conducted time series alignment reveals that the Pt spike (82.2 ppt at 12,887.3 years BP) appears to overlap a period between 12,881 and 12,890 years BP, within the YD-B transect, characterized by a relative lower sodium deposition and flattened seasonality (Figure

8.5b, d). Contrariwise, between 12,891 and 12,908 years BP, and between 12,866 and 12,880 years BP, the time series display a relative higher sodium deposition, with a greater number of sodium winter spikes but less Pt concentration. However, a secondary Pt spike (7.76 ppt at 12,897.8 years BP) is also located within the period between 12,891 and 12,908 years (Figure 8.5c), and coinciding with the largest sodium spike (12,897 years BP) for this period (Figure 8.5d).

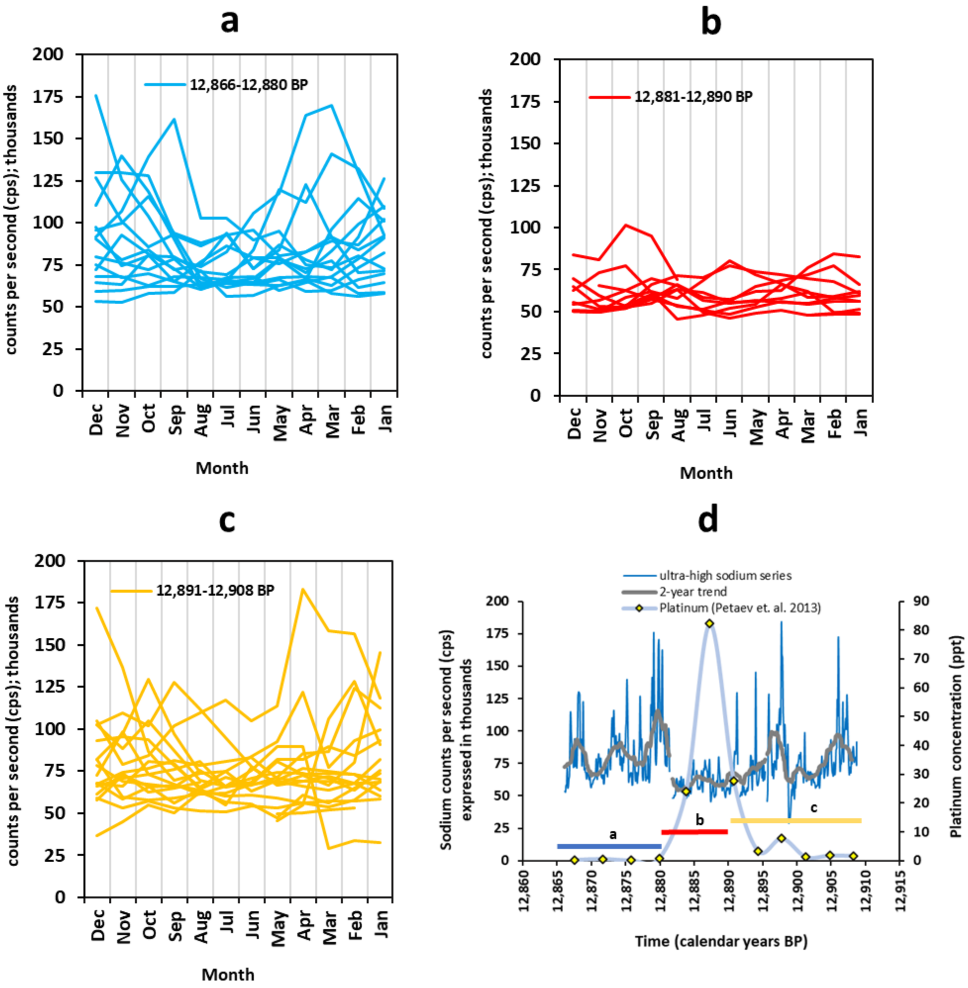

Figure 8.5. Ultra-high resolution sodium time series from GISP2 expressed as thousands of counts per second (cps) per calendar month at the YD onset; between 12,866 and 12,880 years BP (a), between 12,881 and 12,890 years BP (b) and between 12,891 and 12,908 years BP (C). Superimposed of ultra-high sodium record, its 2-year trend, and the Pt record (d).

8.4.4 Sodium spectral variability at the Younger Dryas onset

All the individual spectral analyses results from the four analysed transects have been put together chronologically for showing the progression of the different frequency bands that are statistically significant (ACL > 95%) and representative of the sodium variability

(Figure 8.6). The Pt spike is located within the interval YD-B and peaking 82.2 ppt at 12,887.3 years BP. There is a great similarity in the spectral results between intervals YD-A and YD-C, in which three main spectral bands at periods of ~1 and ~2.5 years have been identified. The interval YD-D (prior to the YD onset) has no similarity with the variability exposed by the intervals YD-A, YD-B and YD-C. The Pt spike marks a recognisable sodium variability swift within the interval YD-B, especially above the frequency of ~0.6, or ~1.6 years of period, as the frequencies below that mark do not seem to have changed that much.

8.5 Discussion

8.5.1 Sodium deposition and wind variables: a close relationship

The sodium deposition at NEGIS reflects well the seasonal cycle peaking in winter (Figure 8.3a, d). The wind speed correlates well with the sodium deposition at lower speed values (<15 m/s) (Figure 8.3c), which is very close to a similar wind speed value (12-14 m/s) that has been associated with enhanced aerosol backscattering in the Southern Ocean (Thomas et al., 2022). The conducted research reveals the close relationship between the sodium aerosol recorded in the Greenland ice and the wind data from atmospheric reanalysis (ERA5). Thus, the existence of significant cross cycles between wind variables and the two ice-cores at different pressure levels (Figure 8.4a, e), has evidenced the connection of the variability of the sodium record and the wind speed at the investigated sub-decadal and decadal scales. The significant periods have been identified at ~2, ~5, ~8 and ~12 years, which speaks of the different scale and timing of the air mass trajectories passing over the deposition site.

Furthermore, it has been found that the two largest sodium spikes in the analysed record; winter of 1984 for NEGIS and winter of 1982 for Summit07 (Figure 8.4b, f), are both associated with the lowest wind speed records (p25) in the 2-year trend, estimated using all pressure levels and independently for each location. The winters of 1993 and 1997 for NEGIS are coeval with other important drops in wind speed values (Figure 8.4b). Consistent low speed values would be behind the largest sodium concentration spikes analysed at monthly and yearly level.

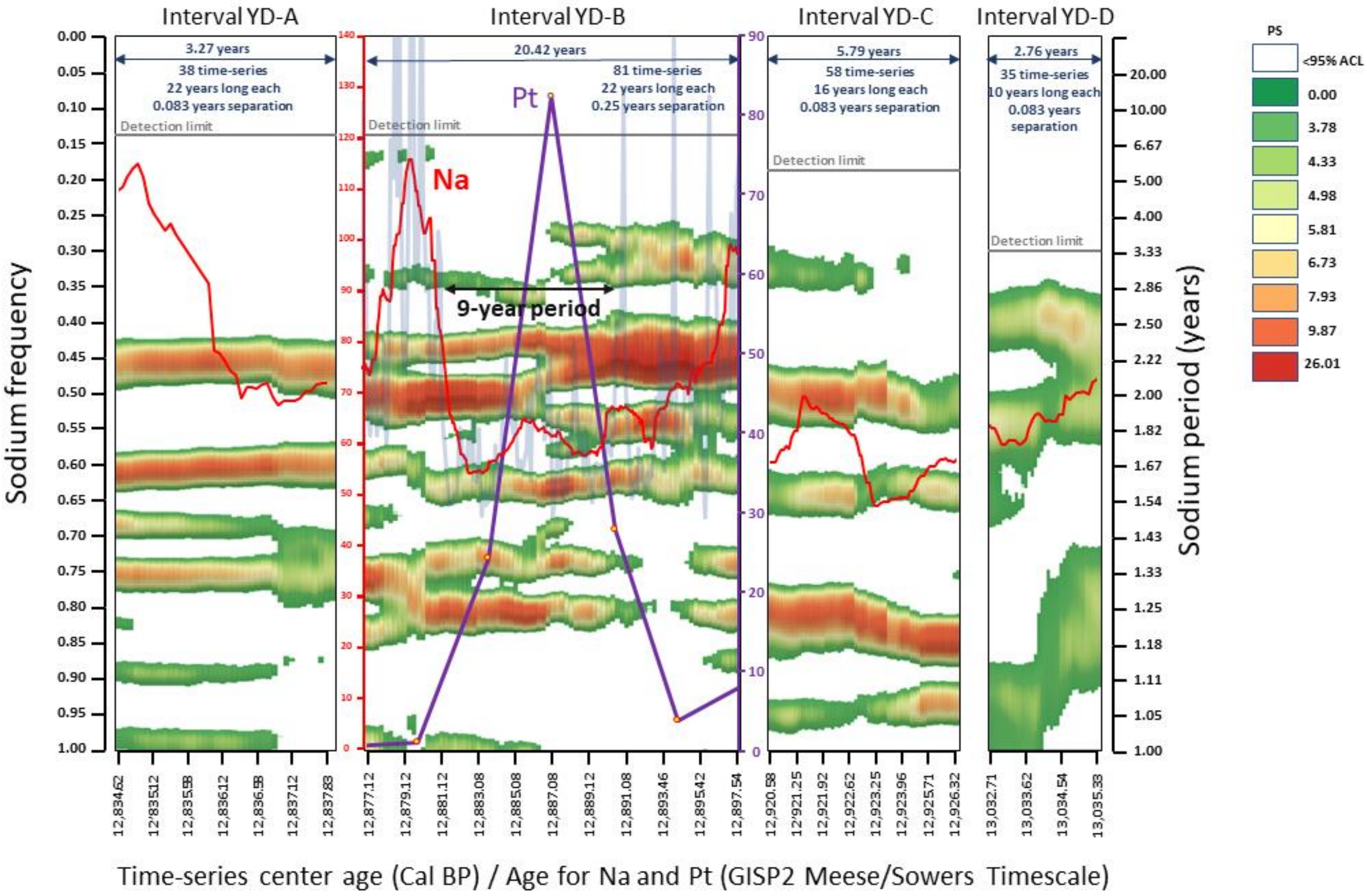

Figure 8.6. Spectrogram showing the distribution and the evolution of all significant frequencies above 95% of achieved confidence, built from the results from the estimated Lomb–Scargle periodogram on sodium data and for the four analysed transects: 12,823-12,848 years BP (YD-A); 12,866-12,908 years BP (YD-B); 12,912-12,934 years BP (YD-C) and 13,027-13,040 years BP. Both Pt record (purple line) and 2-year trend sodium record (red line) from GISP2 are represented in ppt (parts per trillion) and thousands of cps (counts per second) respectively, including the soft blue time series for the non-averaged sodium time series in transect YD-B.

The dominant wind-blowing azimuth values estimated at NEGIS (Figure 8.3b) have consistent directions (S, SW and W), which coincides with those estimated in previous studies; westerly winds (Kahl et al., 1997) and North-Atlantic (Schüpbach et al., 2018). Even though several cross-spectral cycles have been obtained at different pressure levels between the sodium and wind azimuth (Figure 8.4a, e), with periods of ~2-4, ~7, ~9 and ~13 years, the existence of two clusters for both NEGIS and Summit07 around the 500 hPa level speaks of the importance of the rotating air masses at this pressure level in relation to the sodium deposition. However, a closer look shows that the two ice-cores have opposite behaviour in terms of sodium deposition and wind azimuth; the largest NEGIS sodium spikes are associated with reduced azimuth differences (p75-p25)

(Figure 8.4c), whereas the largest Summit07 sodium spikes seem to be enhanced at increased azimuth differences (Figure 8.4g). The analysed wind azimuth differences reflect the importance of the alignment (or no-alignment) of wind blowing directions between higher and lower altitudes.

The vertical velocity share a great number of common periodicities with the sodium in both ice-cores (Figure 8.4a, e), ~2-5, 8, 10-11, 13 and 17 years, evidencing its influence in the sodium deposition at sub-decadal and decadal time scales. The largest NEGIS and Summit07 sodium spikes are associated with positive increases in vertical velocity (downward movement) or descending air masses (Figure 8.4d, h).

The variability of the large-scale atmospheric processes, operating in Greenland, has been identified by wind-related variables and is highly correlated with the sodium variability recorded in the ice (Figures 8.3, 8.4). This relationship is most evident at large sodium concentration spikes and justifies its usage for interpreting the YD onset period.

8.5.2 Sodium variability throughout the YD onset

The YD variability studied on sodium time series generated by the LA-ICP-MS (Sneed et al., 2017) allows its interpretation on a much greater level of temporal detail, or finer time scale resolution, than on series obtained by the conventional CFA technique, and there is good agreement between the two techniques (Sneed et al., 2015). When analysing the seasonality of the sodium in the GISP2 for the YD onset, the results describe well the evolution of the sodium winter deposition pattern between 12,866 and 12,908 years BP (Figure 8.5). A period between 12,881 and 12,890 years BP (Figure 8.5b, d, Figure 8.6) shows a reduced, but also flattened, sodium deposition. The sodium micro variability has been described in detail through the YD onset in four transects, between 12,823 and 13,040 years BP (Figure 8.6). The spectrograms for the four differentiated intervals (YD-A to YD-D) display the results of the sodium spectral bands, in terms of increasing/decreasing power spectra and above the 95% of statistical significance, revealing different discontinuities and/or sharp swifts along the studied intervals. It is the YD-B transect the most complex of all four. Interestingly, the transects YD-A and YD-C are similar, implying that the sodium variability has recovered most of its previous (YD-C) power spectra after crossing the YD-B.

8.5.3 Younger Dryas, impact hypothesis or climatic response

The whole YD period had higher concentrations of sodium and other chemical species than those associated to the Bølling–Allerød and the Holocene (Mayewski et al., 1993). In that context, significant is the markedly lower sodium concentration period during 9 years (between 12,881 and 12,890 years BP) at the initial YD, with the lowest value of ~54,000 cps in the 2-year trend, preceding an immediate increase, with values of ~115,000 cps (Figure 8.2b, Figure 8.5d), and then a steadily higher sodium concentration for the rest of the YD period (Mayewski et al., 1993). This fact, as well as the flattened sodium variability showing winter sodium concentration in this 9-year period reduced ~24% and ~32% to the periods before and after respectively, reflect distinct wind conditions at deposition for this brief period than those before and after. It has been found that the largest sodium concentration spikes for modern times are associated with multiple factors; i) lower wind speed values, ii) increased wind azimuth differences between different altitudes, and iii) positive vertical velocities or descending air masses. Therefore, the observed lower sodium concentration during the 9-year period would be associated with the opposite; i) higher wind speed, ii) reduced wind azimuth differences for different altitudes, and iii) ascending air masses. Certainly, the presence of the large Pt spike (82.2 ppt at 12,887.3 years BP) for this 9-year period, indicates anomalous atmospheric conditions (wind-related), that are favourable for the Pt deposition, but not for the sodium concentration. However, as previously noted, there is a secondary Pt spike (7.76 ppt at 12,897.8 years BP), that is coinciding with the largest sodium spike for the whole period 12,866-12,908 years BP (Figure 8.5d), revealing the prevalence of low wind speed, reduced wind azimuth differences and descending air masses, marked by the coincidence of the sodium spike and the secondary Pt spike.

The Younger Dryas Impact Hypothesis (YDIH) suggests that the impact of a large, fragmented comet led to high concentration of Pt (Petaev et al., 2013), and large-scale biomass burning intensified by high winds that produced the deposition of observed dust and aerosols, including sodium, in the Greenland ice (Wolbach et al., 2018a, 2018b). However, in the case study, according to modern NEGIS and Summit07 sodium records, higher sodium concentrations are associated to lower wind speed values. The absence of high winds during the YD onset could be interpreted as; a) contradicting the YDIH according to Wolbach et al. (2018a, 2018b), b) revealing that the atmosphere dynamics is variable at this time, c) a distinct behaviour of Pt and sodium. The presence of the secondary Pt spike coinciding with another large sodium spike at 12,897.8 years BP supports the variable atmosphere conditions as on this occasion there is a similar behaviour of Pt and sodium. The higher variability of the atmosphere dynamics at the YD onset is also supported by the complexity of the YD-B transect showing the higher number of frequency bands (Figure 8.6). In any case, significant, short, changes in wind variables can be interpreted for a 9-year period at the YD onset.

If the impact crater, yet to be found, took place over a large area of the northern hemisphere's ice-caps, the comet theory would need to invoke interannual wind-related mechanisms capable of producing the Pt spike which was deposited across ~21 years (Petaev et al., 2013). Thus, even though the conducted research reveals atmospheric changes at the start of the Younger Dryas, more detailed studies including new cores and more atmospheric proxies, are necessary for a conclusive interpretation of the involved phenomena.

8.6 Conclusions

Several theories have been proposed for explaining the occurrence of the profusely studied Younger Dryas onset (12.87 ka BP ± 0.03 ka BP), the last return to glacial conditions before the Holocene period, including Dansgaard-Oeschger variability, freshwater forcing, volcanic eruptions, and extra-terrestrial impact. In this research a detailed analysis of the sodium aerosol in both modern (NEGIS and Summit07) and past (GISP2) ice-cores in Greenland has been conducted as an effective and valuable tool to approach the beginning of the Younger Dryas event. Recently published high-resolution and ultra-high resolution sodium records have been used to understand the role of the atmospheric conditions in relation to the transport and deposition of this marine aerosol, through a highly detailed spectral analysis. The linkage between wind variables in the modern atmosphere and the sodium record is recognized, this being key to understand the Younger Dryas onset spectral signature.

The existence of an interval between 12,881 and 12,890 years BP with a markedly different spectral signature in the sodium variability evolution, coinciding with a measured ~9 years period of lower and flattened sodium concentration, evidence significant, short, changes in wind variables. Relevant coincidence between the timing of the spectral changes in sodium evolution and the so-called Pt spike from the same GISP2 ice-core supports a global phenomenon where atmospheric changes are of major importance. This atmospheric change in the Younger Dryas onset reveals of major influence irrespective of the proposed impact origin. Future work using more re-analysis variables and high-resolution aerosol data from ice-cores will allow a more precise understanding of the present and past atmospheric changes associated to drastic paleo-environmental changes.

9 Chapter IX. Conclusions/Resumen

9.1 Conclusions

The conducted PhD Thesis reveals significant conclusions regarding the assessment of the paleoclimate data, the applied methodologies, and the main paleoclimate interpretations.

Respect to the data analysis, after having scrutinised the most powerful sites of open data for paleoclimate research (i.e, NOAA, SISAL, etc.), and assessing the geographical and temporal coverage of their datasets, the usefulness of the studied categories is variable. Amongst the different paleoclimate archives, three categories stood out from all the rest for having greater paleoclimate potential: tree-rings, ice-cores, and speleothems:

The superior geographic distribution of tree-ring datasets, with the only absence in the Tropics, their high temporal coverage for the last centuries and their annual resolution, make them suitable for the study of the paleoclimate evolution of the last centuries at annual level.

Ice-cores datasets shows the highest resolution for the interval between today and the Eemian period or last interglacial, representing one of the oldest available archives for the study of the Quaternary glaciations, reaching back as far as hundreds of thousands of years ago. Their high resolution for the last thousands of years facilitates the study of past abrupt climate shifts, such as the cold Younger-Dryas period.

Speleothems contain the oldest continuous archive for the study of the global paleoclimate signal during the Quaternary, and their associated proxies (i.e., oxygen isotopes) captured the hydro-climate signal and temperature variability for the past millennia.

In relation to the current state-of-art of methodology techniques for the study of Quaternary paleoclimate, several contributions have been presented:

The first is a novel visualization technique using terrain methods on spectral analysis for paleoclimate interpretations that has been applied to the Milankovitch cycles across the dataset LR04 (Global Pliocene-Pleistocene Benthic $\delta^{18}O$ stack). The developed code for improving the resolution and readability of spectral results visualizations has been made open and it can be checked out at https://github.com/jose-sanchez-morales/spectral-analysis-visualization-method, having its main benefit at validating the results derived from time-frequency techniques, such as the wavelet, providing for more precision and resolution, helping with the interpretation process.

The second is the reconstruction of past-climate trends using tree-ring data and kernel smoothing that has been applied to the Andalusia region. This second methodology designed will help with the reconstruction of climate variables in areas where the instrumental measurements are scarce, but where tree-ring data is available. Tree-ring data from *Abies pinsapo* in the Sierra de las Nieves karst aquifer, were smoothed by a moving window running mean using band-widths that had been previously optimised to maximise the absolute value of the correlation coefficient between the tree-ring and the climate time series for the calibration period.

Additionally to those main methodologies, other auxiliary methodologies have been created in the framework of this PhD. For instance, several Python scripts were designed for the compilation and assessment of the paleoclimate proxy data network, as well as the retrieval and manipulation of modern climate data from the Copernicus Climate Change Service (C3S) and its associated Climate Data Store. Also, this research has used different spectral analysis software packages (i.e., SLOMBS, etc.) that have been further extended using Python scripts for automated testing, batch execution and/or visualization purposes. In the conducted meta-analysis of speleothems, a new method has been proposed for comparing trends from oxygen time series in speleothems worldwide. In the spectral analysis domain, this research has supported the usage of the Lomb-Scargle periodogram combined with the Montecarlo method, for assessing the statistical significance of the spectral peaks, both applied to the study of irregular time series in the Quaternary.

Regarding the conducted paleoclimate analyses, several conclusions highlight from the different examples. This research analysed and interpreted climate changes (i.e., continuous, and abrupt) associated with cycles at different time scales (i.e., annual, decadal, centennial, and millennial):

At regional scale, the Andalusia region was analysed using the North Atlantic Oscillation (NAO) and the Mediterranean Oscillation (MO) indexes, combined with precipitation and temperature time series from 707 meteorological stations for the last decades. The results suggested that the MO may play a greater role in the region than the North Atlantic Oscillation than initially expected.

The global climate in the Holocene period was assessed using the framework of cyclostratigraphy, applied on 24 oxygen time series from speleothems located worldwide. The two main conclusions were the different evolution across the Early Holocene, Middle Holocene and Late Holocene between regions, and the proposal of two climate groups named "winter" and "summer" groups for the Eurasia and the rest of the world respectively, that has its origin in a distinctive climate response to insolation and different teleconnections dynamics for the Eurasia region at millennial time scales.

This research has also deepened the understanding of one the most intriguing abrupt climate shifts of the upper-most Quaternary, the so-called Younger Dryas (YD) cold period. A conducted spectral analysis on modern and past marine proxy sodium time series from ice cores, combined with evidenced modern atmosphere cyclicities, suggest important atmosphere variability changes at subdecadal time scales, at the same time other important events occurred during the YD onset, such as the signature of Platinum spikes, associated in the past with volcanic and/or potential comet impact traces.

The conducted PhD Thesis advances in the knowledge of the Quaternary climate, based on a selection of paleoclimate proxies from the most complete sites of open data, the application of new methodologies, and the analysis and interpretation of climate variations associated with cycles at different time scales. This approach reveals significant to be potentially applied to improve knowledge of pre-Quaternary climate, and then to evaluate future climate changes.

9.2 Resumen

La tesis doctoral realizada presenta conclusiones significativas en relación con el estudio del clima en el Cuaternario, sobre la base del análisis de datos paleoclimáticos, las metodologías aplicadas y las principales interpretaciones paleoclimáticas alcanzadas.

Respecto del análisis de datos, después de haber analizado en detalle los repositorios más importantes de datos con acceso libre para investigaciones paleoclimáticas (i.e, NOAA, SISAL, etc.), y caracterizado la disponibilidad geográfica y temporal de sus conjuntos de datos, se ha puesto de manifiesto que la utilidad de los diferentes indicadores estudiados es variable. Considerando los diferentes archivos climáticos, tres categorías sobresalen por encima del resto por su potencial paleoclimático: anillos de árboles, testigos de hielo y espeleotemas:

La mejor distribución geográfica de los conjuntos de datos de anillos de árboles, con la única ausencia en los Trópicos, su alta resolución temporal para los últimos siglos y su resolución anual, los hacen idóneos para el estudio de la evolución paleoclimática de los últimos siglos a resolución anual.

Los datos procedentes de testigos de hielo muestran la resolución más alta para el intervalo comprendido entre la actualidad y el periodo Eemiense, o último periodo interglaciar, y representan uno de los archivos paleoclimáticos más antiguos disponibles para el estudio de las glaciaciones cuaternarias, alcanzando cientos de miles de años atrás. Su alta resolución durante los últimos miles de años facilita el estudio de cambios climáticos bruscos, como por ejemplo el periodo frío Younger-Dryas.

Los datos de espeleotemas representan el archivo continuo más antiguo para el estudio de la señal paleoclimática global durante el Cuaternario, y sus indicadores asociados (i.e., isótopos de oxígeno) reflejan la señal hidro-climática y la variabilidad de temperatura durante los últimos milenios.

En relación con el estado actual de las técnicas metodológicas para el estudio del paleoclima del Cuaternario, se presentan varias contribuciones:

La primera es una técnica de visualización novedosa que utiliza métodos tradicionales de análisis cuantitativo del terreno campo aplicados al análisis espectral, usando como ejemplo el conocido dataset LR04 (*Global Pliocene-Pleistocene Benthic* $\delta^{18}O$ *stack*) y los ciclos de Milankovitch identificados. El código desarrollado mejora la resolución y la lectura de visualizaciones de análisis espectrales. Se encuentra en acceso libre y puede descargarse en https://github.com/jose-sanchez-morales/spectral-analysis-visualization-method. Su principal utilidad es la validación de resultados procedentes de técnicas de tiempo-frecuencia, como el wavelet, proporcionando mayor precision y resolución, y ayudando, por tanto, en la interpretación de resultados.

La segunda es la reconstrucción de tendencias climáticas pasadas usando anillos de árboles y suavizado kernel, aplicada a la región de Andalucía. Esta segunda metodología ayudará a la reconstrucción de variables climáticas en áreas donde las medidas instrumentales son escasas, pero existe información sobre anillos de árboles. Datos de anillos de árboles de la especie *Abies pinsapo* procedentes del acuífero kárstico de la Sierra de las Nieves, han sido suavizados por una media móvil cuyo semi-ancho de banda de la ventana ha sido previamente optimizado con el objetivo de maximizar el valor absoluto del coeficiente de correlación entre los anillos de árboles y las series temporales climáticas para el periodo de calibración.

Además de las metodologías principales, otros métodos auxiliares han sido creados en esta Tesis. Por ejemplo, varios códigos Python fueron diseñados para la compilación y caracterización de la red de datos de indicadores paleoclimáticos, además de para la extracción y manipulación de datos climáticos actuales de "*Copernicus Climate Change Service (C3S)*" y "*Climate Data Store*". Además, esta investigación ha usado diferentes paquetes de software de análisis espectral (i.e., SLOMBS, etc.) que han sido extendidos y/o complementados por códigos Python para su comprobación automática, ejecución en grupos y/o visualización. En el meta-análisis realizado de espeleotemas, un nuevo método ha sido propuesto para comparar tendencias de series temporales del isótopo de oxígeno a nivel global. Para el análisis espectral se ha empleado el periodograma Lomb-Scargle combinado con el método de Montecarlo, para caracterizar la significación estadística de los picos espectrales, ambos aplicados al estudio de series temporales irregulares en el Cuaternario.

Considerando los análisis paleoclimáticos realizados, varias conclusiones se pueden destacar de acuerdo con los diferentes ejemplos. Se han analizado e interpretado cambios climáticos de diferente orden (i.e., continuos y abruptos) asociados con ciclos de varias escalas temporales (i.e., año, década, centena y milenio):

A escala regional, la región de Andalucía se analizó usando los índices de la Oscilación del Atlántico Norte (NAO) y la Oscilación Mediterránea (MO), combinados con series temporales de precipitación y temperatura procedentes de 707 estaciones meteorológicas de las últimas décadas. Los resultados han sugerido que el índice MO juega un papel más importante del inicialmente previsto que el índice NAO.

El clima global en el Holoceno ha sido caracterizado usando el análisis cicloestratigráfico aplicado a 24 series temporales del isótopo de oxígeno en espeleotemas distribuidos a nivel mundial. Las dos principales conclusiones han sido; a) la diferente evolución a través del Holoceno temprano, Holoceno medio y Holoceno tardío entre las regiones, y b) la propuesta de creación de dos grupos denominados "winter" y "summer" para las regiones de Eurasia y resto del Mundo respectivamente, en relación con la distinta respuesta climática a la insolación y las diferentes dinámicas de teleconexiones de Eurasia a escalas temporales de milenios.

Esta investigación ha profundizado además en la caracterización de uno de los más discutidos episodios climáticos bruscos del Cuaternario más tardío, el denominado periodo frío Younger Dryas (YD). El análisis espectral aplicado a series temporales modernas y pasadas de sodio como indicador marino procedentes de testigos de hielo, combinado con el estudio de ciclicidades reconocidas en la atmósfera actual, sugieren cambios importantes de variabilidad atmosférica a escala temporal de décadas junto con otros importantes eventos que ocurrieron al inicio del YD, como picos de platino asociados en el pasado tanto con vulcanismo como con trazas potenciales de impacto de cometa.

Esta investigación avanza en el conocimiento del clima cuaternario, sobre la base de una selección de indicadores paleoclimáticos procedentes de los repositorios de acceso libre más completos, la aplicación de nuevas metodologías, y el análisis e interpretación de variaciones climáticas asociadas con ciclos a diferentes escalas temporales. Esta aproximación se muestra de potencial relevancia para mejorar el conocimiento de climas pre-cuaternarios, así para como evaluar cambios climáticos futuros.

References

Abbott, P.M., Niemeier, U., Timmreck, C., Riede, F., McConnell, J.R., Severi, M., Fischer, H., Svensson, A., Toohey, M., Reinig, F. and Sigl, M., 2021. Volcanic climate forcing preceding the inception of the Younger Dryas: Implications for tracing the Laacher See eruption. Quaternary Science Reviews, 274, 107260. https://doi.org/10.1016/j.quascirev.2021.107260

Abdul, N.A., Mortlock, R.A., Wright, J.D. and Fairbanks, R.G., 2016. Younger Dryas sea level and meltwater pulse 1B recorded in Barbados reef crest coral Acropora palmata. Paleoceanography, 31(2), 330–344. https://doi.org/10.1002/2015PA002847

Ait-Brahim, Y., Wassenburg, J.A., Sha, L., Cruz, F.W., Deininger, M., Sifeddine, A., Bouchaou, L., Spötl, C., Edwards, R.L. and Cheng, H., 2019. North Atlantic ice-rafting, ocean and atmospheric circulation during the Holocene: insights from Western Mediterranean speleothems. Geophysical Research Letters, 46(13), 7614–7623. https://doi.org/10.1029/2019GL082405

Asmerom, Y., Polyak, V., Burns, S. and Rassmussen, J., 2007. Solar forcing of Holocene climate: New insights from a speleothem record, southwestern United States. Geology, 35(1), 1–4. https://doi.org/10.1130/G22865A.1

Atsawawaranunt, K., Comas-Bru, L., Amirnezhad Mozhdehi, S., Deininger, M., Harrison, S.P., Baker, A., Boyd, M., Kaushal, N., Ahmad, S.M., Ait Brahim, Y. and Arienzo, M., 2018. The SISAL database: a global resource to document oxygen and carbon isotope records from speleothems. Earth System Science Data, 10(3), 1687–1713. https://doi.org/10.5194/essd-10-1687-2018

Atsawawaranunt, K., Harrison, S. and Comas Bru, L., 2018. SISAL (Speleothem Isotopes Synthesis and AnaLysis Working Group) Database Version 1.0. https://doi.org/10.17864/1947.147

Azuara, J., Sabatier, P., Lebreton, V., Jalali, B., Sicre, M.A., Dezileau, L., Bassetti, M.A., Frigola, J. and Combourieu Nebout, N., 2020. Mid-to Late-Holocene Mediterranean climate variability: Contribution of multi-proxy and multi-sequence comparison using wavelet spectral analysis in the northwestern Mediterranean basin. Earth-Science Reviews, 208, 103232. https://doi.org/10.1016/j.earscirev.2020.103232

Badgeley, J.A., Steig, E.J., Hakim, G.J. and Fudge, T.J., 2020. Greenland temperature and precipitation over the last 20000 years using data assimilation. Climate of the Past, 16(4), 1325–1346. https://doi.org/10.5194/cp-16-1325-2020

Bajo, P., Drysdale, R.N., Woodhead, J.D., Hellstrom, J.C., Hodell, D., Ferretti, P., Voelker, A.H., Zanchetta, G., Rodrigues, T., Wolff, E. and Tyler, J., 2020. Persistent influence of obliquity on ice age terminations since the Middle Pleistocene transition. Science, 367(6483), 1235–1239. https://doi.org/10.1126/science.aaw1114

Baker, J.L., Lachniet, M.S., Chervyatsova, O., Asmerom, Y. and Polyak, V.J., 2017. Holocene warming in western continental Eurasia driven by glacial retreat and greenhouse forcing. Nature Geoscience, 10(6), 430–435. https://doi.org/10.1038/ngeo2953

Baker, P.A., Fritz, S.C., Garland, J. and Ekdahl, E., 2005. Holocene hydrologic variation at Lake Titicaca, Bolivia/Peru, and its relationship to North Atlantic climate variation. Journal of Quaternary Science: Published for the Quaternary Research Association, 20(7-8), 655–662. https://doi.org/10.1002/jqs.987

Baldini, J.U., Brown, R.J. and Mawdsley, N., 2018. Evaluating the link between the sulfur-rich Laacher See volcanic eruption and the Younger Dryas climate anomaly. Climate of the Past, 14(7), 969–990. https://doi.org/10.5194/cp-14-969-2018

Baldini, L.M., McDermott, F., Baldini, J.U., Arias, P., Cueto, M., Fairchild, I.J., Hoffmann, D.L., Mattey, D.P., Müller, W., Nita, D.C. and Ontañón, R., 2015. Regional temperature, atmospheric circulation, and sea-ice variability within the Younger Dryas Event constrained using a speleothem from northern Iberia. Earth and Planetary Science Letters, 419, 101–110. https://doi.org/10.1016/j.epsl.2015.03.015

Barber, D.C., Dyke, A., Hillaire-Marcel, C., Jennings, A.E., Andrews, J.T., Kerwin, M.W., Bilodeau, G., McNeely, R., Southon, J., Morehead, M.D. and Gagnon, J.M., 1999. Forcing of the cold event of 8,200 years ago by catastrophic drainage of Laurentide lakes. Nature, 400(6742), 344–348. https://doi.org/10.1038/22504

Bell, B., Hersbach, H., Berrisford, P., Dahlgren, P., Horányi, A., Muñoz Sabater, J., Nicolas, J., Radu, R., Schepers, D., Simmons, A., Soci, C. and Thépaut, J-N., 2020. ERA5 monthly averaged data on pressure levels from 1950 to 1978 (preliminary version). Copernicus Climate Change Service (C3S) Climate Data Store (CDS). https://cds.climate.copernicus-climate.eu/cdsapp#!/dataset/reanalysis-era5-pressure-levels-monthly-means-preliminary-back-extension?tab=overview

Berends, C.J., Köhler, P., Lourens, L.J. and van de Wal, R.S.W., 2021. On the cause of the Mid-Pleistocene Transition. Reviews of Geophysics, 59, e2020RG000727. https://doi.org/10.1029/2020RG000727

Berger, A., 1978a. Long-term variations of daily insolation and Quaternary climatic changes. Journal of Atmospheric Sciences, 35(12), 2362–2367. https://doi.org/10.1175/1520-0469(1978)035<2362:LTVODI>2.0.CO;2

Berger, A., 1978b. A Simple Algorithm to Compute Long Term Variations of Daily Insolation. Institut D’Astronomie et de Géophysique, Université Catholique de Louvain, Louvain-la Neuve, 18.

Berger, A., Melice, J.L. and Van Der Mersch, I., 1990. Evolutive spectral analysis of sunspot data over the past 300 years. Philosophical Transactions of the Royal Society of London. Series A, Mathematical and Physical Sciences, 330(1615), 529–541. https://doi.org/10.1098/rsta.1990.0034

Berger, A., Loutre, M.F. and Tricot, C., 1993. Insolation and Earth's orbital periods. Journal of Geophysical Research: Atmospheres, 98(D6), 10341–10362. https://doi.org/10.1029/93JD00222

Berger, A., Li, X.S. and Loutre, M.F., 1999. Modelling northern hemisphere ice volume over the last 3 Ma. Quaternary Science Reviews, 18(1), 1–11. https://doi.org/10.1016/S0277-3791(98)00033-X

Berger, A., Loutre, M.F. and Mélice, J.L., 2006. Equatorial insolation: from precession harmonics to eccentricity frequencies. Climate of the Past, 2(2), 131–136. https://doi.org/10.5194/cp-2-131-2006

Blackman, R.B. and Tukey, J.W., 1958. The measurement of power spectra from the point of view of communications engineering—Part I. Bell System Technical Journal, 37(1), 185–282. https://doi.org/10.1002/j.1538-7305.1958.tb03874.x

Boers, N., Ghil, M. and Rousseau, D.D., 2018. Ocean circulation, ice shelf, and sea ice interactions explain Dansgaard–Oeschger cycles. Proceedings of the National Academy of Sciences, 115(47), E11005–E11014. https://doi.org/10.1073/pnas.1802573115

Bond, G., Broecker, W., Johnsen, S., McManus, J., Labeyrie, L., Jouzel, J. and Bonani, G., 1993. Correlations between climate records from North Atlantic sediments and Greenland ice. Nature, 365(6442), 143–147. https://doi.org/10.1038/365143a0

Bond, G. and Lotti, R., 1995. Iceberg discharges into the North Atlantic on millennial time scales during the last glaciation. Science, 267(5200), 1005–1010. https://doi.org/10.1126/science.267.5200.1005

Bond, G., Showers, W., Cheseby, M., Lotti, R., Almasi, P., DeMenocal, P., Priore, P., Cullen, H., Hajdas, I. and Bonani, G., 1997. A pervasive millennial-scale cycle in North

Atlantic Holocene and glacial climates. Science, 278(5341), 1257–1266. https://doi.org/10.1126/science.278.5341.1257

Bond, G., Kromer, B., Beer, J., Muscheler, R., Evans, M.N., Showers, W., Hoffmann, S., Lotti-Bond, R., Hajdas, I. and Bonani, G., 2001. Persistent solar influence on North Atlantic climate during the Holocene. Science, 294(5549), 2130–2136. https://doi.org/10.1126/science.1065680

Bontemps, J.D. and Esper, J., 2011. Statistical modelling and RCS detrending methods provide similar estimates of long-term trend in radial growth of common beech in north-eastern France. Dendrochronologia, 29(2), 99–107. https://doi.org/10.1016/j.dendro.2010.09.002

Bradley, R.S. and Bakke, J., 2019. Is there evidence for a 4.2 ka BP event in the northern North Atlantic region?. Climate of the Past, 15(5), 1665–1676. https://doi.org/10.5194/cp-15-1665-2019

Braker, O.U. and Schweingruber, F.H., 1984. Standorts-Chronologien Teil 1: Iberische Halbinsel. Eidgenössische Anstalt für das forstliche Versuchswesen, Birmensdorf.

Briffa, K.R., Jones, P.D., Bartholin, T.S., Eckstein, D., Schweingruber, F.H., Karlen, W., Zetterberg, P. and Eronen, M., 1992. Fennoscandian summers from AD 500: temperature changes on short and long timescales. Climate Dynamics, 7(3), 111–119. https://doi.org/10.1007/BF00211153

Broecker, W.S. and Van Donk, J., 1970. Insolation changes, ice volumes, and the O18 record in deep-sea cores. Reviews of Geophysics, 8(1), 169–198. https://doi.org/10.1029/RG008i001p00169

Broecker, W.S., Peteet, D.M. and Rind, D., 1985. Does the ocean–atmosphere system have more than one stable mode of operation?. Nature, 315(6014), 21–26. https://doi.org/10.1038/315021a0

Broecker, W.S., Kennett, J.P., Flower, B.P., Teller, J.T., Trumbore, S., Bonani, G. and Wolfli, W., 1989. Routing of meltwater from the Laurentide Ice Sheet during the Younger Dryas cold episode. Nature, 341(6240), 318–321. https://doi.org/10.1038/341318a0

Broecker, W.S., 1994. Massive iceberg discharges as triggers for global climate change. Nature, 372(6505), 421–424. https://doi.org/10.1038/372421a0

Broecker, W.S., 2006. Was the Younger Dryas triggered by a flood?. Science, 312(5777), 1146–1148. https://doi.org/10.1126/science.1123253

Broecker, W.S., Denton, G.H., Edwards, R.L., Cheng, H., Alley, R.B. and Putnam, A.E., 2010. Putting the Younger Dryas cold event into context. Quaternary Science Reviews, 29(9-10), 1078–1081. https://doi.org/10.1016/j.quascirev.2010.02.019

Bühler, J.C., Axelsson, J., Lechleitner, F.A., Fohlmeister, J., LeGrande, A.N., Midhun, M., Sjolte, J., Werner, M., Yoshimura, K. and Rehfeld, K., 2022. Investigating stable oxygen and carbon isotopic variability in speleothem records over the last millennium using multiple isotope-enabled climate models. Climate of the Past, 18(7), 1625–1654. https://doi.org/10.5194/cp-18-1625-2022

Büntgen, U., Frank, D., Trouet, V. and Esper, J., 2010. Diverse climate sensitivity of Mediterranean tree-ring width and density. Trees, 24(2), 261–273. https://doi.org/10.1007/s00468-009-0396-y

Burg, J.P., 1967. Maximum Entropy Spectral Analysis. 37th Meeting of the Society of Exploration Geophysicists, Oklahoma City, Oklahoma. pp. 34–41.

Burrough, P.A. and McDonell, R.A., 1998. Principles of Geographical Information Systems. Oxford University Press, New York, 190p.

Bustamante, M.G., Cruz, F.W., Vuille, M., Apaéstegui, J., Strikis, N., Panizo, G., Novello, F.V., Deininger, M., Sifeddine, A., Cheng, H. and Moquet, J.S., 2016. Holocene changes in monsoon precipitation in the Andes of NE Peru based on $\delta^{18}O$ speleothem records. Quaternary Science Reviews, 146, 274–287. https://doi.org/10.1016/j.quascirev.2016.05.023

Caccamo, M.T. and Magazù, S., 2021. On the breaking of the Milankovitch cycles triggered by temperature increase: The stochastic resonance response. Climate, 9(4), 67. https://doi.org/10.3390/cli9040067

Cantalejo, B. and Pickering, K.T., 2015. Orbital forcing as principal driver for fine-grained deep-marine siliciclastic sedimentation, Middle-Eocene Ainsa Basin, Spanish Pyrenees. Palaeogeography, Palaeoclimatology, Palaeoecology, 421, 24–47. https://doi.org/10.1016/j.palaeo.2015.01.008

Capron, E., Rasmussen, S.O., Popp, T.J., Erhardt, T., Fischer, H., Landais, A., Pedro, J.B., Vettoretti, G., Grinsted, A., Gkinis, V. and Vaughn, B., 2021. The anatomy of past abrupt warmings recorded in Greenland ice. Nature Communications, 12(1), 1–12. https://doi.org/10.1038/s41467-021-22241-w

Carlson A.E., 2013. The Younger Dryas Climate Event. In: Elias S.A. (Ed.), The Encyclopedia of Quaternary Science. Elsevier, Amsterdam, 3, pp. 126-134.

Cazelles, B., Chavez, M., Berteaux, D., Ménard, F., Vik, J.O., Jenouvrier, S. and Stenseth, N.C., 2008. Wavelet analysis of ecological time series. Oecologia, 156(2), 287–304. https://doi.org/10.1007/s00442-008-0993-2

Chapman, M.R. and Shackleton, N.J., 2000. Evidence of 550-year and 1000-year cyclicities in North Atlantic circulation patterns during the Holocene. The Holocene, 10(3), 287–291. https://doi.org/10.1191%2F095968300671253196

Charvátová, I., 2000. Can origin of the 2400-year cycle of solar activity be caused by solar inertial motion?. Annales Geophysicae, 18(4), 399–405. https://doi.org/10.1007/s00585-000-0399-x

Chen, F., Xu, Q., Chen, J., Birks, H.J.B., Liu, J., Zhang, S., Jin, L., An, C., Telford, R.J., Cao, X. and Wang, Z., 2015. East Asian summer monsoon precipitation variability since the last deglaciation. Scientific Reports, 5(1), 1–11. https://doi.org/10.1038/srep11186

Chen, S., Hoffmann, S.S., Lund, D.C., Cobb, K.M., Emile-Geay, J. and Adkins, J.F., 2016. A high-resolution speleothem record of western equatorial Pacific rainfall: Implications for Holocene ENSO evolution. Earth and Planetary Science Letters, 442, 61–71. http://dx.doi.org/10.1016/j.epsl.2016.02.050

Cheng, H., Sinha, A., Cruz, F.W., Wang, X., Edwards, R.L., d'Horta, F.M., Ribas, C.C., Vuille, M., Stott, L.D. and Auler, A.S., 2013. Climate change patterns in Amazonia and biodiversity. Nature Communications, 4(1), 1–6. https://doi.org/10.1038/ncomms2415

Cheng, H., Spötl, C., Breitenbach, S.F., Sinha, A., Wassenburg, J.A., Jochum, K.P., Scholz, D., Li, X., Yi, L., Peng, Y. and Lv, Y., 2016a. Climate variations of Central Asia on orbital to millennial timescales. Scientific Reports, 6(1), 1–11. https://doi.org/10.1038/srep36975

Cheng, H., Edwards, R.L., Sinha, A., Spötl, C., Yi, L., Chen, S., Kelly, M., Kathayat, G., Wang, X., Li, X. and Kong, X., 2016b. The Asian monsoon over the past 640,000 years and ice age terminations. Nature, 534(7609), 640–646. https://doi.org/10.1038/nature18591

Cheng, H., Zhang, H., Spötl, C., Baker, J., Sinha, A., Li, H., Bartolomé, M., Moreno, A., Kathayat, G., Zhao, J. and Dong, X., 2020. Timing and structure of the Younger Dryas event and its underlying climate dynamics. Proceedings of the National Academy of Sciences, 117(38), 23408–23417. https://doi.org/10.1073/pnas.2007869117

Cita, M.B., Gibbard, P.L. and Head, M.J., 2012. Formal ratification of the GSSP for the base of the Calabrian Stage (second stage of the Pleistocene Series, Quaternary

System). Episodes Journal of International Geoscience, 35(3), 388–397. https://doi.org/10.18814/epiiugs/2012/v35i3/001

Clemens, S.C. and Tiedemann, R., 1997. Eccentricity forcing of Pliocene–early Pleistocene climate revealed in a marine oxygen-isotope record. Nature, 385(6619), 801–804. https://doi.org/10.1038/385801a0

Clemens, S.C., Holbourn, A., Kubota, Y., Lee, K.E., Liu, Z., Chen, G., Nelson, A. and Fox-Kemper, B., 2018. Precession-band variance missing from East Asian monsoon runoff. Nature Communications, 9(1), 1–12. https://doi.org/10.1038/s41467-018-05814-0

Climate Prediction Center, 2018. North Atlantic Oscillation. https://www.cpc.ncep.noaa.gov/products/precip/CWlink/pna/nao.shtml

Climatic Research Unit, 2018. University of East Anglia. Mediterranean Oscillation Indices. https://crudata.uea.ac.uk/cru/data/moi/

Cohen, K.M., Finney, S.C., Gibbard, P.L. and Fan, J.X., 2013. The ICS international chronostratigraphic chart. Episodes Journal of International Geoscience, 36(3), 199–204. http://dx.doi.org/10.18814/epiiugs/2013/v36i3/002

Comas-Bru, L., Harrison, S.P., Werner, M., Rehfeld, K., Scroxton, N. and Veiga-Pires, C., 2019. Evaluating model outputs using integrated global speleothem records of climate change since the last glacial. Climate of the Past, 15(4), 1557–1579. https://doi.org/10.5194/cp-15-1557-2019

Comas-Bru, L., Rehfeld, K., Roesch, C., Amirnezhad-Mozhdehi, S., Harrison, S.P., Atsawawaranunt, K., Ahmad, S.M., Brahim, Y.A., Baker, A., Bosomworth, M. and Breitenbach, S.F., 2020. SISALv2: a comprehensive speleothem isotope database with multiple age–depth models. Earth System Science Data, 12(4), 2579–2606. https://doi.org/10.5194/essd-12-2579-2020

Cook, E.R. and Kairiukstis, L.A., 1989. Methods of Dendrochronology. Applications in the Environmental Sciences. International Institute for Applied Systems Analysis. Kluwer Academic Publishers, Dordrecht, The Netherlands, 394p.

Cooley, J.W. and Tukey, J.W., 1965. An algorithm for the machine calculation of complex Fourier series. Mathematics of Computation, 19(90), 297–301. https://doi.org/10.2307/2003354

Copernicus Climate Change Service (C3S) Climate Data Store (CDS), 2019-2022. https://cds.climate.copernicus.eu/cdsapp#!/dataset/reanalysis-era5-single-levels-monthly-means-preliminary-back-extension?tab=overview

Croll, J., 1875. Climate and time in their geological relations: a theory of secular changes of the earth's climate. Stanford, London.

Crutzen, P.J. and Stoermer, E.F., 2000. The “Anthropocene”. Global Change Newsletter, 41, 17–18.

Cruz, F.W., Burns, S.J., Karmann, I., Sharp, W.D., Vuille, M., Cardoso, A.O., Ferrari, J.A., Silva Dias, P.L. and Viana, O., 2005. Insolation-driven changes in atmospheric circulation over the past 116,000 years in subtropical Brazil. Nature, 434(7029), 63–66. https://doi.org/10.1038/nature03365

Dansgaard, W., Johnsen, S.J., Clausen, H.B., Dahl-Jensen, D., Gundestrup, N.S., Hammer, C.U., Hvidberg, C.S., Steffensen, J.P., Sveinbjörnsdottir, A.E., Jouzel, J. and Bond, G., 1993. Evidence for general instability of past climate from a 250-kyr ice-core record. Nature, 364(6434), 218–220. https://doi.org/10.1038/364218a0

Darby, D.A., Ortiz, J.D., Grosch, C.E. and Lund, S.P., 2012. 1,500-year cycle in the Arctic Oscillation identified in Holocene Arctic sea-ice drift. Nature Geoscience, 5(12), 897–900. https://doi.org/10.1038/ngeo1629

Darbyshire, J.E. and Jenny, B., 2017. Natural-color maps via coloring of bivariate grid data. Computers & Geosciences, 106, 130–138. https://doi.org/10.1016/j.cageo.2017.06.004

Debret, M., Bout-Roumazeilles, V., Grousset, F., Desmet, M., McManus, J.F., Massei, N., Sebag, D., Petit, J.R., Copard, Y. and Trentesaux, A., 2007. The origin of the 1500-year climate cycles in Holocene North-Atlantic records. Climate of the Past, 3(4), 569–575. https://doi.org/10.5194/cp-3-569-2007

De Angelis, M., Steffensen, J.P., Legrand, M., Clausen, H. and Hammer, C., 1997. Primary aerosol (sea salt and soil dust) deposited in Greenland ice during the last climatic cycle: Comparison with east Antarctic records. Journal of Geophysical Research: Oceans, 102(C12), 26681–26698. https://doi.org/10.1029/97JC01298

Dee, S., Okumura, Y., Stevenson, S. and Di Nezio, P., 2020. Enhanced North American ENSO teleconnections during the Little Ice Age revealed by paleoclimate data assimilation. Geophysical Research Letters, 47(15), e2020GL087504. https://doi.org/10.1029/2020GL087504

Deschamps, P., Durand, N., Bard, E., Hamelin, B., Camoin, G., Thomas, A.L., Henderson, G.M., Okuno, J.I. and Yokoyama, Y., 2012. Ice-sheet collapse and sea-level rise at the Bølling warming 14,600 years ago. Nature, 483(7391), 559–564. https://doi.org/10.1038/nature10902

Deser, C., 2000. On the teleconnectivity of the "Arctic Oscillation". Geophysical Research Letters, 27(6), 779–782. https://doi.org/10.1029/1999GL010945

Dong, J., Wang, Y., Cheng, H., Hardt, B., Edwards, R.L., Kong, X., Wu, J., Chen, S., Liu, D., Jiang, X. and Zhao, K., 2010. A high-resolution stalagmite record of the Holocene East Asian monsoon from Mt Shennongjia, central China. The Holocene, 20(2), 257–264. https://doi.org/10.1177%2F0959683609350393

Duesing, W., Kaboth-Bahr, S., Asrat, A., Cohen, A.S., Foerster, V., Lamb, H.F., Schaebitz, F., Trauth, M.H. and Viehberg, F., 2021. Changes in the cyclicity and variability of the eastern African paleoclimate over the last 620 kyrs. Quaternary Science Reviews, 273, 107219. https://doi.org/10.1016/j.quascirev.2021.107219

Durán, J.J., Pardo-Igúzquiza, E., Robledo, P.A. and López-Martínez, J., 2013. Ciclicidad en espeleotemas: ¿qué señales climáticas registran? Boletín Geológico y Minero, 124(2), 307–321.

Dykoski, C.A., Edwards, R.L., Cheng, H., Yuan, D., Cai, Y., Zhang, M., Lin, Y., Qing, J., An, Z. and Revenaugh, J., 2005. A high-resolution, absolute-dated Holocene and deglacial Asian monsoon record from Dongge Cave, China. Earth and Planetary Science Letters, 233(1-2), 71–86. https://doi.org/10.1016/j.epsl.2005.01.036

Elderfield, H., Ferretti, P., Greaves, M., Crowhurst, S., McCave, I.N., Hodell, D. and Piotrowski, A.M., 2012. Evolution of ocean temperature and ice volume through the mid-Pleistocene climate transition. Science, 337(6095), 704–709. https://doi.org/10.1126/science.1221294

EPICA Community Members, 2006. One-to-one coupling of glacial climate variability in Greenland and Antarctica. Nature, 444(7116), 195–198. https://doi.org/10.1038/nature05301

Erhardt, T., Bigler, M., Federer, U., Gfeller, G., Leuenberger, D., Stowasser, O., Röthlisberger, R., Schüpbach, S., Ruth, U., Twarloh, B., Wegner, A., Goto-Azuma, K., Kuramoto, T., Kjær, H. A., Vallelonga, P. T., Siggaard-Andersen, M.-L., Hansson, M. E., Benton, A. K., Fleet, L. G., Mulvaney, R., Thomas, E. R., Abram, N., Stocker, T. F. and Fischer, H., 2022. High-resolution aerosol concentration data from the Greenland NorthGRIP and NEEM deep ice cores. Earth System Science Data, 14, 1215–1231. https://doi.org/10.5194/essd-14-1215-2022

Esper, J., Cook, E.R. and Schweingruber, F.H., 2002. Low-frequency signals in long tree-ring chronologies for reconstructing past temperature variability. Science, 295(5563), 2250–2253. https://doi.org/10.1126/science.1066208

Esper, J., Frank, D.C. and Wilson, R.J., 2004. Climate reconstructions: Low-frequency ambition and high-frequency ratification. EOS, Transactions American Geophysical Union, 85(12), 113–120. https://doi.org/10.1029/2004EO120002

Esper, J., Schneider, L., Smerdon, J.E., Schöne, B.R. and Büntgen, U., 2015. Signals and memory in tree-ring width and density data. Dendrochronologia, 35, 62–70. https://doi.org/10.1016/j.dendro.2015.07.001

Esteban-Parra, M.J., Rodrigo, F.S. and Castro-Diez, Y., 1998. Spatial and temporal patterns of precipitation in Spain for the period 1880–1992. International Journal of Climatology: A Journal of the Royal Meteorological Society, 18(14), 1557–1574. https://doi.org/10.1002/(SICI)1097-0088(19981130)18:14%3C1557::AID-JOC328%3E3.0.CO;2-J

Esteban, L.G., De Palacios, P. and Aguado, L.R.L., 2010. Abies pinsapo forests in Spain and Morocco: threats and conservation. Oryx, 44(2), 276–284. https://doi.org/10.1017/S0030605310000190

Fairbanks, R.G., 1990. The age and origin of the "Younger Dryas climate event" in Greenland ice cores. Paleoceanography, 5(6), 937–948. https://doi.org/10.1029/PA005i006p00937

Fairchild, I.J. and Baker, A., 2012. Speleothem Science: From Process to Past Environments. Wiley-Blackwell, Chichester, 449p.

Fensterer, C., Scholz, D., Hoffmann, D.L., Spötl, C., Schröder-Ritzrau, A., Horn, C., Pajon, J.M. and Mangini, A., 2013. Millennial-scale climate variability during the last 12.5 ka recorded in a Caribbean speleothem. Earth and Planetary Science Letters, 361, 143–151. https://doi.org/10.1016/j.epsl.2012.11.019

Fernández-Cancio, A., NavarroCerrillo, R.M., Fernández, R.F., Hernández, P.G., Meneéndez, E.M. and Martínez, C.C., 2007. Climate classification of Abies pinsapo Boiss. forests in Southern Spain. Forest Systems, 16(3), 222–229. https://doi.org/10.5424/srf/2007163-01011

Fernández-Montes, S. and Rodrigo, F.S., 2015. Trends in surface air temperatures, precipitation and combined indices in the southeastern Iberian Peninsula (1970-2007). Climate Research, 63(1), 43–60. https://doi.org/10.3354/cr01287

Firestone, R.B., West, A., Kennett, J.P., Becker, L., Bunch, T.E., Revay, Z.S., Schultz, P.H., Belgya, T., Kennett, D.J., Erlandson, J.M. and Dickenson, O.J., 2007. Evidence for an extraterrestrial impact 12,900 years ago that contributed to the megafaunal extinctions and the Younger Dryas cooling. Proceedings of the National Academy of Sciences, 104(41), 16016–16021. https://doi.org/10.1073/pnas.0706977104

Fischer, A.G., 1986. Climatic rhythms recorded in strata. Annual Review of Earth and Planetary Sciences, 14, 351–376.

Fischer, A.G., Silva, I.P. and De Boer, P.L., 1990. Cyclostratigraphy. In: Ginsburg, R.N. and Beaudoin, B. (Eds.), *Cretaceous resources, events and rhythms*. NATO ASI Series, 304. Springer, Dordrecht, pp. 139–172. https://doi.org/10.1007/978-94-015-6861-6_8

Fleitmann, D., Burns, S.J., Mangini, A., Mudelsee, M., Kramers, J., Villa, I., Neff, U., Al-Subbary, A.A., Buettner, A., Hippler, D. and Matter, A., 2007. Holocene ITCZ and Indian monsoon dynamics recorded in stalagmites from Oman and Yemen (Socotra). Quaternary Science Reviews, 26(1-2), 170–188. https://doi.org/10.1016/j.quascirev.2006.04.012

Fleitmann, D., Cheng, H., Badertscher, S., Edwards, R.L., Mudelsee, M., Göktürk, O.M., Fankhauser, A., Pickering, R., Raible, C.C., Matter, A. and Kramers, J., 2009. Timing and climatic impact of Greenland interstadials recorded in stalagmites from northern Turkey. Geophysical Research Letters, 36(19), L19707. https://doi.org/10.1029/2009GL040050

Fohlmeister, J., Schröder-Ritzrau, A., Scholz, D., Spötl, C., Riechelmann, D.F.C., Mudelsee, M., Wackerbarth, A., Gerdes, A., Riechelmann, S., Immenhauser, A. and Richter, D.K., 2012. Bunker Cave stalagmites: an archive for central European Holocene climate variability. Climate of the Past, 8(5), 1751–1764. https://doi.org/10.5194/cp-8-1751-2012

Foster, G., 1996. Wavelets for period analysis of unevenly sampled time series. The Astronomical Journal, 112, 1709–1729. https://doi.org/10.1086/118137

Fritts, H.C., Blasing, T.J., Hayden, B.P. and Kutzbach, J.E., 1971. Multivariate techniques for specifying tree-growth and climate relationships and for reconstructing anomalies in paleoclimate. Journal of Applied Meteorology (1962-1982), 845–864. https://www.jstor.org/stable/26175575

Fritts, H.C., 1976. *Tree-rings and Climate*. Academic Press, Great Britain. 582p.

Fuster, M.G., 2007. El crecimiento de Abies pinsapo y el clima de Grazalema: aportaciones dendroecológicas. Investigacion Agraria: Sistemas y recursos forestales, 16(2), 145–157.

Geng, L., Alexander, B., Cole-Dai, J., Steig, E.J., Savarino, J., Sofen, E.D. and Schauer, A.J., 2014. Nitrogen isotopes in ice core nitrate linked to anthropogenic atmospheric acidity change. Proceedings of the National Academy of Sciences, 111(16), 5808–5812. https://doi.org/10.1073/pnas.1319441111

Gfeller, G., Fischer, H., Bigler, M., Schüpbach, S., Leuenberger, D. and Mini, O., 2014. Representativeness and seasonality of major ion records derived from NEEM firn cores. The Cryosphere, 8(5), 1855–1870. https://doi.org/10.5194/tc-8-1855-2014

Ghosh, S., 2018. *Kernel Smoothing: Principles, Methods and Applications*. Wiley, New York, 272p.

Gibbard, P.L., Smith, A.G., Zalasiewicz, J.A., Barry, T.L., Cantrill, D., Coe, A.L., Cope, J.C., Gale, A.S., Gregory, F.J., Powell, J.H. and Rawson, P.F., 2005. What status for the Quaternary?. Boreas, 34(1), 1–6. https://doi.org/10.1111/j.1502-3885.2005.tb01000.x

Gibbard, P.L., Head, M.J., Walker, M.J. and Subcommission on Quaternary Stratigraphy, 2010. Formal ratification of the Quaternary System/Period and the Pleistocene Series/Epoch with a base at 2.58 Ma. Journal of Quaternary Science, 25(2), 96–102. https://doi.org/10.1002/jqs.1338

Gibbard, P.L. and Head, M.J., 2020. Chapter 30 - The Quaternary Period. In: Gradstein, F.M., Ogg, J.G., Schmitz, M.D. and Ogg, G.M. (Eds.), *Geologic Time Scale 2020*. Elsevier, Amsterdam, pp. 1217–1255. https://doi.org/10.1016/B978-0-12-824360-2.00030-9

Gilbert, G.K., 1895. Sedimentary measurement of geologic time. Journal of Geology, 3, 121–127.

GISP2 Meese/Sowers Timescale; gisp2age.txt
https://arcticdata.io/catalog/view/doi:10.18739/A2MS3K19N

GISP2 Ice-core 110,000 Year Ions Data is available from World Data Center (WDC) for Paleoclimatology. https://www.ncdc.noaa.gov/paleo-search/study/17805

Goldstein, B., Joos, F. and Stocker, T.F., 2003. A modeling study of oceanic nitrous oxide during the Younger Dryas cold period. Geophysical Research Letters, 30, 1092. https://doi.org/10.1029/2002GL016418

Good, P., 2000. *Permutation Test: A Practical Guide to Resampling Methods for Testing Hypothesis*, second ed. Springer, New York, 270p.

Gottschalk, J., Skinner, L.C., Misra, S., Waelbroeck, C., Menviel, L. and Timmermann, A., 2015. Abrupt changes in the southern extent of North Atlantic Deep Water during Dansgaard–Oeschger events. Nature Geoscience, 8(12), 950–954. https://doi.org/10.1038/ngeo2558

Gradstein, F.M. and Ogg, J.G., 2020. Chapter 2 - The Chronostratigraphic Scale. In: Gradstein, F.M., Ogg, J.G., Schmitz, M.D. and Ogg, G.M. (Eds.), *Geologic Time Scale 2020*. Elsevier, Amsterdam, pp. 21–32. https://doi.org/10.1016/B978-0-12-824360-2.00002-4

Grant, K.M., Rohling, E.J., Bar-Matthews, M., Ayalon, A., Medina-Elizalde, M., Ramsey, C.B., Satow, C. and Roberts, A.P., 2012. Rapid coupling between ice volume and polar temperature over the past 150,000 years. Nature, 491(7426), 744–747. https://doi.org/10.1038/nature11593

Griffiths, M.L., Drysdale, R.N., Gagan, M.K., Zhao, J.X., Ayliffe, L.K., Hellstrom, J.C., Hantoro, W.S., Frisia, S., Feng, Y.X., Cartwright, I. and Pierre, E.S., 2009. Increasing Australian–Indonesian monsoon rainfall linked to early Holocene sea-level rise. Nature Geoscience, 2(9), 636–639. https://doi.org/10.1038/NGEO605

Groen, M. and Storey, M., 2022. An astronomically calibrated ^{40}Ar/^{39}Ar age for the North Atlantic Z2 Ash: Implications for the Greenland ice core timescale. Quaternary Science Reviews, 293, 107526. https://doi.org/10.1016/j.quascirev.2022.107526

Grudd, H., 2008. Torneträsk tree-ring width and density AD 500–2004: a test of climatic sensitivity and a new 1500-year reconstruction of north Fennoscandian summers. Climate dynamics, 31(7), 843–857. https://doi.org/10.1007/s00382-007-0358-2

Hall, I.R., Bianchi, G.G. and Evans, J.R., 2004. Centennial to millennial scale Holocene climate-deep water linkage in the North Atlantic. Quaternary Science Reviews, 23(14-15), 1529–1536. https://doi:10.1016/j.quascirev.2004.04.004

Hays, J.D., Imbrie, J. and Shackleton, N.J., 1976. Variations in the Earth's Orbit: Pacemaker of the Ice Ages: For 500,000 years, major climatic changes have followed variations in obliquity and precession. Science, 194(4270), 1121–1132. https://doi.org/10.1126/science.194.4270.1121

Head, M.J. and Gibbard, P.L., 2015. Early–Middle Pleistocene transitions: linking terrestrial and marine realms. Quaternary International, 389, 7–46. https://doi.org/10.1016/j.quaint.2015.09.042

Head, M.J., 2019. Formal subdivision of the Quaternary System/Period: Present status and future directions. Quaternary International, 500, 32–51. https://doi.org/10.1016/j.quaint.2019.05.018

Heinrich, H. (1988). Origin and consequences of cyclic ice rafting in the northeast Atlantic ocean during the past 130,000 years. Quaternary Research, 29, 142–152. https://doi.org/10.1016/0033-5894(88)90057-9

Helama, S., Lindholm, M., Timonen, M. and Eronen, M., 2004. Detection of climate signal in dendrochronological data analysis: a comparison of tree-ring standardization methods. Theoretical and Applied Climatology, 79(3), 239–254. https://doi.org/10.1007/s00704-004-0077-0

Helama, S., Melvin, T.M. and Briffa, K.R., 2016. Regional curve standardization: State of the art. The Holocene, 27(1), 172–177. https://doi.org/10.1177/0959683616652709

Hellstrom, J., McCulloch, M. and Stone, J., 1998. A detailed 31,000-year record of climate and vegetation change, from the isotope geochemistry of two New Zealand speleothems. Quaternary research, 50(2), 167–178. https://doi.org/10.1006/qres.1998.1991

Hernández-Molina, F.J., Sierro, F.J., Llave, E., Roque, C., Stow, D.A.V., Williams, T., Lofi, J., Van der Schee, M., Arnáiz, A., Ledesma, S. and Rosales, C., 2016. Evolution of the gulf of Cadiz margin and southwest Portugal contourite depositional system: Tectonic, sedimentary and paleoceanographic implications from IODP expedition 339. Marine Geology, 377, 7–39. https://doi.org/10.1016/j.margeo.2015.09.013

Herrera, S., Gutiérrez, J.M., Ancell, R., Pons, M.R., Frías, M.D. and Fernández, J., 2012. Development and analysis of a 50-year high-resolution daily gridded precipitation dataset over Spain (Spain02). International Journal of Climatology, 32(1), 74–85. https://doi.org/10.1002/joc.2256

Herrera, S., Fernández, J. and Gutiérrez, J.M., 2016. Update of the Spain02 gridded observational dataset for EURO-CORDEX evaluation: assessing the effect of the interpolation methodology. International Journal of Climatology, 36(2), 900–908. https://doi.org/10.1002/joc.4391

Hersbach, H., Bell, B., Berrisford, P., Biavati, G., Horányi, A., Muñoz Sabater, J., Nicolas, J., Peubey, C., Radu, R., Rozum, I., Schepers, D., Simmons, A., Soci, C., Dee, D. and Thépaut, J-N., 2019. ERA5 monthly averaged data on pressure levels from 1959 to present. Copernicus Climate Change Service (C3S) Climate Data Store (CDS). https://doi.org/10.24381/cds.6860a573

Hinnov, L.A., 2000. New perspectives on orbitally forced stratigraphy. Annual Review of Earth and Planetary Sciences, 28(1), 419–475. https://doi.org/10.1146/annurev.earth.28.1.419

Hinnov, L.A. and Hilgen, F.J., 2012. Chapter 4 - Cyclostratigraphy and Astrochronology. In: Gradstein, F.M., Ogg, J.G., Schmitz, M.D. and Ogg, G.M. (Eds.), *The Geologic Time Scale 2012*. Elsevier, Amsterdam, pp. 63–83. https://doi.org/10.1016/B978-0-444-59425-9.00004-4

Holliday, V.T., Surovell, T., Meltzer, D.J., Grayson, D.K. and Boslough, M., 2014. The Younger Dryas impact hypothesis: a cosmic catastrophe. Journal of Quaternary Science, 29(6), 515–530. https://doi.org/10.1002/jqs.2724

Holmgren, K., Lee-Thorp, J.A., Cooper, G.R., Lundblad, K., Partridge, T.C., Scott, L., Sithaldeen, R., Talma, A.S. and Tyson, P.D., 2003. Persistent millennial-scale climatic variability over the past 25,000 years in Southern Africa. Quaternary Science Reviews, 22(21-22), 2311–2326. http://dx.doi.org/10.1016/S0277-3791(03)00204-X

Hong, Y.T., Hong, B., Lin, Q.A., Shibata, Y., Hirota, M., Zhu, Y.X., Leng, X.T., Wang, Y., Wang, H. and Yi, L., 2005. Inverse phase oscillations between the East Asian and Indian Ocean summer monsoons during the last 12 000 years and paleo-El Niño. Earth and Planetary Science Letters, 231(3-4), 337–346. https://doi.org/10.1016/j.epsl.2004.12.025

Horn, B.K., 1981. Hill shading and the reflectance map. Proceedings of the IEEE, 69(1), 14–47. https://doi.org/10.1109/PROC.1981.11918

Hu, F.S., Kaufman, D., Yoneji, S., Nelson, D., Shemesh, A., Huang, Y., Tian, J., Bond, G., Clegg, B. and Brown, T., 2003. Cyclic variation and solar forcing of Holocene climate in the Alaskan subarctic. Science, 301(5641), 1890–1893. https://doi.org/10.1126/science.1088568

Hu, J., Emile-Geay, J., Tabor, C., Nusbaumer, J. and Partin, J., 2019. Deciphering oxygen isotope records from Chinese speleothems with an isotope-enabled climate model. Paleoceanography and Paleoclimatology, 34(12), 2098–2112. https://doi.org/10.1029/2019PA003741

Huang, S., Pollack, H.N. and Shen, P.Y., 2000. Temperature trends over the past five centuries reconstructed from borehole temperatures. Nature, 403(6771), 756–758. https://doi.org/10.1038/35001556

Huybers, P. and Wunsch, C., 2005. Obliquity pacing of the late Pleistocene glacial terminations. Nature, 434(7032), 491–494. https://doi.org/10.1038/nature03401

Huybers, P., 2007. Glacial variability over the last two million years: an extended depth-derived age model, continuous obliquity pacing, and the Pleistocene progression. Quaternary Science Reviews, 26(1-2), 37–55. https://doi.org/10.1016/j.quascirev.2006.07.013

Iizuka, Y., Uemura, R., Fujita, K., Hattori, S., Seki, O., Miyamoto, C., Suzuki, T., Yoshida, N., Motoyama, H. and Matoba, S., 2018. A 60 year record of atmospheric aerosol depositions preserved in a high-accumulation dome ice core, southeast Greenland. Journal of Geophysical Research: Atmospheres, 123(1), 574–589. https://doi.org/10.1002/2017JD026733

Imbrie, J. and Imbrie, J.Z., 1980. Modelling the climatic response to orbital variations. Science, 207(4434), 943–953. https://doi.org/10.1126/science.207.4434.943

Imbrie, J., Hays, J.D., Martinson, D.G., McIntyre, A., Mix, A.C., Morley, J.J., Pisias, N.G., Prell, W.L. and Shackleton, N.J., 1984. The orbital theory of Pleistocene climate: support from a revised chronology of the marine d^{18}O record. In: Berger, A., Hays, J., Kukla, G. and Saltzman, B. (Eds.), *Milankovitch and Climate*. Reidel, Dordrecht, pp. 269–305.

Imbrie, J., Boyle, E.A., Clemens, S.C., Duffy, A., Howard, W.R., Kukla, G., Kutzbach, J., Martinson, D.G., McIntyre, A., Mix, A.C. and Molfino, B., 1992. On the structure and origin of major glaciation cycles 1. Linear responses to Milankovitch forcing. Paleoceanography, 7(6), 701–738. https://doi.org/10.1029/92PA02253

Imbrie, J., Berger, A., Boyle, E.A., Clemens, S.C., Duffy, A., Howard, W.R., Kukla, G., Kutzbach, J., Martinson, D.G., McIntyre, A. and Mix, A.C., 1993. On the structure and origin of major glaciation cycles 2. The 100,000-year cycle. Paleoceanography, 8(6), 699–735. https://doi.org/10.1029/93PA02751

Jaynes, E.T., 1957. Information Theory and Statistical Mechanics. The Physical Review, 106(4), 620–630.

Jiménez-Espejo, F.J., García-Alix, A., Jiménez-Moreno, G., Rodrigo-Gámiz, M., Anderson, R.S., Rodríguez-Tovar, F.J., Martínez-Ruiz, F., Giralt, S., Huertas, A.D. and Pardo-Igúzquiza, E., 2014. Saharan aeolian input and effective humidity variations over western Europe during the Holocene from a high altitude record. Chemical Geology, 374, 1–12. https://doi.org/10.1016/j.chemgeo.2014.03.001

Jiménez-Moreno, G., Aziz, H.A., Rodríguez-Tovar, F.J., Pardo-Igúzquiza, E. and Suc, J.P., 2007. Palynological evidence for astronomical forcing in Early Miocene lacustrine deposits from Rubielos de Mora Basin (NE Spain). Palaeogeography, Palaeoclimatology, Palaeoecology, 252(3-4), 601–616. http://dx.doi.org/10.1016/j.palaeo.2007.05.013

Jones, K.H., 1998. A comparison of algorithms used to compute hill slope as a property of the DEM. Computers & Geosciences, 24(4), 315–323. https://doi.org/10.1016/S0098-3004(98)00032-6

Kaboth-Bahr, S., Bahr, A., Zeeden, C., Yamoah, K.A., Lone, M.A., Chuang, C.K., Löwemark, L. and Wei, K.Y., 2021. A tale of shifting relations: East Asian summer and winter monsoon variability during the Holocene. Scientific Reports, 11(1), 1–10. https://dx.doi.org/10.1038%2Fs41598-021-85444-7

Kahl, J.D., Martinez, D.A., Kuhns, H., Davidson, C.I., Jaffrezo, J.L. and Harris, J.M., 1997. Air mass trajectories to Summit, Greenland: A 44-year climatology and some episodic events. Journal of Geophysical Research: Oceans, 102(C12), 26861–26875. https://doi.org/10.1029/97JC00296

Kennett, J.P., Kennett, D.J., Culleton, B.J., Aura Tortosa, J.E., Bischoff, J.L., Bunch, T.E., Daniel Jr, I.R., Erlandson, J.M., Ferraro, D., Firestone, R.B. and Goodyear, A.C., 2015. Bayesian chronological analyses consistent with synchronous age of 12,835–12,735 Cal BP for Younger Dryas boundary on four continents. Proceedings of the National Academy of Sciences, 112(32), E4344–E4353. https://doi.org/10.1073/pnas.1507146112

Kinzie, C.R., Que Hee, S.S., Stich, A., Tague, K.A., Mercer, C., Razink, J.J., Kennett, D.J., DeCarli, P.S., Bunch, T.E., Wittke, J.H. and Israde-Alcantara, I., 2014. Nanodiamond-rich layer across three continents consistent with major cosmic impact at 12,800 cal BP. The Journal of Geology, 122(5), 475–506. https://doi.org/10.1086/677046

Kirby, J.F., 2005. Which wavelet best reproduces the Fourier power spectrum? Computers & Geosciences, 31(7), 846–864. https://doi.org/10.1016/j.cageo.2005.01.014

Kirdyanov, A.V., Treydte, K.S., Nikolaev, A., Helle, G. and Schleser, G.H., 2008. Climate signals in tree-ring width, density and δ^{13}C from larches in Eastern Siberia (Russia). Chemical geology, 252(1-2), 31–41. https://doi.org/10.1016/j.chemgeo.2008.01.023

Kostadinov, T.S. and Gilb, R., 2014. Earth Orbit v2.1: a 3-D visualization and analysis model of Earth's orbit, Milankovitch cycles and insolation. Geoscientific Model Development, 7(3), 1051–1068. https://doi.org/10.5194/gmd-7-1051-2014

Kovesi, P., Holden, E.J. and Wong, J., 2014. Interactive multi-image blending for visualization and interpretation. Computers & Geosciences, 72, 147–155. https://doi.org/10.1016/j.cageo.2014.07.010

Krause, C.E., Gagan, M.K., Dunbar, G.B., Hantoro, W.S., Hellstrom, J.C., Cheng, H., Edwards, R.L., Suwargadi, B.W., Abram, N.J. and Rifai, H., 2019. Spatio-temporal evolution of Australasian monsoon hydroclimate over the last 40,000 years. Earth and Planetary Science Letters, 513, 103–112. https://doi.org/10.1016/j.epsl.2019.01.045

Lachniet, M.S., 2009. Climatic and environmental controls on speleothem oxygen-isotope values. Quaternary Science Reviews, 28(5-6), 412–432. https://doi.org/10.1016/j.quascirev.2008.10.021

Lachniet, M.S., Denniston, R.F., Asmerom, Y. and Polyak, V.J., 2014. Orbital control of western North America atmospheric circulation and climate over two glacial cycles. Nature Communications, 5(1), 1–8. https://doi.org/10.1038/ncomms4805

Lachniet, M.S., 2020. Illuminating the meaning of Asian monsoon cave speleothem records. Paleoceanography and Paleoclimatology, 35(1), e2019PA003841. http://dx.doi.org/10.1029/2019PA003841

Lambeck, K., Rouby, H., Purcell, A., Sun, Y. and Sambridge, M., 2014. Sea level and global ice volumes from the Last Glacial Maximum to the Holocene. Proceedings of the National Academy of Sciences, 111(43), 15296–15303. https://doi.org/10.1073/pnas.1411762111

Lamy, F., Arz, H.W., Bond, G.C., Bahr, A. and Pätzold, J., 2006. Multicentennial-scale hydrological changes in the Black Sea and northern Red Sea during the Holocene and the Arctic/North Atlantic Oscillation. Paleoceanography, 21(1), PA1008. http://dx.doi.org/10.1029/2005PA001184

Laskar, J., Robutel, P., Joutel, F., Gastineau, M., Correia, A.C.M. and Levrard, B., 2004. A long-term numerical solution for the insolation quantities of the Earth. Astronomy & Astrophysics, 428(1), 261–285. https://doi.org/10.1051/0004-6361:20041335

Laskar, J., Fienga, A., Gastineau, M. and Manche, H., 2011a. La2010: a new orbital solution for the long-term motion of the Earth. Astronomy & Astrophysics, 532, A89. https://doi.org/10.1051/0004-6361/201116836

Laskar, J., Gastineau, M., Delisle, J.B., Farrés, A. and Fienga, A., 2011b. Strong chaos induced by close encounters with Ceres and Vesta. Astronomy & Astrophysics, 532, L4. https://doi.org/10.1051/0004-6361/201117504

Laskar, J., 2020. Chapter 4 – Astrochronology. In: Gradstein, F.M., Ogg, J.G., Schmitz, M.D. and Ogg, G.M. (Eds.), *Geologic Time Scale 2020*. Elsevier, Amsterdam, pp. 139–158. https://doi.org/10.1016/B978-0-12-824360-2.00004-8

Legrand, M. and Mayewski, P., 1997. Glaciochemistry of polar ice cores: A review. Reviews of Geophysics, 35(3), 219–243. https://doi.org/10.1029/96RG03527

Lenoir, G. and Crucifix, M., 2018. A general theory on frequency and time–frequency analysis of irregularly sampled time series based on projection methods – Part 1: Frequency analysis. Nonlinear Processes in Geophysics, 25(1), 145–173. http://dx.doi.org/10.5194/npg-25-145-2018

Lenoir, G. and Crucifix, M., 2018. A general theory on frequency and time–frequency analysis of irregularly sampled time series based on projection methods – Part 2: Extension to time–frequency analysis. Nonlinear Processes in Geophysics, 25(1), 175–200. http://dx.doi.org/10.5194/npg-25-175-2018

Li, C. and Born, A., 2019. Coupled atmosphere-ice-ocean dynamics in Dansgaard-Oeschger events. Quaternary Science Reviews, 203, 1–20. https://doi.org/10.1016/j.quascirev.2018.10.031

Li, G. and Piper, D.J., 2015. The influence of meltwater on the Labrador Current in Heinrich event 1 and the Younger Dryas. Quaternary Science Reviews, 107, 129–137. https://doi.org/10.1016/j.quascirev.2014.10.021

Linares, J.C. and Carreira, J.A., 2009. Temperate-like stand dynamics in relict Mediterranean-fir (Abies pinsapo, Boiss.) forests from southern Spain. Annals of Forest Science, 66(6), 1–10. https://doi.org/10.1051/forest/2009040

Linares, J.C., Camarero, J.J. and Carreira, J.A., 2009. Plastic responses of Abies pinsapo xylogenesis to drought and competition. Tree Physiology, 29(12), 1525–1536. https://doi.org/10.1093/treephys/tpp084

Lindner, M., Maroschek, M., Netherer, S., Kremer, A., Barbati, A., Garcia-Gonzalo, J., Seidl, R., Delzon, S., Corona, P., Kolström, M. and Lexer, M.J., 2010. Climate change impacts, adaptive capacity, and vulnerability of European forest ecosystems. Forest Ecology and Management, 259(4), 698–709. https://doi.org/10.1016/j.foreco.2009.09.023

Lisiecki, L.E. and Raymo, M.E., 2005. A Pliocene-Pleistocene stack of 57 globally distributed benthic $\delta^{18}O$ records. Paleoceanography, 20(1), PA1003. https://doi.org/10.1029/2004PA001071

Lisiecki, L.E., 2010. Links between eccentricity forcing and the 100,000-year glacial cycle. Nature Geoscience, 3(5), 349–352. https://doi.org/10.1038/ngeo828

Liu, Z., Cleaveland, L.C. and Herbert, T.D., 2008. Early onset and origin of 100-kyr cycles in Pleistocene tropical SST records. Earth and Planetary Science Letters, 265(3-4), 703–715. https://doi.org/10.1016/j.epsl.2007.11.016

Liu, X., Liu, J., Chen, S., Chen, J., Zhang, X., Yan, J. and Chen, F., 2020. New insights on Chinese cave $\delta^{18}O$ records and their paleoclimatic significance. Earth-Science Reviews, 207, 103216. https://doi.org/10.1016/j.earscirev.2020.103216

Loáiciga, H.A., Maidment, D.R. and Valdes, J.B., 2000. Climate-change impacts in a regional karst aquifer, Texas, USA. Journal of Hydrology, 227(1-4), 173–194. https://doi.org/10.1016/S0022-1694(99)00179-1

Lofi, J., Voelker, A.H.L., Ducassou, E., Hernández-Molina, F.J., Sierro, F.J., Bahr, A., Galvani, A., Lourens, L.J., Pardo-Igúzquiza, E., Pezard, P., Rodríguez-Tovar, F.J. and Williams, T., 2016. Quaternary chronostratigraphic framework and sedimentary processes for the Gulf of Cadiz and Portuguese Contourite Depositional Systems derived from Natural Gamma Ray records. Marine Geology, 377, 40–57. https://doi.org/10.1016/j.margeo.2015.12.005

Lomb, N.R., 1976. Least-squares frequency analysis of unequally spaced data. Astrophysics and Space Science, 39(2), 447–462. https://doi.org/10.1007/BF00648343

Longley, P.A., Goodchild, M.F., Maguire, D.J., Rhind, D.W., 2015. *Geographic Information Science and Systems*, 4th edition. John Wiley & Sons, 496p.

Lourens, L., Hilgen, F., Shackleton, N., Laskar, J. and Wilson, D., 2005. The Neogene Period. In: Gradstein, F., Ogg, J. and Smith, A. (Eds.), *A Geologic Time Scale 2004*. Cambridge University Press, Cambridge, pp. 409–440. https://10.1017/CBO9780511536045.022

Luque-Espinar, J.A., Chica-Olmo, M., Pardo-Igúzquiza, E. and García-Soldado, M.J., 2008. Influence of climatological cycles on hydraulic heads across a Spanish aquifer. Journal of Hydrology, 354(1-4), 33–52. https://doi.org/10.1016/j.jhydrol.2008.02.014

Maheswaran, R. and Khosa, R., 2012. Comparative study of different wavelets for hydrologic forecasting. Computers & Geosciences, 46, 284–295. https://doi.org/10.1016/j.cageo.2011.12.015

Mann, L.E., Robel, A.A. and Meyer, C.R., 2021. Synchronization of Heinrich and Dansgaard-Oeschger Events through Ice-Ocean Interactions. Paleoceanography and Paleoclimatology, 36(11), e2021PA004334. https://doi.org/10.1029/2021PA004334

Mann, M.E., Bradley, R.S. and Hughes, M.K., 1999. Northern hemisphere temperatures during the past millennium: Inferences, uncertainties, and limitations. Geophysical research letters, 26(6), 759–762. https://doi.org/10.1029/1999GL900070

Mann, M.E., Zhang, Z., Hughes, M.K., Bradley, R.S., Miller, S.K., Rutherford, S. and Ni, F., 2008. Proxy-based reconstructions of hemispheric and global surface temperature variations over the past two millennia. Proceedings of the National Academy of Sciences, 105(36), 13252–13257. https://doi.org/10.1073/pnas.0805721105

Mann, M.E., Zhang, Z., Rutherford, S., Bradley, R.S., Hughes, M.K., Shindell, D., Ammann, C., Faluvegi, G. and Ni, F., 2009. Global signatures and dynamical origins of the Little Ice Age and Medieval Climate Anomaly. Science, 326(5957), 1256–1260. https://doi.org/10.1126/science.1177303

Maraun, D., Kurths, J. and Holschneider, M., 2007. Nonstationary Gaussian processes in wavelet domain: Synthesis, estimation, and significance testing. Physical Review E, 75(1), 016707. https://doi.org/10.1103/PhysRevE.75.016707

Martinson, D.G., Pisias, N.G., Hays, J.D., Imbrie, J., Moore, T.C. and Shackleton, N.J., 1987. Age Dating and the Orbital Theory of the Ice Ages: Development of a High-Resolution 0 to 300,000-Year Chronostratigraphy1. Quaternary Research, 27(1), 1–29. https://doi.org/10.1016/0033-5894(87)90046-9

Maslin, M.A. and Ridgwell, A.J., 2005. Mid-Pleistocene revolution and the ‘eccentricity myth’. Geological Society, London, Special Publications, 247(1), 19–34. https://doi.org/10.1144/GSL.SP.2005.247.01.02

Maslin, M., 2016. Forty years of linking orbits to ice ages. Nature, 540(7632), 208–209. https://doi.org/10.1038/540208a

Matero, I.S.O., Gregoire, L.J., Ivanovic, R.F., Tindall, J.C. and Haywood, A.M., 2017. The 8.2 ka cooling event caused by Laurentide ice saddle collapse. Earth and Planetary Science Letters, 473, 205–214. https://doi.org/10.1016/j.epsl.2017.06.011

Matskovsky, V. and Helama, S., 2016. Direct transformation of tree-ring measurements into palaeoclimate reconstructions in three-dimensional space. The Holocene, 26(3), 439–449. https://doi.org/10.1177/0959683615609748

Mayewski, P.A., Meeker, L.D., Whitlow, S., Twickler, M.S., Morrison, M.C., Alley, R.B., Bloomfield, P. and Taylor, K., 1993. The atmosphere during the Younger Dryas. Science, 261(5118), 195–197. https://doi.org/10.1126/science.261.5118.195

Mayewski, P.A., Meeker, L.D., Twickler, M.S., Whitlow, S., Yang, Q., Lyons, W.B. and Prentice, M., 1997. Major features and forcing of high-latitude northern hemisphere atmospheric circulation using a 110,000-year-long glaciochemical series. Journal of Geophysical Research: Oceans, 102(C12), 26345–26366. https://doi.org/10.1029/96JC03365

Mayewski, P.A., Rohling, E.E., Stager, J.C., Karlén, W., Maasch, K.A., Meeker, L.D., Meyerson, E.A., Gasse, F., van Kreveld, S., Holmgren, K. and Lee-Thorp, J., 2004. Holocene climate variability. Quaternary Research, 62(3), 243–255. https://doi.org/10.1016/j.yqres.2004.07.001

Mayewski, P.A., Carleton, A.M., Birkel, S.D., Dixon, D., Kurbatov, A.V., Korotkikh, E., McConnell, J., Curran, M., Cole-Dai, J., Jiang, S. and Plummer, C., 2017. Ice core and climate reanalysis analogs to predict Antarctic and Southern Hemisphere climate changes. Quaternary Science Reviews, 155, 50–66. https://doi.org/10.1016/j.quascirev.2016.11.017

Melott, A.L., Thomas, B.C., Dreschhoff, G. and Johnson, C.K., 2010. Cometary airbursts and atmospheric chemistry: Tunguska and a candidate Younger Dryas event. Geology, 38(4), 355–358. https://doi.org/10.1130/G30508.1

Melvin, T.M. and Briffa, K.R., 2008. A "signal-free" approach to dendroclimatic standardisation. Dendrochronologia, 26(2), 71–86. https://doi.org/10.1016/j.dendro.2007.12.001

Menviel, L.C., Skinner, L.C., Tarasov, L. and Tzedakis, P.C., 2020. An ice–climate oscillatory framework for Dansgaard–Oeschger cycles. Nature Reviews Earth & Environment, 1(12), 677–693. https://doi.org/10.1038/s43017-020-00106-y

Mitchell, J.M., 1976. An overview of climatic variability and its causal mechanisms. Quaternary Research, 6(4), 481–493. https://doi.org/10.1016/0033-5894(76)90021-1

Northeast Greenland Ice Stream (NEGIS), 2012. Ice-core Chemistry and Density is available from World Data Center (WDC) for Paleoclimatology. https://www.ncdc.noaa.gov/paleo-search/study/20427

Milankovitch, M., 1941. *Kanon der Erdbestrahlung und seine Anwendung auf das Eiszeiten-problem*. Sp. Acad. Royale Serbe, Belgrade (English translation: *Canon of Insolation and Ice Age Problem, Israel program for Scientific Translation*. U.S. Department of Commerce and the National Science Foundation), 633p.

Moore Jr, T.C., 2005. The Younger Dryas: From whence the fresh water?. Paleoceanography, 20(4), PA4021. https://doi.org/10.1029/2005PA001170

Moore, C.R., West, A., LeCompte, M.A., Brooks, M.J., Daniel, I.R., Goodyear, A.C., Ferguson, T.A., Ivester, A.H., Feathers, J.K., Kennett, J.P. and Tankersley, K.B., 2017. Widespread platinum anomaly documented at the Younger Dryas onset in North American sedimentary sequences. Scientific Reports, 7(1), 1–9. https://doi.org/10.1038/srep44031

Morgan, P., Smrekar, S.E., Lorenz, R., Grott, M., Kroemer, O. and Müller, N., 2017. Potential effects of surface temperature variations and disturbances and thermal convection on the Mars In Sight HP3 heat-flow determination. Space Science Reviews, 211(1), 277–313. https://doi.org/10.1007/s11214-017-0388-y

Morrill, C., Anderson, D.M., Bauer, B.A., Buckner, R., Gille, E.P., Gross, W.S., Hartman, M. and Shah, A., 2013. Proxy benchmarks for intercomparison of 8.2 ka simulations. Climate of the Past, 9(1), 423–432. https://doi.org/10.5194/cp-9-423-2013

Muller, R.A. and MacDonald, G.J., 2002. *Ice ages and astronomical causes: data, spectral analysis and mechanisms*. Springer Science & Business Media, Berlin, Heidelberg, 318p.

Murton, J.B., Bateman, M.D., Dallimore, S.R., Teller, J.T. and Yang, Z., 2010. Identification of Younger Dryas outburst flood path from Lake Agassiz to the Arctic Ocean. Nature, 464(7289), 740–743. https://doi.org/10.1038/nature08954

Muschitiello, F., D'Andrea, W.J., Schmittner, A., Heaton, T.J., Balascio, N.L., DeRoberts, N., Caffee, M.W., Woodruff, T.E., Welten, K.C., Skinner, L.C. and Simon, M.H., 2019. Deep-water circulation changes lead North Atlantic climate during deglaciation. Nature Communications, 10(1), 1–10. https://doi.org/10.1038/s41467-019-09237-3

Nie, J., King, J. and Fang, X., 2008. Late Pliocene-early Pleistocene 100-ka problem. Geophysical Research Letters, 35(21), L21606. https://doi.org/10.1029/2008GL035265

O'Brien, S.R., Mayewski, P.A., Meeker, L.D., Meese, D.A., Twickler, M.S. and Whitlow, S.I., 1995. Complexity of Holocene climate as reconstructed from a Greenland ice core. Science, 270(5244), 1962–1964. https://doi.org/10.1126/science.270.5244.1962

Obrochta, S.P., Miyahara, H., Yokoyama, Y. and Crowley, T.J., 2012. A re-examination of evidence for the North Atlantic "1500-year cycle" at Site 609. Quaternary Science Reviews, 55, 23–33. https://doi.org/10.1016/j.quascirev.2012.08.008

Papoulis, A., 1984. *Probability, Random Variables and Stochastic Processes*, second ed. McGraw-Hill International, Singapore, 576p.

Pardo-Igúzquiza, E., Chica-Olmo, M. and Rodríguez-Tovar, F.J., 1994. CYSTRATI: a computer program for spectral analysis of stratigraphic successions. Computers & Geosciences, 20(4), 511–584. https://doi.org/10.1016/0098-3004(94)90080-9

Pardo-Igúzquiza, E. and Rodŕiguez-Tovar, F.J., 2000. The permutation test as a non-parametric method for testing the statistical significance of power spectrum estimation in cyclostratigraphic research. Earth and Planetary Science Letters, 181(1-2), 175–189. https://doi.org/10.1016/S0012-821X(00)00191-6

Pardo-Igúzquiza, E., Schwarzacher, W. and Rodriguez-Tovar, F.J., 2000. A library of computer programs for assisting teaching and research in cyclostratigraphic analysis. Computers & Geosciences, 26(7), 723–740. https://doi.org/10.1016/S0098-3004(99)00139-9

Pardo-Igúzquiza, E. and Rodríguez-Tovar, F.J., 2006. Maximum entropy spectral analysis of climatic time series revisited: Assessing the statistical significance of estimated spectral peaks. Journal of Geophysical Research: Atmospheres, 111, D10102. https://doi.org/10.1029/2005JD006293

Pardo-Iguzquiza, E. and Rodríguez-Tovar, F.J., 2011. Implemented Lomb-Scargle periodogram: a valuable tool for improving cyclostratigraphic research on unevenly sampled deep-sea stratigraphic sequences. Geo-Marine Letters, 31(5), 537–545. http://dx.doi.org/10.1007/s00367-011-0247-x

Pardo-Igúzquiza, E., Durán-Valsero, J.J., Dowd, P.A., Guardiola-Albert, C., Liñan-Baena, C. and Robledo-Ardila, P.A., 2012. Estimation of spatio-temporal recharge of aquifers in mountainous karst terrains: application to Sierra de las Nieves (Spain). Journal of Hydrology, 470, 124–137. https://doi.org/10.1016/j.jhydrol.2012.08.042

Pardo-Igúzquiza, E. and Rodríguez-Tovar, F.J., 2012. Spectral and cross-spectral analysis of uneven time series with the smoothed Lomb–Scargle periodogram and Monte

Carlo evaluation of statistical significance. Computers & Geosciences, 49, 207–216. https://doi.org/10.1016/j.cageo.2012.06.018

Pardo-Igúzquiza, E. and Rodríguez-Tovar F.J., 2013. Análisis espectral de series temporales de variables geológicas con muestreo irregular. Boletín Geológico y Minero, 124(2), 323–337.

Pardo-Igúzquiza, E. and Rodríguez-Tovar, F.J., 2015. Comparison of the Performance of Two Advanced Spectral Methods for the Analysis of Times Series in Paleoceanography. Journal of Marine Science and Engineering, 3(3), 957–967. https://doi.org/10.3390/jmse3030957

Pardo-Igúzquiza, E., Durán, J.J., Luque-Espinar, J.A., Robledo-Ardila, P.A., Martos-Rosillo, S., Guardiola-Albert, C. and Pedrera, A., 2015. Karst massif susceptibility from rock matrix, fracture and conduit porosities: a case study of the Sierra de las Nieves (Málaga, Spain). Environmental Earth Sciences, 74(12), 7583–7592. https://doi.org/10.1007/s12665-015-4545-x

Pardo-Igúzquiza, E. and Dowd, P.A., 2020. Maximum entropy spectral analysis of uneven time series in the geosciences. Boletín Geológico y Minero, 131(2), 325–337. https://doi.org/10.21701/bolgeomin.131.2.007

Pardo-Igúzquiza, E. and Rodríguez-Tovar, F.J., 2021. Maximum Entropy Spectral Analysis. In: *Encyclopedia of Mathematical Geosciences*, Cham: Springer International Publishing, pp. 1–8.

Parzen, E., 1968. *Statistical Spectral Analysis (Single Channel Case) in 1968*. Stanford Univ. Press, Stanford.

Pedro, J.B., Andersson, C., Vettoretti, G., Voelker, A.H.L., Waelbroeck, C., Dokken, T.M., Jensen, M.F., Rasmussen, S.O., Sessford, E.G., Jochum, M. and Nisancioglu, K.H., 2022. Dansgaard-Oeschger and Heinrich event temperature anomalies in the North Atlantic set by sea ice, frontal position and thermocline structure. Quaternary Science Reviews, 289, 107599. https://doi.org/10.1016/j.quascirev.2022.107599

Peristykh, A.N. and Damon, P.E., 2003. Persistence of the Gleissberg 88-year solar cycle over the last~ 12,000 years: Evidence from cosmogenic isotopes. Journal of Geophysical Research: Space Physics, 108(A1), SSH-1. https://doi.org/10.1029/2002JA009390

Perşoiu, A., Ionita, M. and Weiss, H., 2019. Atmospheric blocking induced by the strengthened Siberian High led to drying in west Asia during the 4.2 ka BP event–a hypothesis. Climate of the Past, 15(2), 781–793. http://dx.doi.org/10.5194/cp-15-781-2019

Petaev, M.I., Huang, S., Jacobsen, S.B. and Zindler, A., 2013. Large Pt anomaly in the Greenland ice core points to a cataclysm at the onset of Younger Dryas. Proceedings of the National Academy of Sciences, 110(32), 12917–12920. https://doi.org/10.1073/pnas.1303924110

Pinter, N., Scott, A.C., Daulton, T.L., Podoll, A., Koeberl, C., Anderson, R.S. and Ishman, S.E., 2011. The Younger Dryas impact hypothesis: A requiem. Earth-Science Reviews, 106(3-4), 247–264. https://doi.org/10.1016/j.earscirev.2011.02.005

Press, H.W., Teukolsky, S.A., Vetterling, W.T. and Flannery, B.P., 1992. *Numerical Recipes in Fortran*, second ed. Cambridge University Press, New York, 963p.

Quézel, P., Médail, F., Loisel, R. and Barbero, M., 1999. Biodiversity and conservation of forest species in the Mediterranean basin. Unasylva, 50, 21–28. https://hdl.handle.net/10535/9505

Rahmstorf, S., 2002. Ocean circulation and climate during the past 120,000 years. Nature, 419(6903), 207–214. https://doi.org/10.1038/nature01090

Railsback, L.B., Gibbard, P.L., Head, M.J., Voarintsoa, N.R.G. and Toucanne, S., 2015. An optimized scheme of lettered marine isotope substages for the last 1.0 million years, and the climatostratigraphic nature of isotope stages and substages. Quaternary Science Reviews, 111, 94–106. https://doi.org/10.1016/j.quascirev.2015.01.012

Ramos-Calzado, P., Gómez-Camacho, J., Pérez-Bernal, F. and Pita-López, M.F., 2008. A novel approach to precipitation series completion in climatological datasets: application to Andalusia. International Journal of Climatology: A Journal of the Royal Meteorological Society, 28(11), 1525–1534. https://doi.org/10.1002/joc.1657

Rasmussen, S.O., Andersen, K.K., Svensson, A.M., Steffensen, J.P., Vinther, B.M., Clausen, H.B., Siggaard-Andersen, M.L., Johnsen, S.J., Larsen, L.B., Dahl-Jensen, D. and Bigler, M., 2006. A new Greenland ice core chronology for the last glacial termination. Journal of Geophysical Research: Atmospheres, 111, D06102. https://doi.org/10.1029/2005JD006079

Rasmussen, S.O., Bigler, M., Blockley, S.P., Blunier, T., Buchardt, S.L., Clausen, H.B., Cvijanovic, I., Dahl-Jensen, D., Johnsen, S.J., Fischer, H. and Gkinis, V., 2014. A stratigraphic framework for abrupt climatic changes during the Last Glacial period based on three synchronized Greenland ice-core records: refining and extending the INTIMATE event stratigraphy. Quaternary Science Reviews, 106, 14–28. https://doi.org/10.1016/j.quascirev.2014.09.007

Raspopov, O.M., Dergachev, V.A., Esper, J., Kozyreva, O.V., Frank, D., Ogurtsov, M., Kolström, T. and Shao, X., 2008. The influence of the de Vries (~ 200-year) solar cycle on climate variations: Results from the Central Asian Mountains and their global link. Palaeogeography, Palaeoclimatology, Palaeoecology, 259(1), 6–16. https://doi.org/10.1016/j.palaeo.2006.12.017

Raymo, M.E., 1997. The timing of major climate terminations. Paleoceanography, 12(4), 577–585. https://doi.org/10.1029/97PA01169

Raymo, M.E. and Nisancioglu, K.H., 2003. The 41 kyr world: Milankovitch's other unsolved mystery. Paleoceanography, 18(1), 1011. https://doi.org/10.1029/2002PA000791

Reddy, P. and Gandhi, N., 2022. Indian Summer Monsoon variability on different timescales and deciphering its oscillations from irregularly spaced paleoclimate data using different spectral techniques. In: *Holocene Climate Change and Environment*, Elsevier, Amsterdam, pp. 339–368. https://doi.org/10.1016/B978-0-323-90085-0.00025-5

Rehfeld, K., Marwan, N., Heitzig, J. and Kurths, J., 2011. Comparison of correlation analysis techniques for irregularly sampled time series. Nonlinear Processes in Geophysics, 18(3), 389–404. https://doi.org/10.5194/npg-18-389-2011

Reinig, F., Cherubini, P., Engels, S., Esper, J., Guidobaldi, G., Jöris, O., Lane, C., Nievergelt, D., Oppenheimer, C., Park, C. and Pfanz, H., 2020. Towards a dendrochronologically refined date of the Laacher See eruption around 13,000 years ago. Quaternary Science Reviews, 229, 106128. https://doi.org/10.1016/j.quascirev.2019.106128

Reinig, F., Wacker, L., Jöris, O., Oppenheimer, C., Guidobaldi, G., Nievergelt, D., Adolphi, F., Cherubini, P., Engels, S., Esper, J. and Land, A., 2021. Precise date for the Laacher See eruption synchronizes the Younger Dryas. Nature, 595(7865), 66–69. https://doi.org/10.1038/s41586-021-03608-x

Renssen, H., Seppä, H., Crosta, X., Goosse, H. and Roche, D.M., 2012. Global characterization of the Holocene thermal maximum. Quaternary Science Reviews, 48, 7–19. https://doi.org/10.1016/j.quascirev.2012.05.022

Renssen, H., Goosse, H., Roche, D.M. and Seppä, H., 2018. The global hydroclimate response during the Younger Dryas event. Quaternary Science Reviews, 193, 84–97. https://doi.org/10.1016/j.quascirev.2018.05.033

Rhodes, R.H., Yang, X. and Wolff, E.W., 2018. Sea ice versus storms: what controls sea salt in arctic ice cores?. Geophysical Research Letters, 45(11), 5572–5580. https://doi.org/10.1029/2018GL077403

Rio, D., Sprovieri, R., Castradori, D. and Di Stefano, E., 1998. The Gelasian Stage (Upper Pliocene): A new unit of the global standard chronostratigraphic scale. Episodes Journal of International Geoscience, 21(2), 82–87. https://doi.org/10.18814/epiiugs/1998/v21i2/002

Risebrobakken, B., Jansen, E., Andersson, C., Mjelde, E. and Hevrøy, K., 2003. A high-resolution study of Holocene paleoclimatic and paleoceanographic changes in the Nordic Seas. Paleoceanography, 18(1), 1017. https://doi.org/10.1029/2002PA000764

Rodrigo, F.S., Esteban-Parra, M.J., Pozo-Vázquez, D. and Castro-Díez, Y., 1999. A 500-year precipitation record in Southern Spain. International Journal of Climatology: A Journal of the Royal Meteorological Society, 19(11), 1233–1253. https://doi.org/10.1002/(SICI)1097-0088(199909)19:11%3C1233::AID-JOC413%3E3.0.CO;2-L

Rodrigo, F.S., Esteban-Parra, M.J., Pozo-Vázquez, D. and Castro-Díez, Y., 2000. Rainfall variability in southern Spain on decadal to centennial time scales. International Journal of Climatology: A Journal of the Royal Meteorological Society, 20(7), 721–732. https://doi.org/10.1002/1097-0088(20000615)20:7%3C721::AID-2007JOC520%3E3.0.CO;2-Q

Rodrigo, F.S., 2007. The Andalusian Climate Through Historical Records. In: *El cambio climático en Andalucía: evolución y consecuencias medioambientales*. Consejería de Medio Ambiente (Junta de Andalucía), pp. 25–41.

Rodrigo, F.S., Gómez-Navarro, J.J. and Montávez Gómez, J.P., 2012. Climate variability in Andalusia (southern Spain) during the period 1701–1850 based on documentary sources: evaluation and comparison with climate model simulations. Climate of the Past, 8(1), 117–133. https://doi.org/10.5194/cp-8-117-2012

Rodrigo-Gámiz, M., Martínez-Ruiz, F., Rodríguez-Tovar, F.J., Jiménez-Espejo, F.J. and Pardo-Igúzquiza, E., 2014. Millennial-to centennial-scale climate periodicities and forcing mechanisms in the westernmost Mediterranean for the past 20,000 yr. Quaternary Research, 81(1), 78–93. https://doi:10.1016/j.yqres.2013.10.009

Rodrigo-Gámiz, M., Martínez-Ruiz, F., Rodríguez-Tovar, F.J., Pardo-Igúzquiza, E. and Ortega-Huertas, M., 2018. Appraising timing response of paleoenvironmental proxies to the Bond cycle in the western Mediterranean over the last 20 kyr. Climate Dynamics, 50(7), 2925–2934. http://dx.doi.org/10.1016/j.yqres.2013.10.009

Rodríguez-Tovar, F.J., Reolid, M. and Pardo-Igúzquiza, E., 2010. Planktonic versus benthic foraminifera response to Milankovitch forcing (Late Jurassic, Betic Cordillera): testing methods for cyclostratigraphic analysis. Facies, 56(3), 459–470. http://dx.doi.org/10.1007/s10347-010-0216-2

Rodríguez-Tovar, F.J., 2014. Orbital climate cycles in the fossil record: from semidiurnal to million-year biotic responses. Annual Review of Earth and Planetary Sciences, 42, 69–102. https://doi.org/10.1146/annurev-earth-120412-145922

Rodríguez-Tovar, F.J., Pardo-Igúzquiza, E., Reolid, M. and Bartolini, A., 2016. Spectral analysis of Toarcian sediments from the Valdorbia Section (Umbria-Marche-Apennines): the astronomical input in the foraminiferal record. Rivista Italiana di Paleontologia e Stratigrafia, 122(2), 45–60.

Ruddiman, W.F., Raymo, M. and McIntyre, A., 1986. Matuyama 41,000-year cycles: North Atlantic Ocean and northern hemisphere ice sheets. Earth and Planetary Science Letters, 80(1-2), 117–129. https://doi.org/10.1016/0012-821X(86)90024-5

Ruggieri, E., Herbert, T., Lawrence, K.T. and Lawrence, C.E., 2009. Change point method for detecting regime shifts in paleoclimatic time series: Application to $\delta^{18}O$ time series of the Plio-Pleistocene. Paleoceanography, 24(1), PA1204. https://doi.org/10.1029/2007PA001568

Russell, J.M. and Johnson, T.C., 2005. Late Holocene climate change in the North Atlantic and equatorial Africa: Millennial-scale ITCZ migration. Geophysical Research Letters, 32(17), L17705. https://doi.org/10.1029/2005GL023295

Sakerin, S.M., Kabanov, D.M., Makarov, V.I., Pol’kin, V.V., Popova, S.A., Chankina, O.V., Pochufarov, A.O., Radionov, V.F. and Rize, D.D., 2020. Spatial Distribution of Atmospheric Aerosol Physicochemical Characteristics in the Russian Sector of the Arctic Ocean. Atmosphere, 11(11), 1170. https://doi.org/10.3390/atmos11111170

Sánchez-Morales, J., Pardo-Igúzquiza, E., Rodríguez-Tovar, F.J. and Dowd, P.A., 2019. A new method for reconstructing past-climate trends using tree-ring data and kernel smoothing. Dendrochronologia, 55, 1-15. https://doi.org/10.1016/j.dendro.2019.03.002

Sánchez-Morales, J., Pardo-Igúzquiza, E. and Rodríguez-Tovar, F.J., 2019. Spatial distribution of climatic cycles in Andalusia (Southern Spain). In: Valenzuela, O., Rojas, F., Pomares, H. and Rojas, I. (Eds.), *Theory and Applications of Time Series Analysis*. Elsevier, Amsterdam, pp. 243–255. https://doi.org/10.1007/978-3-030-26036-1

Scargle, J.D., 1982. Studies in astronomical time series analysis. II-Statistical aspects of spectral analysis of unevenly spaced data. The Astrophysical Journal, 263, 835–853. https://doi.org/10.1086/160554

Scargle, J.D., 1997. Wavelet methods in astronomical time series analysis, In: Rao, T. S., Priestley M. B. and Lessi, O. (Eds.), Applications of Time Series Analysis in Astronomy and Meteorology, Chapman & Hall, New York, NY, pp. 226–248.

Schulz, M. and Stattegger, K., 1997. SPECTRUM: Spectral analysis of unevenly spaced paleoclimatic time series. Computers & Geosciences, 23(9), 929–945. https://doi.org/10.1016/S0098-3004(97)00087-3

Schulz, M., 2002. On the 1470-year pacing of Dansgaard-Oeschger warm events. Paleoceanography, 17(2). https://doi.org/10.1029/2000PA000571

Schulz, M. and Paul, A., 2002. Holocene climate variability on centennial-to-millennial time scales: 1. Climate records from the North-Atlantic realm. In: *Climate development and history of the North Atlantic realm*, Springer, Berlin, Heidelberg, pp. 41–54.

Schulz, M. and Mudelsee, M., 2002. REDFIT: estimating red-noise spectra directly from unevenly spaced paleoclimatic time series. Computers & Geosciences, 28(3), 421–426. https://doi.org/10.1016/S0098-3004(01)00044-9

Schüpbach, S., Fischer, H., Bigler, M., Erhardt, T., Gfeller, G., Leuenberger, D., Mini, O., Mulvaney, R., Abram, N.J., Fleet, L. and Frey, M.M., 2018. Greenland records of aerosol source and atmospheric lifetime changes from the Eemian to the Holocene. Nature Communications, 9(1), 1–10. https://doi.org/10.1038/s41467-018-03924-3

Schwarzacher, W., 1975. *Sedimentation models and quantitative stratigraphy*. Elsevier, Amsterdam, 381p.

Schwarzacher, W., 2000. Repetitions and cycles in stratigraphy. Earth-Science Reviews, 50(1-2), 51–75. https://doi.org/10.1016/S0012-8252(99)00070-7

Schweingruber, F.H., 1987. *Tree Rings, Basics and Applications of Dendrochronology*. Reidel Publishing Company, Dordrecht, 276p.

Scargle, J.D., 1997. Wavelet methods in astronomical time series analysis. In: Rao, T. S., Priestley M. B. and Lessi, O. (Eds.), *Applications of Time Series Analysis in Astronomy and Meteorology*. Chapman & Hall, New York, pp. 226–248. https://doi.org/10.1029/2000PA000571

Seierstad, I.K., Abbott, P.M., Bigler, M., Blunier, T., Bourne, A.J., Brook, E., Buchardt, S.L., Buizert, C., Clausen, H.B., Cook, E. and Dahl-Jensen, D., 2014. Consistently dated records from the Greenland GRIP, GISP2 and NGRIP ice cores for the past 104 ka reveal regional millennial-scale $\delta^{18}O$ gradients with possible Heinrich event imprint. Quaternary Science Reviews, 106, 29–46. https://doi.org/10.1016/j.quascirev.2014.10.032

Sen, A.K., Filippelli, G.M. and Flores, J.A., 2009. An application of wavelet analysis to paleoproductivity records from the Southern Ocean. Computers & Geosciences, 35(7), 1445–1450. https://doi.org/10.1016/j.cageo.2008.10.003

Shackleton, N.J., 1969. The last interglacial in the marine and terrestrial records. Proceedings of the Royal Society of London. Series B. Biological Sciences, 174(1034), 135–154. https://doi.org/10.1098/rspb.1969.0085

Shackleton, N.J., Berger, A. and Peltier, W.R., 1990. An alternative astronomical calibration of the lower Pleistocene timescale based on ODP Site 677. Earth and Environmental Science Transactions of the Royal Society of Edinburgh, 81(4), 251–261. https://doi.org/10.1017/S0263593300020782

Shannon, C.E., 1948. A mathematical theory of communication. The Bell System Technical Journal, 27(3), 379–423. https://doi.org/10.1002/j.1538-7305.1948.tb01338.x

Sneed, S.B., Mayewski, P.A., Sayre, W.G., Handley, M.J., Kurbatov, A.V., Taylor, K.C., Bohleber, P., Wagenbach, D., Erhardt, T. and Spaulding, N.E., 2015. New LA-ICP-MS cryocell and calibration technique for sub-millimeter analysis of ice cores. Journal of Glaciology, 61(226), 233–242. https://doi.org/10.3189/2015JoG14J139

Sneed, S.B., 2017. Ultra-High Resolution Laser Ablation Inductively Coupled Plasma Mass Spectrometry (LA-ICP-MS) measurements of Younger Dryas onset in the Greenland Ice Sheet Project 2 (GISP2) ice-core, Greenland. Arctic Data Center. https://doi.org/10.18739/A2MS3K19N

Sone, T., Kano, A., Okumura, T., Kashiwagi, K., Hori, M., Jiang, X. and Shen, C.C., 2013. Holocene stalagmite oxygen isotopic record from the Japan Sea side of the Japanese Islands, as a new proxy of the East Asian winter monsoon. Quaternary Science Reviews, 75, 150–160. https://doi.org/10.1016/j.quascirev.2013.06.019

Sonnet, C.P., 1984. Very long solar periods and the radiocarbon record. Reviews of Geophysics, 22(3), 239–254. https://doi.org/10.1029/RG022i003p00239

Sorrel, P., Debret, M., Billeaud, I., Jaccard, S.L., McManus, J.F. and Tessier, B., 2012. Persistent non-solar forcing of Holocene storm dynamics in coastal sedimentary archives. Nature Geoscience, 5(12), 892–896. https://doi.org/10.1038/ngeo1619

Speer, J.H., 2010. *Fundamental of Tree-Ring Research*. University of Arizona Press, Arizona, 333p.

Spicer, R. and Gartner, B.L., 2001. The effects of cambial age and position within the stem on specific conductivity in Douglas-fir (Pseudotsuga menziesii) sapwood. Trees, 15(4), 222–229. https://doi.org/10.1007/s004680100093

Stuiver, M. and Braziunas, T.F., 1989. Atmospheric ^{14}C and century-scale solar oscillations. Nature, 338(6214), 405–408. https://doi.org/10.1038/338405a0

Suganuma, Y., Okada, M., Head, M.J., Kameo, K., Haneda, Y., Hayashi, H., Irizuki, T., Itaki, T., Izumi, K., Kubota, Y. and Nakazato, H., 2021. Formal ratification of the global boundary stratotype section and point (GSSP) for the Chibanian stage and middle Pleistocene subseries of the Quaternary system: the Chiba section, Japan. Episodes Journal of International Geoscience, 44(3), 317–347. https://doi.org/10.18814/epiiugs/2020/020080

Sun, N., Brandon, A.D., Forman, S.L., Waters, M.R. and Befus, K.S., 2020. Volcanic origin for Younger Dryas geochemical anomalies ca. 12,900 cal BP. Science Advances, 6(31), eaax8587. https://doi.org/10.1126/sciadv.aax8587

Svensson, A., Andersen, K.K., Bigler, M., Clausen, H.B., Dahl-Jensen, D., Davies, S.M., Johnsen, S.J., Muscheler, R., Rasmussen, S.O., Röthlisberger, R. and Steffensen, J.P., 2006. The Greenland ice core chronology 2005, 15–42 ka. Part 2: comparison to other records. Quaternary Science Reviews, 25(23-24), 3258–3267. https://doi.org/10.1016/j.quascirev.2006.08.003

Svensson, A., Andersen, K.K., Bigler, M., Clausen, H.B., Dahl-Jensen, D., Davies, S.M., Johnsen, S.J., Muscheler, R., Parrenin, F., Rasmussen, S.O. and Roethlisberger, R., 2008. A 60000-year Greenland stratigraphic ice core chronology. Climate of the Past, 4(1), 47–57. https://doi.org/10.5194/cp-4-47-2008

Svensson, A., Dahl-Jensen, D., Steffensen, J.P., Blunier, T., Rasmussen, S.O., Vinther, B.M., Vallelonga, P., Capron, E., Gkinis, V., Cook, E. and Kjær, H.A., 2020. Bipolar volcanic synchronization of abrupt climate change in Greenland and Antarctic ice cores during the last glacial period. Climate of the Past, 16(4), 1565–1580. https://doi.org/10.5194/cp-16-1565-2020

Sweatman, M.B., 2021. The Younger Dryas impact hypothesis: review of the impact evidence. Earth-Science Reviews, 218, 103677. https://doi.org/10.1016/j.earscirev.2021.103677

Tarasov, L. and Peltier, W.R., 2005. Arctic freshwater forcing of the Younger Dryas cold reversal. Nature, 435(7042), 662–665. https://doi.org/10.1038/nature03617

Thakur, G., Brevdo, E., Fučkar, N.S. and Wu, H.T., 2013. The synchrosqueezing algorithm for time-varying spectral analysis: Robustness properties and new paleoclimate applications. Signal Processing, 93(5), 1079–1094. https://doi.org/10.1016/j.sigpro.2012.11.029

Thomas, M.A., Devasthale, A. and Kahnert, M., 2022. Marine aerosol properties over the Southern Ocean in relation to the wintertime meteorological conditions. Atmospheric Chemistry and Physics, 22(1), 119-137. https://doi.org/10.5194/acp-22-119-2022

Thomson, D.J., 1982. Spectrum analysis and harmonic analysis. Proc. IEEE, 70(9), 1055–1096.

Thompson, W.G. and Goldstein, S.L., 2006. A radiometric calibration of the SPECMAP timescale. Quaternary Science Reviews, 25(23-24), 3207–3215. https://doi.org/10.1016/j.quascirev.2006.02.007

Tibshirani, R.J. and Efron, B., 1993. *An introduction to the bootstrap*. Monographs on statistics and applied probability, 57, Chapman & Hall, New York, 436p.

Timmermann, A., An, S.I., Kug, J.S., Jin, F.F., Cai, W., Capotondi, A., Cobb, K.M., Lengaigne, M., McPhaden, M.J., Stuecker, M.F. and Stein, K., 2018. El Niño–southern oscillation complexity. Nature, 559(7715), 535–545. https://doi.org/10.1038/s41586-018-0252-6

Torrence, C. and Compo, G.P., 1998. A practical guide to wavelet analysis. Bulletin of the American Meteorological Society, 79(1), 61–78. https://doi.org/10.1175/1520-0477(1998)079%3C0061:APGTWA%3E2.0.CO;2

Trauth, M.H., 2021. Spectral analysis in Quaternary sciences. Quaternary Science Reviews, 270, 107157. https://doi.org/10.1016/j.quascirev.2021.107157

Stoffel, M., Bollschweiler, M., Butler, D.R. and Luckman, B.H., 2010. *Tree rings and natural hazards. A State-of-the Art*. In: Stoffel, M., Bollschweiler, M., Butler, D.R. and

Luckman, B.H. (Eds.), Advances in Global Change Research 41. Springer, Heidelberg, New York, 505p.

Turney, C., Baillie, M., Clemens, S., Brown, D., Palmer, J., Pilcher, J., Reimer, P. and Leuschner, H.H., 2005. Testing solar forcing of pervasive Holocene climate cycles. Journal of Quaternary Science: Published for the Quaternary Research Association, 20(6), 511–518. https://doi.org/10.1002/jqs.927

Tzedakis, P.C., Crucifix, M., Mitsui, T. and Wolff, E.W., 2017. A simple rule to determine which insolation cycles lead to interglacials. Nature, 542(7642), 427–432. https://doi.org/10.1038/nature21364

Ultra-High Resolution Laser Ablation Inductively Coupled Plasma Mass Spectrometry (LA-ICP-MS) measurements of Younger Dryas onset in the Greenland Ice Sheet Project 2 (GISP2) ice-core is available from the NSF Arctic Data Center. https://doi.org/10.18739/A2MS3K19N

Usoskin, I.G., Gallet, Y., Lopes, F., Kovaltsov, G.A. and Hulot, G., 2016. Solar activity during the Holocene: the Hallstatt cycle and its consequence for grand minima and maxima. Astronomy & Astrophysics, 587, A150. https://doi.org/10.1051/0004-6361/201527295

Van Hoesel, A., Hoek, W.Z., Pennock, G.M. and Drury, M.R., 2014. The Younger Dryas impact hypothesis: a critical review. Quaternary Science Reviews, 83, 95–114. https://doi.org/10.1016/j.quascirev.2013.10.033

Vallelonga, P., Christianson, K., Alley, R.B., Anandakrishnan, S., Christian, J.E.M., Dahl-Jensen, D., Gkinis, V., Holme, C., Jacobel, R.W., Karlsson, N.B. and Keisling, B.A., 2014. Initial results from geophysical surveys and shallow coring of the Northeast Greenland Ice Stream (NEGIS). The Cryosphere, 8(4), 1275–1287. https://doi.org/10.5194/tc-8-1275-2014

Vasiliev, S.S. and Dergachev, V.A., 2002. The ~2400-year cycle in atmospheric radiocarbon concentration: bispectrum of 14 C data over the last 8000 years. Annales Geophysicae, 20(1), 115–120. https://doi.org/10.5194/angeo-20-115-2002

Vegas, J., Pardo-Igúzquiza, E., Galán, L. and García-Cortés, A., 2013. Ciclicidad en el registro sedimentario de la laguna del maar de Fuentillejo: historia climática de los últimos 47000 años cal BP. Boletín Geológico y Minero, 124(2), 217–234.

Verdon, D.C. and Franks, S.W., 2006. Long-term behaviour of ENSO: Interactions with the PDO over the past 400 years inferred from paleoclimate records. Geophysical Research Letters, 33(6), L06712. https://doi.org/10.1029/2005GL025052

Walker, M., Head, M.J., Berkelhammer, M., Björck, S., Cheng, H., Cwynar, L., Fisher, D., Gkinis, V., Long, A., Lowe, J. and Newnham, R., 2018. Formal ratification of the subdivision of the Holocene Series/Epoch (Quaternary System/Period): two new Global Boundary Stratotype Sections and Points (GSSPs) and three new stages/subseries. Episodes Journal of International Geoscience, 41(4), 213–223. https://doi.org/10.18814/epiiugs/2018/018016

Walker, M., Head, M.J., Lowe, J., Berkelhammer, M., BjÖrck, S., Cheng, H., Cwynar, L.C., Fisher, D., Gkinis, V., Long, A. and Newnham, R., 2019. Subdividing the Holocene Series/Epoch: formalization of stages/ages and subseries/subepochs, and designation of GSSPs and auxiliary stratotypes. Journal of Quaternary Science, 34(3), 173–186. https://doi.org/10.1002/jqs.3097

Wang, C. and Fiedler, P.C., 2006. ENSO variability and the eastern tropical Pacific: A review. Progress in Oceanography, 69(2-4), 239–266. https://doi.org/10.1016/j.pocean.2006.03.004

Wang, P., Gao, J. and Wang, Z., 2014. Time-frequency analysis of seismic data using synchrosqueezing transform. IEEE Geoscience and Remote Sensing Letters, 11(12), 2042–2044. https://doi.org/10.1109/LGRS.2014.2317578

Wang, Y., Cheng, H., Edwards, R.L., He, Y., Kong, X., An, Z., Wu, J., Kelly, M.J., Dykoski, C.A. and Li, X., 2005. The Holocene Asian monsoon: links to solar changes and North Atlantic climate. Science, 308(5723), 854–857. https://doi.org/10.1126/science.1106296

Wanner, H., Solomina, O., Grosjean, M., Ritz, S.P. and Jetel, M., 2011. Structure and origin of Holocene cold events. Quaternary Science Reviews, 30(21-22), 3109–3123. https://doi.org/10.1016/j.quascirev.2011.07.010

Weedon, G.P., 2003. *Time-series analysis and cyclostratigraphy: examining stratigraphic records of environmental cycles*. Cambridge University Press, Cambridge, 259p.

Welch, P., 1967. The use of fast Fourier transform for the estimation of power spectra: a method based on time averaging over short, modified periodograms. IEEE Transactions on audio and electroacoustics, 15(2), 70–73. https://doi.org/10.1109/TAU.1967.1161901

Wilson, J.P. and Gallant, J.C., 2000. *Terrain Analysis: Principles and Applications*. In: Wilson, J.P. and Gallant, J.C. (Eds.). John Wiley & Sons, New York, 512p.

Wilson, R.J., Luckman, B.H. and Esper, J., 2005. A 500 year dendroclimatic reconstruction of spring–summer precipitation from the lower Bavarian Forest region, Germany. International Journal of Climatology: A Journal of the Royal Meteorological Society, 25(5), 611–630. https://doi.org/10.1002/joc.1150

Wimmer, R. and Vetter, R.E., 1999. *Tree Ring Analysis: Biological, Methodological and Environmental Aspects*. CABI Publishing, Wallingford, 302p.

Witt, A. and Schumann, A.Y., 2005. Holocene climate variability on millennial scales recorded in Greenland ice cores. Nonlinear Processes in Geophysics, 12(3), 345–352. https://doi.org/10.5194/npg-12-345-2005

Wolbach, W.S., Ballard, J.P., Mayewski, P.A., Adedeji, V., Bunch, T.E., Firestone, R.B., French, T.A., Howard, G.A., Israde-Alcántara, I., Johnson, J.R. and Kimbel, D., 2018. Extraordinary biomass-burning episode and impact winter triggered by the Younger Dryas cosmic impact~ 12,800 years ago. 1. Ice cores and glaciers. The Journal of Geology, 126(2), 165–184. https://doi.org/10.1086/695703

Wolbach, W.S., Ballard, J.P., Mayewski, P.A., Parnell, A.C., Cahill, N., Adedeji, V., Bunch, T.E., Domínguez-Vázquez, G., Erlandson, J.M., Firestone, R.B. and French, T.A., 2018. Extraordinary biomass-burning episode and impact winter triggered by the Younger Dryas cosmic impact~ 12,800 years ago. 2. Lake, marine, and terrestrial sediments. The Journal of Geology, 126(2), 185–205. https://doi.org/10.1086/695704

Wolff, E.W., Chappellaz, J., Blunier, T., Rasmussen, S.O. and Svensson, A., 2010. Millennial-scale variability during the last glacial: The ice core record. Quaternary Science Reviews, 29(21-22), 2828–2838. https://doi.org/10.1016/j.quascirev.2009.10.013

Wolff, E.W., Fischer, H., van Ommen, T. and Hodell, D.A., 2022. Stratigraphic templates for ice core records of the past 1.5 Myr. Climate of the Past, 18(7), 1563–1577. https://doi.org/10.5194/cp-18-1563-2022

Wu, Y., Sharma, M., LeCompte, M.A., Demitroff, M.N. and Landis, J.D., 2013. Origin and provenance of spherules and magnetic grains at the Younger Dryas boundary. Proceedings of the National Academy of Sciences, 110(38), E3557–E3566. https://doi.org/10.1073/pnas.1304059110

Wurtzel, J.B., Abram, N.J., Lewis, S.C., Bajo, P., Hellstrom, J.C., Troitzsch, U. and Heslop, D., 2018. Tropical Indo-Pacific hydroclimate response to North Atlantic forcing during the last deglaciation as recorded by a speleothem from Sumatra, Indonesia. Earth and Planetary Science Letters, 492, 264–278. https://doi.org/10.1016/j.epsl.2018.04.001

Xu, T., Shi, Z. and An, Z., 2018. Responses of ENSO and NAO to the external radiative forcing during the last millennium: Results from CCSM4 and MPI-ESM-P simulations. Quaternary International, 487, 99–111. https://doi.org/10.1016/j.quaint.2017.12.038

Yang, H., Johnson, K.R., Griffiths, M.L. and Yoshimura, K., 2016. Interannual controls on oxygen isotope variability in Asian monsoon precipitation and implications for paleoclimate reconstructions. Journal of Geophysical Research: Atmospheres, 121(14), 8410–8428. https://doi.org/10.1002/2015JD024683

Yevjevich, V., 1972. *Stochastic process in hydrology*. Water Resources Publications, Fort Collins, 276p.

Zhai, S., McConnell, J., Geng, L., Cole-Dai, J. and Alexander, B., 2021. Ice-core data of Sodium (Na), Chlorine (Cl), and Acidity from 6 Greenland ice-cores 1750-2012. Arctic Data Center. https://doi.org/10.18739/A2XS5JJ1N

Zhang, H.L., Yu, K.F., Zhao, J.X., Feng, Y.X., Lin, Y.S., Zhou, W. and Liu, G.H., 2013. East Asian Summer Monsoon variations in the past 12.5 ka: High-resolution $\delta^{18}O$ record from a precisely dated aragonite stalagmite in central China. Journal of Asian Earth Sciences, 73, 162–175. https://doi.org/10.1016/j.jseaes.2013.04.015

Zhang, H., Ait Brahim, Y., Li, H., Zhao, J., Kathayat, G., Tian, Y., Baker, J., Wang, J., Zhang, F., Ning, Y. and Edwards, R.L., 2019. The Asian summer monsoon: Teleconnections and forcing mechanisms—A review from Chinese speleothem $\delta^{18}O$ records. Quaternary, 2(3), 26. https://doi.org/10.3390/quat2030026

Zhao, N., Yan, H., Yang, Y., Liu, C., Ma, X., Wang, G., Zhou, P., Wen, H., Qu, X. and Dodson, J., 2021. A 23.7-year long daily growth rate record of a modern giant clam shell from South China Sea and its potential in high-resolution paleoclimate reconstruction. Palaeogeography, Palaeoclimatology, Palaeoecology, 583, 110682. https://doi.org/10.1016/j.palaeo.2021.110682

Żywiec, M., Muter, E., Zielonka, T., Delibes, M., Calvo, G. and Fedriani, J.M., 2017. Long-term effect of temperature and precipitation on radial growth in a threatened thermo-Mediterranean tree population. Trees, 31(2), 491–501. https://doi.org/10.1007/s00468-016-1472-8

Appendixes

“Global evolution of paleoclimate during the Quaternary Period: cyclostratigraphic integration of terrestrial and marine proxies”

José Sánchez-Morales

Granada, 2023

APPENDIXES

1 Data Sources

1.1 Copernicus Climate Change Service Datasets

List of **131** datasets available at https://cds.climate.copernicus.eu/cdsapp#!/search?type=dataset after the conducted analysis in May-2022

Datasets	Tags
In situ observations of meteorological variables from the Integrated Global Radiosounding Archive and the Radiosounding Harmonization dataset from 1978 onward	'In-situ observations', 'Global', 'Atmosphere (upper air)'
Global land surface atmospheric variables from 1755 to 2020 from comprehensive in-situ observations	'In-situ observations', 'Global', 'Atmosphere (surface)'
CMIP5 monthly data on single levels	'Global', 'Atmosphere (surface)', 'Atmosphere (upper air)', 'Climate projections'
CMIP6 climate projections	'Global', 'Atmosphere (surface)', 'Atmosphere (upper air)', 'Climate projections'
CMIP5 daily data on single levels	'Global', 'Atmosphere (surface)', 'Atmosphere (upper air)', 'Climate projections'
In situ total column ozone and ozone soundings from 1924 to present from the World Ozone and Ultraviolet Radiation Data Centre	'In-situ observations', 'Atmosphere (composition)', 'Atmosphere (surface)', 'Atmosphere (upper air)', 'Global'
Global marine surface meteorological variables from 1851 to 2010 from comprehensive in-situ observations	'In-situ observations', 'Atmosphere (surface)', 'Global'
CMIP5 monthly data on pressure levels	'Global', 'Atmosphere (surface)', 'Atmosphere (upper air)', 'Climate projections'
CMIP5 daily data on pressure levels	'Global', 'Atmosphere (surface)', 'Atmosphere (upper air)', 'Climate projections'
ERA5 hourly data on single levels from 1950 to 1978 (preliminary version)	'Atmosphere (surface)', 'Atmosphere (upper air)', 'Global', 'Reanalysis'
ERA5 monthly averaged data on single levels from 1950 to 1978 (preliminary version)	'Atmosphere (surface)', 'Atmosphere (upper air)', 'Global', 'Reanalysis'
ERA5 monthly averaged data on pressure levels from 1950 to 1978 (preliminary version)	'Atmosphere (surface)', 'Atmosphere (upper air)', 'Global', 'Reanalysis'
ERA5 hourly data on pressure levels from 1950 to 1978 (preliminary version)	'Atmosphere (surface)', 'Atmosphere (upper air)', 'Global', 'Reanalysis'
Ozone monthly gridded data from 1970 to present derived from satellite observations	'Atmosphere (composition)', 'Satellite observations', 'Global'
Methane data from 2002 to present derived from satellite observations	'Atmosphere (composition)', 'Satellite observations', 'Global'

Datasets	Tags
Climate and energy indicators for Europe from 2005 to 2100 derived from climate projections	'Energy', 'Europe', 'Atmosphere (surface)', 'Climate projections'
Essential climate variables for water sector applications derived from climate projections	'Climate projections', 'Global', 'Atmosphere (surface)'
Climate data for the European energy sector from 1979 to 2016 derived from ERA-Interim	'Energy', 'Reanalysis', 'Europe'
Arctic route availability and cost projection derived from climate projections of ice concentration and thickness	'Climate projections', 'Global', 'Atmosphere (surface)'
Marine biogeochemistry data for the Northwest European Shelf and Mediterranean Sea from 2006 up to 2100 derived from climate projections	'Coastal regions', 'Climate projections', 'Europe'
Hydrology-related climate impact indicators from 1970 to 2100 derived from bias adjusted European climate projections	'Europe', 'Climate projections', 'Water management'
Performance indicators for offshore wind farms in Europe from 1977 to 2100 derived from climate projections	'Energy', 'Climate projections'
Temperature and precipitation climate impact indicators from 1970 to 2100 derived from European climate projections	'Europe', 'Climate projections', 'Water management'
Ocean surface wave time series for the European coast from 1976 to 2100 derived from climate projections	'Coastal regions', 'Climate projections', 'Europe', 'Ocean (physics)'
Multi-model seasonal reforecasts of river discharge for Europe	'Europe', 'Seasonal forecasts', 'Land (hydrology)', 'Water management'
Ocean surface wave indicators for the European coast from 1977 to 2100 derived from climate projections	'Coastal regions', 'Climate projections', 'Europe', 'Ocean (physics)'
Water level change time series for the European coast from 1977 to 2100 derived from climate projections	'Water management', 'Disaster risk reduction', 'Climate projections', 'Europe', 'Ocean (physics)'
Water quantity indicators for Europe	'Water management', 'Europe', 'Land (hydrology)', 'Climate indices'
Water quality indicators for European rivers	'Water management', 'Europe', 'Land (hydrology)', 'Climate indices'
River discharge and related historical data from the European Flood Awareness System	'Reanalysis', 'Europe', 'Land (hydrology)'
Precipitation monthly and daily gridded data from 2000 to 2017 derived from satellite microwave observations	'Satellite observations', 'Global', 'Land (hydrology)', 'Atmosphere (surface)'
Seasonal forecast monthly statistics on single levels	'Global', 'Seasonal forecasts'
Seasonal forecast monthly statistics on pressure levels	'Global', 'Seasonal forecasts'
Climate and energy indicators for Europe from 1979 to present derived from reanalysis	'Energy', 'Reanalysis', 'Europe'
Seasonal reforecasts of river discharge and related data from the Global Flood Awareness System	'Global', 'Land (hydrology)'
Reforecasts of river discharge and related data by the European Flood Awareness System	'Europe', 'Land (hydrology)'
Near surface meteorological variables from 1979 to 2019 derived from bias-corrected reanalysis	'Global', 'Atmosphere (surface)'

Datasets	Tags
Reforecasts of river discharge and related data by the Global Flood Awareness System	'Global', 'Land (hydrology)'
Temperature and precipitation gridded data for global and regional domains derived from in-situ and satellite observations	'Global', 'Atmosphere (surface)', 'In-situ observations', 'Satellite observations'
In situ temperature, relative humidity and wind profiles from 2006 to March 2020 from the GRUAN reference network	'In-situ observations', 'Global', 'Atmosphere (upper air)'
Alpine gridded monthly precipitation data since 1871 derived from in-situ observations	'Europe', 'Atmosphere (surface)', 'In-situ observations'
Seasonal reforecasts of river discharge and related data by the European Flood Awareness System	'Europe', 'Land (hydrology)'
Glaciers elevation and mass change data from 1850 to present from the Fluctuations of Glaciers Database	'In-situ observations', 'Satellite observations', 'Global', 'Land (cryosphere)'
Glaciers distribution data from the Randolph Glacier Inventory for year 2000	'Global', 'Land (cryosphere)', 'Satellite observations'
Nordic gridded temperature and precipitation data from 1971 to present derived from in-situ observations	'Atmosphere (surface)', 'In-situ observations'
CORDEX regional climate model data on single levels	'Europe', 'Atmosphere (surface)', 'Atmosphere (upper air)', 'Climate projections'
Data Rescue Service from the Copernicus Climate Change Service	'Global', 'External services'
Complete UERRA regional reanalysis for Europe from 1961 to 2019	'Reanalysis', 'Europe', 'Atmosphere (upper air)'
Carbon dioxide data from 2002 to present derived from satellite observations	'Atmosphere (composition)', 'Satellite observations', 'Global'
UERRA regional reanalysis for Europe on single levels from 1961 to 2019	'Reanalysis', 'Europe', 'Atmosphere (upper air)'
UERRA regional reanalysis for Europe on pressure levels from 1961 to 2019	'Reanalysis', 'Europe', 'Atmosphere (upper air)'
UERRA regional reanalysis for Europe on height levels from 1961 to 2019	'Reanalysis', 'Europe', 'Atmosphere (upper air)'
UERRA regional reanalysis for Europe on soil levels from 1961 to 2019	'Reanalysis', 'Europe', 'Land (hydrology)'
Leaf area index and fraction absorbed of photosynthetically active radiation 10-daily gridded data from 1981 to present	'Satellite observations', 'Land (biosphere)', 'Global'
Fire radiative power and active fire pixels from 2020 to present derived from satellite observations	'Satellite observations', 'Global', 'Land (biosphere)'
Lake water levels from 1992 to present derived from satellite observations	'Satellite observations', 'Global', 'Land (hydrology)'
Fire burned area from 2001 to present derived from satellite observations	'Satellite observations', 'Global', 'Land (biosphere)'
Greenland ice sheet annual gridded velocity data from 2017 to present derived from satellite observations	'Land (cryosphere)', 'Satellite observations'
Lake surface water temperature from 1995 to present derived from satellite observations	'Satellite observations', 'Global'

Datasets	Tags
Gravimetric mass balance data for the Antarctic and Greenland ice sheets from 2003 to 2017 derived from satellite observations	'Land (cryosphere)', 'Satellite observations'
Sea level daily gridded data from satellite observations for the global ocean from 1993 to present	'Global', 'Satellite observations', 'Ocean (physics)'
Sea surface temperature daily gridded data from 1981 to 2016 derived from a multi-product satellite-based ensemble	'Satellite observations', 'Global', 'Ocean (physics)'
Monthly total column water vapour over land and ocean from 2002 to 2012 derived from satellite observations	'Satellite observations', 'Global', 'Atmosphere (upper air)'
Monthly and 6-hourly total column water vapour over ocean from 1988 to 2020 derived from satellite observations	'Satellite observations', 'Atmosphere (upper air)'
Sea level daily gridded data from satellite observations for the Mediterranean Sea from 1993 to 2020	'Europe', 'Satellite observations', 'Ocean (physics)'
Sea level daily gridded data from satellite observations for the Black Sea from 1993 to 2020	'Europe', 'Satellite observations', 'Ocean (physics)'
Agroclimatic indicators from 1951 to 2099 derived from climate projections	'Agriculture', 'Climate projections', 'Global', 'Land (biosphere)'
Upper tropospheric humidity gridded data from 1999 to present derived from satellite observations	'Global', 'Atmosphere (upper air)', 'Satellite observations'
Eutrophication indicators for the Northwest European Shelf and Mediterranean Sea from 2006 up to 2100	'Coastal regions', 'Climate projections', 'Global'
Fish abundance and catch data for the Northwest European Shelf and Mediterranean Sea from 2006 to 2098 derived from climate projections	'Coastal regions', 'Climate projections', 'Europe'
Synthetic windstorm events for Europe from 1986 to 2011	'Europe', 'Atmosphere (surface)'
Ocean fronts data for the Northwest European Shelf and Mediterranean Sea from 1991 up to 2100	'Coastal regions', 'Satellite observations', 'Climate projections', 'Europe', 'Ocean (physics)'
Climate extreme indices and heat stress indicators derived from CMIP6 global climate projections	'Global', 'Land (biosphere)', 'Climate indices', 'Climate projections'
Winter windstorm indicators for Europe from 1979 to 2021 derived from reanalysis	'Europe', 'Atmosphere (surface)', 'Reanalysis'
Climatic suitability for the presence and seasonal activity of the Aedes albopictus mosquito for Europe derived from climate projections	'Health', 'Europe', 'Climate projections', 'Land (biosphere)'
Heat waves and cold spells in Europe derived from climate projections	'Health', 'Europe', 'Climate projections', 'Atmosphere (surface)'
Mountain tourism meteorological and snow indicators for Europe from 1950 to 2100 derived from reanalysis and climate projections	'Tourism', 'Climate projections', 'Europe', 'Land (hydrology)'
Climate suitability indicators for tourism from 1970 to 2100 over Europe derived from climate projections	'Tourism', 'Europe', 'Land (biosphere)', 'Climate projections'
Water sector indicators of hydrological change across Europe from 2011 to 2095 derived from climate simulations	'Europe', 'Climate projections', 'Land (hydrology)', 'Water management'
Water level change indicators for the European coast from 1977 to 2100 derived from climate projections	'Water management', 'Disaster risk reduction', 'Climate projections', 'Europe', 'Ocean (physics)'
Soil erosion indicators for Italy from 1981 to 2080	'Agriculture', 'Infrastructure', 'Climate projections', 'Reanalysis',

Datasets	Tags
	'In-situ observations', 'Europe', 'Land (hydrology)'
Ship performance along standard shipping routes derived from reanalysis and seasonal forecasts	'Reanalysis', 'Global', 'Atmosphere (surface)'
Temperature statistics for Europe derived from climate projections	'Europe', 'Climate projections', 'Atmosphere (surface)'
Seasonal forecast anomalies on single levels	'Global', 'Seasonal forecasts'
Seasonal forecast daily and subdaily data on single levels	'Global', 'Seasonal forecasts'
Seasonal forecast subdaily data on pressure levels	'Global', 'Seasonal forecasts'
Seasonal forecast anomalies on pressure levels	'Global', 'Seasonal forecasts'
Multi-model seasonal forecasts of river discharge for Europe from January 2021 to present	'Europe', 'Seasonal forecasts', 'Land (hydrology)', 'Water management'
ORAS5 global ocean reanalysis monthly data from 1958 to present	'Reanalysis', 'Global', 'Ocean (physics)'
Ice sheet surface elevation change rate for Greenland and Antarctica from 1992 to present derived from satellite observations	'Land (cryosphere)', 'Satellite observations'
Surface radiation budget from 1982 to present derived from satellite observations	'Satellite observations', 'Atmosphere (surface)', 'Global'
Land cover classification gridded maps from 1992 to present derived from satellite observations	'Satellite observations', 'Global', 'Land (hydrology)', 'Land (biosphere)'
Downscaled bioclimatic indicators for selected regions from 1950 to 2100 derived from climate projections	'Biodiversity', 'Global', 'Land (biosphere)'
Global bioclimatic indicators from 1950 to 2100 derived from climate projections	'Biodiversity', 'Global', 'Land (biosphere)'
Fire danger indicators for Europe from 1970 to 2098 derived from climate projections	'Europe', 'Land (biosphere)', 'Climate projections'
Global bioclimatic indicators from 1979 to 2018 derived from reanalysis	'Biodiversity', 'Reanalysis', 'Global', 'Land (biosphere)'
E-OBS daily gridded meteorological data for Europe from 1950 to present derived from in-situ observations	'Europe', 'Atmosphere (surface)', 'In-situ observations'
Extreme precipitation risk indicators for Europe and European cities from 1950 to 2019	'Europe', 'Land (hydrology)', 'Climate indices'
Flood risk indicators for European cities from 1989 to 2018	'Disaster risk reduction', 'Water management', 'Europe', 'Land (hydrology)', 'Climate indices'
Climate variables for cities in Europe from 2008 to 2017	'Europe', 'Reanalysis', 'Atmosphere (surface)'
Downscaled bioclimatic indicators for selected regions from 1979 to 2018 derived from reanalysis	'Biodiversity', 'Reanalysis', 'Global', 'Land (biosphere)'
Aerosol properties gridded data from 1995 to present derived from satellite observations	'Global', 'Atmosphere (composition)', 'Satellite observations'
Precipitation monthly and daily gridded data from 1979 to present derived from satellite measurements	'Satellite observations', 'Global', 'Land (hydrology)', 'Atmosphere (surface)'
Surface albedo 10-daily gridded data from 1981 to present	'Satellite observations', 'Land (biosphere)', 'Global'
ERA5-Land hourly data from 1950 to present	'Reanalysis', 'Global', 'Land (hydrology)', 'Land (biosphere)'

Datasets	Tags
ERA5-Land monthly averaged data from 1950 to present	'Reanalysis', 'Global', 'Land (hydrology)', 'Land (biosphere)'
Ocean colour daily data from 1997 to present derived from satellite observations	'Ocean (biochemistry)', 'Satellite observations', 'Global'
Essential climate variables for assessment of climate variability from 1979 to present	'Global', 'Reanalysis'
Earth's radiation budget from 1979 to present derived from satellite observations	'Satellite observations', 'Atmosphere (upper air)', 'Global'
ERA5 monthly averaged data on single levels from 1979 to present	'Atmosphere (surface)', 'Atmosphere (upper air)', 'Global', 'Reanalysis'
ERA5 monthly averaged data on pressure levels from 1979 to present	'Atmosphere (surface)', 'Atmosphere (upper air)', 'Global', 'Reanalysis'
Soil moisture gridded data from 1978 to present	'Satellite observations', 'Global', 'Land (hydrology)'
Seasonal forecasts of river discharge and related data by the European Flood Awareness System	'Seasonal forecasts', 'Europe', 'Land (hydrology)'
Seasonal forecasts of river discharge and related data by the Global Flood Awareness System	'Seasonal forecasts', 'Global', 'Land (hydrology)'
Arctic regional reanalysis on single levels from 1991 to present	'Reanalysis', 'Atmosphere (upper air)'
Arctic regional reanalysis on pressure levels from 1991 to present	'Reanalysis', 'Atmosphere (upper air)'
Arctic regional reanalysis on model levels from 1991 to present	'Reanalysis', 'Atmosphere (upper air)'
Arctic regional reanalysis on height levels from 1991 to present	'Reanalysis', 'Atmosphere (upper air)'
River discharge and related forecasted data by the European Flood Awareness System	'Europe', 'Land (hydrology)'
Sea ice thickness monthly gridded data for the Arctic from 2002 to present derived from satellite observations	'Satellite observations', 'Ocean (physics)', 'Global'
Tropospheric humidity profiles averaged monthly and zonally from 2006 to present derived from satellite observations	'Global', 'Atmosphere (upper air)', 'Satellite observations'
Sea ice edge and type daily gridded data from 1978 to present derived from satellite observations	'Satellite observations', 'Ocean (physics)', 'Global'
Sea ice concentration daily gridded data from 1979 to present derived from satellite observations	'Satellite observations', 'Ocean (physics)', 'Global'
Sea surface temperature daily data from 1981 to present derived from satellite observations	'Satellite observations', 'Global', 'Ocean (physics)'
Agrometeorological indicators from 1979 to present derived from reanalysis	'Agriculture', 'Reanalysis', 'Global', 'Land (biosphere)'
Fire danger indices historical data from the Copernicus Emergency Management Service	'Reanalysis', 'Global', 'Land (biosphere)'
Thermal comfort indices derived from ERA5 reanalysis	'Reanalysis', 'Global'
River discharge and related forecasted data by the Global Flood Awareness System	'Reanalysis', 'Global', 'Land (hydrology)'
River discharge and related historical data from the Global Flood Awareness System	'Reanalysis', 'Global', 'Land (hydrology)'

Datasets	Tags
ERA5 hourly data on pressure levels from 1979 to present	'Atmosphere (surface)', 'Atmosphere (upper air)', 'Global', 'Reanalysis'
ERA5 hourly data on single levels from 1979 to present	'Atmosphere (surface)', 'Atmosphere (upper air)', 'Global', 'Reanalysis'

1.2 Copernicus Climate Change Service Applications

List of **20** applications available at https://cds.climate.copernicus.eu/cdsapp#!/search?type=dataset after the conducted analysis in May-2022.

Applications	Tags
Monthly climate explorer for COVID-19	
Marine spatial planning explorer	Coastal regions', 'Climate projections', 'Europe'
The number of heat wave days for European countries derived from climate projections	Health', 'Europe'
Heat wave days and heat related mortality for nine European cities derived from climate projections	Health', 'Europe'
European temperature statistics derived from climate projections	Health', 'Europe'
Heat wave days for Europe derived from ERA5 reanalysis	Health', 'Europe'
Date of birch pollen season onset from 2010 to 2019 derived from reanalysis	Health', 'Europe'
Urban climate for cities in Europe from 2008 to 2017	Health', 'Europe'
Urban heat island intensity for European cities from 2008 to 2017 derived from reanalysis	Health', 'Europe'
European temperature statistics derived from ERA5 reanalysis	Health', 'Europe'
Soil erosion explorer for Italy from 1981 to 2080	Agriculture', 'Infrastructure'
Global latitude-height distribution of tropospheric humidity	Global', 'Satellite observations'
Mountain tourism meteorological and snow indicators for Europe from 1986 to 2100 derived from reanalysis and climate projections	Tourism', 'Europe'
Satellite soil moisture explorer	Satellite observations', 'Global', 'Land (hydrology)'
Surface radiation budget analysis tool for observations from the ESA Cloud_CCI project	Global', 'Satellite observations', 'Atmosphere (surface)'
Fire weather indicators for Europe from 1970 to 2098 derived from reanalysis and climate projections	Tourism', 'Europe'
Climate monitoring and volcanic eruptions	Europe', 'Disaster risk reduction'
Global temperature trend monitor	Global'
Indicators of water level change for European coasts in the 21st Century	Coastal regions', 'Europe'
White, white, wet: when might we have our last white Christmas?	

2 Methodology

2.1 Visualization of evolutive spectral time series

List of used input parameters for running the tests on the code hosted at https://github.com/jose-sanchez-morales/spectral-analysis-visualization-method.

Parameter	Default value	Description
ACHIEVED_CONFIDENCE_LEVEL	95	The confidence level (0-100) of the power spectrum to be used as the limit for differentiating between displayed and non-displayed values in the visualization.
HIGHEST_FREQUENCY_TO_EVALUATE	0.06	The highest frequency evaluated in the spectral analysis and it indicates the maximum value of the y-axis (top).
LOWEST_FREQUENCY_TO_EVALUATE	0.00	The lowest frequency evaluated in the spectral analysis and it indicates the minimum value of the y-axis (top).
NUMBER_OF_FREQUENCIES	500	The number of frequencies evaluated (i.e. Lomb-Scargle periodogram). It is also the number of records per time sub-series file.
NODATA	-999	The NoData values representing the absence of data in the output raster files.
REMOVE_TEMP	False	For deciding on whether to keep the intermediate files, or just the final output raster file.
DATA_FOLDER	“pipeline\data\subseries_stack_combined”	The relative path of the input folder where the input files are located (.ACL, .LOM, .prn)
RUN_NAME	"d18stack_assesment_" + capture	The root or basename of the output files. It adds the time stamp of the execution (capture).

Parameter	Default value	Description
template_filename	"d18-0001.prn"	The filename with extension of any input file of the time sub-series containing the frequencies and the power spectrum. It is there for validation purposes.
search_expression	"d18"	A portion of the basename of the input files. In the event of having different paleoclimate time series in the same folder, this parameter ensures that only certain files meeting the condition will be picked up by the code.
tile_plot	"LR04 Global Pliocene-Pleistocene Benthic delta-O-18 Stack Power Spectra"	The tile of the plot for producing the enhanced visualization in the final module.
OUTPUT_FOLDER	“pipeline\output”	The relative path of the output folder where the output raster files will be saved.
PROJECTION_FILE_TEMPLATE	“pipeline\templates\projection_file.prj“	The relative path of the location of the projection file (.prj) used for the specifics in the terrain analysis operations. The coordinate system by default is the British National Grid (EPSG:27700), which operates in meters.
COLOR_FILE_TEMPLATE	“pipeline\templates\color-ramp-PW-stack.clr”	The relative path of the location of the colour ramp file (.clr) containing the power spectrum value and the associated RGB colour. This file must be edited to incorporate new values and/or colours.

Parameter	Default value	Description
SLOPESHADE_FILE_TEMPLATE	“pipeline\templates\color_slope.txt”	The relative path of the location of the colour slope file (.txt) containing the angle of the slope and the associated RGB colour. By default uses whites for flat surfaces and blacks for Sloping terrain.
MAPNIK_TEMPLATE	“pipeline\templates\mapnik_template.xml”	The relative path of the location of the mapnik template (.xml) which incorporates the opacity values and the relative order of the color relief, slopeshade and hillshade files.
MAPNIK_FOLDER	“pipeline\code\pipeline_modules”	The relative path of the location of the folder where the mapnik_blending.py” script is located, which performs the blending operation of the individual raster files. This script is run in a different manner by the pipeline.

3 Speleothems. A case study using speleothems data

3.1 Estimated Lomb–Scargle power spectrum

A detailed summary of all the significant frequencies found on the 24 individual speleothems when estimating the Lomb-Scargle power spectrum.

Speleothem (SISAL entity code)	Period (years)	99% ACL	95% ACL	90% ACL
048	T > 1,000	1639	1639	1639
	500 < T < 1,000	855, 662, 549, 521	855, 662, 549, 521	855, 662, 549, 521
	500 < T	389, 273, 245, 162, 154, 145	389, 301, 273, 245, 225, 211, 187, 162, 154, 145, 107	389, 301, 273, 245, 225, 211, 187, 176, 169, 162, 154, 145, 133, 119, 113, 107
054	T > 1,000	3333, 1923, 1124	3333, 1923, 1124	3333, 1923, 1124
	500 < T < 1,000	826, 641	826, 641, 510	826, 641, 510
	T < 500	-	-	-
117	T > 1,000	2381, 1389	2381, 1389	2381, 1389
	500 < T < 1,000	625	625	625
	T < 500	459, 383, 350, 266	459, 383, 350, 266, 121	459, 383, 350, 300, 266, 235, 186, 176, 155, 121
124	T > 1,000	2174, 1031	2174, 1031	2174, 1031
	500 < T < 1,000	-	-	629
	T < 500	-	-	-
205	T > 1,000	1818, 1176	1818, 1176	1818, 1176
	500 < T < 1,000	-	-	-
	T < 500	-	-	337
238	T > 1,000	2222, 1176	2222, 1176	2222, 1176
	500 < T < 1,000	943, 588	943, 588	943, 588
	T < 500	426, 369, 290, 109	426, 369, 290, 194, 137, 126, 109	426, 369, 290, 194, 158, 137, 126, 113, 109
244	T > 1,000	2857, 1299	2857, 1299	2857, 1299
	500 < T < 1,000	917, 714, 602	917, 714, 602	917, 714, 602
	T < 500	483, 360, 332, 323, 290, 264, 258, 237, 225, 206, 197, 180,	483, 360, 332, 323, 290, 264, 258, 237, 225, 206, 197, 180,	483, 360, 332, 323, 290, 264, 258, 237, 225, 206, 197, 180,

Speleothem (SISAL entity code)	Period (years)	99% ACL	95% ACL	90% ACL
		172, 166, 159, 150, 142, 135, 130, 128, 124, 119, 116, 112, 109, 106, 104, 101	172, 166, 159, 150, 142, 135, 130, 128, 124, 119, 116, 112, 109, 106, 104, 101	172, 166, 159, 150, 142, 135, 130, 128, 124, 119, 116, 112, 109, 106, 104, 101
292	T > 1,000	2439, 1351	2439, 1351	2439, 1351
	500 < T < 1,000	971, 704	971, 704	971, 704
	T < 500	485, 400, 347, 313, 282, 266, 244, 225, 128, 122	485, 400, 347, 313, 282, 266, 244, 225, 208, 194, 181, 141, 134, 128, 122, 119	485, 400, 347, 313, 282, 266, 244, 225, 208, 194, 181, 141, 134, 128, 122, 119, 106
298	T > 1,000	2857, 2222, 1471	2857, 2222, 1471	2857, 2222, 1471
	500 < T < 1,000	909, 741, 690, 592	909, 741, 690, 592	909, 741, 690, 592
	T < 500	478, 435, 383	478, 435, 383	478, 435, 383, 207
305	T > 1,000	2128, 1099	2128, 1099	2128, 1099
	500 < T < 1,000	752, 588, 505	752, 588, 505	752, 588, 505
	T < 500	444, 389, 322, 293, 258, 235, 223, 204, 185, 177, 168, 153, 141, 135, 125, 120, 115	444, 389, 322, 293, 258, 235, 223, 204, 185, 177, 168, 153, 141, 135, 125, 120, 115, 101	444, 389, 322, 293, 258, 235, 223, 204, 185, 177, 168, 153, 141, 135, 125, 120, 115, 101
312	T > 1,000	1667	1667	1667
	500 < T < 1,000	-	-	-
	T < 500	-	-	-
350	T > 1,000	-	1852	1852
	500 < T < 1,000	-	-	-
	T < 500	285	285, 225	317, 285, 225, 215
351	T > 1,000	1852, 1010	1852, 1010	1852, 1010
	500 < T < 1,000	685, 543	685, 543	685, 543
	T < 500	467, 420, 353, 342, 318, 231, 196, 163, 152, 134, 101	467, 420, 353, 342, 318, 231, 196, 163, 152, 134, 101	467, 420, 353, 342, 318, 231, 196, 163, 152, 134, 101
354	T > 1,000	1429	1429	1429
	500 < T < 1,000	532	532	532
	T < 500	392, 353, 331, 271, 180, 156, 137, 128, 102	392, 353, 331, 271, 201, 180, 156, 137, 128, 102	532, 392, 353, 331, 271, 236, 201, 180, 156, 137, 128, 102
395	T > 1,000	3226, 1205	3226, 1205	3226, 1205
	500 < T < 1,000	758, 549	758, 549	758, 549

Speleothem (SISAL entity code)	Period (years)	99% ACL	95% ACL	90% ACL
	T < 500	476, 373, 339, 289, 269, 220, 207, 195, 159, 131	476, 373, 339, 289, 269, 220, 207, 195, 159, 137, 131, 126, 107	476, 373, 339, 289, 269, 249, 220, 207, 195, 185, 168, 159, 137, 131, 126, 120, 112, 107
410	T > 1,000	-	2083, 1493	2083, 1493
	500 < T < 1,000	-	-	508
	T < 500	-	121	266, 179, 121
434	T > 1,000	2326, 1333	2326, 1333	2326, 1333
	500 < T < 1,000	926, 690, 541	926, 690, 541	926, 690, 541
	T < 500	417, 377, 321, 296, 265, 248, 216, 201, 181, 174, 162, 154, 148, 138, 125, 119, 114, 103	417, 377, 321, 296, 265, 248, 216, 201, 181, 174, 162, 154, 148, 138, 125, 119, 114, 109, 103	417, 377, 321, 296, 265, 248, 216, 201, 181, 174, 162, 154, 148, 138, 125, 119, 114, 109, 103
436	T > 1,000	3448, 1587, 1176	3448, 1587, 1176	3448, 1587, 1176
	500 < T < 1,000	719	719	719
	T < 500	493, 444, 162	493, 444, 299, 260, 162	493, 444, 350, 299, 260, 201, 162
446	T > 1,000	2083	2083	2083
	500 < T < 1,000	901, 667, 585, 508	901, 667, 585, 508	901, 667, 585, 508
	T < 500	403, 352, 293, 275, 259, 240, 212, 187, 172, 164, 156, 147, 139, 132, 126, 115	403, 352, 293, 275, 259, 240, 212, 187, 172, 164, 156, 147, 139, 132, 126, 119, 115, 112, 109	403, 352, 293, 275, 259, 240, 212, 187, 172, 164, 156, 147, 139, 132, 126, 119, 115, 112, 109, 103
496	T > 1,000	1471	1471	1471
	500 < T < 1,000	613	613	613
	T < 500	403, 372, 220, 205, 174, 153, 140, 130, 116	485, 403, 372, 306, 270, 242, 220, 205, 174, 161, 153, 140, 135, 130, 116	485, 403, 372, 306, 270, 242, 220, 205, 184, 174, 161, 153, 140, 135, 130, 116, 111, 105
523	T > 1,000	2500, 1266	2500, 1266	2500, 1266
	500 < T < 1,000	-	-	662
	T < 500	-	-	-
589	T > 1,000	1923, 1042	1923, 1042	1923, 1042
	500 < T < 1,000	725	725	725

Speleothem (SISAL entity code)	Period (years)	99% ACL	95% ACL	90% ACL
	T < 500	613, 472, 405, 347, 323, 280, 180, 163, 153, 130	613, 472, 405, 347, 323, 280, 180, 163, 153, 130, 125, 114, 108, 105, 104	613, 472, 405, 347, 323, 280, 180, 169, 163, 153, 146, 130, 125, 114, 108, 105, 104
613	T > 1,000	3571, 1613, 1176	3571, 1613, 1176	3571, 1613, 1176
	500 < T < 1,000	917, 763, 610	917, 763, 610	917, 763, 610
	T < 500	493, 364	493, 448, 364, 250, 226, 179	493, 448, 364, 265, 250, 226, 179, 126
650	T > 1,000	1449, 1111	1449, 1111	1449, 1111
	500 < T < 1,000	806, 526	806, 526	806, 526
	T < 500	481	481, 407, 190, 175, 105	481, 407, 292, 190, 175, 105

Table 3.1. Comparative between all detected frequencies above 99%, 95% and 90% of achieved confidence level (ACL), expressed as period in years, for all 24 analysed speleothems' residuals, using the estimated Lomb–Scargle power spectrum.

4 Ice cores. A case study using ice cores data

4.1 Spectral Methods

A summary of all the parameters used in both the SLOMBS and CSLOMBS programs.

Fig. Number Main document	DATASET/S	Parameters			P1	P2	P3	P4	P5	P6	Significant cycles acceptance criteria
		Software used	Number of series (runs)	Time length / number records per series	Highest frequency to evaluate (1/T)	Number of frequencies in the interval	Number of permutations	Integer random number (seed)	Smoothing (0: NO SMOOTHING, 1 MEAN SMOOTHING, 2 LINEAR	Number of smoothing terms	
Fig. 8a	High res NEGIS sodium 2003 – 1979 AD	CSLOMBS	1	295 months (25 yr)	0.5 (2 yr)	1,000	2,000	75,654	2	3	ACL>90% COH > 0.8
	ERA5 wind vertical velocity 2003 – 1979 AD		37								
	High res NEGIS sodium 2003 – 1979 AD	CSLOMBS	1	295 months (25 yr)	0.5 (2 yr)	1,000	2,000	75,654	2	3	ACL>90% COH > 0.8
	ERA5 wind azimuth 2003 – 1979 AD		37								
	High res NEGIS sodium 2003 – 1979 AD	CSLOMBS	1	295 months (25 yr)	0.5 (2 yr)	1,000	2,000	75,654	2	3	ACL>90% COH > 0.8
	ERA5 wind speed 2003 – 1979 AD		37								
Fig. 8e	SUMMIT07 sodium 2006 – 1950 AD	CSLOMBS	1	57 yr	0.5 (2 yr)	1,000	5,000	75,654	2	3	ACL>90% COH > 0.8
	ERA5 wind vertical velocity 2006 – 1950 AD		37								
	SUMMIT07 sodium 2006 – 1950 AD	CSLOMBS	1	57 yr	0.5 (2 yr)	1,000	5,000	75,654	2	3	ACL>90% COH > 0.8
	ERA5 wind azimuth 2006 – 1950 AD		37								
	SUMMIT07 sodium 2006 – 1950 AD	CSLOMBS	1	57 yr	0.5 (2 yr)	1,000	5,000	75,654	2	3	ACL>90% COH > 0.8
	ERA5 wind speed 2006 – 1950 AD		37								
Fig. 8.6	High res NEGIS sodium series 2005 – 1610 AD	SLOMBS	86	51 yr / 608	1 (1 yr)	1,000	2,000	75,654	2	31	ACL>95%
	Ultra-high res GISP2 sodium series 12,824 – 12,849 yr BP	SLOMBS	38	22 yr / 255	1 (1 yr)	1,000	2,000	75,654	2	31	ACL>95%
	Ultra-high res GISP2 sodium series 12,866 – 12,909 yr BP	SLOMBS	81	22 yr / 261	1 (1 yr)	1,000	2,000	75,654	2	31	ACL>95%
	Ultra-high res GISP2 sodium series 12,913 – 12,934 yr BP	SLOMBS	58	16 yr / 180	1 (1 yr)	1,000	2,000	75,654	2	31	ACL>95%
	Ultra-high res GISP2 sodium series 13,028 – 13,040 yr BP	SLOMBS	35	10 yr / 121	1 (1 yr)	1,000	2,000	75,654	2	31	ACL>95%